Multiscale Determination of In Situ Stress and Fracture Properties in Reservoirs

by

Samantha Grandi-Karam

S.M., Massachusetts Institute of Technology (2003)
Geophysical Engineer, Universidad Simón Bolívar (1995)

Submitted to the Department of Earth, Atmospheric and Planetary Sciences
in partial fulfillment of the requirements for the degree of

Doctor of Philosophy

at the

MASSACHUSETTS INSTITUTE OF TECHNOLOGY

February 2008

Author .....
Department of Earth, Atmospheric and Planetary Sciences
February 1st, 2008

Certified by .....
M. Nafi Toksöz
Professor of Geophysics
Thesis Supervisor

Certified by .....
Mark E. Willis
Research Scientist
Co-Thesis Advisor

Accepted by .....
Maria T. Zuber
E.A. Griswold Professor of Geophysics
Head, Department of Earth, Atmospheric and Planetary Sciences

Multiscale Determination of In Situ Stress and Fracture Properties in Reservoirs

by

Samantha Grandi-Karam

Submitted to the Department of Earth, Atmospheric and Planetary Sciences
on February 1st, 2008, in partial fulfillment of the
requirements for the degree of
Doctor of Philosophy

Abstract

In this thesis we address the problem of determining in situ stress and fracture properties in reservoirs using borehole logs and surface seismic reflection data. The dissertation covers four subtopics.

The first is the determination of horizontal stress magnitudes from measurements in a borehole. Two types of data used are stress-induced rock failures in the borehole, known as "breakouts," and the dispersions of polarized flexural waves which propagate along the borehole. Traditionally these data are analyzed to derive stress orientations but not magnitudes. To determine the magnitude of stresses directly from breakouts, we use an iterative elastic modeling of stresses around the borehole and Mohr-Coulomb failure criterion to match the borehole deformation. As a second method we use dispersion curves of the two polarized flexural waves and their crossover points. These methods are applied to data from a well in northeastern Venezuela. The combination of these two techniques provides a complete profile of stress as a function of depth since the first method is applied at the breakout depths and the second is applied everywhere else in the borehole. Both borehole methods agree in the estimation of stress orientation and magnitude. The maximum horizontal stress is in the NNW-SSE direction, in agreement with a regional stress model calculated from the relative motions of the Caribbean and South America plates. The magnitudes of principal stresses are on average, $SHmax \simeq 1.1Sv$ (Sv: vertical stress) and $Shmin \simeq 0.9Sv$ ($Shmin$: minimum horizontal stress). This suggests strike-slip faulting, consistent with earthquake mechanisms in the region.

The in situ stresses play an important role on determining the properties of fractured formation. The azimuth of $SHmax$ determines the preferred orientation of open fractures. Surface seismic reflection data provide the means for detecting the fractures. The second contribution of this thesis is developing a method to detect discrete fractures, and to determine their orientation and average spacing. We developed a novel and practical technique, called the F-K method, based on the frequency-wavenumber (f-k) domain analysis of seismic coda. The fractured medium targeted in this study is a network of rather regularly spaced, parallel, sub-vertical fractures,

with dimensions similar to seismic wavelength. The seismic response of a fractured medium is studied by finite difference numerical models for a variety of situations where orientation, spacing, height, and fracture compliance are varied. In the direction normal to fractures, scattered waves propagate with slower apparent velocities than waves propagating along the fractures. The orientation of fractures is well-constrained from the azimuthal dependence of scattering. The spectral characteristics (frequency, wavenumber and amplitude) of the backscattered waves are related to fracture properties like spacing, compliance, and height. The dominant wavenumber is very sensitive to fracture spacing.

We use the *F-K* method to analyze a data set from the Lynx Field in Canada. Characterization of fracture properties in this field is important for development plans to maximize the gas production. In the field data, the acquisition geometry results in irregular fold, with under sampling of certain azimuths and offsets. We address the acquisition footprint issue by controlling the azimuth binning of the data and neglecting the low/irregular fold gathers in the fracture analysis. We also apply the Scattering Index (*SI*) method (Willis et al., 2006) to the same data from the Lynx Field. The *SI* method is a robust method to detect fractures and to provide fracture orientations using multi-azimuth/multi-offset pre-stack data. In the realm of existing 3D seismic surveys, data with such acquisition characteristics are few. The fourth contribution of this thesis is therefore the conception of a post-stack version of the *SI* method that extends the scope of this method to practically every 3D seismic surface data set. In this version, a scattering index is computed for a fully stacked trace per CMP gather. As long as the bin contains traces parallel to the fracture strike, the stacking process of all azimuths and offsets preserves the reverberating character introduced by the fractures. The post-stack *SI* at a fractured location has a large value in comparison to a non-fractured location. The variations of post-stack *SI* values across the field reveal the distribution of highly fractured areas. Fracture strike cannot be determined in this case because it does not include the azimuthal behavior of the scattering. However, the results from the post-stack *SI* are helpful to identify areas of interest to focus the more specialized scattering analysis methods. We apply the *F-K* and *SI* methods to the Lynx Field seismic data and compare the results. Since spatial resolution of the two methods are different we upscale the *SI* maps to match the resolution of the *F-K* method. The combined analysis of the Lynx Field indicates that the preferred fracture orientation is N40°E, which agrees with the regional stress field. The distribution of highly fractured regions appears to be associated to the geological features, such as folds and faults. The average fracture spacing, obtained by the *F-K* method shows that, in the Lynx Field, fracture spacing decreases in the west side of the field where the structural dips are higher.

Thesis Supervisor: M. Nafi Toksöz
Title: Professor of Geophysics

Co-Thesis Advisor: Mark E. Willis
Title: Research Scientist

Acknowledgments

I wish to thank my advisor, Prof. Nafi Toksöz, first for giving me the opportunity to do this PhD and having the right vision about my professional future had I returned home at those confused times. Second, I am most grateful for his guidance throughout this long journey. His endless dedication to the Earth sciences sets an unmatched example of the excellency, rigorousness, and passion that should define any great scientist. Nafi has always pushed us to think freely and critically, be curious and innovative.

I heard somewhere that besides these and other qualities, a great scientist has to have impeccable communication skills. Dr. Mark Willis, my co-advisor, has selfishless taught me the importance of getting across our ideas clearly and honestly. I can only hope that my papers and proposals in the future show the same attention to detail and consideration to the readers that Mark puts in all his communications. But this is secondary in front of the great appreciation I have for Mark's technical knowledge, his spark to come up with so many good ideas, his integral understanding of the impact and applicability of what we do, and the love and fun he finds in his work. I am deeply thankful to Mark for the invaluable support he gave me in every step of this research and preparing this thesis.

Dan Burns (the soul of ERL) has also given me an immense support all these years. I am very grateful to Dan for the eye-opening technical discussions and his always contagious eagerness. Dan Burns and Rama Rao followed my research very keenly, while giving me excellent advice on how to test and present most of the ideas in this thesis. I learnt a huge deal from them and especially enjoyed the long hours we worked together in borehole acoustic problems. I also thank Prof. Dale Morgan for his unconventional and useful advising, not only in geosciences but in the everyday life.

I am grateful to several other people in ERL and MIT. Many thanks go to Sue Turbak, Liz Henderson, Carol Sprague, Linda Meinke, and Scott Blomquist. It has been a real pleasure to have worked close to Bill Rodi, Sadi Kuleli, Zenhya Zhu,

Stéphane Rondenay, Robert Reilinger, and my peers and ex-peers students and post-docs, especially, Victoria, Burke, Sudipta, Rongrong, Darrell, Youshun, Xin, Yang, Fred, Xiaojun, Mary, Xander; and my ex-office mates Jonathan, Sophie, and Fuxian. Above all, I have to thank all these people for their human quality. There is no doubt that these years have been difficult. Learning and pursuing any research is generally painful, stressful, and often frustrating, but to have met these driven and good people makes this a beautiful and rewarding experience.

My years at MIT were financially supported first by the former Exploration Division of Petróleos de Venezuela (PDVSA), and then by the U.S. Department of Energy, the Borehole Acoustics and Logging Consortium, and the Founding Member Consortium of the Earth Resources Laboratory at MIT.

I am thankful to my former managers in PDVSA, especially Carlos Sánchez and Richard Aymard, for believing in me. PDVSA provided the borehole data presented in this thesis, and I got great technical support from many people in the company, in particular Franklin Ruíz. The Lynx field data was provided by ConocoPhillips and VeritasDGC. I would like to thank Tad Smith from VeritasDGC, and Doug Foster, Ethan Nowak, and Dean Sinnott from ConocoPhillips, for the valuable discussions and technical information; and Doug Foster for also being part of my committee and for his useful comments to improve this thesis.

Thanks to ERL's industry consortia I had the opportunity to meet and collaborate with other great scientists that directly or indirectly helped me at some point in my research. They are: Sung Yuh and Ramin Nawab from Total, Gopa De and Dennis Schmitt from Chevron, Laura Vetri from AGIP-ENI, Randolph Martin and Stephen Brown from New England Research, Brian Hornby from BP, and Bikash Sinha from Schlumberger-Doll Research.

Life is full of unforeseen events and being in a foreign country did not make it any easier. The only way I could possibly persist sanely in this long endeavor was thanks to God and my family and friends' unconditional love. My aunts: Faride, Zoed, Mariett, Nora, and Lordett; and cousins: Farida, Miguel and Karen, are my fortitude. My friends: JK (the guardian angel), Fabio, Jean Paul, Daniel, Igor, Javier,

Patricia, and Manuel, stayed all these years closed to me and did not let me dismay. My mother, Ross Marie, is the source of all my inspiration, the reason of all. This degree is for her and because of her.

I dedicate this thesis to my mother, my grandmother Emelí and my uncle Jesús.

Contents

List of Figures

List of Tables

Chapter 1

Introduction

Knowledge of the current stress state at depth is essential in several stages of the exploration, production, and development of hydrocarbon and water reservoirs. Stresses in the lithosphere are responsible for the formation of geological structures, for example, salt diapirism, folding and faulting; therefore, stresses control the formation of the majority of hydrocarbon traps.

In particular, the stress field determines the geomechanical conditions of the reservoirs and the surrounding rock formations. As such, stress-strain information is critical to build and constrain geomechanical models of the reservoir evolution as it is depleted (Sen and Settari, 2005; Hatchell and Bourne, 2005). During reservoir drawdown the stress changes are due to variations of pore pressure that can lead to deformations, often manifested in field subsidence by compaction (Barkved and Kristiansen, 2005), or in an increase of microseismicity activity (Adushkin et al., 2000; Sze, 2005).

Stress conditions must be considered in the drilling and completion plans with the intention of avoiding wellbore and structures instability. Instability includes complete well failures (e.g. casing deformation) (Frederick et al., 1988; Addis et al., 1993), undesired sand production (Acock et al., 2004), reservoir damage due to over estimations of the drilling mud pressure (Charlez and Onaisi, 2001; Last, 2001), and blow-outs due to unpredicted over pressurized zones (Sayers, 2006; Lee et al., 1999). Another area in which the geomechanical integrity of reservoirs is of utmost importance is

CO_2 sequestration. It is necessary to properly estimate the minimum stress and the fracture breakdown pressure to effectively inject the CO_2 and avoid leaks from the sequestration unit (Hawkes et al., 2005). Understanding the reservoir's geomechanics is key to avoiding some of these hazards.

In situ stress also controls the availability of open fractures in the reservoir and the extension, aperture, and direction of propagation of hydraulic fractures. Hydraulic fractures are sometimes induced during enhanced recovery operations in the oil and gas and geothermal industries (Willis et al., 2007; Haimson and Cornet, 2003; Li et al., 1998). In some hydrocarbon reservoirs the presence of natural fractures can account for all or most of the porosity and permeability. As a consequence, knowledge of the existence of fractures improves estimates of reserves that may be decisive in the categorization of the reservoir. A coherent picture of the stress field and the fractures is critical not only in reservoir evaluation but also for planning the development of the field more efficiently. The permeability anisotropy introduced by the fractures has to be considered in well placement and infill drilling to optimally drain the reservoir (Sayers, 2007).

These two applications (proper reservoir evaluation and optimization of drilling paths) are specifically related to two fracture properties: the fracture intensity or degree of fracturing, which determines the storage capacity of naturally fractured reservoirs along with primary porosity (Aguilera, 1998); and the fractured orientation, which dictates the preferred direction of fluid flow. Fracture spacing (or density) in naturally fractured reservoirs is another relevant property. Typical calculations of fracture permeability and porosity are both proportional to the ratio of the width of the fractures to the distance between fractures (Nelson, 2001). Fracture spacing also determines how quickly oil (or gas) moves from the matrix into the fractures and enters the calculation of optimal drilling direction of slanted wells (Bratton et al., 2006).

1.1 Objective and Approach

The objective of this research is to determine in situ stress and fracture properties from a variety of geophysical data. We approach this problem in a practical fashion looking into strategies and methodologies to characterize the stress state and the fracture network in reservoirs. Characterization of in situ stress is understood here as the quantitative description of principal stresses in terms of their magnitudes and orientations. Similarly, the characterization of fractures has a wide scope involving the detection of fractures and the quantitative estimation of fracture orientation, size, spacing, intensity, aperture, compliance, fluid properties, and so forth.

The problem that we face in order to achieve this objective is mainly related to resolution differences among the various types of data utilized, which range from macroscopical failures and cracks around boreholes, to seismic scattering signals, to stress distributions in extensive tectonic regions. Fracture or stress estimations from borehole logs can be verified with core data or direct observations (e.g. image logs) and experiments in the borehole environment (e.g. microfracturing, leak-off tests). However, it is well known that the stress field, thus the fracture properties, change with depth and spatially (Bruno and Winterstein, 1994). Therefore, we would like to investigate lateral changes in the state of stress, away from the well. In order to accomplish this task, we complement the characterization of the stress field near boreholes with the characterization of naturally fractured reservoirs using multi-offset/multi-azimuth surface seismic data.

In this thesis an implicit reciprocity between the in situ stress and the fracture system is assumed. This is a common assumption supported by experimental data (Bourbie et al., 1987; Lo et al., 1986). Crampin et al. (1984) establishes that the widespread anisotropy observed in the upper crust is largely caused by cracks aligned by the stress field. Nelson (2001) discusses the interpretation of fracture system origins based on the premise that the natural fracture pattern depicts the local state of stress at the time of fracturing and, conversely, that any physical or mathematical model of deformation that depicts stress or strain fields can by various levels of extrapolation

be used as a fracture distribution model.

The ideas developed in this thesis are applied to field data from two fractured areas: The Macal Field in northeastern Venezuela and the Lynx Field in western Canada. There are many similarities between these two fields. Both are located in the foothills of mountain systems as part of foreland basins bounded by Thrust Belts. In these areas, the crystalline basement and the geological structures are similar. Tectonic processes have primarily reverse-faulted the sedimentary strata in both cases. Both fields are relatively close to plate boundaries (120 Km in the Venezuelan case and about 500 Km in the Canadian case). Both are onshore fields and the reservoir rocks are sandstones. However, sandstones from the Naricual formation in Venezuela are younger (Oligocene) than the Cadotte reservoir in Canada (Aptian-Albian) and they are found at different depths (Naricual is deeper). In terms of the fluid type, Cadotte (in the Lynx Field) is a tight-gas sandstone, whereas Naricual (in the exploratory Macal Field) is expected to be an oil bearing sandstone.

1.2 Outline

The thesis is divided into 6 chapters.

Chapter 2 addresses the problem of extracting stress information from well data. It is a study of in situ stress in northeastern Venezuela. In situ stress is characterized in orientation and magnitude from two types of borehole data. The borehole measurements are then compared with a regional model of stress distribution based on the plate motions.

Chapter 3 addresses the problem of extracting fracture properties from seismic data. Seismic scattering off discrete fracture networks is studied using numerical models of wave propagation. A new methodology is proposed to detect and characterize fractured reservoirs in terms of fracture orientation and spacing.

The ideas presented in chapter 3 are demonstrated by a field application to fractured reservoirs in the Lynx Field which is described in chapter 4. A great part of chapter 5 is dedicated to the important issue of pre-processing the seismic data in

order to separate fracture effects from fold artifacts. Seismic scattering methods used to study fractured reservoirs are evaluated and compared in chapter 5.

1.3 The Stress Field

Within the lithosphere, the principal stress axes are, in general, oriented horizontally and vertically (Zoback and Zoback, 1989). $SHmax$ describes the maximum principal horizontal stress and $Shmin$ the minimum principal horizontal stress. The vertical principal stress, Sv, is the stress induced by the weight of the overlying rock. Typically in the Earth, the vertical stress is the greatest of the principal stresses, however, there are some areas, particularly at plate boundaries, where tectonic processes take place and one or both horizontal stresses can exceed the vertical (Zoback, 2007). The relative values of stresses determines which kind of faults are more likely in a region: in areas of normal faulting, $Sv \geq SHmax \geq Shmin$; in areas of strike slip faulting $SHmax \geq Sv \geq Shmin$; and in areas of reverse faulting $SHmax \geq Shmin \geq Sv$ (Anderson, 1951).

1.4 Fracture Corridors

In this thesis we attempt to extract fracture properties from the scattered waves, also known as coda waves, which are generated by fractures comparable in size to the seismic wavelengths (Lynn, 2004a; Willis et al., 2006). In geology, such features are known as fracture corridors. Fracture corridors are zones of fracture clustering that consist of parallel, usually sub vertical fractures. In fracture corridors, joints are typically spaced a few meters to hundreds of meters, and they can extend from hundreds of meters to a few kilometers (Ozkaya et al., 2003). Such dimensions distinguish fracture corridors from the diffuse micro-fractures and from fault systems which are in many cases structures of regional character. Fracture corridors provide fluid flow paths; therefore, detecting their existence and extracting their properties is relevant in the assessment of fractured reservoirs.

We shall frequently refer to fracture corridors throughout this thesis as fracture systems, fracture networks, fracture sets, or multiple fracture sets.

Chapter 2

In Situ Stress from Borehole Measurements and Plate Tectonic Models

There are well established methods to measure the in situ stress field; among them, overcoring, strain recovery methods, breakout analysis, extended leakoff tests, and earthquake focal plane mechanisms (e.g. Ljunggren et al., 2003; Zoback et al., 1986). Different evidence of stress can be found in well data. To determine stress orientation from well data, caliper dipmeter and image logs record the deformed state of the borehole and thus contain stress information (Moos and Zoback, 1990; Plumb and Hickman, 1985). Borehole guided waves recorded in VSPs (Barton and Zoback, 1988) and in sonic logging (Sinha and Kostek, 1996) have also been used successfully to estimate stress directions. Few practical methods exist, however, to estimate stress magnitudes from well data. Simple, but weak, assumptions are frequently made- for example, horizontal stresses are considered equal and related to the vertical stress by a function of Poisson's ratio. Such a relationship assumes that no deformations take place in the horizontal plane. Hydrofracture experiments provide reliable stress magnitudes as well as orientations, but this technique, being expensive and formation damaging, must be limited to specific locations. Zoback et al. (1985) determined the magnitude of horizontal principal stresses from measurements of the breakout shape

in borehole image logs. Estimations of stress magnitudes have also been attempted from acoustic data. Huang (2003) implemented a multifrequency inversion of borehole flexural and Stoneley wave dispersions based on a perturbation theoretical framework (Sinha et al., 1994; Sinha and Kostek, 1996), and applied it to a particular log of slow formations.

In this chapter, stress information (orientation and magnitude) around a borehole is obtained independently from caliper data and cross-dipole well logs. Well data comes from a location in Venezuela. Stress distribution is also obtained from a regional scale model (section 2.4). First, the field data are presented and the rock parameters, needed for the stress calculations, are derived in section 2.1. Following this, the methodology applied to infer stress orientation and magnitudes where the borehole is deformed is described (section 2.2). In section 2.3, we describe a second method to determine stresses; this method is appropriate for the intervals where the borehole is not deformed.

2.1 Field Data

A whole suite of logs at an inland borehole location of the Macal field in northeast Venezuela is available for the present analysis. This field is in the Eastern Basin of Venezuela, in the province known as the Maturín Subbasin. The well is on the north flank at the foothills of the mountain ranges known as "Serranía Oriental del Interior" (figure 2-1). The tectonically complex environment includes compressional structures formed as a consequence of the still active oblique collision of the Caribbean and the South American Plates. The location is affected by tectonic elements such as the Pirital overthrust system (south) and the Urica system of ramps (west).

The four-arm dipmeter tool provides two perpendicular measurements of the borehole diameter. One pair of arms align with the long axis and the other with the short axis in the case of a borehole of non-circular cross section. The determination of the azimuth of the elongated side is possible since the dipmeter includes a tool that measures the sonde orientation with respect to magnetic North everywhere downhole.

Figure 2-2 shows two sections of the wellbore where conditions are different. Apart from some rugosities and minor washouts, the borehole between 6500 and 8500 ft can be considered stable, with no failures or "in gauge," its diameter being close to the bit size (12.25 in). This is the type of section where the second method based on the dispersion of cross-dipole waveforms, will be implemented. In contrast, on the right of the same figure, two perpendicular diameters are shown between 9000 and 12000 ft. The borehole wall has washout areas and cavings. At some depths, one diameter is significantly larger than the other, indicating that the borehole shape has a certain ellipticity. We shall apply the method based on borehole deformation to estimate stresses in sections with these characteristics.

The dipmeter tool rotates as it moves uphole, which is evident from the tool orientation on the right of both intervals in figure 2-2. In the stable case, the tool completes about four full rotations in 2000 ft, whereas in the second section it barely rotates more than once over the same distance. The depth of the cavings into the formation interrupts the normal tool rotation.

In the following calculations, several formation properties are required. For instance, the model of in situ stress requires various inputs: elastic constants, pore pressure, fluid pressure in the borehole, and rock compressive strength at every depth. The dynamic elastic constants are derived from the P-wave velocity (V_p), shear wave velocity (V_s), and rock bulk density (ρ) using equations:

$$\begin{aligned} E &= \rho V_s^2 \frac{3V_p^2 - 4V_s^2}{V_p^2 - V_s^2} \\ \nu &= \frac{V_p^2 - 2V_s^2}{2(V_p^2 - V_s^2)} \end{aligned} \tag{2.1}$$

where E and ν refer to Young's modulus and Poisson's ratio respectively.

In the earth, rock deformation takes place under static conditions. Therefore, static, rather than dynamic moduli are needed for the modeling. In order to obtain static parameters from dynamic measurements, several empirical relationships, have been reported. The static Young's modulus is calculated in this study using the procedure in Fjaer (1999) developed for weak sandstones. On average, the static-

dynamic ratio is about 0.65 for these data.

The compressive strength (C_0) can be computed from well logs using the Coates and Denoo (1981) empirical relationship for consolidated rocks which is based on the Mohr-Coulomb failure criterion:

$$C_0 = 50000 E_s K_s (0.008 V_{sh} + 0.0045(1 - V_{sh})) \frac{cos\theta}{1 - sin\theta} \tag{2.2}$$

where E_s and K_s are the static Young's and bulk modulus, given in 10^6 psi, and θ refers to the angle of internal friction which is a function of rock consolidation (40° is suggested for sandstones). V_{sh} is the shale volume that can be computed from the gamma ray log. In general, log-derived compressive strength would require further calibration with core data. Static Young's modulus, Poisson's ratio, and rock compressive strength are shown in figure 2-3.

The variation of pore pressure with depth is assumed equal to the hydrostatic gradient ($10\ MPa/km$), and the vertical stress is estimated from the integrated weight of the overburden:

$$S_v = \int \rho(z) g \, dz \tag{2.3}$$

Pore pressure, drilling mud pressure, and vertical stress are shown in figure 2-4. Calculated properties at a few specific depths are extracted in table 2.1.

As input to the second method, cross-dipole data are necessary. Cross-dipole acoustic information in this well is measured with the DSI[1] tool. This type of acquisition consists in alternating the firing of the upper and lower dipole sources, which are oriented orthogonally, and also alternating the recording in the inline and crossline receivers (figure 2-5). In this way, four sets of 8 traces each are generated: (1) upper dipole source-inline receivers, (2) lower dipole source-inline receivers, (3) upper dipole source-crossline receivers, and (4) lower dipole source-crossline receivers. The two middle sets are called the cross-components. The crossline receivers are oriented parallel to the upper dipole source, whereas the inline receivers are oriented parallel to the lower dipole source. The sampling interval is 40 μsec, and the sources oper-

[1]Dipole Shear Sonic Imager, mark of Schlumberger

ate at low frequencies (with peak frequency around 2 kHz). The phase difference introduced by the separation of the sources and the delay between firings is corrected for in the field (B. Sinha - Schlumberger-Doll Research, personal communication). The main borehole wave recorded at such frequencies and with this source symmetry (dipole) is the flexural mode. This wave is dispersive at logging frequencies.

2.2 Method I: Borehole Deformations

In order to infer the stress field, the first method uses the observations of the borehole cross-sectional area at every depth level. This information is obtained from standard caliper tools, four- or three-arm dipmeter tools, or image logs.[2]

The borehole can present instabilities as a consequence of one or several processes acting together, such as chemical reactions between mud components and some formation minerals; time-dependent changes in pore pressure; well deviation; high angle of penetration relative to bedding dip; reinitiated fractures, and so forth. In particular, the wellbore can deform as a response to stress. These special deformations are referred to as "breakouts" in the oil industry. Breakouts are localized compressive shear failures.

Breakouts occur symmetrically (180° apart), and at a consistent azimuth throughout the well section corresponding to the minimum horizontal (principal) stress and the maximum concentration of compressive stress near the borehole. Since the borehole diameters and their orientation can be measured at every depth, these data provide a means of estimating principal stress directions.

The occurrence of stress-induced failures around a borehole is explained in terms of the hoop stress accumulation relative to the strength of the rock surrounding the well. Stresses around a circular hole in a homogeneous, isotropic, elastic plate subjected to maximum and minimum effective stresses in the far field and a fluid pressure in the

[2]Image logs provide a 360° ultrasonic or resistivity image of the borehole wall.

hole are given by:

$$\begin{aligned}
\sigma_r &= \frac{1}{2}(SHmax + Shmin)(1 - \frac{R^2}{r^2}) + \frac{1}{2}(SHmax - Shmin)... \\
&\quad ...(1 - 4\frac{R^2}{r^2} + 3\frac{R^4}{r^4})\cos(2\theta) + \frac{\Delta P R^2}{r^2} \\
\sigma_\theta &= \frac{1}{2}(SHmax + Shmin)(1 + \frac{R^2}{r^2}) - \frac{1}{2}(SHmax - Shmin)... \\
&\quad ...(1 + 3\frac{R^4}{r^4})\cos(2\theta) - \frac{\Delta P R^2}{r^2} \\
\tau_{r\theta} &= -\frac{1}{2}(SHmax + Shmin)(1 + 2\frac{R^2}{r^2} - 3\frac{R^4}{r^4})\sin(2\theta)
\end{aligned} \tag{2.4}$$

(Jaeger and Cook, 1979); where σ_r is the radial stress, σ_θ is the circumferential stress, $\tau_{r\theta}$ is the tangential shear stress, R is the radius of the hole, θ is the azimuth measured from the direction of $SHmax$, and ΔP is the difference between the fluid pressure in the borehole and that in the formation (positive indicates excess pressure in the borehole); $SHmax$ and $Shmin$ refer to the effective horizontal stresses, that is, the stresses supported by rock and pore fluid.

Hoop stress is defined by equation 2.4 when $r = R$. Figure 2-6 shows the variation of hoop stress as a function of azimuth for different values of $SHmax$ and $Shmin$. Hoop stresses are maximum at 90° and minimum at 0°:

$$\begin{aligned}
\sigma_{0^\circ} &= 3Shmin - SHmax - \Delta P \\
\sigma_{90^\circ} &= 3SHmax - Shmin - \Delta P
\end{aligned} \tag{2.5}$$

Failure occurs when the strength of the rock is exceeded by the concentrated stress. For instance, if the rock had a strength $C_0 = 150\ MPa$, as shown in figure 2-6, failure around the borehole would be restricted to the angle ranges $\theta = -45°$ to $-90°$ and 45° to 90°, given $SHmax = 2.2\ Sv$ and $Shmin = 1.25\ Sv$. Not to have any failures under this stress field, the rock has to have a compressive strength larger than 250 MPa. On the contrary, if it is as weak as 25 MPa, it will fail at all azimuths. The function σ_θ steepens as the difference between $SHmax$ and $Shmin$ becomes large.

2.2.1 In Situ Stress Elastic Model

Figure 2-6 suggests that borehole failures also contain information about the relative magnitude of the stresses. Based on an elastic approach, we solve for the concentration of stresses around the borehole and compare hoop stress values with rock strength.

Unless the rock column is being deformed by compaction, the deformations of a borehole are confined to the horizontal plane, perpendicular to the borehole axis. Such a case is represented in elasticity under the plane strain assumption where no deformations take place in the z-direction (borehole axis), and the displacements in x and y are only functions of x and y but not z (see appendix A).

An infinitely thin plate containing a circular hole and under plane strain represents a borehole subjected to far field stresses. In the model, the particle displacements in x and y (u and v) are computed at every point solving Navier's equations in static equilibrium:

$$\begin{aligned} -\frac{\partial}{\partial x}[c_1\frac{\partial u}{\partial x}+c_2\frac{\partial v}{\partial y}]-\frac{\partial}{\partial y}[c_3(\frac{\partial u}{\partial y}+\frac{\partial v}{\partial x})] &= 0 \\ -\frac{\partial}{\partial x}[c_3(\frac{\partial u}{\partial y}+\frac{\partial v}{\partial x})]-\frac{\partial}{\partial y}[c_2\frac{\partial u}{\partial x}+c_1\frac{\partial v}{\partial y}] &= 0 \\ -\frac{\partial}{\partial y}[c_3(\frac{\partial u}{\partial y}+\frac{\partial v}{\partial x})]-\frac{\partial}{\partial z}[c_2(\frac{\partial u}{\partial x}+\frac{\partial v}{\partial y})] &= 0 \end{aligned} \tag{2.6}$$

where body forces are disregarded, and $c1$, $c2$, and $c3$ are the only non-zero components of the isotropic material constants tensor. In terms of Young's modulus and Poisson's ratio:

$$\begin{aligned} c_1 &= \frac{E(1-\nu)}{(1+\nu)(1-2\nu)} \\ c_2 &= \frac{\nu E}{(1+\nu)(1-2\nu)} \\ c_3 &= \frac{E}{2(1+\nu)} \end{aligned} \tag{2.7}$$

Once the displacements are solved, the normal and shear strains in the $x-y$ plane are obtained by taking derivatives. To get stresses, strains and the stiffness matrix

are substituted into the linear elastic constitutive relation. Normal stresses in the z-direction are not neglected; however, by Hooke's law shear stresses in the z-plane vanish. The complete formulation of the governing equations modeled is presented in appendix A.

A numerical solution of equations 2.6 at every point is found using a finite element approximation (we use the commercial program Femlab by Comsol). Appendix B explains the basics of the finite element method and the derivation of the finite element equations solved in this model.

In the model, the radius of the undeformed borehole is chosen as that of the actual well, 0.1556 m. The area is meshed with curved triangular elements that refine towards the borehole wall. In order to obtain a stable solution, boundary conditions must be imposed. The outer edges are considered fixed in the direction perpendicular to the stress applied. At the same borders, forces per unit area representing the far field stresses are specified, $SHmax = F_x$ and $Shmin = F_y$. Force per unit area corresponding to the mud pressure is specified at the boundary of the hole (figure 2-7).

Stresses in porous media are dependent on fluid pressures in cracks and pores. To take into account the presence of fluid, effective stresses are the actual magnitudes sought. Effective stresses are related to total stresses through Terzaghi's law (Bourbie et al., 1987); for example, the maximum horizontal effective stress is defined as:

$$SHmax = SH - \alpha P_p \tag{2.8}$$

where SH represents the total stress, P_p is the pore pressure, and α is the Biot constant taken as 1 hereinafter.

The modeling is performed at each depth level and iterated for different boundary conditions (the far field stresses) until the hoop stress equals the rock strength at a radial distance that coincides with the long radius of the borehole. Borehole size is known from the 4-arm caliper measurement. Because there is a breakout at the modeled depth, stresses are assumed to have exceeded the rock mechanical resis-

tance, leading to failure and resulting in an elongated borehole cross section. Hoop stresses are expected to be different around the hole and maximum compressive in the direction of the smallest stress acting in the far field.

Calculated stresses at every point in the region are related to cylindrical stresses by the linear system (Huang et al., 2000):

$$\begin{bmatrix} \sigma_x \\ \sigma_y \\ \sigma_{xy} \end{bmatrix} = \frac{1}{x^2+y^2} \begin{bmatrix} x^2 & y^2 & -2xy \\ y^2 & x^2 & 2xy \\ xy & -xy & x^2-y^2 \end{bmatrix} \begin{bmatrix} \sigma_r \\ \sigma_\theta \\ \tau_{r\theta} \end{bmatrix} \tag{2.9}$$

A solution for displacements is obtained in cartesian coordinates and the analysis of the hoop stress distribution requires a coordinate transformation. Hoop, radial, tangential, and normal stress in the axial direction, are obtained solving system 2.9.

2.2.2 Results

Stress Directions

The field data are classified according to the borehole radius into sections where the borehole is considered stable and intervals where it presents some instabilities (i.e. one diameter is significantly larger than the bit size). In the latter case, the orientation of the elongated size of the borehole is calculated from the dipmeter data. After correcting by the magnetic declination and summing the contributions from orientations separated 180°, a histogram of azimuths is plotted in figure 2-8. The dominant azimuths are observed between 250° and 260°. Since they are consistent on the well section, the corresponding elongated borehole cross-sections are considered breakouts.

At 10120 ft, for instance, the borehole has a breakout. The long diameter is 16 in whereas the minor axis length is about 13.5 in (bit size: 12.25 in). The larger axis is at 253° with respect to the geographic north. Since breakouts align with the minimum horizontal stress, $Shmin$ is also oriented at 253° azimuth. Thus, $Shmin$ strike is about ENE-WSW and $SHmax$ is oriented NNW-SSE.

Stress Magnitudes

Following the procedure described, we solve for hoop stresses in the region around the borehole for a range of combinations of maximum and minimum horizontal stresses. The actual magnitudes of $SHmax$ and $Shmin$ acting on the far field are those that induce the accumulation of hoop stresses greater than rock strength up to the deformed borehole radius. The maximum horizontal stress magnitudes are varied between 0.8 S_v and 1.5 S_v. $Shmin$ is increased from 0.6 S_v to 1.45 S_v.

For instance, boundary conditions of $Shmin = 69.39\ MPa$ and $SHmax = 76.33\ MPa$ are specified on the horizontal and vertical outer edges of a model that represents the formation at 10120 ft (parameters are specified in table 2.1). Calculated hoop stresses are shown in figure 2-9. As expected, the maximum concentration of stresses occurs at the azimuth of $Shmin$ (north-south in the figure), the region that undergoes compressive failure. Caliper data indicates that a breakout at this depth increments the borehole radius in the direction of $Shmin$ to about 0.204 m; that is, about 5 cm larger than the nominal size. The short axis is approximately its non-deformed length.

Resultant hoop stresses for such far field values are larger than the compressive strength of the rock from the non-deformed borehole wall to a depth of about 5 cm into the formation. Hoop stresses at the azimuth of $SHmax$ are not enough to overcome the strength of the rock, hence no failure is predicted at this location. Given that this hoop stress distribution explains the observations at 10120 ft, the far field stresses applied as boundary conditions are interpreted as the in situ horizontal stresses.

The vertical stress needs to be recomputed in order to take into account the normal stress (equation **??**). The new S_v comes from the vertical stress calculated from the overburden plus σ_z. In terms of the vertical stress, the relative magnitudes found at 10120 ft are $SHmax \simeq 0.9893\ S_v$ and $Shmin \simeq 0.9134\ S_v$.

The iterated modeling and analysis is performed every 10 ft in the breakout sections of the well. Depths where a combination of washouts and breakouts is suspected are not modeled. Similarly, depths where the elongated size seems to be larger than

the maximum extension of the caliper tool are left out. Relative horizontal to vertical stresses magnitudes are obtained and shown in figure 2-10. The maximum horizontal stress varies between 0.91 and 1.1612 times the vertical stress, and the minimum horizontal stress remains the smallest in the whole depth section, with values ranging between 0.7781 and 1.0361 S_v. These relative magnitudes indicate that the area is under a combination of strike slip tectonics, in which the vertical is the intermediate stress, and normal faulting, in which the vertical stress is the largest. Colmenares and Zoback (2003) characterize northeastern South America with the same combination of stress regimes.

2.3 Method II: Stress-induced Velocity Anisotropy

The second borehole method to obtain stress information is based on crossovers observed in the dispersion of flexural waves as recorded in cross-dipole logs. The flexural wave corresponds to the normal mode whose azimuthal order is 1, meaning that pressures in the fluid and displacements in the solid change sign at 180° (Ellefsen, 1990). For typical logging frequencies only the lower order radial modes are excited. The flexural wave velocity approaches the formation shear wave velocity at low frequencies and the compressional fluid velocity at the high frequency end (figure 2-11). This wave does not possess a theoretical cutoff, but its excitation becomes extremely small below a transition frequency leading to an effective cutoff; in practice this is at about 2 kHz.

Velocities in sedimentary rocks depend on the state of stress. They increase with increasing effective pressures and the increment gradually becomes smaller. Such a behavior is attributed to the increase of rigidity or stiffness of the rock matrix when a hydrostatic compressive stress is applied.

The variations in velocity under a uniaxial stress depend on the direction of wave propagation with respect to the direction of applied stress. Cracks, or any soft inclusion in the material that is preferentially aligned perpendicular to the direction of the applied stress, close under low effective pressures and an uniaxial stress, while

cracks oriented parallel would open. As a consequence, the rock becomes stiffer in the direction of the applied stress and waves propagating in this direction travel faster, thus creating an anisotropic velocity field (Fjaer and Holt, 1994). Shear waves polarize into a slow and a fast direction in the presence of an uniaxial compressive stress with the fast shear wave polarization being parallel to the applied stress direction, or equivalently, normal to the preferential orientation of fractures, pores, or grains (figure 2-12). In the case of an homogeneous and intrinsically isotropic formation, the elastic velocity anisotropy is attributed to the stress field (Winkler, 1997).

In the presence of a borehole, the stress distribution must adapt to the circular boundary condition by deforming around it. The circumferential stress increases and the maximum compressive stress concentrates in the direction where the far field stress is less compressive. Therefore, the rock stiffness changes radially as well as azimuthally, and elastic waves observe it. In particular, flexural waves, which travel parallel to the borehole axis, split in the horizontal plane, and because these waves are dispersive, they are sensitive to the radial change in properties (Winkler et al., 1998). At low frequencies, flexural waves have long radial depth of investigation and are not significantly affected by the stress-induced altered zone. As frequency increases, flexural waves (and all surface modes) become localized at the borehole wall; thus they are influenced by the near field stresses around the borehole. As a result, the dispersion curves of flexural waves recorded by two perpendicular dipoles are expected to cross at some frequency (figure 2-13).

An appropriate rotation of the cross dipole waveforms to the principal flexural wave polarization maximizes the crossover and provides the angles to the fast and slow direction. Knowing the orientation of the dipole, the direction of the maximum horizontal stress is deduced. On the other hand, the difference in velocities at the far field (low frequencies) in the two orthogonal directions can be compared to experimental results in which shear velocity is measured as confining pressure is increased. In such a way, assuming the vertical stress is the intermediate stress, the ratio of the principal stresses is determined. Since the vertical stress is estimated from the overburden, values of horizontal stress can be calculated.

Analysis of flexural wave crossover are performed in locations where the borehole is stressed but not deformed. Crossovers are indicators of stress induced anisotropy dominating over other sources of anisotropy.

2.3.1 Results

Stress Directions

Due to the tool rotation on its way uphole, cross-dipole data need to be rotated at each depth in order to align the dipole's orientation with the principal axes of anisotropy. Figure 2-13 and 2-14 show some example depths where crossovers are observed. At these depths, the stress concentration has not exceeded the strength of the rock. As a consequence, the borehole is stable in the sense that its original radius is preserved. Since stress has not been released, waves in the surrounding rock propagate with different velocities depending on the polarization direction with respect to the orientation of minimum and maximum horizontal stresses. At these levels we are unable to apply the first method to estimate stresses since no failure is taking place; however, the crossover on the dispersion of flexural waves contains information about the principal stress directions, as explained before.

For instance, at 6700 ft the crossline component is oriented in such a way that the low frequency flexural wave arrives earlier (or travels faster) than the flexural wave polarized in the orientation of the upper dipole source (top left plot in figure 2-14). The upper dipole source is oriented at 55° azimuth; hence, the lower dipole is at 145°. Before rotating the data we already know that the maximum stress direction should not be oriented more than 90° apart from the actual position of the tool, otherwise the upper dipole would have registered the fast component at low frequencies, and this is not the case. Therefore, the fast direction must be limited to the range between 55° and 235° azimuth.

The dispersion curves after rotating the data using a method that minimizes the energy on the waveforms recorded by the cross-components are also shown in figure

2-14 (bottom left).[3] For the data at 6700 ft, the angle of the fast orientation is about 32°. Adding this value to the tool orientation indicates that the direction of the maximum far field stress is 177° (or 357°) azimuth.

The same analysis was performed at several other depths. The maximum stress orientations obtained with this technique vary in the range between 334 and 14 degrees azimuth. Figure 2-15 shows minimum horizontal stress azimuth at some depths derived from both borehole methods. Mean values agree to within 10 degrees. We conclude that maximum horizontal stress runs approximately NNW-SSE, hence *Shmin* lies in the east-west direction.

Stress Magnitudes

The situation of one stress orientation being dominant in the Earth can be compared to laboratory experiments where rock samples are submitted to different confining pressures. For instance, Lo et al. (1986) measured ultrasonic P, SH, and SV wave velocities in sample rocks of a typical granite, shale, and sandstone, while varying the confining pressure from 5 to 100 MPa. The experiments were performed for several directions of wave propagation. For Berea sandstone, velocities were measured parallel, perpendicular, and at an oblique direction with respect to bedding. Samples were not saturated. The results suggest that Berea sandstone is transversely isotropic and therefore satisfies the condition of isotropicity required by the stress-induced anisotropy method. Figure 2-16 shows two orthogonal shear wave velocities reported in Lo et al. (1986) corresponding to a perpendicular direction of propagation with respect to bedding planes. We based our next calculations on the experimental results presented in figure 2-16.

The estimation of stress magnitudes from the cross-dipole data begins by measuring flexural wave velocity anisotropy at low frequencies, that is, prior to the crossover occurrence and where energy content peaks. Table 2.2 lists mud pressure values, anisotropy percentages and differences between fast and slow velocity observed at some depths.

[3]Coded by Dr. Beltram Nolte and Dr. Xiaojun Huang while at ERL, MIT.

We proceed by calculating the velocity corresponding to where confining and mud pressure are equal according to the experiments on Berea sandstone. Such pair velocity-stress represents the intermediate stress conditions, or in this case, the vertical stress close to the borehole. The difference in velocity measured from the orthogonal flexural waves is centered at these coordinates in the velocity-stress plane for the Berea sandstone and the corresponding limiting stresses are estimated. Finally, ratios between maximum and minimum stress with respect to confining pressure are calculated. We assume these ratios to be similar to the relative magnitudes of principal in situ stresses.

To exemplify the procedure, let us take the case depth at 6700 ft. Mud pressure is 20 MPa and Berea sandstone shows a shear velocity of 2480 m/s at this confining pressure. The anisotropy measured on the rotated cross-dipole data, as shown in figure 2-14, is 22 m/s (at around 2 kHz, the peak frequency). This difference between fast and slow velocities translates into the velocity range 2469 to 2491 m/s for the experimental results. Confining pressures of 19.09 and 21.4 MPa are predicted for these velocities and by taking their ratio with the mud pressure, we obtain $Shmax/Sv = 1.07$ and $Shmin/Sv = 0.9545$. Figure 2-17 shows the results at this and other depths. $SHmax/Sv$ ratios vary between 1.07 and 1.2962. $Shmin/Sv$ ranges between 0.7788 and 0.9545. Mean values estimated are $SHmax/Sv = 1.1663$ and $Shmin/Sv = 0.8602$. With an estimation of overburden, absolute values of horizontal stress can be calculated. The combined results of methods I and II are shown in figure 2-18.

2.4 Regional Stress Model

To investigate whether the direction of the principal stresses derived from the in situ measurements correspond to the regional tectonic stress field, an intraplate stress distribution is calculated. Only tractions at plate boundaries are considered. Therefore, the model is purely kinematic and largely simplified by assuming constant velocities along main boundary segments. The results (displayed in figures 2-22 and 2-23) agree

with the orientation of the in situ stresses obtained.

In order to determine the regional stress directions, a finite element solution is computed for a model representing the relative motion between the Caribbean and South American plates. The process is similar to the one described in section 2.2.1 except that a plane stress approximation of the elasticity equations is assumed (see appendix A).

The plates' geometry is obtained from digital maps[4] corresponding to the model NUVEL-1A (DeMets et al., 1994). Figure 2-19 shows the model features and the location of the well. In the same figure we have shown a map of the main tectonic plates in the area of study. As observed, the model geometry represents fairly the dimensions and location of the Caribbean and South American plates. Figure 2-20 depicts the finite element mesh which refines toward the boundary Caribbean-South America.

Displacement conditions are imposed in all boundaries by solving differential equations of the form:

$$\frac{\partial \mathbf{u}}{\partial t} = \mathbf{U} \tag{2.10}$$

where $\mathbf{u}$ is the displacement vector. $\mathbf{U}$ represents East and North components of the velocity, assumed constant along the particular boundary (figure 2-21). Plate velocity can be obtained from global models describing the motion of a certain number of assumed-rigid plates. These global models are in general based on the geomagnetic reversal time scale, transform fault azimuths, earthquake slip vectors and, more recently, on space geodetic measurements. In table 2.3 we have listed the East and North velocities corresponding to plate boundary coordinates from the center of the model edges, numbered as shown in figure 2-19. For comparison, Euler vectors from three different global models were used in the velocity calculations: NUVEL-1A (DeMets et al., 1994, 1990); REVEL (Sella, 2002); and the 2004 version of GSRM[5] (Kreemer et al., 2003). Edge 11, representing the limit between the South America and North America plates is left fixed (zero displacement condition). Figure 2-22 shows the

[4] http://jules.unavco.org/GMT/

[5] Global Strain Rate Map, http://gsrm.unavco.org/intro/

velocities from REVEL specified at the model boundaries.

At the well site the maximum compressive principal stress is oriented 33 degrees west of north if REVEL velocities are imposed (figure 2-22). NUVEL-1A velocities give an azimuth of 2.5 degrees for the $SHmax$ direction while GSRM velocities, being similar to REVEL, result in an orientation of 36 degrees west of north. The solution is not sensitive to conditions imposed on edges far from the well, but it is highly sensitive to the relative velocity of the Caribbean and Nazca plates. The relative motion between the Caribbean and South America plate fits poorly with NUVEL-1A and other models (Weber et al., 2001). However, recent GPS measurements (Pérez et al., 2001) suggest that along the San Sebastián - El Pilar fault system, the Caribbean plate moves at a rate of 20.5 ± 2 mm/yr with an azimuth of N84±2°E. Such velocity is similar to the one assigned as the boundary condition according to the models REVEL and GSRM. In general, NUVEL-1A velocities at edges 5, 9 and 10 are about 50% slower than the other two more recent models, which incorporate present day rates in contrast to NUVEL-1A that averages motion over 3 million years. Increasing the Caribbean plate velocity relative to fixed South America has the effect of rotating the maximum stress to the west.

Nazca's velocity relative to stable South America is overestimated by approximately 15% in NUVEL-1A with respect to REVEL and GSRM. This difference has been interpreted as a deceleration in the convergence Nazca-South America, probably related to the Andes growth initiated about 20 Ma (Norabuena et al., 1999). Unlike the Caribbean-South America boundary zone that is characterized by a predominantly strike-slip motion, the Nazca plate subducts beneath South America. Moreover, it has been observed that site velocities decrease from the interior of the Nazca plate to the interior of South America (Norabuena et al., 1998) indicating that only a percentage of the plate velocity measured at GPS stations on the Nazca plate should be associated with the continental deformation. Norabuena et al. (1998) estimate that about 50% of the overall convergence is accumulated on the locked plate interface squeezing South America and released in earthquakes. Another 20%, i.e. 12 to 15 mm/yr, is related to crustal shortening forming the Andes. The remaining 30%

of the net convergence is associated with stable sliding of the Nazca plate.

A decrease in the velocity at the boundary Nazca-South America in our model also rotates the direction of principal maximum stress towards the west. For instance, a 50% decrease of REVEL velocities on edges 4 and 7 (Nazca-South America boundaries), rotates the orientation of maximum stress 12° counterclockwise with respect to the orientation found previously. Therefore, $SHmax$ azimuth falls within the range 315-327°. Similarly, reducing GSRM model velocities yields $SHmax$ azimuth between 314-324°. A corresponding 319° azimuth is obtained when half of the velocity predicted by NUVEL-1A is assigned to the Nazca-South America boundaries (figure 2-23).

In comparison with the principal stresses direction estimated from well-bore breakouts and acoustic data, the regional model provides consistent results, that is, $SHmax$ is oriented NNW-SSE (figure 2-23). Combining both borehole methods, $SHmax$ azimuth is observed at 345° and this is about 20° away from the most likely direction found with the global models. Stress orientation calculated mostly from focal mechanisms is available at the World Stress Map (Reinecker et al., 2005). Data corresponding to events close to the well location are also indicated in figure 2-23 where it is observed that the average $SHmax$ azimuth estimated with this method is about 330°. Figure 2-24 shows other stress measurements in the region of our well reported in the World Stress Map.

2.5 Summary

The orientation of horizontal principal stresses at a well location in northeastern Venezuela has been obtained by a combination of breakout analysis and flexural wave crossovers, and from regional stress models calculated from plate motions. Borehole methods give the maximum horizontal stress direction to be slightly west of north. Specifically, breakouts indicate that $SHmax$ is oriented at 345±5° azimuth (measured clockwise from North), whereas the range derived from crossdipole data rotation is wider, between 334 and 14°.

One of the main advantages of doing this kind of integrated data analysis is that flexural waves can provide stress information in those places where breakouts do not occur. Maximum stress direction from regional stress models ranges from 314° to 2.5° azimuth, depending on plate motion constraints. The regional stress model is most sensitive to the velocities of the Nazca Plate and of the Caribbean Plate. In conclusion, all methods suggest that $SHmax$ is oriented NNW-SSE, approximately perpendicular to El Pilar fault. Yale (2003) relates velocity anisotropy to the differential horizontal stress. According to this paper the anisotropy we observed, in average 3.4%, would classify this area as one of high differential horizontal stress. In regions of high differential horizontal stress small scale faulting affects the regional trends only in an area within a few hundred meters of the fault which would explain the consistency found in the orientation of stresses.

The magnitudes of horizontal stresses obtained by modeling stress distributions around the borehole and matching the static deformed state suggest that the intermediate stress is the vertical. Stress ratios determined by comparing velocity anisotropy with stress differences in experiments on Berea sandstone confirm that horizontal maximum stress and minimum stress magnitudes are about 1.1 and 0.9 times the vertical stress, respectively.

Table 2.1: Formation parameters at various depths. Static Young's modulus (E_s) is in GPa; pore (P_p) and mud pressure ($Pmud$), vertical stress (S_v), and strength (C_0) units are MPa. R_{max} refers to the maximum borehole radius in meters and ν to Poisson's ratio.

Depth[ft]	E_s	ν	C_0	Pp	Pmud	S_v	R_{max}
5610	24.33	0.32	40.85	17.11	16.84	39.8	0.18073
5815	33.03	0.2296	45.91	17.74	17.45	36.03	0.1594
6700	38.21	0.2107	75.45	20.44	20	42.89	0.1619
7100	44.59	0.1839	78.28	21.66	21.68	45.97	0.1652
7510	32.64	0.248	61.5	22.91	22.81	54.2	0.1715
8680	32.24	0.2781	66.26	26.47	26.02	58.19	0.1593
8760	39.57	0.233	52.44	26.72	26.26	58.81	0.18013
9330	42.95	0.128	65	28.46	28.43	68.13	0.18784
10120	29.55	0.31	57.03	30.87	31.02	69.4	0.20399
10980	31.69	0.266	55.05	33.49	33.42	80.75	0.25899
11700	43.12	0.182	61.98	35.69	35.58	81.75	0.23847
12130	38.23	0.29	86.28	36.89	36.99	89.64	0.20259
12750	33.98	0.2524	55.05	38.89	4099	89.88	0.1604

Table 2.2: Velocity anisotropy at the far field and mud pressure (MPa) at some crossover depths

Depth[ft]	Anisotropy %	ΔV_s m/s	Pmud
5815	2.78	56	17.45
6115	1.86	44	18.56
6490	2.44	44	19.72
6700	0.897	22	20
6772.5	2.89	80	20.39
7000	5.12	99	21.37
7100	3.41	89	21.68
7445	10.44	255	22.62
7500	4.43	99	22.78
8000	1.5	36	24.35
8120	4.78	117	24.82
8280	2.51	66	25.18
8680	2.45	47	26.02
12750	2.46	49	40.99

Edge #	Description	REVEL N	REVEL E	GSRM N	GSRM E	NUVEL-1A N	NUVEL-1A E
1	CA-CO	72.69	32.4	72.69	32.4	70.95	37.54
2	CA-NA	5.04	18.45	5.1	18.01	1.84	11.27
3	CA-NZ	12.52	28.67	10.26	29.07	14.09	47.05
4	NZ-SA (north)	14.06	66	12.82	63.74	16.76	76.93
5	CA-SA (west)	-2.27	21.63	-0.8	20.97	-1.87	14.15
6	SA-AN (west)	1.97	18.68	0.09	16.53	1.05	20.38
7	NZ-SA (south)	11.53	69.15	10.56	65.51	14.16	78.32
8	SA-ST	2.48	15.45	4.47	4.35	2.6	4.98
9	CA-SA (central)	0.71	20.04	1.84	19.56	0.3	13
10	CA-SA (east)	2.17	18.33	3.13	18.05	1.37	11.78
12	SA-AF (north)	-1.96	-25.43	-1.75	-26.03	-1.5	-28.35
13	SA-AN (southeast)	-2.35	-12.43	0.8	-12.38	-0.66	-15.88
14	SA-AF (northeast)	-4.23	-27.66	-3.73	-28.01	-4.06	-30.88
15	SA-AF (southeast)	-6.53	-29.83	-5.74	-29.32	-6.69	-33.52
16	SA-AF (southeast)	-7.52	-27.18	-6.62	-26.32	-7.85	-30.68
17	SA-AF (northeast)	-6.64	-29.83	-5.84	-29.75	-6.82	-33.41

Table 2.3: North and East plate velocities and boundary conditions used in the regional stress models. All velocities are in mm/yr. CA: Caribbean, CO: Cocos, NA: North America, NZ: Nazca, SA: South America, AN: Antarctic, ST: Scotia, AF: Africa

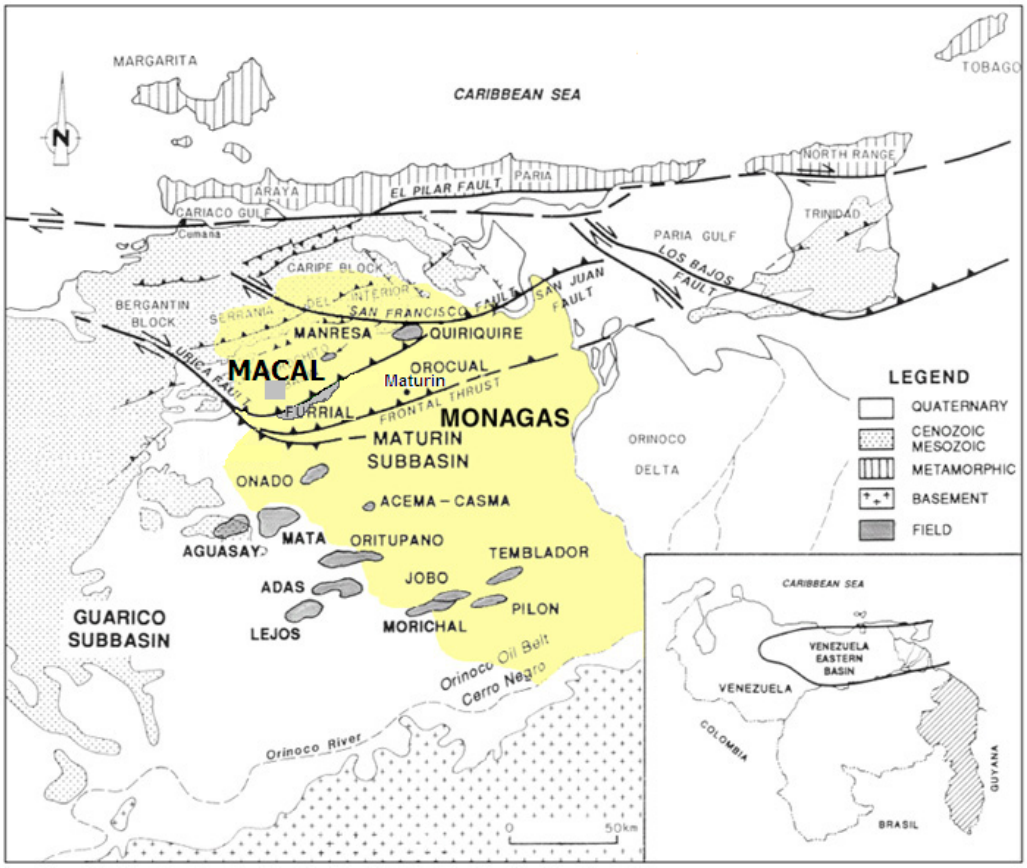

Figure 2-1: Tectonic map of the Eastern Venezuelan Basin. Macal field's location is approximated. Modified from Parnaud et al. (1995).

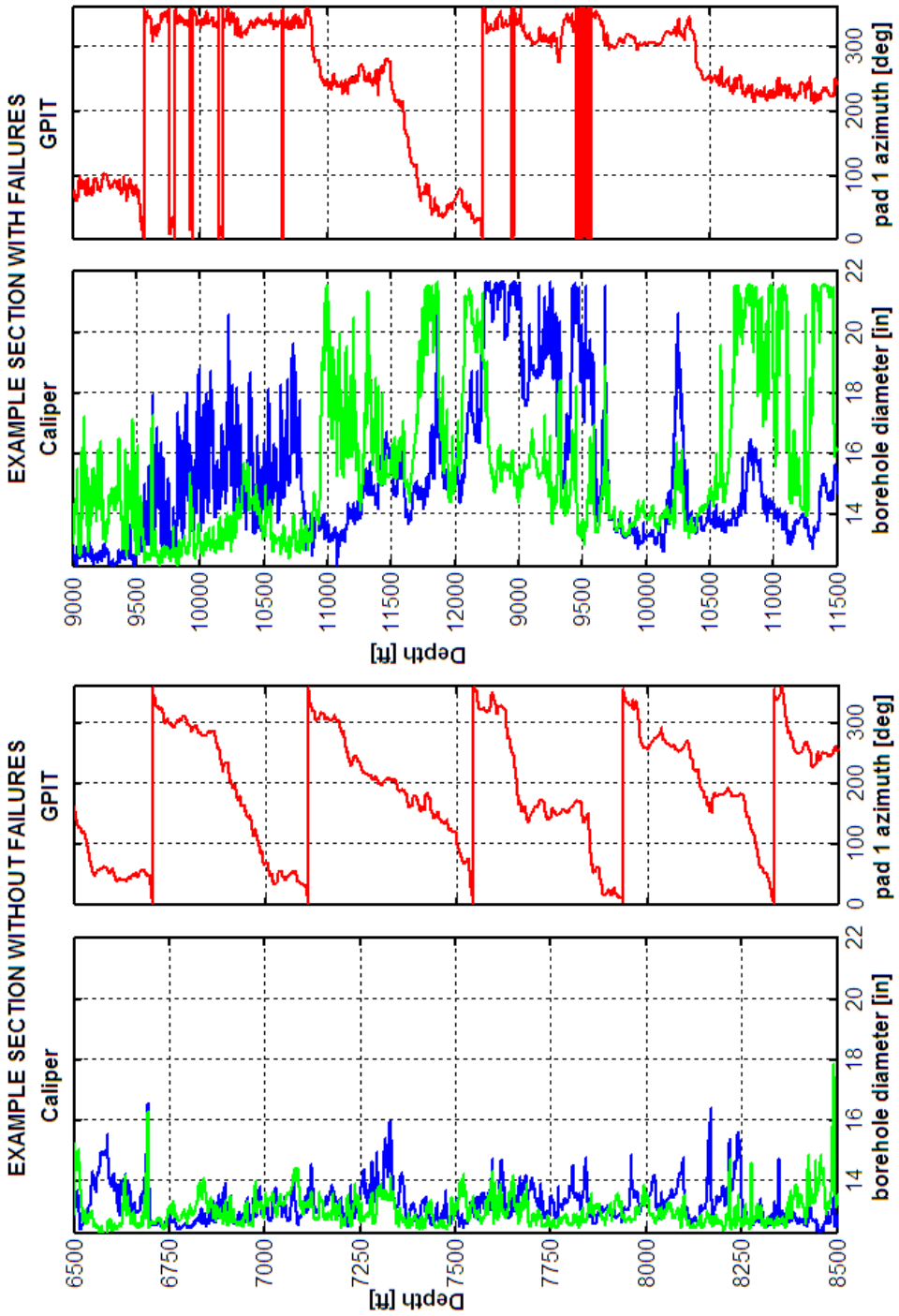

Figure 2-2: Four-arm caliper data in two depth intervals. On the left two panels, long and short borehole diameter and magnetic orientation of the dipmeter tool between 6500 and 8500 ft. On the right, data between 9000 and 12000 ft. GPIT: Schlumberger's General Purpose Inclinometry Tool.

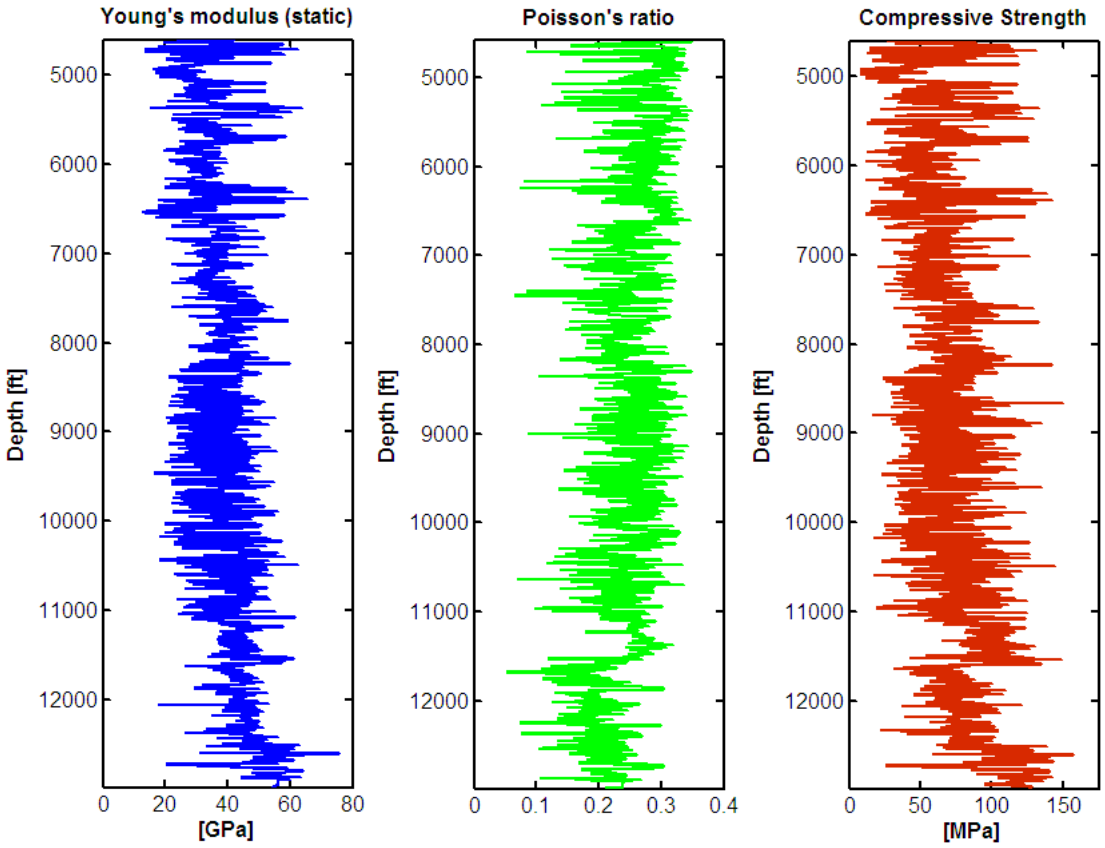

Figure 2-3: From left to right, Young's modulus, Poisson's ratio, and compressive rock strength derived from log data.

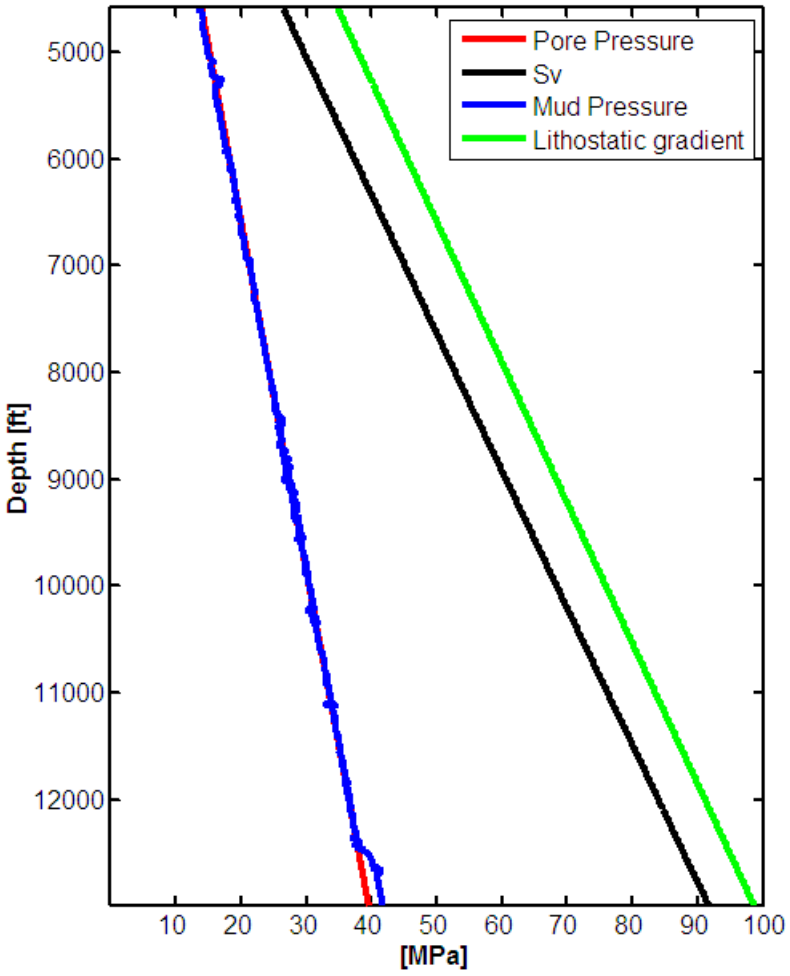

Figure 2-4: Vertical stress computed from the weight of the overburden (in black). Pore pressure (red) is assumed equal to the hydrostatic gradient of 10 MPa/Km; the drilling mud pressure (blue); and the lithostatic gradient of 25 MPa/Km (green).

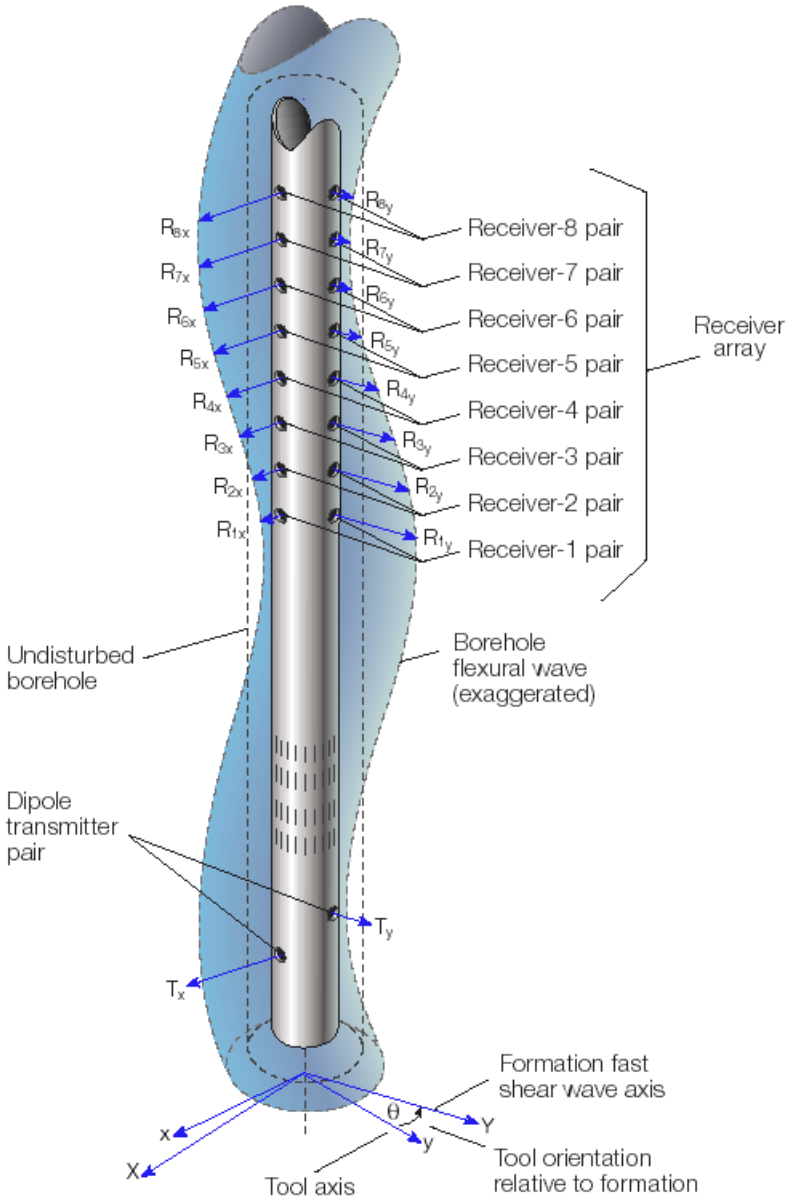

Figure 2-5: DSI tool diagrammatic configuration. Modified from Brie et al. (1998).

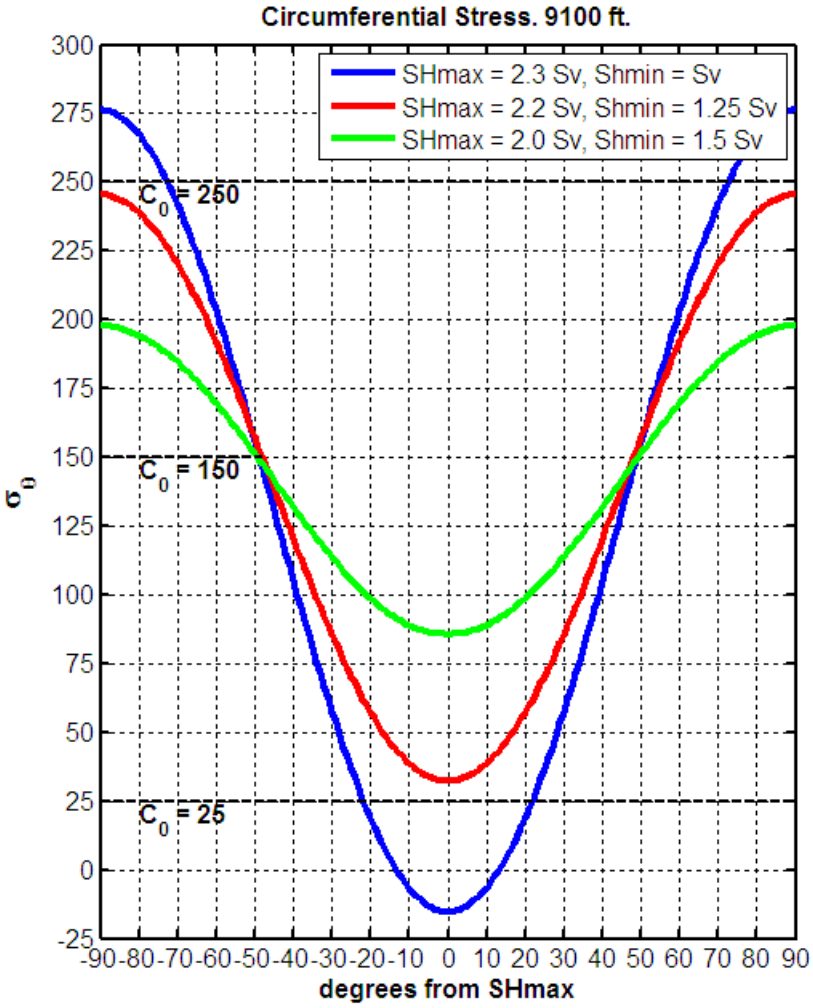

Figure 2-6: Hoop stress as a function of azimuth as described by equation 2.4 when $r = R$, $P_p = 27.8\ MPa$ and $\Delta P = -1\ MPa$. Three cases are shown and for all of them Sv is 56 MPa: (1) $SHmax = 2.3Sv$, $Shmin = Sv$ (blue); (2) $SHmax = 2.2Sv$, $Shmin = 1.25Sv$ (red); (3) $SHmax = 2.0Sv$, $Shmin = 1.5Sv$ (green). When hoop stress exceeds the rock mechanical resistance at a particular angle, failures are expected. Because hoop stress is not constant everywhere around the hole, it is possible that failures are localized. In this example, when the rock strength is 250 MPa, failures only take place for case (1) and at azimuths -70° to -90° and 70° to 90°. When the rock strength is 150 MPa, failures are observed in all cases but still localized between -45° and -90° and 45-90°. For a strength of 25 MPa, failures occur at all azimuths for cases (2) and (3).

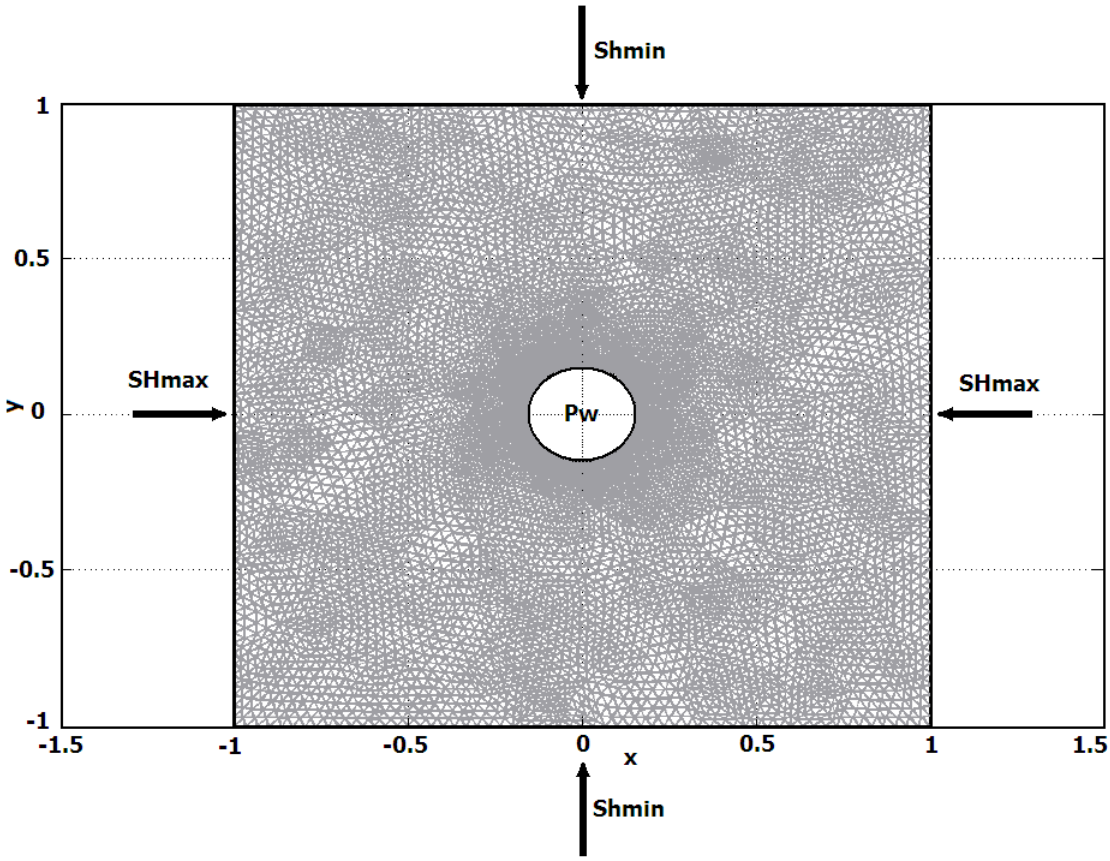

Figure 2-7: Model geometry, mesh, and boundary conditions. $SHmax$ is applied parallel to the x-direction. $Shmin$ is the boundary condition applied in the y-direction. P_w in the figure refers to mud pressure. Units in x and y are meters.

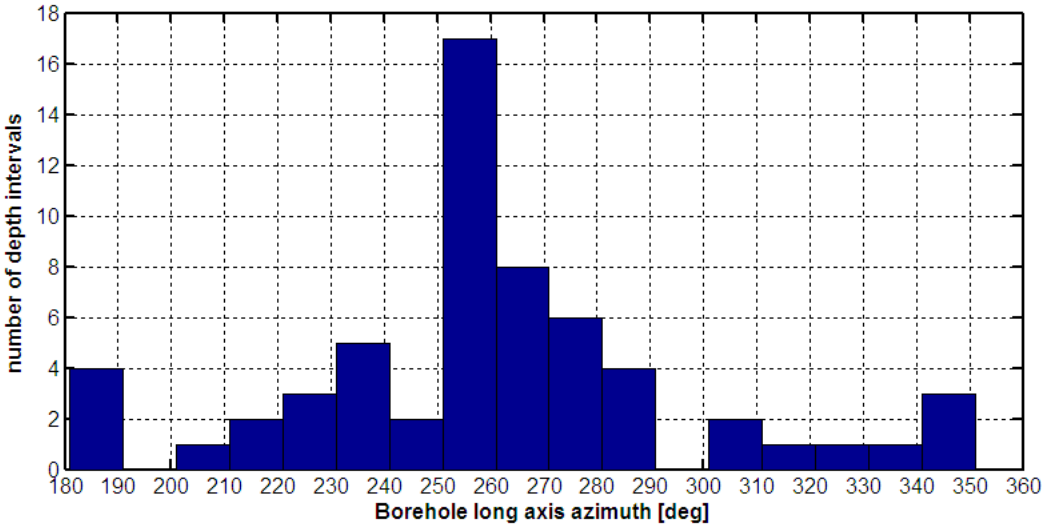

Figure 2-8: Histogram of *Shmin* azimuths derived from breakouts orientations at different depths and throughout the well section.

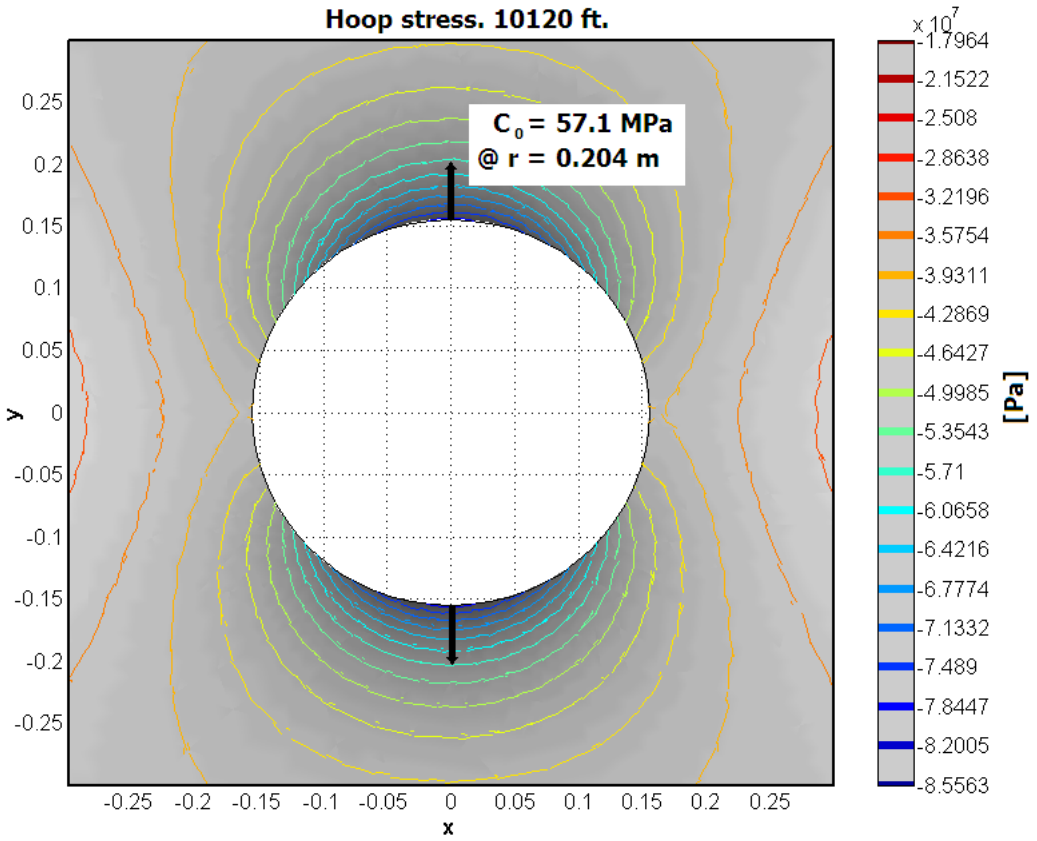

Figure 2-9: Model results. Contours represent hoop stress around the borehole. Formation properties for this model correspond to the data at 10120 ft. Hoop stress values similar to the compressive rock strength (57.1 MPa) concentrate at approximately the borehole maximum radius observed at this breakout depth.

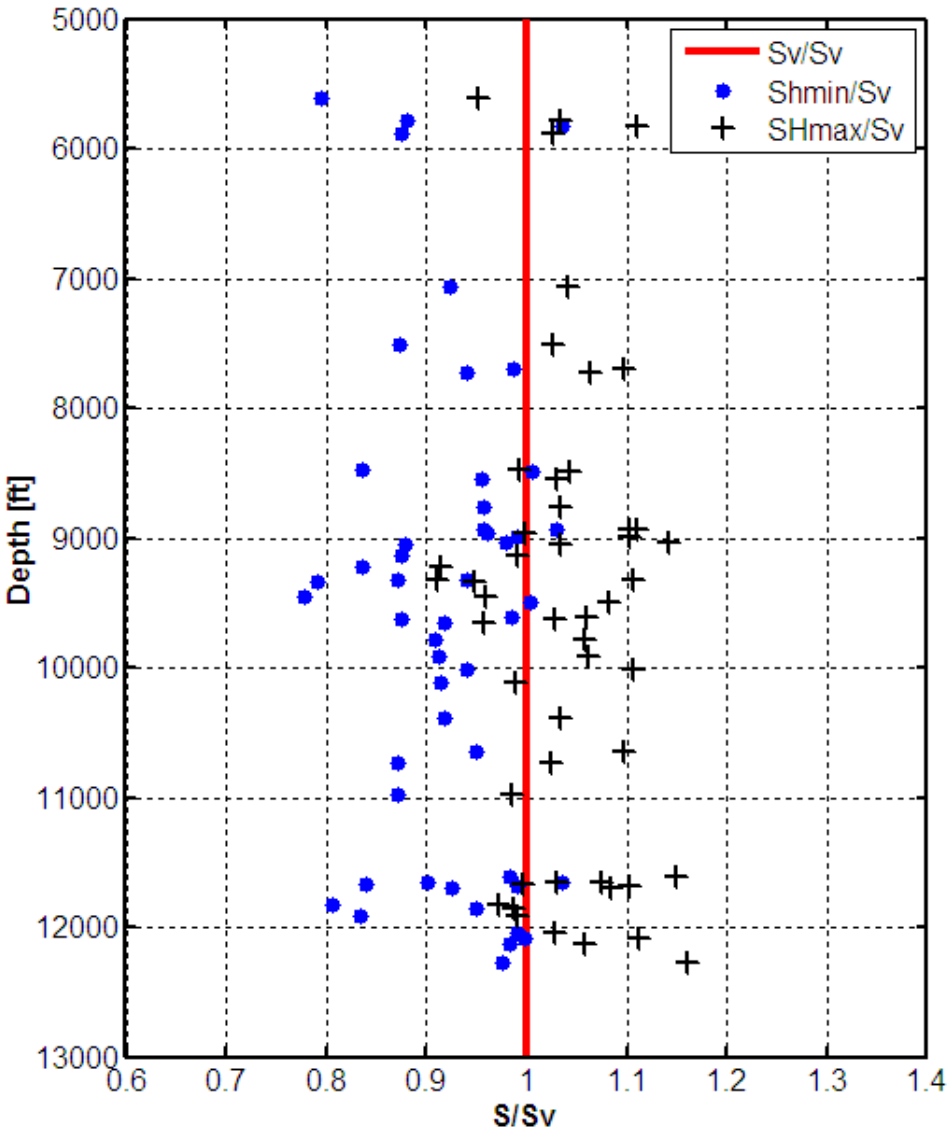

Figure 2-10: Maximum (black plus signs) and minimum (blue dots) horizontal stresses magnitudes relative to the vertical stress in depth. Data points are the results obtained from the stress modeling.

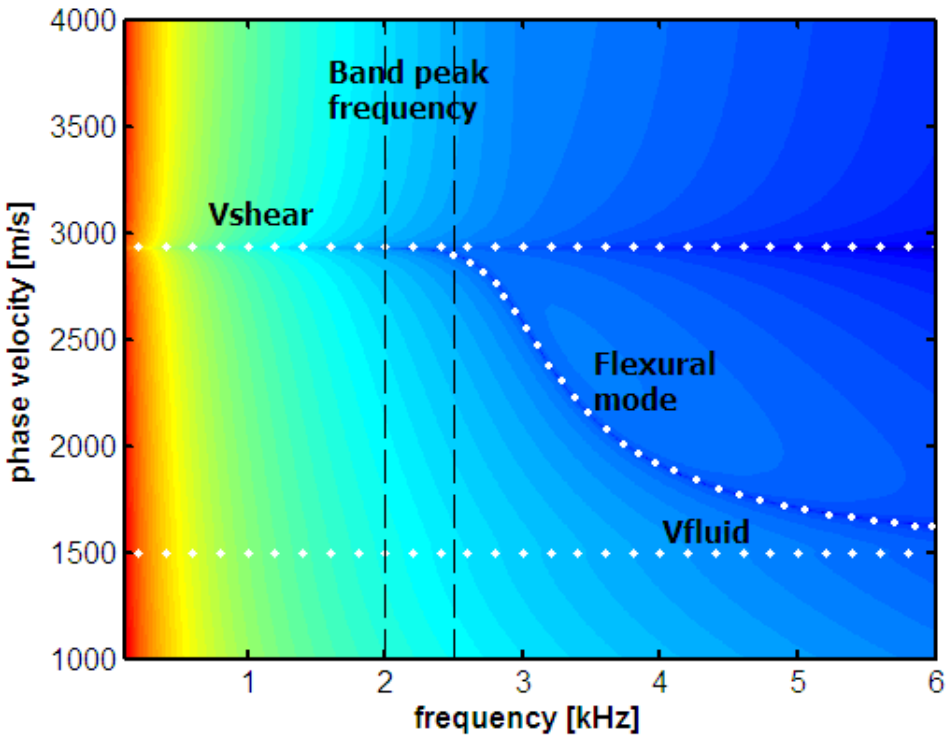

Figure 2-11: Roots of the period equation corresponding to azimuthal order 1 (flexural mode) in the phase velocity-frequency plane (coded by Dr. Rama Rao at ERL, MIT). The formation and borehole properties modeled correspond to those observed at 8280 ft. The shear wave velocity is 2930 m/s. Fluid velocity is 1500 m/s. The flexural wave asymptotes the S-wave velocity at low frequencies and the fluid velocity at high frequencies.

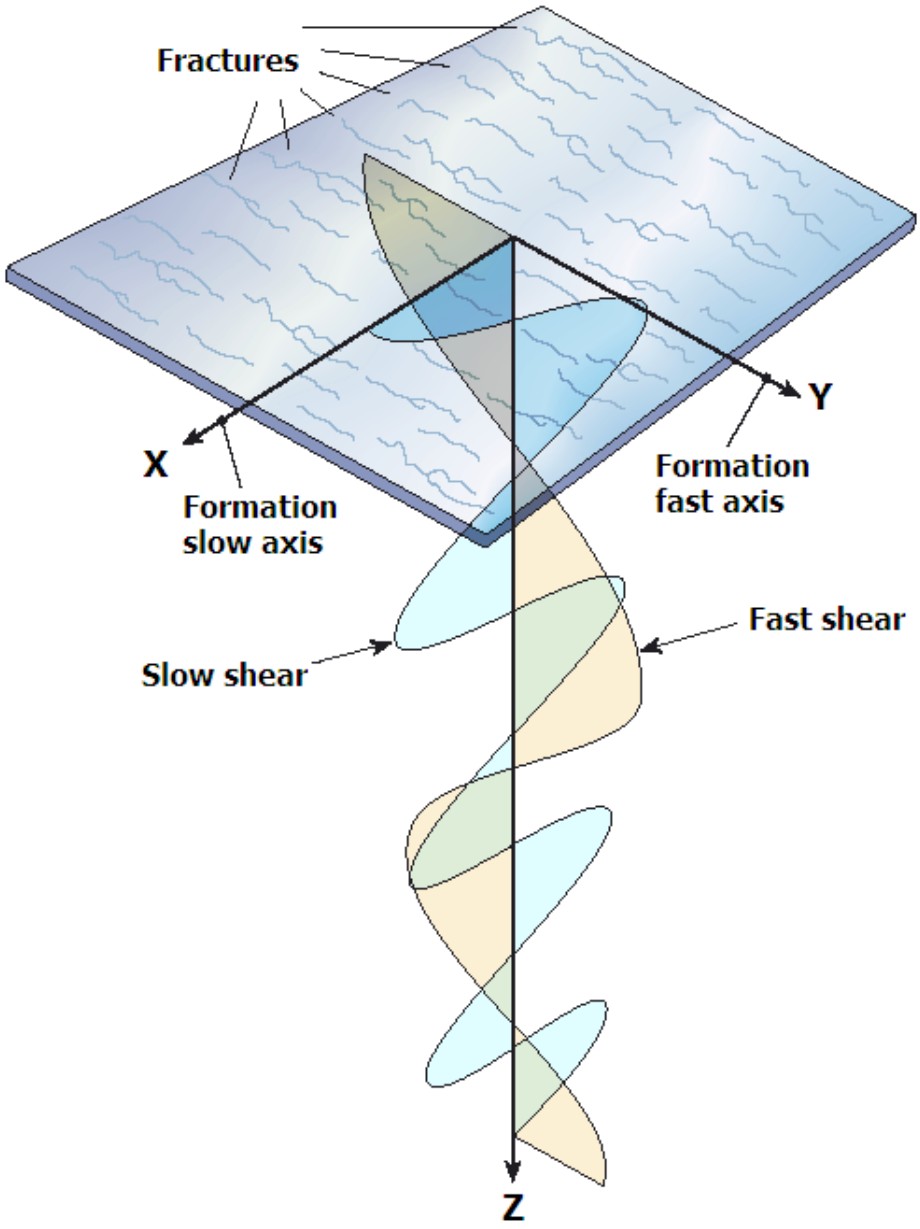

Figure 2-12: Diagram of shear wave splitting in an anisotropic formation. Modified from Brie et al. (1998). Waves propagate in the z-direction while particle displacements polarize in the horizontal plane. The slow shear direction is perpendicular to the orientation of fractures or similarly to the direction of the minimum horizontal stress.

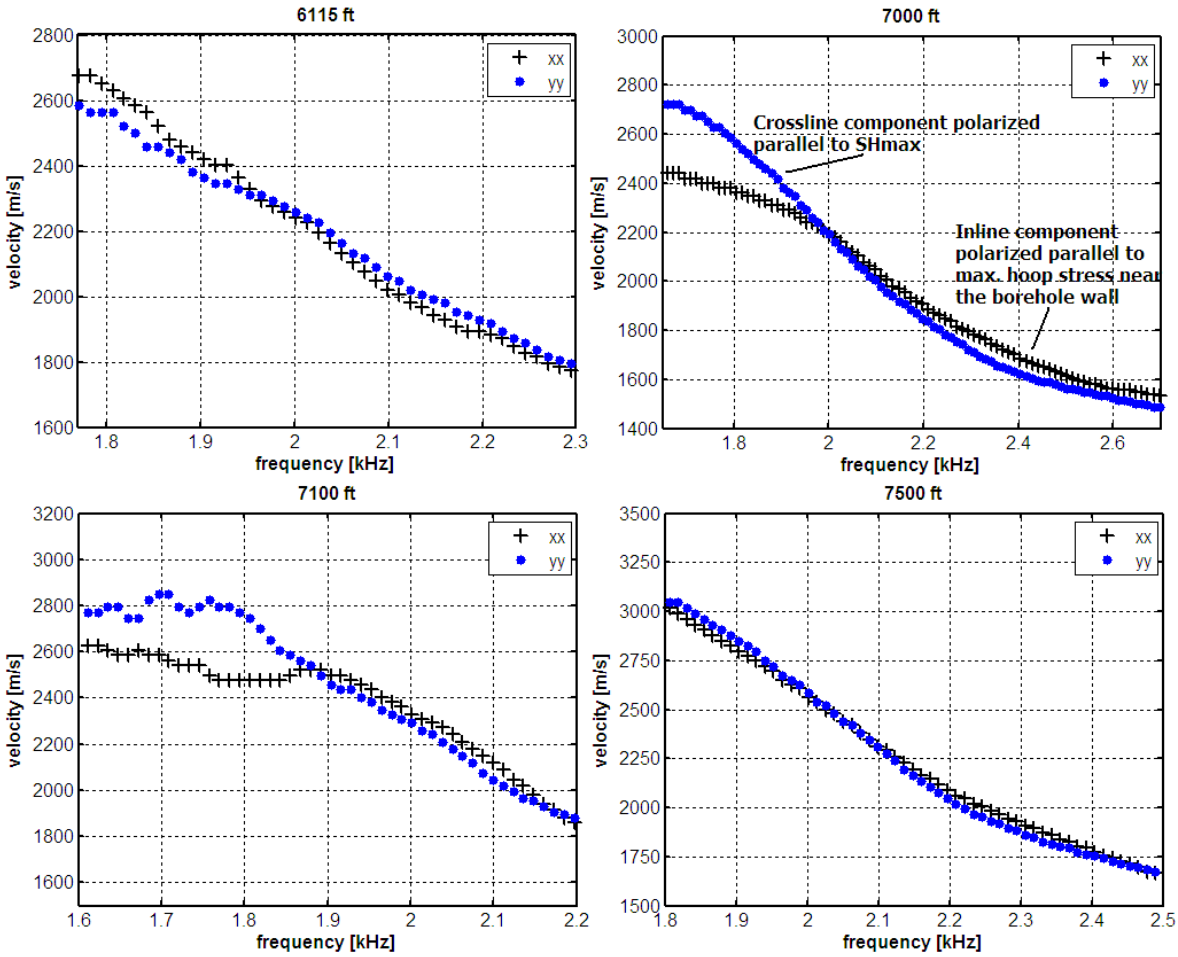

Figure 2-13: Example depths where crossovers in the dispersion curves of dipole data are observed. Black plus signs are used for the dispersion obtained from the inline component (xx). Blue dots correspond to the crossline component (yy). The flexural dispersion curves are expected to cross at some frequency when an anisotropic stress field is superimposed on an isotropic or weakly anisotropic rock formation. As indicated on the 7000 ft dispersion plot (top right), the shear-wave component polarized parallel to the maximum stress direction is the fastest at low frequencies. In this case, the crossline component is aligned parallel to the maximum stress direction. At high frequencies, hoop stresses are more compressive 90° away, which is the polarization direction of the inline component (xx), thus becoming the fastest.

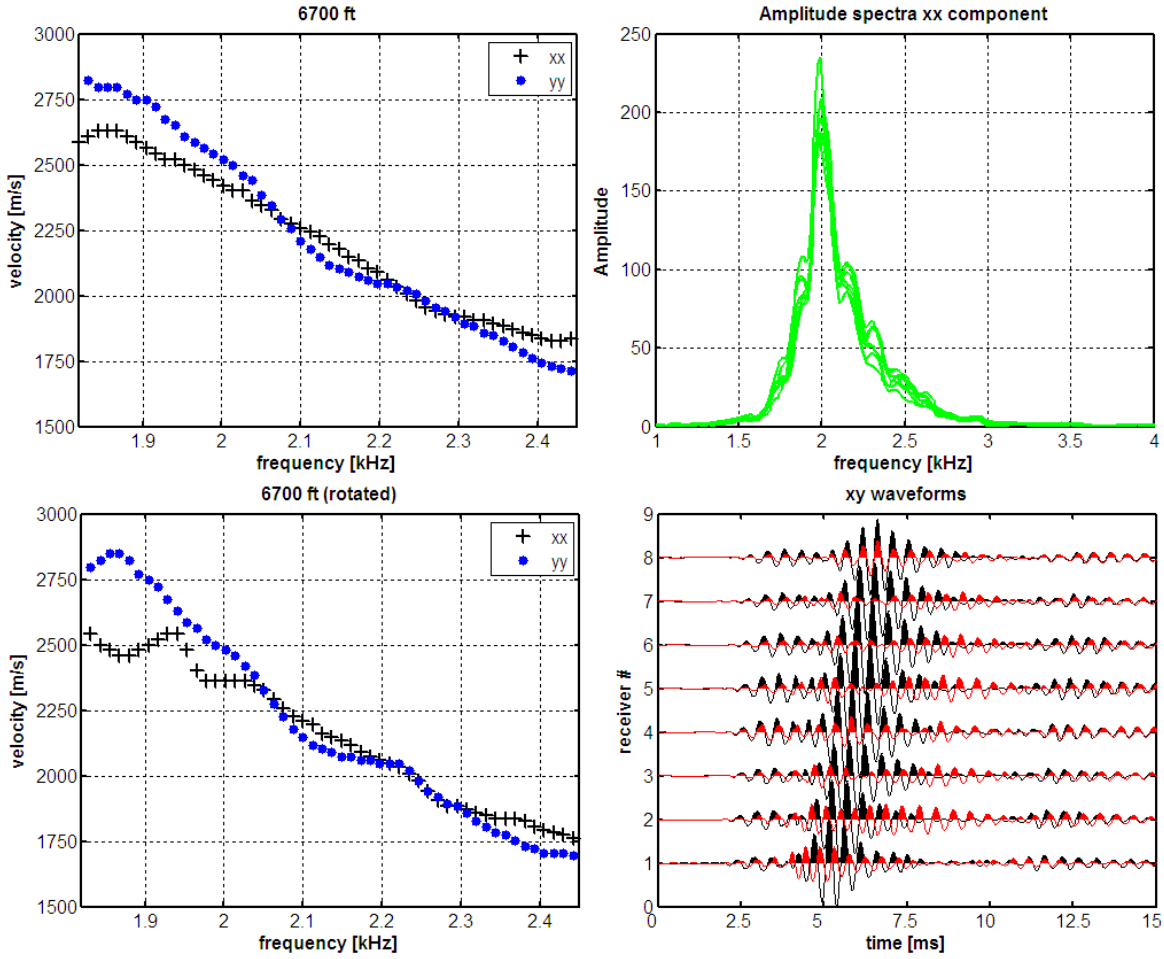

Figure 2-14: Processing results at 6700 ft, a depth where a crossover of the inline and crossline components is observed (top left). At the bottom left, the inline and crossline dispersion curves of the flexural mode are rotated the to the principal axes of stress anisotropy. The effectiveness of the rotation can be verified in the lower right plot where the cross-component (xy) is plotted before (black) and after rotation (red). Energy of the flexural wave is minimized in all receiver signals. The velocity anisotropy is measured at peak frequency which is around 2 kHz as indicated by the frequency spectrum of the inline component (xx) in the figure at the top right.

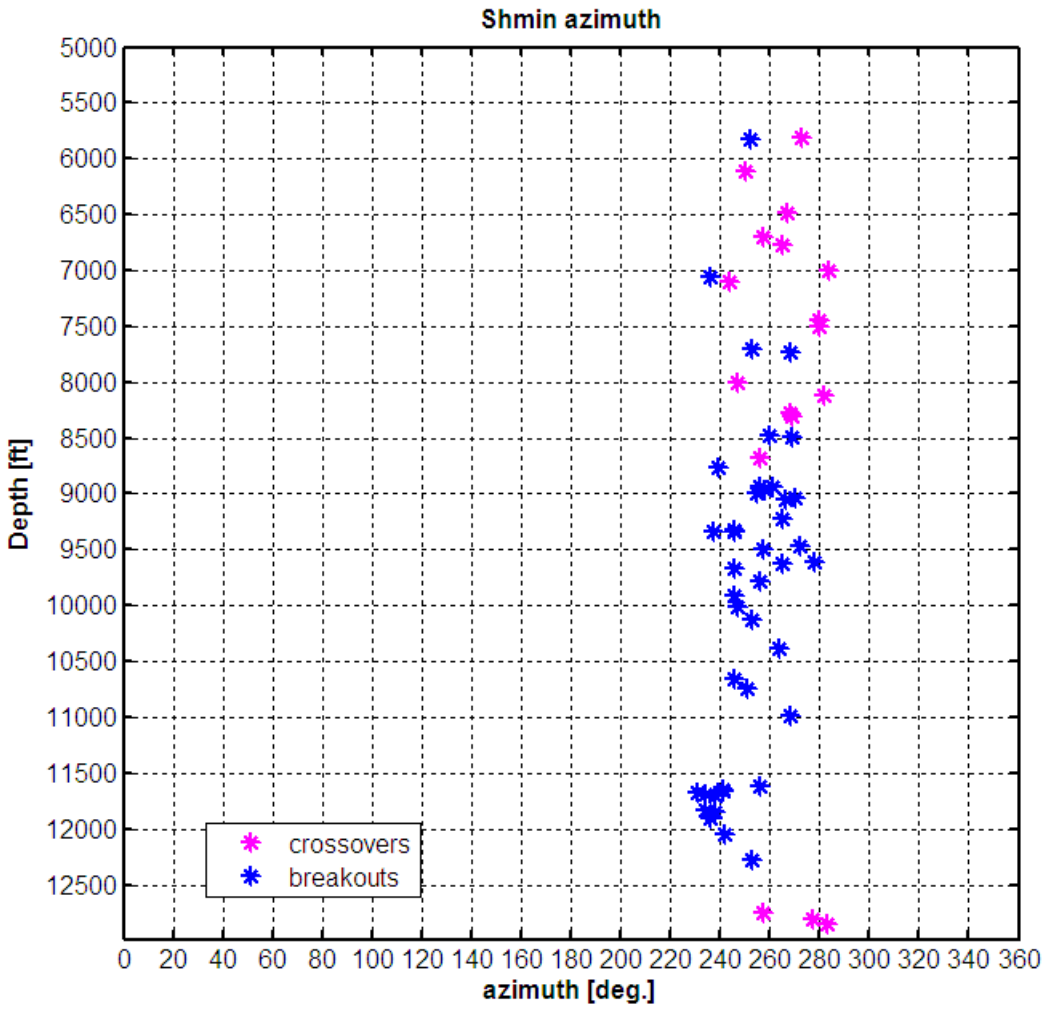

Figure 2-15: *Shmin* azimuths obtained from cross-dipole data rotation (magenta). The orientations computed from breakouts are displayed with blue stars. *Shmin* direction is well constrained from these two measurements to be around 260°, giving a dominant strike E10N-W10S.

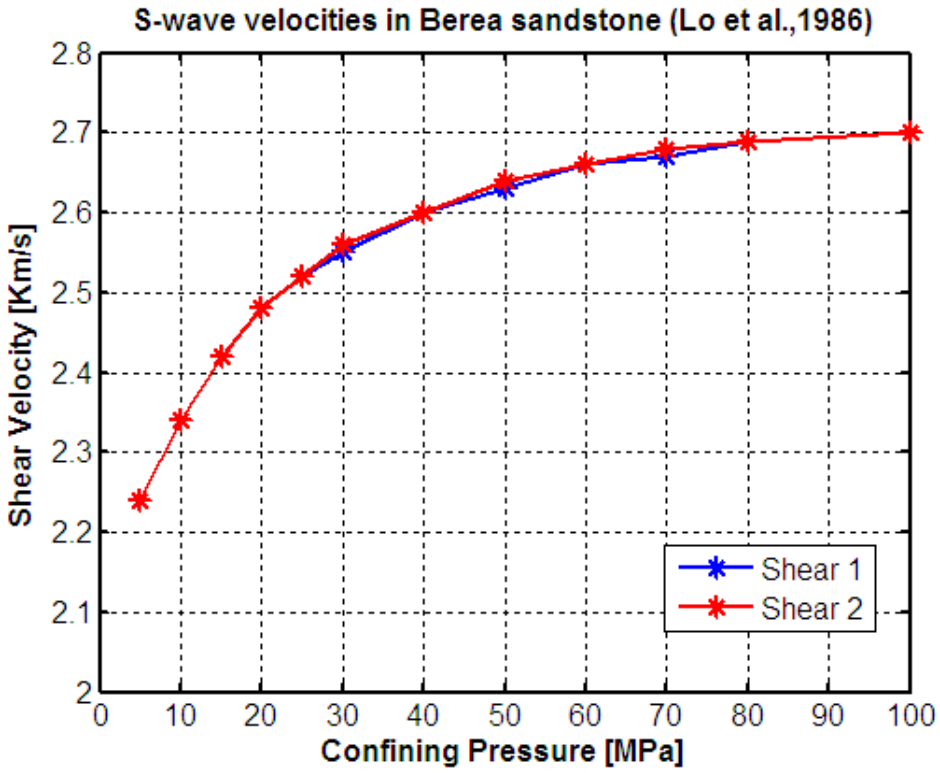

Figure 2-16: Shear wave velocities with increasing confining pressures measured perpendicularly to bedding planes in Berea sandstone at two orthogonal transducers. Data from Lo et al. (1986).

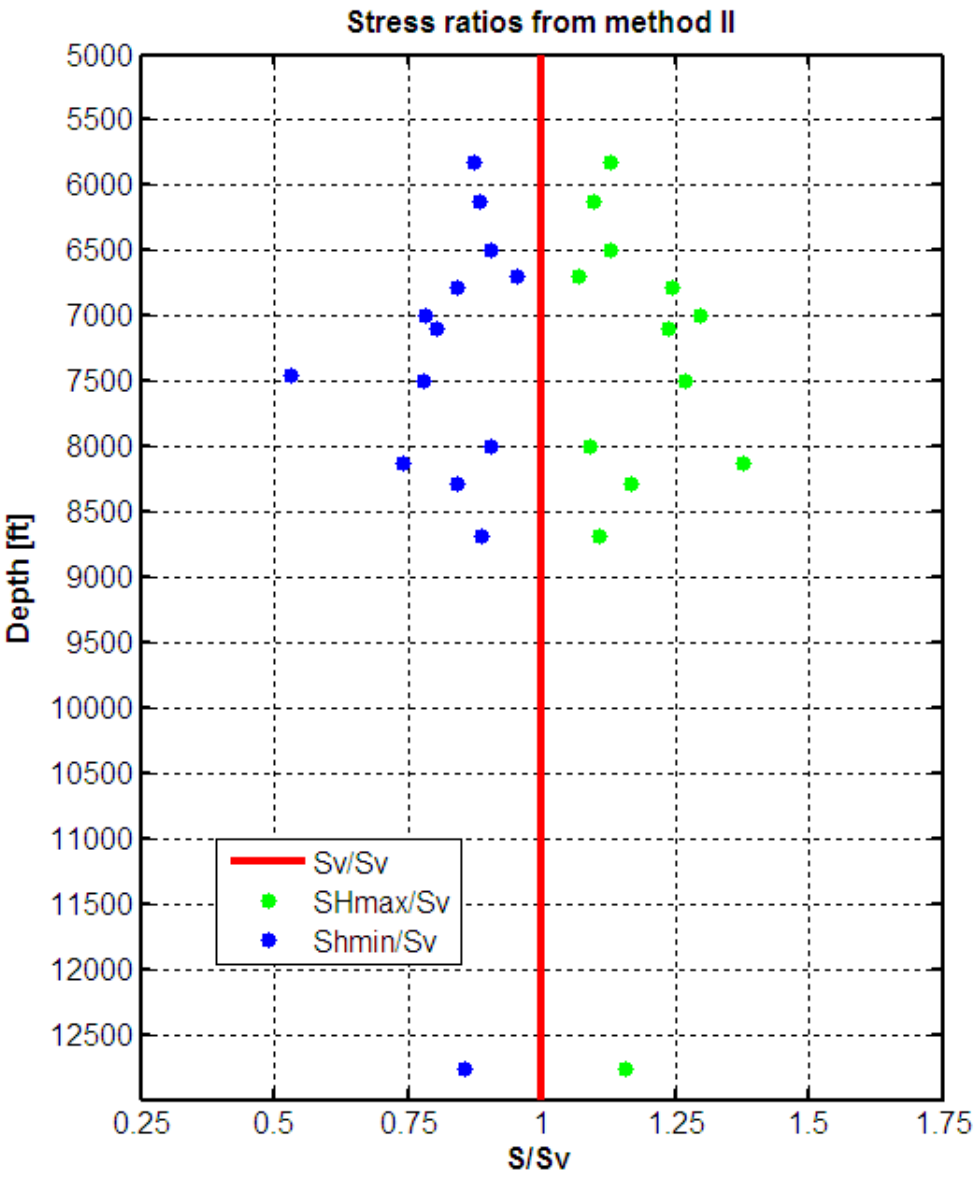

Figure 2-17: Ratios of maximum (green) and minimum (blue) stress to vertical stress estimated from stress-induced velocity anisotropy at crossover depths. Experimental data used as base of comparisons are elastic velocities of Berea sandstone reported in Lo et al. (1986).

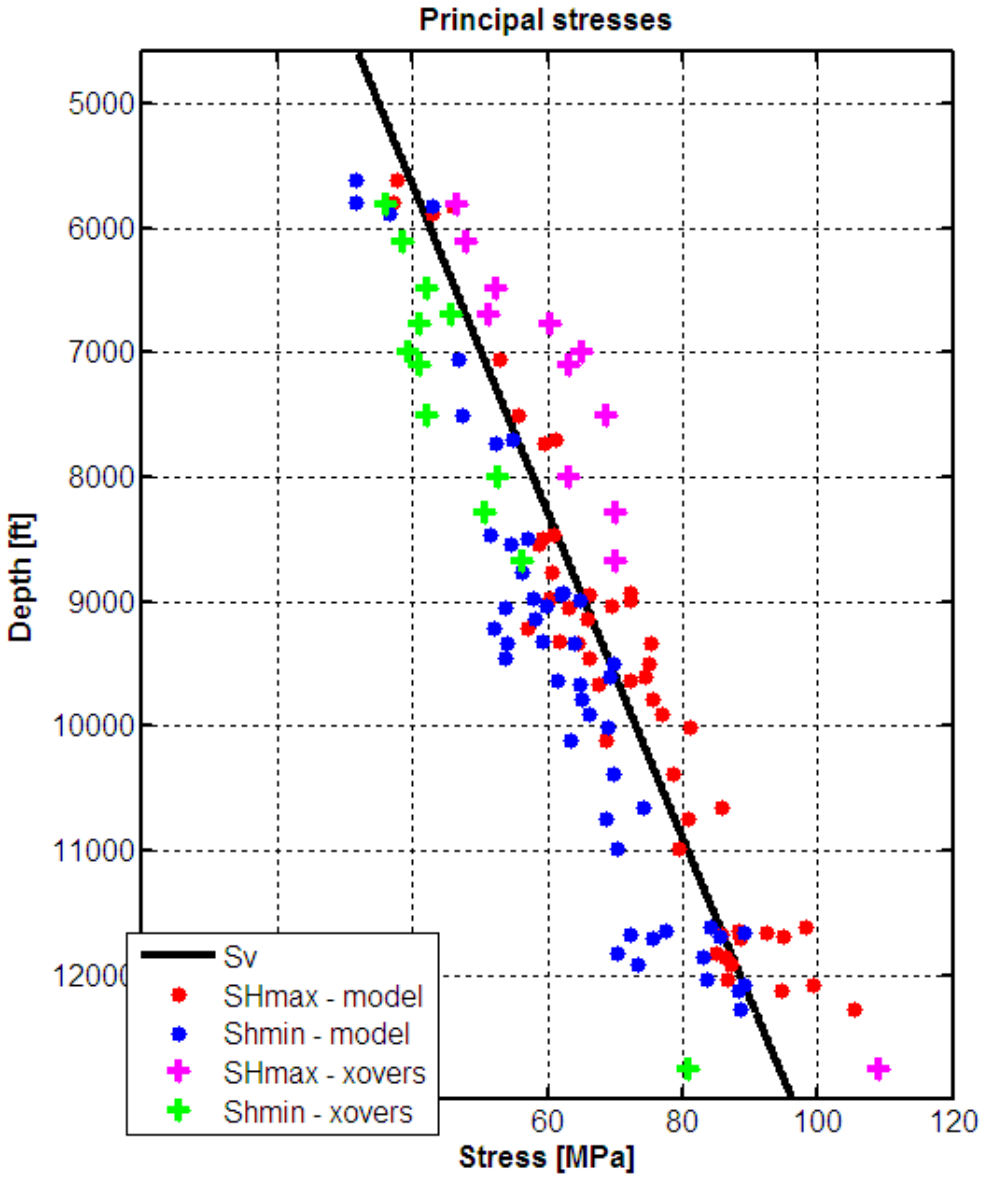

Figure 2-18: Principal stresses magnitudes vs. depth. Vertical stress is plotted in black. Horizontal stresses derived from the elastic model are shown in red (maximum) and blue dots (minimum). Equivalent results from shear velocity anisotropy are plotted with plus signs.

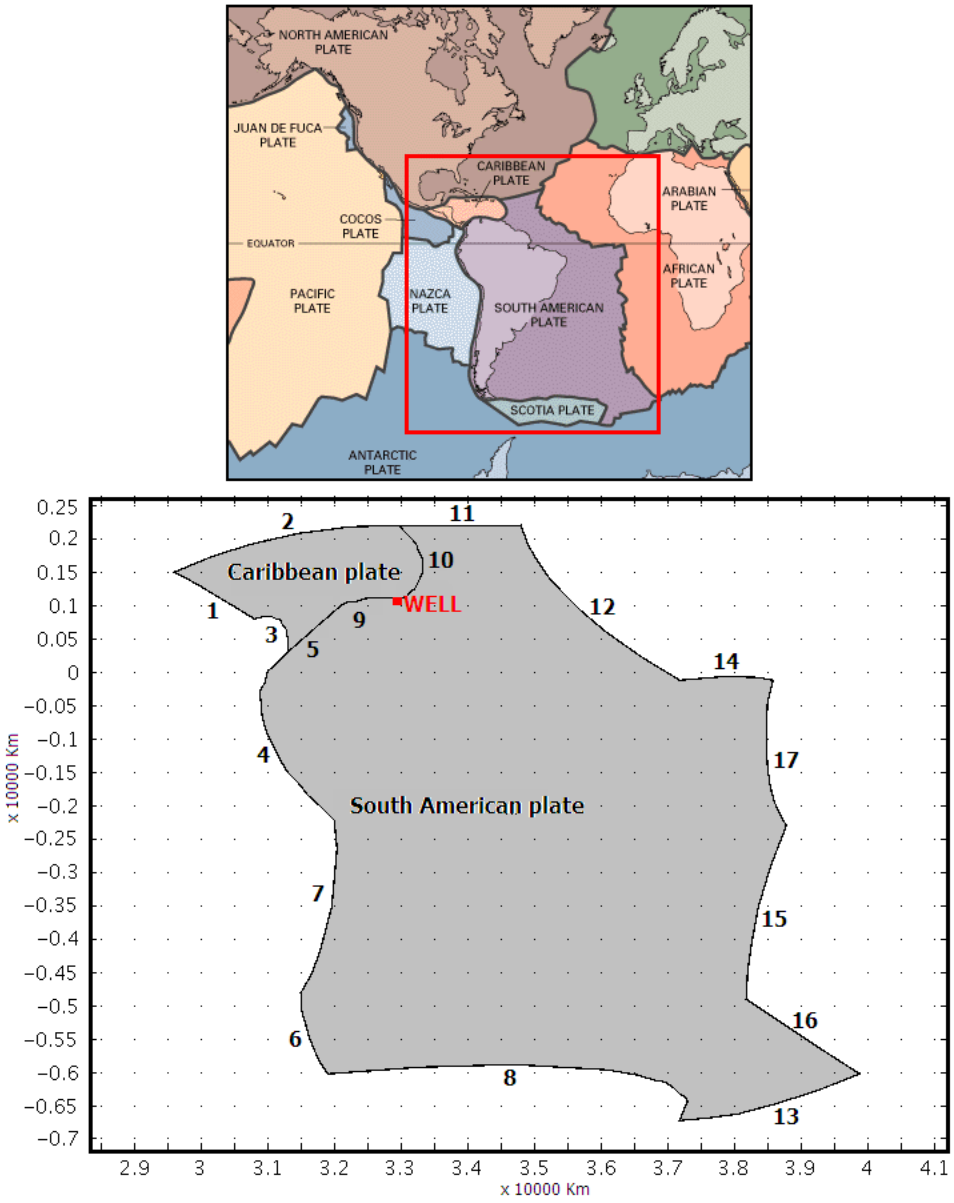

Figure 2-19: Geometry of the regional stress model. The model is a 2D (map view) representation of the Caribbean and South America plates. The well location and the numbering of the model boundaries are indicated.

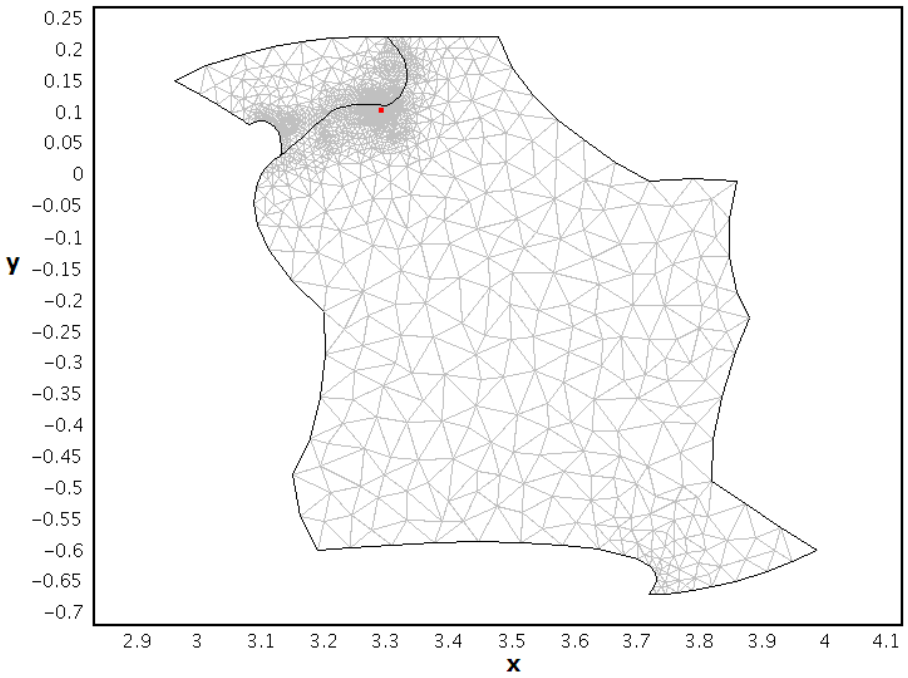

Figure 2-20: Finite element mesh of the regional stress model.

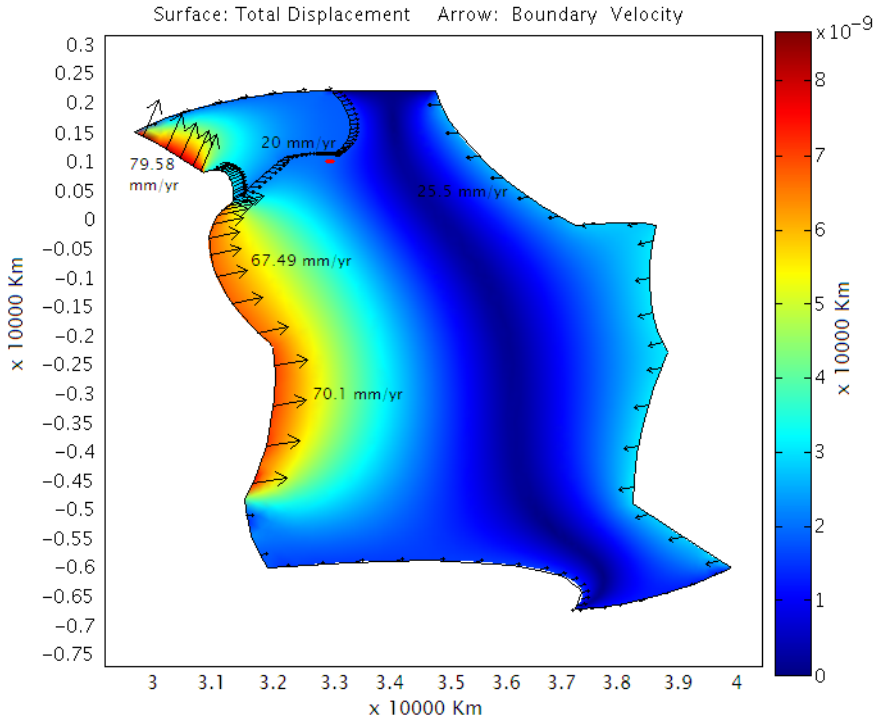

Figure 2-21: Boundary conditions corresponding to velocities from the global model REVEL. Arrows' length is proportional to velocity magnitude at the plate boundary location. The surface plot shows total displacement. Units are 10^{10} mm.

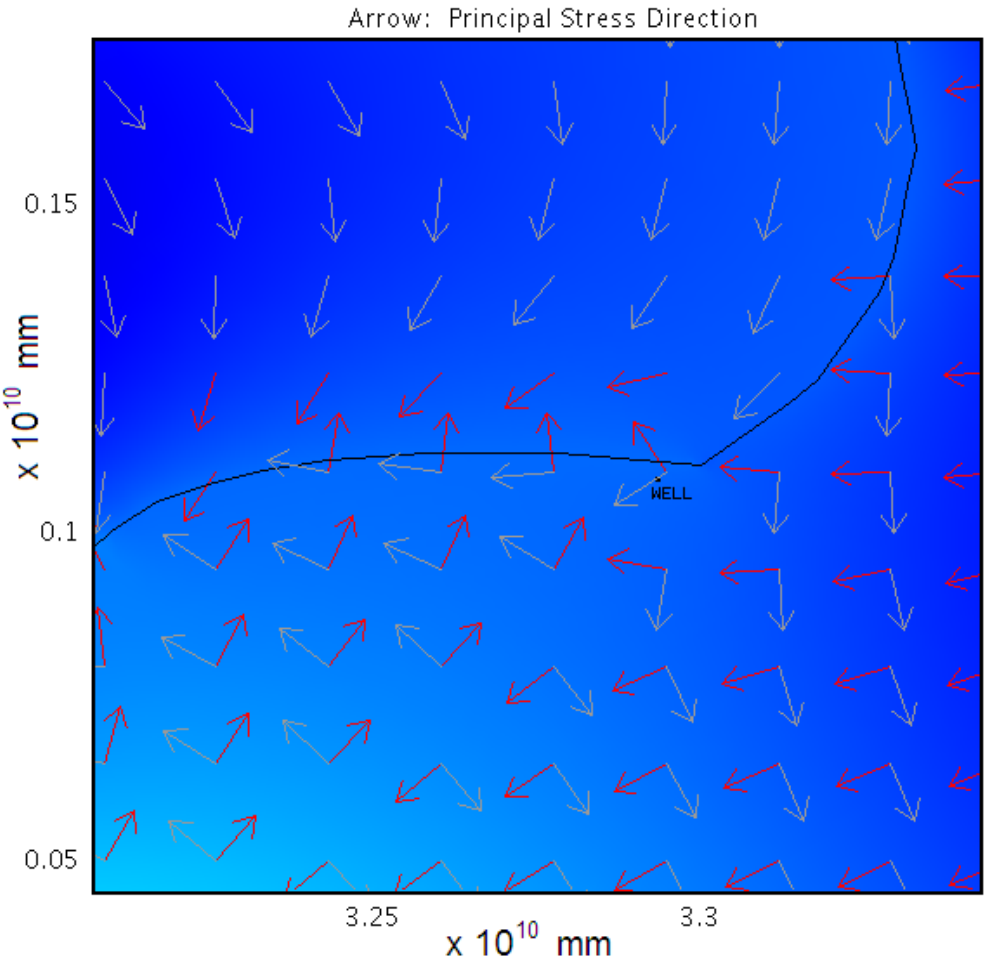

Figure 2-22: Principal stresses direction around the well location for REVEL velocities imposed at the model boundaries. Red arrows represent maximum horizontal stress. Minimum stress orientation is indicated in gray.

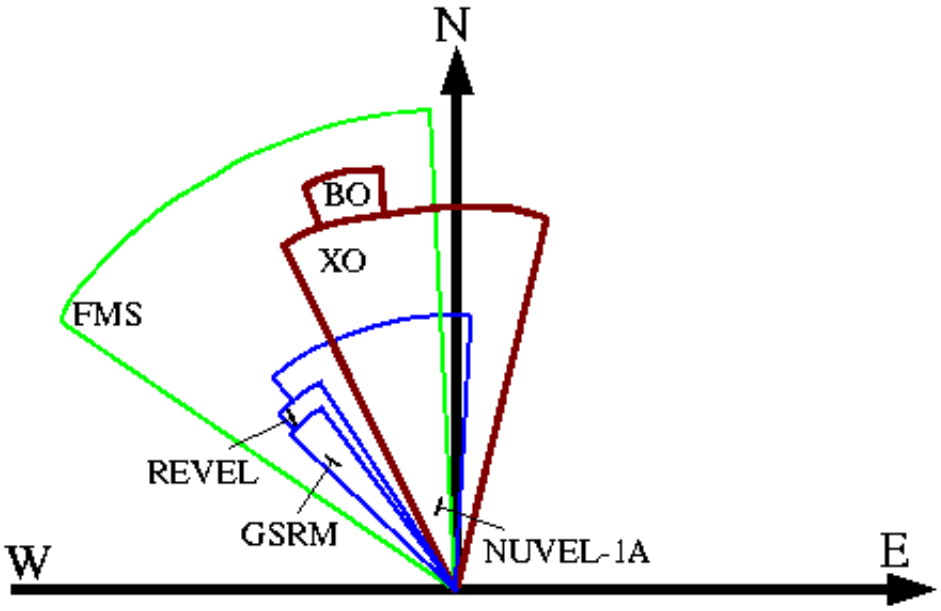

Figure 2-23: $SHmax$ direction. Breakout data (BO) indicate that $SHmax$ azimuth is in the range 340-350°. $SHmax$ azimuth obtained from crossovers (XO) is between 334 and 14°. Maximum stress orientation according to the regional stress models are indicated in blue. The western limit of the three models correspond to results when Nazca's velocity is reduced in 50%. NUVEL-1A, REVEL and GSRM velocities give $SHmax$ azimuth ranges of 319-2.5°, 315-327° and 314-324° respectively. In green, a range of $SHmax$ azimuths obtained from focal mechanisms (FMS) in the World Stress Map (304-357°).

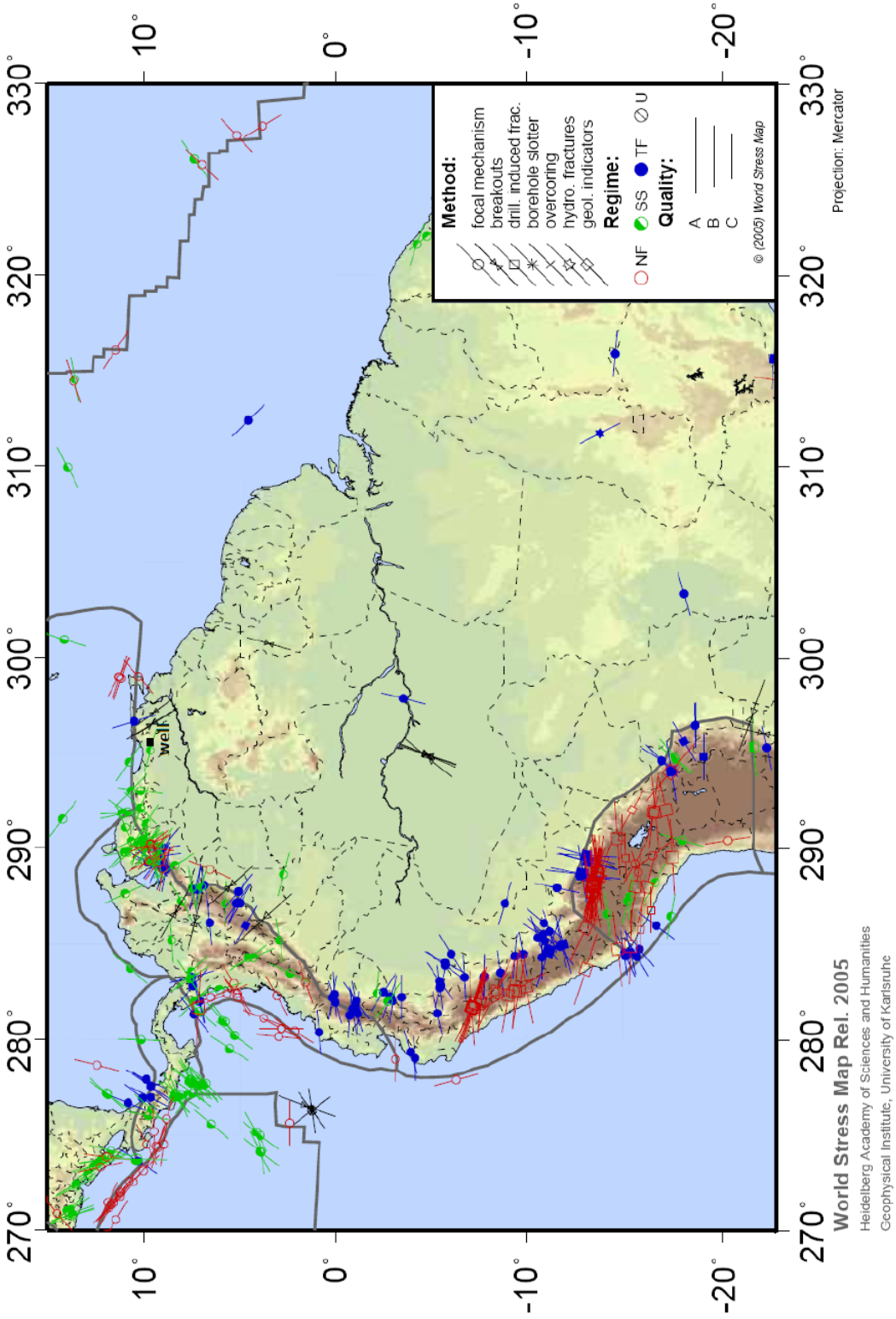

Figure 2-24: Stress map of north of South America and the Caribbean. From Reinecker et al. (2005).

.

Chapter 3

Analysis of Seismic Scattering to Estimate Reservoir Fracture Properties

This chapter reports some of the results of our recent research in characterizing fractured reservoirs using surface seismic data.

The detection of reservoir fractures using seismic methods has been traditionally based on effective medium theories that assume fractures in a rock mass are much smaller than the wavelengths, and their effects are distributed throughout the bulk. Nowadays well-developed techniques to characterize fractured reservoirs include the processing of converted waves, AVOA analyses of P wave, NMO ellipticity, and others (e.g. Pérez et al., 1999; Lynn, 2004a,b; Ata and Michelena, 1995). In these techniques, the medium, composed of rock and fractures, is described by an equivalent anisotropic medium. Therefore, effective medium approaches are convenient to study the seismic response of microcracks.

Another approach consists of accounting for the fractures as discrete inclusions in the medium. Discrete approaches are valid in the limit where the seismic wavelength is comparable to the fracture dimensions. The normal resolution of seismic waves at depths of common reservoirs is 20-100 Hz which corresponds to wavelengths on the order of 10 to 300 m for typical rock velocities. Therefore, discrete approaches are

convenient to study the seismic response of large joints (macrofractures) and fracture corridors.

Numerous modeling (e.g. Groenenboom and Falk, 2000; Nihei et al., 2002; Yi et al., 1998; Vlastos et al., 2003; Willis et al., 2006) and laboratory experiments (e.g. Pyrak-Nolte et al., 1987; Xian et al., 2001; Nihei et al., 1999; Pyrak-Nolte and Roy, 2000; Pyrak-Nolte et al., 1990; Hsu and Schoenberg, 1993; Groenenboom and Falk, 2000) have been done in order to understand the seismic response of discrete fractures. These studies have significantly increased our knowledge about the wave propagation phenomena developed around a single fracture and multiple sets of fractures. The wave phenomena that take place in these situations have been revealed as a combination of seismic scattering and wave guiding.

In 3D models of multiple sets of fractures, the waves generated by the fractures appear as coda waves (Willis et al., 2006; Vlastos et al., 2003; Nakagawa et al., 2003). In standard signal processing, coda waves are often considered noise. However, the apparent noise is indeed a complicated effect of the presence of fractures in the wave paths. As such, it contains valuable information about the fracture geometry and properties. In order to extract some of this fracture information from the coda waves, Willis et al. (2006) presents a practical methodology, called the Scattering Index method. To our knowledge, this is the only method that exists heretofore to systematically detect fracture corridors and estimate their preferred orientation from 3D field data. The *SI* method is explained in section 3.6.

In this chapter, we develop another methodology to characterize fracture corridors. The proposed method, called the *F-K* method, estimates the mean spacing and orientation of fracture corridors from the spectral response of coda waves. Details of the *F-K* method are presented in section 3.4; and both methods, (*F-K* and *SI*), are applied to a field dataset in chapter 5.

Various numerical models containing vertical periodic fractures are also discussed throughout this chapter. The numerical simulations serve for three purposes: (1) to demonstrate the general wavefield that develops around multiple parallel discrete fractures (section 3.2), (2) to study the characteristics of the fracture signals in the

frequency-wavenumber domain (section 3.3), and (3) to understand the sensitivity of these fracture signals to different fracture properties (section 3.5). The following section, (section 3.1), explains the theoretical framework and modeling approach adopted in these numerical experiments.

3.1 The Discrete Fracture Model

In order to find wave solutions when elastic media are in contact, different boundary conditions can be imposed on the tractions and displacement field, depending on the particular wave phenomenon under study. Free surfaces and welded contacts are examples of these boundary conditions. Discrete fractures embedded in a rock mass can be explicitly expressed using a special boundary condition, known as the linear slip condition (Schoenberg, 1980). Unlike perfectly bonded interfaces (welded), the linear slip condition is considered an imperfect bonding condition because displacement across the surface is not continuous. Instead, the displacement jump (Δu) across the interface is linearly related to the traction (τ) through the fracture stiffness (κ) (Schoenberg, 1980):

$$\tau = \kappa \Delta u \tag{3.1}$$

The linear slip model is also referred as the displacement-discontinuity model. This model predicts velocity, amplitude, and phase differences measured when seismic waves propagate through fractured samples (Pyrak-Nolte et al., 1987; Hsu and Schoenberg, 1993). The matching of the experimental observations is attained because the displacement-discontinuity theory predicts a frequency dependent seismic response. In other words, the effective velocity of the rock plus fractures, as well as the reflection and transmission coefficients, are function of frequency. These quantities are also dependent on the contrast of fracture stiffness to medium impedance and on the fracture length or number of fractures per unit length (Schoenberg, 1980; Pyrak-Nolte et al., 1987; Pyrak-Nolte, 1996).

In order to describe fractured media using the linear slip deformation model, Schoenberg and Sayers (1995) develop an effective medium theory in which the effec-

tive compliance of a fractured rock is expressed as the sum of the unfractured rock compliance, plus an excess compliance per each set of aligned fractures. When the fractures are planar and parallel, the components of the fracture system compliance tensor are related to jump discontinuities in the displacements. If the set of fractures is rotationally invariant, the compliance is only a function of its shear and normal components. In the presence of just one set of fractures in an isotropic background, the medium becomes transversely isotropic with its symmetry axis perpendicular to the fractures. In this case only five parameters are needed to define the effective medium: the Lamé parameters of the host rock (λ and μ) and the two fracture compliances. Fracture normal and tangential compliance can be calculated experimentally (Hsu and Schoenberg, 1993) or related to microstructural parameters like crack aspect ratio, density, and saturation (Liu et al., 2000; Schoenberg and Douma, 1988).

The displacement-discontinuity theory has been used to examine the properties of guided waves between two parallel fractures (Nihei et al., 1994, 1999; Xian et al., 2001; Pyrak-Nolte and Roy, 2000) and to build models of wave propagation in the presence of multiple parallel fracture sets. The simulations of fracture scattering assume different numerical techniques, including the pseudospectral method (Vlastos et al., 2003), a hybrid method combining the finite element and plane wave methods (Nakagawa et al., 2003), and finite differences (Yi et al., 1997, 1998; Daley et al., 2002; Nihei et al., 2002; Willis et al., 2006). In particular, implementation of the linear slip model in finite differences is simplified using the Coates and Schoenberg method (Coates and Schoenberg, 1995), in which all grid cells containing the fracture interface are replaced by grid cells with modified properties estimated with the homogenous equivalent medium discussed above. The resulting line of grid cells represents a layer whose width corresponds to the size of the grid cell and whose elastic stiffness is replaced by some appropriate anisotropic stiffness that try to mimic the same scattering behavior of the linear-slip interface.

3.2 Modeling of Wave Propagation Through Fracture Corridors

We are interested in studying the effects of fracture corridors on the seismic wave propagation. In this section, fracture scattering is analyzed through synthetic models generated with the ERL's in-house seismic modeling code (ERLSMP).[1] ERLSMP is a 3D elastic and anisotropic finite-difference code. It is based on a velocity-stress formulation of the wave equation which is discretized in a standard staggered grid. The approximation uses an explicit operator, 4th order in space and 2nd order in time (Krasovec et al., 2003).

Discrete fracture zones are modeled following the Coates and Schoenberg's approach (Coates and Schoenberg, 1995). As explained above, this approach allows the implementation of discrete fractures in a finite difference numerical framework. Fractures of negligible thickness relative to the seismic wavelengths are represented by assigning an effective anisotropic stiffness tensor to one or several cells in the finite difference grid. Grid size is 5 m for all the models discussed hereinafter.

The Coates and Schoenberg's method is a simplifying approach to model the very complicated wave propagation that takes place around a real fracture, including reflection, transmission, and diffraction of body waves and of guided waves. This approach attempts to model the gross effects of these phenomena but will not match all of them. For instance, a Rayleigh wave, propagating mainly along the fracture surface, re-diffractions of this wave at the tips of the fracture, and a slow channel wave propagating in the fluid inside the fracture have all been identified in other numerical experiments using a different modeling approach (Groenenboom and Falk, 2000). The slow channel wave cannot be modeled using Coates and Schoenberg's method because fractures are represented by interfaces with a vanishing width. Typical roughness of the fracture surfaces and presence of cementation material, among others, would increase the complexity of the propagation phenomena even more.

[1] Earth Resources Laboratory Seismic Modeling Project

3.2.1 1-Fracture 2D Model

In order to explain the first order effects of fracture corridors on the seismic wave propagation, we start with a relatively simple 2D model shown in figure 3-1. The model consists of three isotropic horizontal layers with typical sedimentary rock velocities and densities listed in table 3.1. The middle layer contains a vertical fracture simulated by an anisotropic medium with horizontal symmetry (HTI). It is one column of single grid cells as tall as the layer thickness (200 m). The velocities of the fractured layer are plotted as a function of incident angle in figure 3-2. As it can be seen in this figure, the P-wave velocity of the fractured zone in the layer is slower than the P-wave velocity of the background at all incident angles. The fractured medium supports two shear waves with orthogonal particle motions and velocities that also vary with the angle of incidence. The anisotropic elastic coefficients assigned to the fractured zone are equivalent to having fractures with normal and tangential compliances of 4 x $10^9 Pa/m$.

A point source is located at the center of the model, close to the surface. The source is represented by a Ricker wavelet with center frequency 40 Hz. Two component (x,z) and pressure receivers are located every 5 m on both sides of the source. The vertical component (velocity) recorded is shown on the leftmost panel in figure 3-3. The divergence and curl components of the modeled data are also shown. By plotting the divergence and curl, we split the compressional and shear energy received at the surface. The equivalent shot records obtained from the same model but without the fracture are shown for comparison in figure 3-4. All the records in these figures were muted to remove the direct arrivals.

The most prominent waves generated by the horizontal interfaces are denoted by the following numbers on the non-fractured model records in figure 3-4:

1. The P wave reflected from the top of the second layer (PP). This wave arrives at around 0.11 s at zero offset.

2. The converted shear wave at the top of the second layer (PS). This wave arrives at around 0.15 s at zero offset.

3. The P wave reflected from the bottom of the second layer as a P wave (PPPP). This wave is recorded at zero offset at around 0.21 s.

4. The waves transmitted into the second layer as P (or S) and reflected at the bottom of the second layer as S (or P). On the way up, they are transmitted into the first layer as P waves (PPSP and PSPP). Because they travel as the slower shear wave one way in the middle layer, they are slightly delayed with respect to the PPPP wave (0.25 s).

5. The wave traveling as a P wave until it converts to S as it re-enters the top layer (PPPS). It arrives at about 0.26 s at zero offset. This wave is received at the surface as a shear wave and therefore it has a strong curl component, similarly to the PS wave.

6. The wave traveling as only P wave in the first layer and as only S wave in the second layer (PSSP). It arrives at around 0.28 s.

7. The waves transmitted into the second layer as P (or S) and reflected at the bottom of the second layer as S (or P). On the way up, they are transmitted into the first layer as S waves (PPSS and PSPS). These waves are also better observed in the curl component. Their arrival time is approximately 0.29 s at zero offset.

8. The P wave generated at the source point is transmitted as a shear wave into the second layer. It propagates the rest of the way as a shear wave and therefore is the slowest, arriving at approximately 0.32 s (PSSS).

Figure 3-5 shows the seismograms obtained by taking the difference between the data from the fractured and non-fractured models. The pressure component has been included in this figure to ease the identification of pure compressional events. Since the waves enumerated before are common to the fractured and non-fractured models, they are absent in the difference records shown in figure 3-5. The most prominent waves generated by the fracture are identified in these difference records:

1. The P wave diffracted as P at the top tip of the fracture (PdP).

2. The P wave diffracted as S at the top tip of the fracture (PdS).

3. The P wave transmitted as P into the second layer and diffracted as P at the bottom tip of the fracture (PPdPP).

4. The P wave reflected at the bottom of the second layer from the incident Rayleigh wave propagating along the fracture (PRPP).

5. The P wave transmitted as P (or S) into the second layer, diffracted as S (or P) at the bottom tip of the fracture, and transmitted as P back into the first layer (PPdSP and PSdPP).

6. The P wave diffracted at the bottom tip of the fracture and transmitted as S wave into the first layer (PPdPS).

7. The P wave transmitted as P (or S) into the second layer, diffracted as S (or P) at the bottom tip of the fracture and transmitted as S back into the first layer (PPdSS and PSdPS).

It is clear from the divergence and curl panels that the energy received at the surface is a combination of compressional and shear motion. Some of the waves have been singly and multiply converted into shear energy. These conversions occur both at the fracture tips and wall. Additional modeling results (e.g., using fracture tips only) show that the fracture wall induces significant changes in the amplitude, polarization and moveout of these events. To visualize the propagation of the Rayleigh and PdS waves, figure 3-6 shows snapshots of the curl component at 125, 150, 175 and 200 ms. The different snapshots are independently scaled to track the wavefronts as they become progressively weaker. We also observe in these snapshots the propagation of the conversions P to S at the top and bottom of the second layer (PS and PPS). The PSdS or PPdS waves (shear or P-wave diffracted as shear) at the bottom tip of the fracture is hardly noticeable at 175 ms. At 200 ms, some of the Rayleigh energy reflected as shear wave at the bottom of the second layer (PRS) appears very weakly.

3.2.2 2-Fracture 2D Model

We add another fracture to the previous model as despicted in figure 3-7. The record on the left in figure 3-8 shows the corresponding modeled vertical component (Vz). The propagation of waves is more complex in this case due to interference between the scattering from both fractures. The record on the middle is the trace by trace difference of the 1-fracture model from the 2-fracture model. It shows only the scattering energy caused by the second fracture. For convenience, the 1-fracture Vz difference of figure 3-5 has been reproduce here. As expected we see that much of the newly scattered energy appears shifted to the right. However, additional significant energy is present which comes from multiple bounces between the two fractures.

3.2.3 N-Fracture 2D Model

We continue adding fractures to the same model as shown in figure 3-9. The Vz data for the multiple parallel fracture model, shown in figure 3-10, are characterized by numerous forward and backscattered events composed of both, P and S scattered energy. This scattered energy appears immediately after the P reflection from the top of the fractured layer and extends for the rest of the recorded time. This perturbs the arrivals reflected from the layer below.

3.2.4 N-Fracture 3D Model

The previous models are 2D, thus the propagation of waves is constrained to the x-z plane, containing the source and receivers. However, geometrical spreading is different in 2D and in 3D, and the waves identified above are expected to have complex travelpaths in the 3D space. Therefore, in order to describe the propagation of scattered waves from fracture corridors in the x-y-z plane, we build a 3D model as illustrated in figure 3-11. This 3D model consists of 5 horizontal, isotropic, layers in which the three layers in the middle have the same elastic properties as the 2D models. The velocities and densities of the layers are listed in table 3.2. The third layer simulates a reservoir with vertically aligned fractures, regularly spaced every 35 m, that extend

to the edges of the model and through the reservoir thickness (200 m).

A shot record is obtained from a point source in one corner of the model, and three-component receivers every 5 m in the x-y plane. The source is again modeled as a 40 Hz Ricker wavelet, hence wavelengths in the reservoir layer are approximately 100 m for the P wave (λ_P) and 59 m for the S wave (λ_S). The dimensions of the multiple fracture set are similar to the dominant seismic wavelengths. The fracture vertical height is $2\lambda_P$, the horizontal length is about $10\lambda_P$ and the spacing is about $\lambda_P/3$. The fracture channels are long enough to act as wave guides and, as in the multiple fracture 2D model, the spacing between fractures is such that seismic waves are expected to scatter.

Figures 3-12 to 3-15 show snapshots at 125, 175, 225, 275 ms in the x-z plane (left) and in the y-z plane (right). After 125 ms the energy propagating from the point source reaches the second layer. At this early time, the P-wave reflected and transmitted at the top of the second layer look the same in both planes since the wavefront has not hit the fractured layer. Waves continue to propagate and by 175 ms, energy transmitted into the third layer starts to be scattered by the fractures. At this time, the interference of the fracture scattering with the main P-wavefront is evident in the x-z plane but not so noticeable in the y-z plane. At 225 ms, when the converted wavefront enters the fractured layer, the scattering becomes obvious in both planes. However, the character of this scattered energy is different in several ways:

- In the y-z plane, the scattered waves propagate behind the main wavefronts whereas in the x-z plane such wavefronts interfere with the diffraction tails at the fracture locations.

- Scattered waves in the y-z plane preserve the hyperbolic character of the incident waves, whereas in the x-z plane forward and backscattered waves have an almost linear character.

- Consequently, in the y-z plane, the P-reflection from the bottom of the layer is barely identifiable whereas in the x-z plane is completely masked by the fracture

scattering.

In the snapshots at 275 ms the P, PS, and previously diffracted waves continue to scatter into the medium below and above the fractures.

To illustrate the scattering characteristics at intermediate azimuths, the data are sorted into 10-degree azimuthal gathers. Figure 3-16 shows schematically the convention used to sort the data into azimuthal gathers: the direction normal to fractures corresponds to the 0° azimuth whereas the direction parallel to fractures corresponds to the 90° azimuth. The vertical component, at every azimuth, is shown in figures 3-17 and 3-18. As a reference, the first record in figure 3-17 corresponds to the same model but without fractures. A mute function was applied to all azimuthal gathers to remove the direct arrival. The P reflections generated at zero offset from the top of the second layer, the top and base of the reservoir, and the top of the fifth layer, arrive at about 170, 290, 395 and 500 ms, respectively. There is a strong arrival at about 220 ms which corresponds to the converted S wave from the top of the second layer. All these arrivals are identifiable irrespective of the acquisition orientation, however, the fractures introduce significant energy that obscures the last two reflectors. The character of this energy varies progressively with azimuth, exhibiting reverse moveout at 0° and changing with azimuth until it displays similar moveout to the primaries in the direction of the fractures (90°). At 90°, the energy trapped between the fracture system is received multiple times at the surface.

3.3 Spectral Character of the Fracture Scattering

In the previous section we described the differences in the seismic response of the modeled data as the azimuth of propagation varies with respect to the fracture orientation. It was established in figures 3-17 and 3-18 that as the observation plane becomes oriented normal to fracture strike, the coda contains strong backscattered energy.

Back or side scattered energy is conventionally treated in seismic processing as unwanted coherent noise. In field records, it is common to observe backscattered

components of guided (Scholte) waves when the ocean bottom presents irregularities or due for example to sea-bottom pipelines (Yilmaz, 2001). In land data, ground roll may exhibit a backscattered component as well due to near surface irregularities. In these cases, the irregularities act as point scatterers. Filters in the frequency-wavenumber domain have proven successful in attenuating the effects of scatterers, because the scattered energy moveout is different that the primary reflection moveout and thus they separate in the *f-k* space. This allows dip filtering in the *f-k* space to be effective.

The scattering characteristics of parallel fractures are somewhat different to the examples above because fractures are not entirely random features. Instead they tend to occur as part of regular fracture sets with a certain preferred orientation, similar length, rather constant spacing and are usually confined to particular mechanical rock units. The wavelengths scattered by discrete fractures are similar not only to the individual fracture geometry but also to that of the fracture system.

Figure 3-19 shows the *f-k* spectrum of some of the azimuthal gathers of the 3D model described in the previous section. The one on the left corresponds to the no fractures case. The one in the middle is the *f-k* spectrum of the data collected at 0° or normal to the fractures. The one on the far right corresponds to the spectrum of the data collected at the 90° azimuth or, in other words, parallel to the fractures' strike.

First we identify how the main events in the time-offset space map into the frequency-wavenumber domain:

1. Reflections (hyperbolas) at near offsets, are almost flat or of infinite apparent velocity. Such signals map onto the zero wavenumber axis. As the offset increases, reflectors become curved towards positive (later) time, and so their energy map to the positive wavenumber plane.

2. Residuals of the direct arrivals, mute artifacts, mode conversions, and tails of hyperbolas at large offsets (all of which have a linear positive moveout in the time-offset space) transform in the positive wavenumber plane also as linear

events. Since the velocities of these events are relatively slow, spatial aliasing could occur in the form of wrap around into the negative wavenumber plane. Some wrap-around artifacts can be reduced by padding with zeros before the Fourier transform is applied.

By comparison with the no fractures case, we then identify the changes in the *f-k* domain introduced by the presence of fractures, as well as the sensitivity to orientation:

3. Parallel to fracture strike, the number of coherent reflections in the time domain below the P-P reflector associated to the top of the reservoir has increased significantly. This results in an increased number of events close to the zero wavenumber axis. Since these events have similar moveout (positive) to the primaries, they are indistinguishable from the primary energy.

4. Normal to fracture strike, the backscattered energy shows reverse linear moveout in the time-offset space. In the *f-k* domain, this energy maps in the negative wave number plane which is key in our analysis. The forward scattered signal from the fractures maps into the positive wave number quadrant, with the slowest velocity, and is smeared out (4a in figure 3-19).

3.4 The *F-K* Method

At this point we have shown that the fracture scattering, in either time-offset or frequency-wavenumber domain, exhibits different character depending on the angle between the fracture direction and the source-receiver orientation. The comparison of the spectra in the normal and parallel directions reveals that the character differences are distinct and separable in the frequency-wavenumber domain. This suggests that it is possible to discriminate fracture orientation by recognizing the fracture scattering characteristics in the Fourier domain.

In this section, the previous observations are developed into a methodology to extract properties of reservoir fracture corridors. The proposed strategy could be

easily incorporated in the processing sequence of surface seismic data at a very early stage since it is applied to field SHOT records. The *F-K* method consists of two steps: first, the preferred fracture orientation is identified, and then, fracture spacing is estimated. The fracture scattering can also be isolated with the *F-K* method. As a consequence, it is possible that fracture properties other than orientation and spacing could also be extracted, for instance, fracture aperture and stiffness. However, this is out of the scope of this thesis.

3.4.1 Determining Fracture Orientation

Figure 3-20 shows the *f-k* spectrum of the 10° azimuthal gathers from the 3D model in which fractures are spaced 35 m. Unlike the spectra in figure 3-19, the 2D Fourier transforms are computed here in a window in time and offset indicated at the bottom right corner of figure 3-20. The window starts after the reflector associated with the top of the resevoir (the 3rd layer in our model) and extends for approximately 300 ms. The time window includes the reservoir and the long coda introduced by the fractures that interferes with the reflections coming from layers below. Data windowing is necessary to isolate the main signal related to the fractured level from overlying formations that in a field data case might contain other scatterers. Offsets are windowed between 0 and about 300 m in order to neglect conversions observed at far offsets, direct arrivals, and mute artifacts.

In the figure, we can observe how the frequency-wavenumber spectra change in the intermediate azimuths between the normal and the parallel to fracture directions. At 0°, the spectral energy is spread out in the frequency-wavenumber plane. Some energy, falling close to the zero wavenumber axis, at this and other azimuths, corresponds to the near offset reflectors from the bottom of the 3rd and 4th layers. This energy does not change with azimuth since the layers are flat and isotropic. As the azimuth increases, the energy in both positive and negative wavenumber quadrants moves towards the zero wavenumber axis until, at 90° all the significant energy is concentrated at this axis. As observed in the time gathers, the fracture signals become "flatter" as the azimuth becomes aligned with the fracture strike. In the

f-k space, "flatter" means the signal has no periodicity in space and therefore the moveout velocity tends toward infinity. Note that as the azimuth increases the dominant wavenumbers of the fracture signals change significantly whereas the frequency bandwidth and peaks remain almost constant.

A methodology to characterize the fracture energy can be based upon this observation that the backscattered energy appears isolated and detectable in the negative wavenumber quadrant. Thus, to determine fracture orientation, we define the backscattered energy (E_{scatt}) as the sum of the square of the amplitudes in the negative wave number quadrant:

$$E_{scatt} = \sum_{-k_N}^{-k_o} A^2 \tag{3.2}$$

where k_N refers to the Nyquist wave number and k_o is chosen so that energy falling onto the $k = 0$ axis is not included in the sum. This value is in practice required to be greater than zero given the intrinsic resolution of the Fourier transform of band-limited signals.

E_{scatt} is computed at each azimuth. The preferred orientation of fractures is derived by comparing the backscattered energy at different azimuths as shown by the red line in the left plot of figure 3-21. In this case, k_o is chosen as indicated by the white dash line in the spectrum on the right of the same figure. As expected, E_{scatt} (red line) maximizes when the orientation is perpendicular to fracture strike (0°) and minimizes in the parallel direction (90°). E_{scatt} decreases rapidly at intermediate azimuths and at a slower rate as the azimuth approaches the parallel to fracture strike direction.

3.4.2 Fracture Spacing Determination

A regular fracture spacing of multiple fracture or joint sets, like in fracture corridors, generates multiple scattered events that are received at the surface in a characteristic fashion. At 0°, normal to the fracture strike, a strong component of this characteristic fracture signal appears as back-scattered. The multiple backscattered events at this

azimuth have the slowest negative velocity or, in other words, the largest negative dip in the time-offset domain. The periodicity of the backscattering in space and time introduces a high energy peak in the negative wavenumber-positive frequency space. Moreover, the fracture backscattering is the only signal from the fractures that is conveniently separated from the primaries and other fracture signals in the *f-k* space.

Another advantage of analyzing fracture signals in the *f-k* domain is the ability to determine the nominal spacing between fractures. Once the direction normal to fractures is identified as explained above, fracture spacing (D) is estimated from the spectral components of the backscattered energy at this azimuth. Fracture spacing is obtained by taking one-half of the inverse of the dominant wave number (k) or, alternatively, estimating the characteristic apparent velocity of the backscattered events (V) and their dominant frequency (f), then:

$$D = \frac{1}{2}\frac{V}{f} = \frac{1}{2}\frac{1}{|k|} \tag{3.3}$$

The spectrum of the windowed 0° azimuthal gather is shown on the right of figure 3-21 where the high energy peak associated to the fracture backscattering is clearly observed at 57.6 Hz and -0.0143 $1/m$. The velocity of any event can be estimated in the *f-k* spectrum from the slope of a line connecting the event with the origin (0,0). In this case, the backscattering apparent velocity is estimated to be -4040 m/s. Substituting these values in equation 3.3 results in an estimation of fracture spacing of 35.1 m. The fracture spacing in the model is 35 m.

A similar relationship between fracture spacing and frequency was observed by Rao et al. (2005), who analyzed the spectral notches of transfer functions extracted from azimuthal stacks. Equation 3.3 was derived from the analysis of synthetic data from this model and others in which fracture spacing was varied (see section 3.5). However, the relationship found between spacing and wavenumber agrees with Bragg's law. The spacing between planes in a crystal atomic lattice (d) is related to the wavelength (λ)

of X-rays and the angle between the incident and scattered rays (θ) by:

$$n\lambda = 2dsin\theta \tag{3.4}$$

where n is and integer.[2] Bragg's law (equation 3.4) expresses the condition to have constructive interference of electromagnetic waves which results in a diffraction pattern useful to study crystal structures. Bragg's law applies as well to radio waves and acoustic waves. For example, an interesting application of Bragg's scattering theory to ocean waves is discussed in Naciri and Mei (1988). In this civil engineering application, breakwaters are designed according to Bragg's law to better control currents and mitigate storms damaging to drilling sea platforms.

3.4.3 Extraction of Fracture Signals

The backscattered signal can be isolated from the rest by designing reject-pass filters in the *f-k* space. Once the wave field exclusively related to fractures is extracted, the estimation of fracture properties should be largely simplified. The windowed shot record oriented at 0° (left record) is next filtered as shown in figure 3-22. An *f-k* filter is implemented such that signal falling into the negative wavenumber quadrant is passed, while positive wavenumber signals are rejected (amplitudes in the positive wavenumber quadrant are zeroed out and the resultant *f-k* spectrum is inverse transformed.) The resulting filtered (middle) record in figure 3-22 shows that the filter has effectively removed the forward propagating energy which boosts the signal directly related to the fractures. In practical applications, a data cube of backscattered signal could be generated for all azimuths.

3.5 Other Modeling Studies

In this section we evaluate the performance of the *F-K* method when the fracture properties are different from the idealized situation of the 3D 5-layer model discussed

[2] http://www-outreach.phy.cam.ac.uk/camphy/xraydiffraction/

above. For convenience, we will refer to this model as the control model hereinafter. In particular, we aim to investigate the sensitivity of the fracture scattering signal to changes in fracture height, fracture compliance, and fracture spacing. We carry out this sensitivity study by modeling different fracture properties and then applying the F-K methodology to the modeled data.

3.5.1 Fracture Height

First, we look into the problem of reservoir thickness. Many reservoirs are often thin in comparison to the seismic wavelengths. In these situations, the top and bottom interfaces of the reservoir layer may not be resolved by the seismic frequencies at the depth of the reservoir. Traditionally, the seismic response of thin beds is examined through tuning effects and bright spots, and several methods have been proposed to quatify the thickness (Widess, 1973; Partyka et al., 1999). Assuming the fractures are confined to the reservoir layer, reservoir thickness determines the fracture vertical length or height. We showed in the previous section that the fracture scattering signal in our models is composed of the contributions from the energy diffracted from the tips, energy propagating along the fracture interface and energy guided between the fracture planes. Therefore, we expect to observe variations in the character of the fracture signal when this fracture dimension is varied.

Figure 3-23 shows the Vz data gathered at the normal and parallel direction of four models. The basic geometry and the velocities and densities of these models are exactly as the control model of figure 3-11 and table 3.2. In particular, these models and the control model have in common the fracture spacing (35 m) and the material properties of the fracture zones (fracture stiffness is 4 x $10^9 Pa/m$ for all cases). What changes between the cases is the thickness of the third layer, or the fracture vertical length. It is reduced progressively from 100 m to 10 m as illustrated by the x-z plane views of each model at the top of figure 3-23. In terms of the P wavelength (λ), the fracture height shrinks from left to right, from λ to $\lambda/10$. In the control model the fractures were as tall as 2λ.

The reflector associated with the bottom of the reservoir arrives sooner as the

thickness of this layer is reduced. The top and bottom reflector cannot be distinguished visually when the thickness is 25 m or less ($\lambda/4$ and $\lambda/10$ cases). The fracture scattering signal is attenuated as the thickness is reduced; however, it is strong enough to still be noticeable in the thin-bed cases. In figure 3-23, the amplitude attenuation is better appreciated when the 100 m and 10 m cases are compared, especially at the 90° azimuthal gathers. The previous observations suggest that even in cases where the fractured reservoir layer is below seismic resolution, fractures at the seismic scale may be detectable. The scattered and primary wave fields are fundamentally different and, as such, are sensitive in a different way to the layer thickness. The amount of scattered energy is directly related to the presence of the multiple fracture system that causes constructive interference of the propagated waves. The reduction of fracture length results in an attenuation of the scattered energy, basically because the fractures are not long enough to support the guided waves. However, in the thin-bed cases the compliance contrast between the fracture zones and the background medium still accounts for the strong diffracted energy.

Moreover, figure 3-23 shows that the azimuthal characteristics of the scattering are similar regardless of the fracture vertical length. Following the F-K technique we compute the backscattered energy (equation 3.2) for all cases and compare the results with the control model in the left plot of figure 3-24. In this figure, backscattered energy functions are labeled in terms of λ. The behavior of the backscattered energy function is similar for all thickness models and, as expected, E_{scatt} decays as the angle of acquisition becomes oriented with the fractures strike. The determination of fracture orientation with the F-K method seems insensitive to the fracture height, or reservoir thickness, under the conditions of the numerical experiments analyzed here.

The graph on the right of figure 3-24 shows the variation of spectral amplitude of the backscattered waves as a function of azimuth and fracture height. This spectral amplitude corresponds to the amplitude of the highest energy peak in the negative wavenumber interval of the f-k spectrum computed at every azimuth. Because the scattered fracture energy is dominantly backscattered at 0°, the backscattered spectral amplitude maximizes at this angle. At 90°, most of the fracture energy is forward

scattered. The contrast between the amount of backscattered energy at 0 and 90° decreases as the fracture height is reduced. In the 10 m thickness case the maximum backscattered amplitude is about 30% weaker than in the thick-200 m model. The measured amplitude differences depend upon the time window input selected for the f-k analysis. This is because the interference of the scattered energy changes due to the time shift associated with the reduced thickness of the layer with fractures and the smaller amount of scattered energy (figure 3-23). Although figure 3-24 only compares the backscattering amplitude, the forward scattered fracture signal is expected to be attenuated as the thickness decreases judging from the character of the data parallel to fractures in figure 3-23.

Determination of fracture spacing following the F-K methodology is carried out in figure 3-25 where the f-k spectrum of gathers perpendicular to fracture strike are analyzed. The time-offset window extracted for the 2D Fourier transformation is indicated on the control model data on the top right corner of the figure. The maximum energy in the negative wavenumber interval is found at the f-k values indicated with the white plus (+) symbols. All the spectra are normalized to the amplitude of the backscattered waves in the control case which is the highest amongst all the different thickness models. Normalizing the spectra in this way reveals the attenuation of the fracture signals in the thin-bed models with respect to the thick-bed ones. The f-k values of the backscattered component picked on the spectra are compared at the bottom right figure. The characteristic frequency and wavenumber of the fracture backscattering are not sensitive to the fracture vertical length. This is very fortunate because the determination of fracture spacing is accurate in all cases modeled.

3.5.2 Fracture Compliance

Fracture compliance depends on numerous factors including: the probing seismic wavelengths (frequency), the fracture size (aperture, welded contact area, spacing, length), the elastic properties of the rock matrix and of the fluid inside the fractures, and the role of cementation and stress as a function of depth and geological time.

Worthington (2007) discusses that the lack of macrofracture compliance experimental data is in part due to the complex interdependence of these factors. The same author compiled the few laboratory and field data of fracture compliance found in the current published literature and observed an approximate linear dependence between fracture compliance and fracture dimension scale. According to this linear approximation fractures on the scale of seismic wavelengths (tens of meters) would have compliances on the order of 10^{-10} - $10^{-9} m/Pa$; however, Worthington (2007) argues that it has not been proved conclusively that any macrofracture exists below the surface with such high values of compliance.

The fracture stiffness chosen for the control model and the variable fracture height models, discussed above, was 4 x $10^9 Pa/m$, which is near the high limit of realistic fracture compliance detectable with a reflection seismic experiment. However, Daley et al. (2002) developed a conceptual model, based on lab scale observations, to calculate the average stiffness of a fracture represented by a series of void spaces. These authors, as well as Willis et al. (2006), assigned a stiffness of 8 x $10^8 Pa/m$ to discrete fracture models similar to ours. Such a high compliance would represent a gas-filled fracture with a large crack aspect ratio.

We build a model using this fracture compliance and compare the data with the control case (lower compliance) in figure 3-26. These two models have identical fracture spacing (35 m). The model dimensions and the rock properties of the 5 layers are also the same. The velocities as a function of incidence angle for the high compliant fracture material were depicted in figure 3-2 (right). The effect of increasing the fracture compliance is evident in the gathers. In both azimuths, the fracture scattering is considerably stronger for the larger compliance case, to the point that the reflectors from the bottom of the 3rd and 4th layer are barely recognized in the high compliance modeled data. The azimuthal differences in character seem to be preserved. This is confirmed in figure 3-27 where the backscattered energy is plotted as a function of azimuth and fracture stiffness at the top left graph. The results of analyzing another model with a slightly higher compliance (Z = 3 x $10^9 Pa/m$) than in the control case are also included. The backscattered energy maximizes at the

normal to fracture orientation and minimizes in the parallel direction. This allows the fracture orientation to be determined irrespective of the fracture compliance chosen in the model. However, the strength of the backscattering signal depends upon the fracture compliance as illustrated on the top right plot in the same figure. When the fractures are one order of magnitude stiffer the maximum backscattering amplitude is only about 70% of the value obtained in the compliant model.

Next we consider the sensitivity of the *F-K* method to the location and size of the analysis window. The lower plots in figure 3-27 show the backscattered energy and backscattered amplitude as a function of azimuth for the same models but computed in a shorter data window. Both windows of analysis are indicated on the gathers at 0° in figure 3-28. The red window is a long window of about 300 ms; the yellow window is a short window between the reflectors associated to the fractured layer. Figure 3-27 reveals that the backscattering behavior with orientation is pretty much unaffected by the window length. On the other hand, the differences in amplitude observed as a function of fracture compliance are greater when the analysis uses the short window near the fractured layer. The drop in amplitude with increasing stiffness, at 0°, is now around 50%.

The *f-k* spectra of the two compliance models are presented in figure 3-28. The top row of plots corresponds to the highly compliant (Z = 8 x $10^8 Pa/m$) fractured model, whereas the bottom row panels depict the data and *f-k* analyses of the control model. The 2D Fourier spectra for all cases exhibit distinct energy peaks at the negative wavenumber interval. The spectral energy for the low compliant control model is weaker. When the analysis is constrained to a small window in the reservoir, the spectrum contains fewer events and picking of the dominant backscattered signal is simplified. The frequency-wavenumber pairs picked for all cases are compared in figure 3-29. The results for the long window are shown on the left. It is obvious that the frequency component of the backscattering is the most affected by the window length. Frequency increases as the window is shortened. The wavenumber component however is a great estimator of the fracture spacing since it is almost insensitive to the time window length or to the fracture compliance. The fracture spacing is estimated

with equation 3.3.

3.5.3 Fracture Spacing

Fractures in layered sedimentary rocks are often periodically distributed with spacing linearly related to the thickness of the fracture layer (Bai and Pollard, 2000). Typical ratios of fracture spacing to layer thickness have been estimated mainly from outcrops (e.g. Narr and Suppe, 1991; Ortega et al., 2006), and predicted by recent numerical models that correlate the fracture spacing to stress transitions determined by the layer thickness (Bai and Pollard, 2000). In these studies it has been suggested that fracture spacing to layer thickness ratio varies between 0.8 and 1.2. If we assume this range of ratios in our models, including the thin-bed models discussed above, fracture spacing should be chosen between 8 and 160 m.

Willis et al. (2006) presented a fracture analysis of a series of models in which fracture spacing was varied. The fracture spacings modeled were 10 m, 25 m, 35 m, 50 m, 100 m, and, a pseudo-Gaussian distribution with mean spacing 35 m and standard deviation 10 m. The model of fractures spaced 10 m was found to be below the scattering limit. The source was modeled as a Ricker wavelet with a center frequency 40 Hz. The velocities, densities, and dimensions of the layers and fractures in these models are consistent with the highly compliant fractured model discussed in the previous section. The normal and tangential stiffness assigned to the fractured zones are 8 x $10^8 Pa/m$.

We use the same models from Willis et al. (2006) to study the sensitivity of the spectral characteristics of the fracture signals to different fracture spacings. Figure 3-30 shows the data collected at 0° and 90° for the 25 m, pseudo-Gaussian distribution, 50 m, and 100 m spacing models. The schematics of every model are shown in the top row of the figure. As illustrated in the x-z view of the models, fracture spacing increases from left to right. The character of the scattering recorded at 0° changes significantly with fracture spacing. Firstly, we note the relative attenuation of amplitudes in the 25 m model case. Secondly, the diffracted (back and forward scattered) waves appear more closely spaced in the time-offset domain for the 25 m

model than for the 100 m model. The primary reflections from the bottom of the 3rd and 4th layers are less continuous in the pseudo-Gaussian and 50 m models than in the 25 m or 100 m models. This suggests that the strength of the fracture scattering signal may not depend linearly with fracture spacing as it did with fracture height or compliance. The differences in character of the fracture scattering between the 0 and 90° orientations are evident in all cases.

The backscattered energy function is maximized when the orientation is perpendicular to fracture strike. Such behavior is consistent in all modeled cases where we have varied the fracture spacing (left plot in figure 3-31). Comparing the backscattered amplitudes as a function of azimuth and fracture spacing (right plot in figure 3-31) we observe two effects: (1) it seems that the backscattered energy is more attenuated as the fracture spacing decreases; however, the 100 m case does not fit this tendency probably because of resolution limitations of the *f-k* transform as the wavenumber approaches zero; (2) the contrast between the amount of backscattered signal at 0 and 90 degrees seems to increase with fracture spacing (except for the 100 m model case), thus increasing the accuracy in the determination of fracture orientation and spacing.

Figure 3-32 shows the spectral analysis to estimate the fracture spacing. We have computed the *f-k* spectrum of the 0° data in the same short window inside the reservoir for all cases. The 35 m fracture spacing case was presented in figure 3-28. The distribution of energy in the *f-k* space changes with fracture spacing. The spectra are normalized by the maximum amplitude which is found in the 50 m spacing case. A maximum energy peak focuses in the negative wavenumber interval in all models. The frequency-wavenumber component of this energy is indicated in the spectra and re-plotted on the left bottom graph for all cases. As fracture spacing increases, the backscattered signal contains lower frequency-wavenumber components and therefore the fracture spacing can be recovered from the peak wavenumber in every case.

In the normal plane, the number of peaks in the spectrum increases with fracture spacing. This is better appreciated when longer windows are input in the analysis as illustrated in figure 3-33. In this figure, we compare only the 25 m, 50 m, and 100 m

spectra. The window of analysis was indicated in red in figure 3-28. In this window as well the 50 m modeled data contains the highest amplitude; hence the other two spectra are normalized to this maximum. Extending the window length has the effect of lowering the dominant frequency of the backscattered waves. As a consequence, the frequency-wavenumber band is insufficient to resolve the fracture spacing of 100 m. Instead, energy in the negative wavenumber interval peaks at an aliased frequency-wavenumber (white plus sign on the 100 m spectrum). Coincidentally, the maximum energy occurs at a wavenumber corresponding to a fracture spacing of about 35 m. Two other peaks can be distinguished in the 100 m case (magenta plus signs). These lower energy peaks correspond to half (50 m) and one quarter (25 m) of the nominal fracture spacing in the model and are associated to higher order periods. The 25 m wavenumber component can also be observed in the 50 m case spectrum (magenta plus sign). However, the backscattered dominant frequency-wavenumber in this case is within the resolution band and therefore the fracture spacing is estimated accurately.

The analysis of modeled data suggests that the backscattered signal exhibits lower frequency-wave number when the spacing is larger whereas fracture vertical length or stiffness has little effect on the spectral components. Peak frequency decreases as the window of analysis is extended or shifted in time, but peak wavenumber remains constant. Models with different fracture stiffness show that the more compliant the fractures are the more the fracture signals interfere with the reflections and conversions from the interfaces. An increase of fracture stiffness decreases the spectral amplitudes of backscattered waves. There is a range of fracture spacings (35-50 m) which produce significant scattered energy whereas spacings smaller and larger than these dimensions appear to dampen the amount of scattering. Shortening the vertical length of the fractures (the thickness of the fractured bed) causes backscattered amplitudes to drop. The effects of fractures on the seismic spectral response are azimuthally dependent and stronger in the direction normal to fractures where properties can be conveniently estimated.

3.6 The Scattering Index Method

The Scattering Index (SI) method is another way of processing scattered signals (or coda waves) to derive fracture properties. The SI method is a novel concept developed in the Earth Resources Laboratory at MIT in the recent years (Willis et al., 2003, 2004b,a, 2006; Burns et al., 2007). The Scattering Index method has been tested on synthetic 3D data generated with finite difference approximations, and it has been applied successfully to field data where independent information about fractures exists (Willis et al., 2006; Grandi et al., 2006). As the F-K method, determination of fracture distribution and orientations using the Scattering Index method is based on the principle that fractures of dimensions similar to dominant seismic wavelengths scatter energy. Such signals have different characteristics depending on the angle of observation.

During the course of processing, coda waves stack constructively when the acquisition direction is parallel to fractures and stack destructively normal to fractures. Figure 3-34a shows the azimuthal stacks obtained processing the data from the control model. The azimuthal gathers were shown in figures 3-17 and 3-18. The azimuthal stacks are very similar at early times, before the reflection from the top of the fractured layer that arrives at about 0.25 s. At later times, the stacked scattered energy appears differently with azimuth. In the direction normal to fracture strike, the stacked scattering is very weak and clearly overpowered by the primaries. The azimuthal stack at this azimuth is practically identical to the no-fracture case. In the direction parallel to fracture strike, most of the signals generated by the fractures have similar moveout to the primary reflections. As a result, the scattering stacks constructively and appears with significant amplitude at this azimuth. The SI method measures these differences in scattering coherence captured by the stacked traces at different directions.

The Scattering Index analysis consists of two steps. In the first step, transfer functions for each azimuthal stack of the fractured zone are obtained. Upper and lower wavelets are extracted from zones above and below the reservoir level in each

stacked azimuth. For the modeled data, we choose the upper and lower windows as depicted in figure 3-34a. Then, a transfer function is derived by deconvolving the upper wavelet from the lower wavelet. The corresponding transfer functions for the control model are shown in figure 3-34b. They exhibit the same attributes as the stacked coda waves: they reverberate and are less temporally compact in the direction parallel to fracture corridors.

The second step consists of the calculation of the scattering indices. The scattering index, *SI*, is a number that measures the amount of ringing in the transfer function. It is defined in Willis et al. (2006), as:

$$SI = \sum_{i=0}^{m} |t_i| i^n \tag{3.5}$$

where i is the time lag, t_i is the transfer function amplitude at lag i (in the time domain), m is a lag at which there is no more significant energy in the transfer function, and n is an exponent, generally taken as one.

Because this expression gives greater weight to larger lags, the more the transfer function reverberates, the larger the value of *SI*, thus *SI* is expected to be the largest parallel to fractures. We compute scattering indices for the modeled data and display the results as a function of azimuth in figure 3-34c. The scattering index increases very rapidly as the azimuth becomes oriented with the fracture strike.

Since the method looks for differences in the wavelet as a function of depth (or time down the trace), it is intrinsically insensitive to overprinting. In other words, the stationarity of the signal is only assumed along the time window of analysis. Given a 3D seismic set with a full range of azimuths, the particular characteristics of the transfer functions and the comparison of azimuthal scattering indices would allow the identification of fractured areas and the determination of fracture strike at the reservoir level.

Application of the *SI* method requires the selection of several parameters, including:

1. The maximum offset input in the stacking process. In general, widening the

range of offsets has the effect of making the *SI* response sharper, that is, it increases the difference between maximum and minimum *SI*.

2. The horizon time associated with the upper boundary of the fractured level. Since usually some structure is present, a seismic interpretation is required for field data processing.

3. The time windows to extract input and output wavelets, defined around the horizon time. In general, as the windows become more localized around the fractured level, the difference between the scattering indices in the parallel and normal direction increases.

4. A pre-whitening or noise level to stabilize the Wiener deconvolution (Yilmaz, 2001). The transfer functions in figure 3-34b were computed with an implementation of the Wiener deconvolution. In practice, any type of deconvolution could be used.[3] This parameter is established by evaluating the decay of amplitudes with lag in the transfer functions.

5. The maximum lag to take into account for the calculation of *SI*, m in equation 3.5, which is decided according to the transfer function behavior as a function of lag.

As far as the sensitivity of the *SI* method to variations in the fracture properties, figure 3-35 shows a comparison of the *SI* analysis of the models discussed in section 3.5. The parameters used in the *SI* calculations are the same in all cases. The maximum offset stacked is 500 m and the time windows to extract input and output wavelets are chosen as indicated in figure 3-34a.

Figure 3-35a depicts the scattering index as a function of azimuth obtained from the models in which the fracture height is varied. The orientation of the fractures can be detected with accuracy in all cases because the scattering index attains a clear

[3]The original *SI* algorithm and codes to compute transfer functions and scattering indices were written by Mark E. Willis in Fortran 77. I optimized these codes by substituting the linear inversion with an implementation of the Levinson recursion algorithm (Press et al., 1999; Claerbout, 1985; Robinson and Treitel, 1980). The new version is about 8 times faster.

maximum at the azimuth parallel to fracture strike. When the scattering indices are normalized as in the figure, the scattering amplitude dependence on fracture height is revealed. As the fracture height increases the parallel to normal scattering index ratio increases.

The *SI* method is also evaluated in cases where the compliance of the fractures is higher than in the control model (figure 3-35b). The parallel to normal scattering index ratio slightly increases with stiffness. The differences between the low and high compliance models are greater as the quality of the stack decreases (less traces are stacked) and as the windows of analysis are shortened (not shown).

Figure 3-35c shows the *SI* as a function of azimuth and fracture spacing taken from Willis et al. (2006). Note that the convention for azimuths was different in that study, such that the normal direction is rotated 90° with respect to our convention. The orientation of fractures is predicted by the *SI* method in all the models independently of the fracture spacing. The 35 m spacing model has the largest scattering index parallel to fracture direction suggesting that this fracture spacing is tuned to the seismic wavelengths (Willis et al., 2006).

The numerical experiments demonstrate that the ringing signature of the fracture scattering varies in moveout as a function of the angle between source-receiver line and fracture plane. The amplitudes of the coda waves, translated into scattering indices, are sensitive to: (1) the relationship between fracture spacing and dominant seismic wavelength; (2) the compliance contrast between the fracture and surrounding medium; and (3) the vertical extension of the fractures or reservoir thickness. The coda energy has a moveout most similar to the primaries in the direction parallel to the strike of fractures; therefore, it is enhanced by the stacking process. The amplitudes of the coda waves are the largest when the wavelength is tuned to fracture spacing, when fractures have high compliance, and when the reservoir is thicker.

3.7 Summary

Based on numerical models of wave propagation through discrete fracture sets, we studied the characteristics of the fracture scattering and derived a methodology to estimate fracture orientation and spacing. We assumed that the multiple parallel fractures are vertical, with a preferred orientation and rather regular spacing. The signature of the fractures scattering changes with the angle between the acquisition orientation and the fracture strike. The *F-K* method develops from the evidence that backscattered seismic waves are generated from fracture systems. Backscattered signals appear in the negative wavenumber-positive frequency quadrant of the *f-k* spectrum, and as such, they can be isolated using *f-k* filters. In the *f-k* domain, backscattered energy decreases as the observation angle becomes oriented with fracture strike. Fracture spacing was found to be proportionally inverse to the dominant wavenumber. The *SI* method was also applied to the same synthetic data. We analyzed the sensitivity of these two methods to fracture compliance, thickness and spacing.

Table 3.1: Velocities and Densities of 1-Fracture, 2-Fracture and N-Fracture 2D Models. T: reservoir (2nd. layer) thickness, D: fracture spacing, Zn: normal stiffness, Zt: tangential stiffness.

Layer No.	Vp $[m/s]$	Vs $[m/s]$	Density $[g/cc]$
1	3500	2060	2.25
2	4000	2353	2.3
3	3500	2060	2.25
fractures	Zt = 4 x $10^9 Pa/m$	Zn = 4 x $10^9 Pa/m$	2.3
	D = 100 m	T = 200 m	

Table 3.2: 3D Model velocities and densities. T: reservoir (3rd. layer) thickness, D: fracture spacing, Zn: normal stiffness, Zt: tangential stiffness.

Layer	Vp $[m/s]$	Vs $[m/s]$	Density $[g/cc]$
1	3000	1765	2.2
2	3500	2060	2.25
3	4000	2353	2.3
4	3500	2060	2.25
5	4000	2353	2.3
fractures	Zt = 4 x $10^9 Pa/m$	Zn = 4 x $10^9 Pa/m$	2.3
	D = 35 m	T = 200 m	

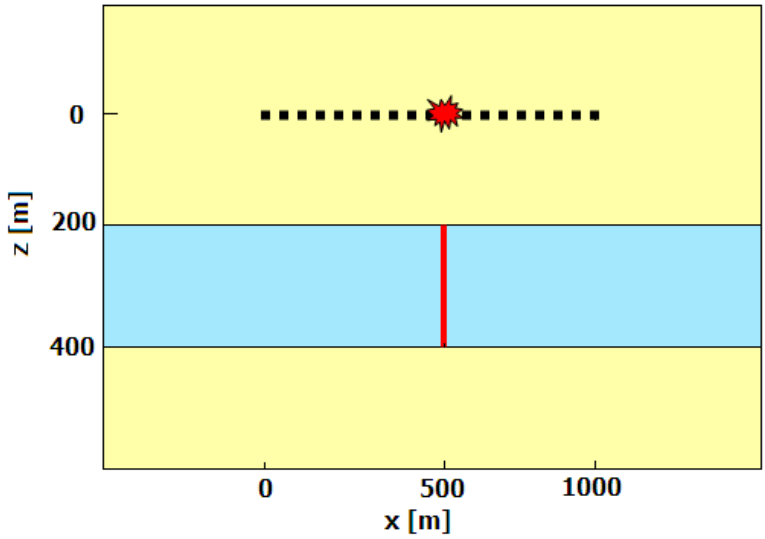

Figure 3-1: 1-Fracture 2D Model Geometry.

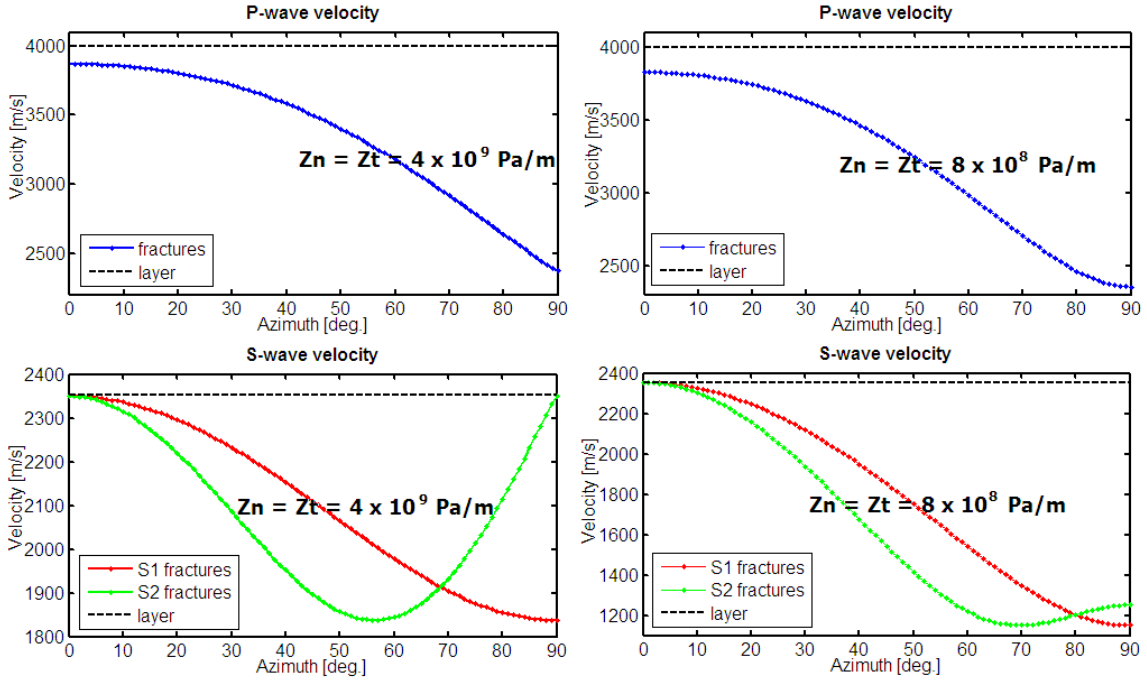

Figure 3-2: P-wave (top) and S-wave (bottom) velocities as a function of the angle of incidence of the anisotropic fracture zones and the isotropic reservoir layer in the 2D and 3D models discussed in section 3.2 (left). On the right, equivalent velocities for a model in which fractures have a lower tangential and normal stiffness of 8 x $10^8 Pa/m$ (section 3.5).

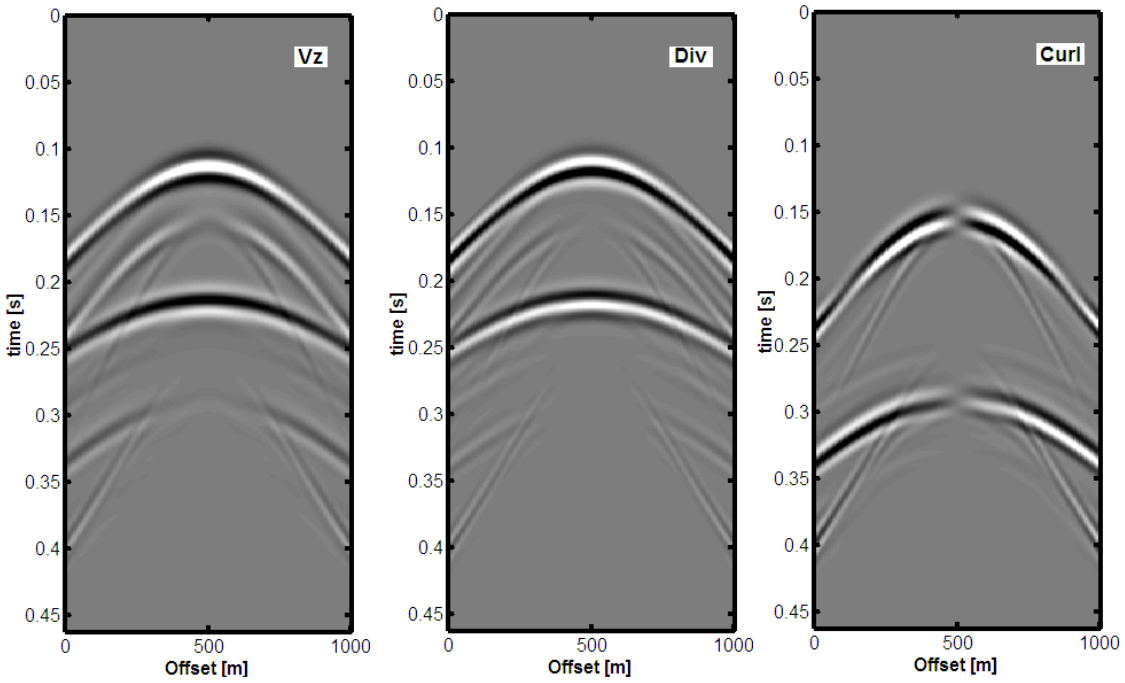

Figure 3-3: Seismograms from the 1-fracture 2D model. From left to right: vertical component (Vz), divergence and curl.

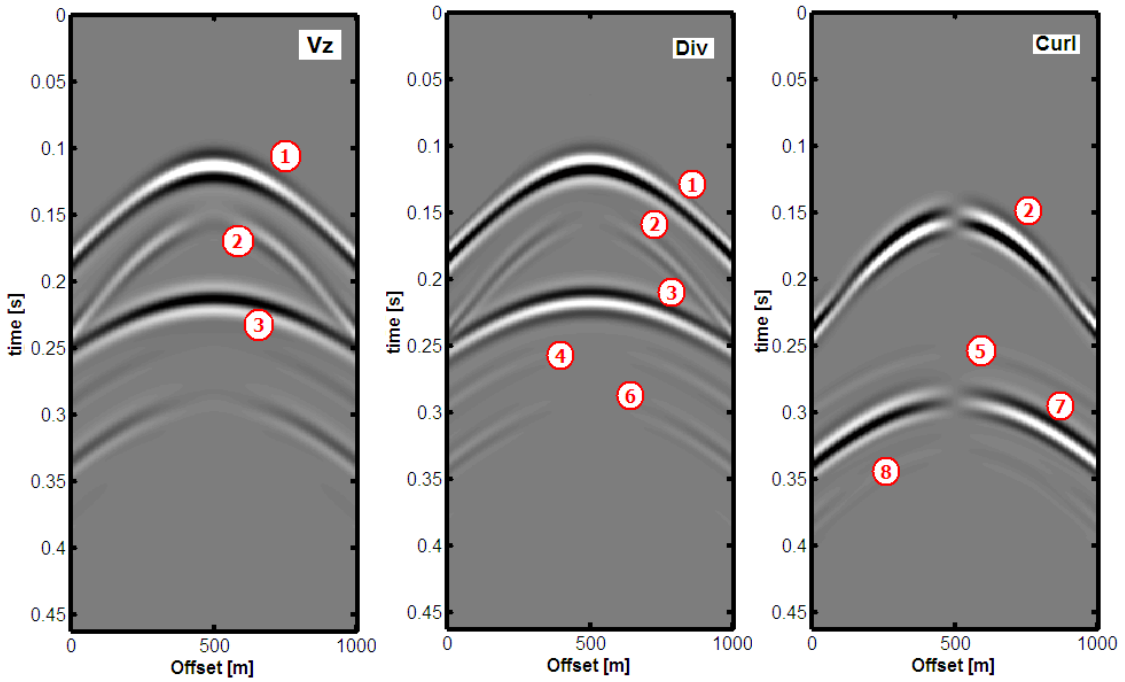

Figure 3-4: Seismograms from the no-fracture 2D model. From left to right: vertical component (Vz), divergence and curl. The numbered events are explained in the text.

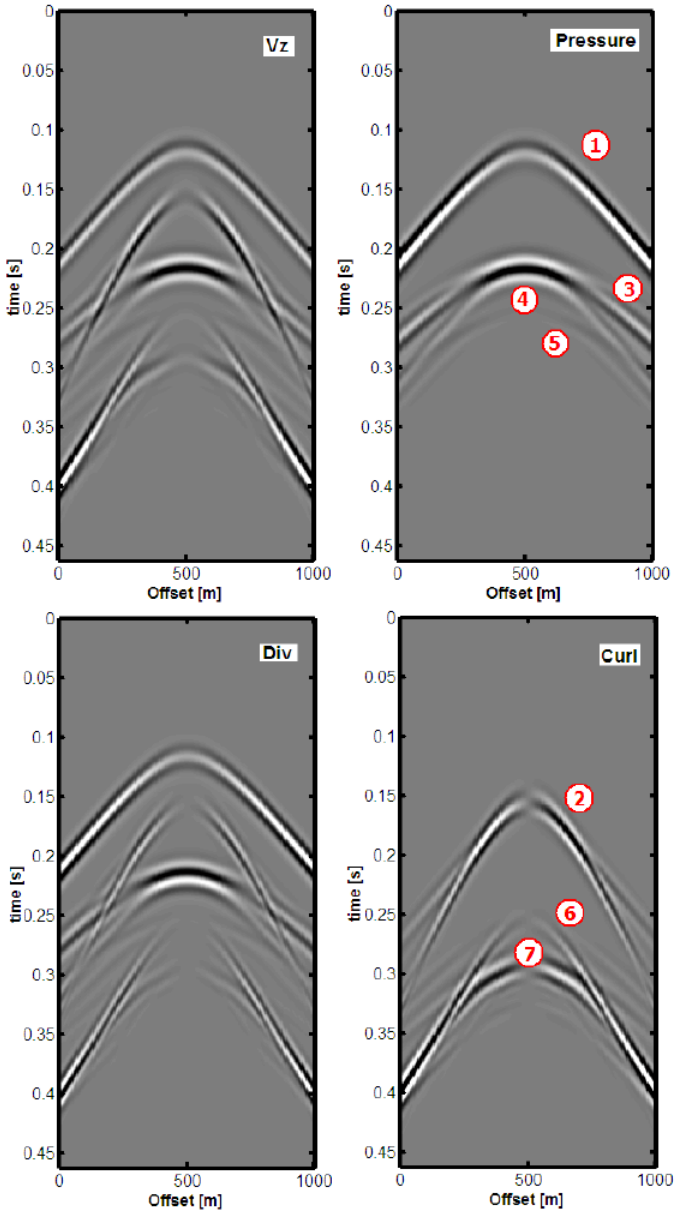

Figure 3-5: Seismograms obtained by substracting the no-fracture from the 1-fracture 2D modeled data. At the top: vertical component (Vz) (left) and pressure (right). At the bottom: divergence (left) and curl (right). The numbered events are explained in the text.

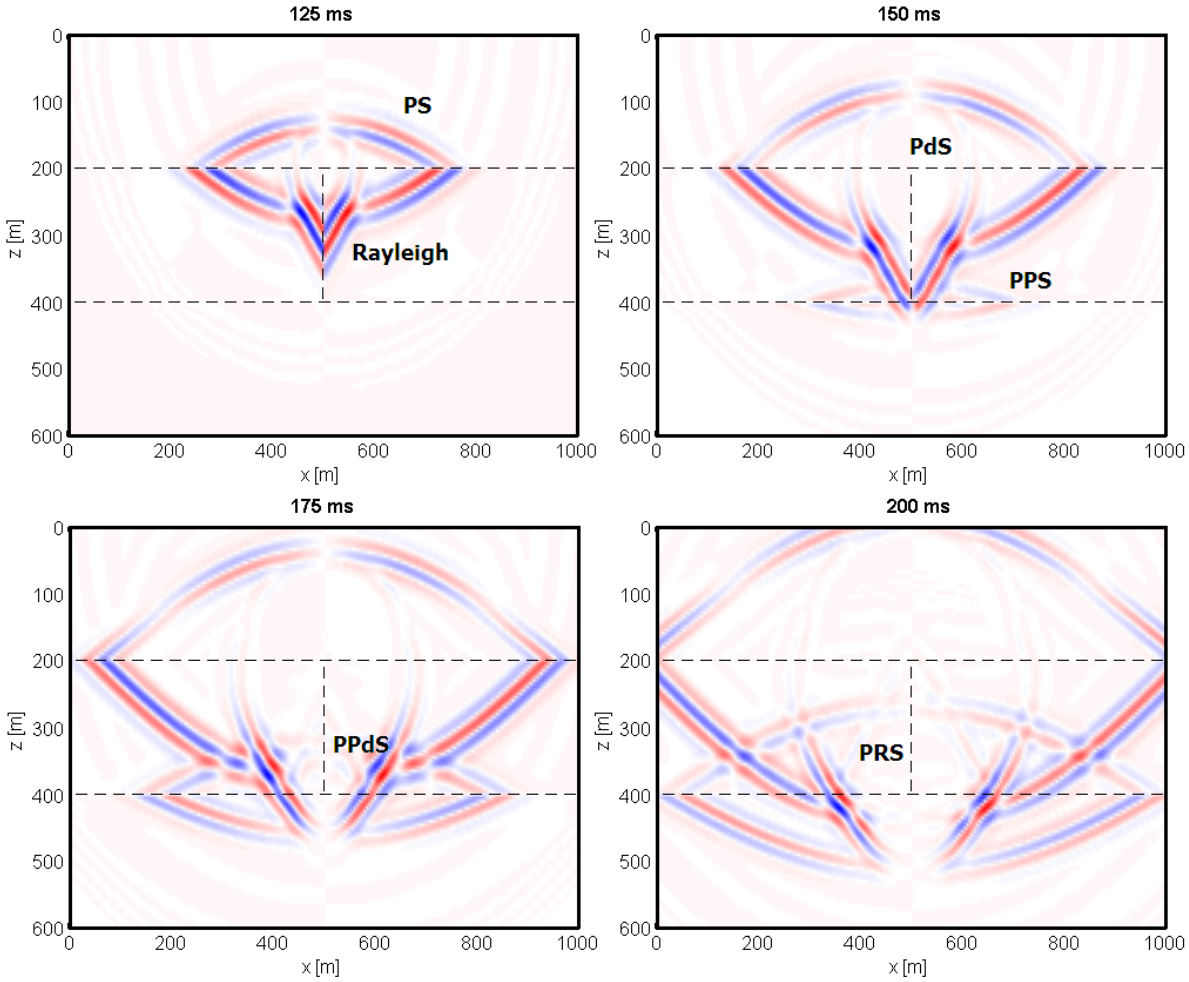

Figure 3-6: Snapshots of the curl component from the 1-fracture 2D model. Model interfaces are indicated with dashed black lines. PS: converted wave at the first interface; PdS: shear diffracted wave from the top tip of the fracture; PPS: shear wave reflected from the second interface; PPdS: shear diffracted wave from the bottom tip of the fracture; PRS: shear-reflected wave from the incident Rayleigh wave at the second interface.

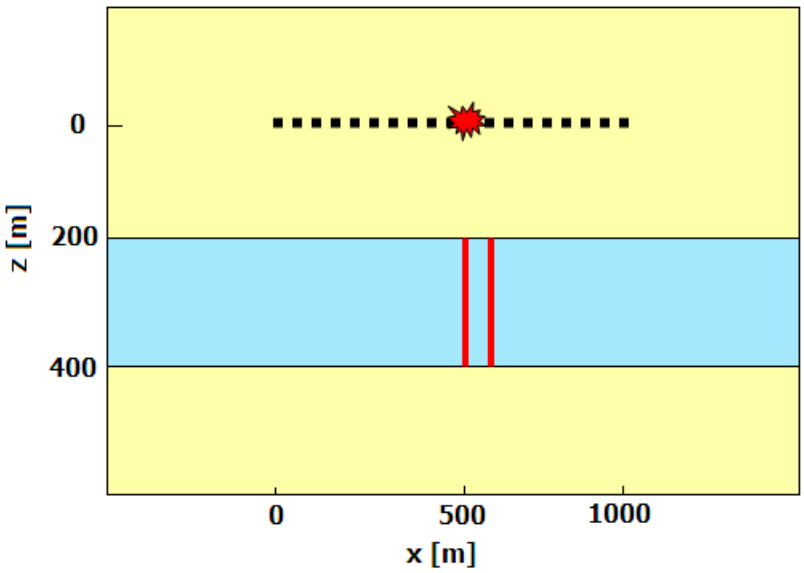

Figure 3-7: 2-Fracture 2D Model Geometry.

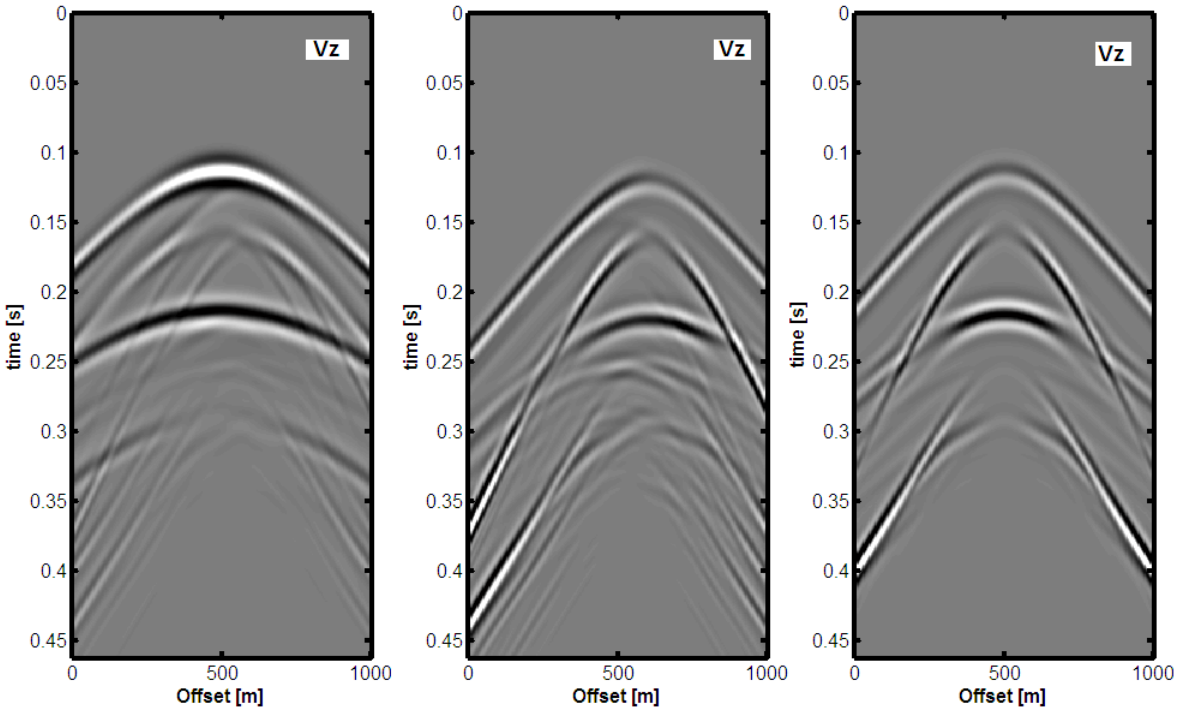

Figure 3-8: Seismograms from the 2-fracture 2D model. All records show the vertical component (Vz). The middle record was obtained substracting the no-fracture from the 2-fracture modeled data (left). The right record corresponds to the difference record between the 1-fracture and the no-fracture modeled data that is also shown in figure 3-5.

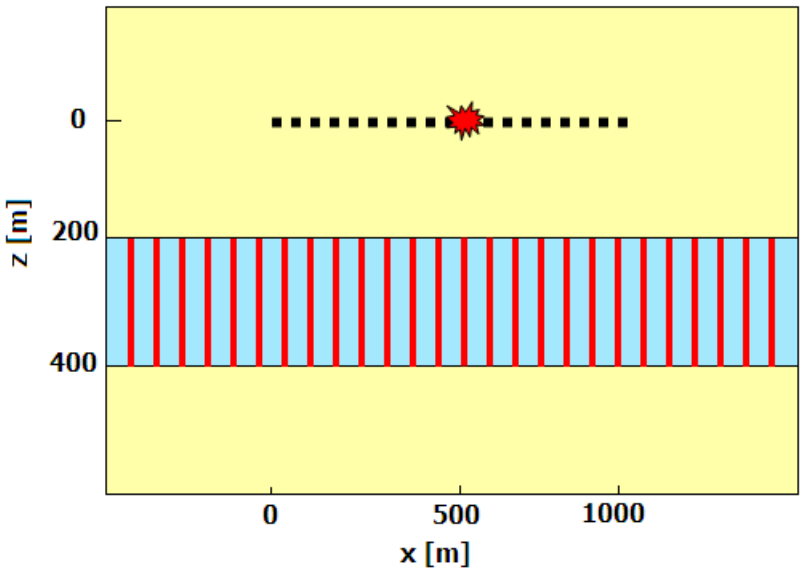

Figure 3-9: N-fracture 2D model geometry.

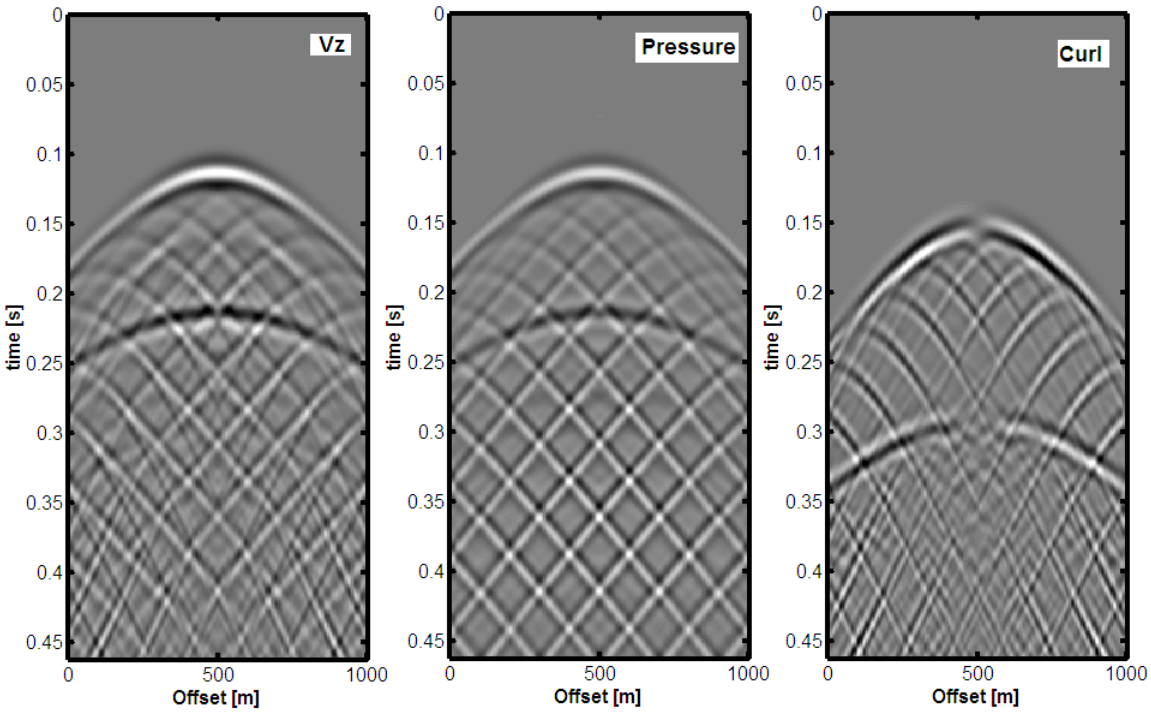

Figure 3-10: Seismograms from the N-fracture 2D model. From left to right: vertical component (Vz), pressure and curl.

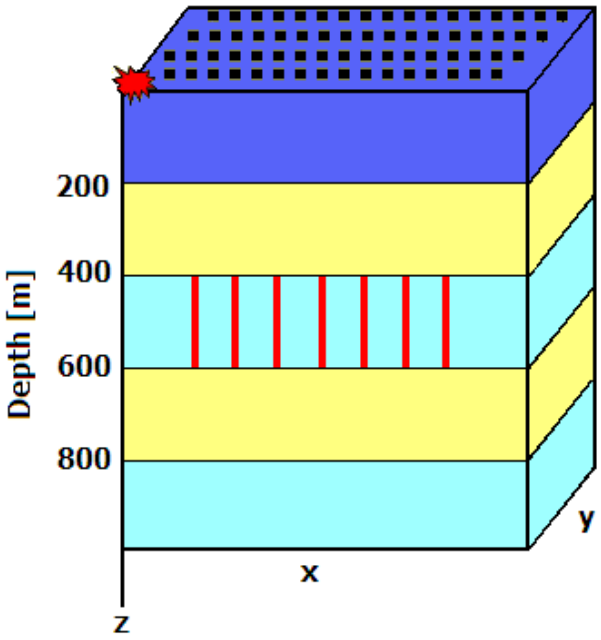

Figure 3-11: 3D Model Geometry. Fractures in the reservoir/middle layer are spaced 35 meters.

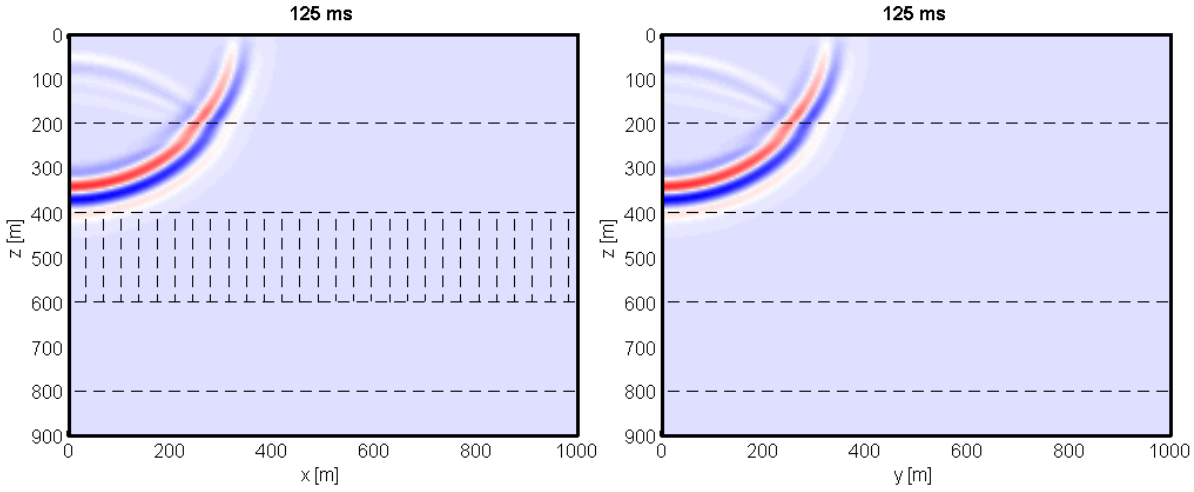

Figure 3-12: Snapshots of the vertical component (Vz) at 125 ms in the x-z (left) and y-z (right) plane. Data correspond to the 3D model with fracture spacing 35 m.

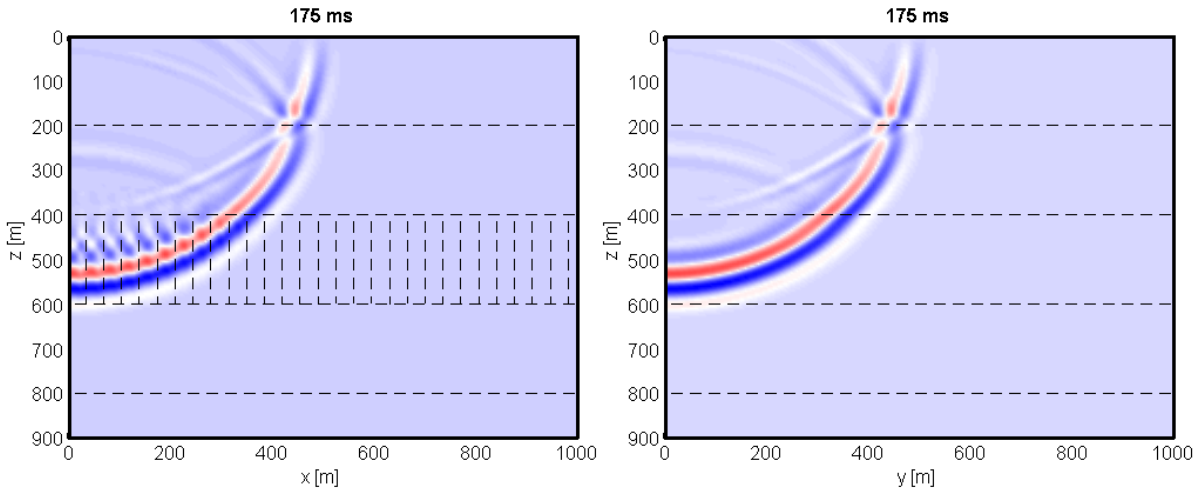

Figure 3-13: Snapshots of the vertical component (Vz) at 175 ms in the x-z (left) and y-z (right) plane. Data correspond to the 3D model with fracture spacing 35 m.

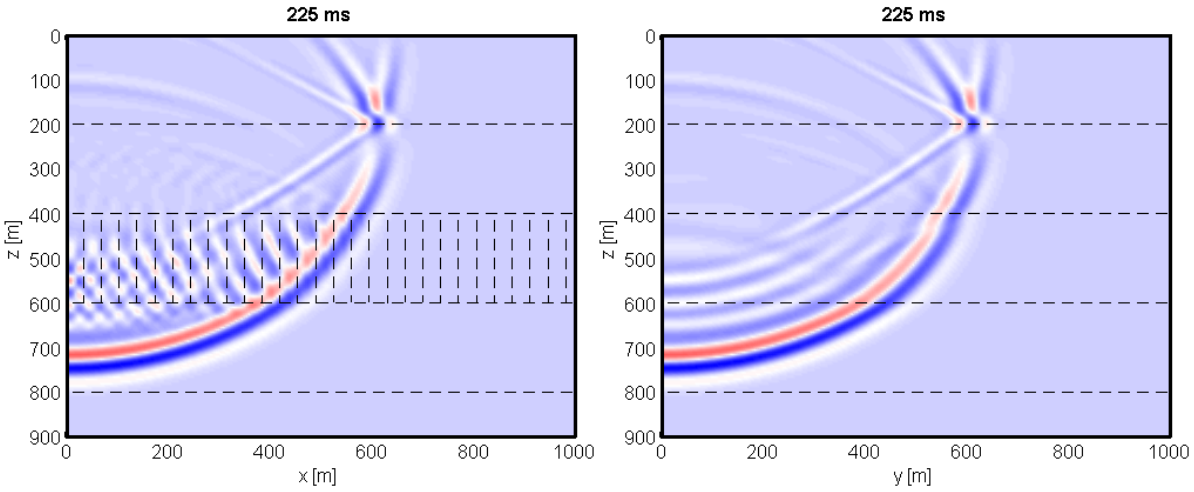

Figure 3-14: Snapshots of the vertical component (Vz) at 225 ms in the x-z (left) and y-z (right) plane. Data correspond to the 3D model with fracture spacing 35 m.

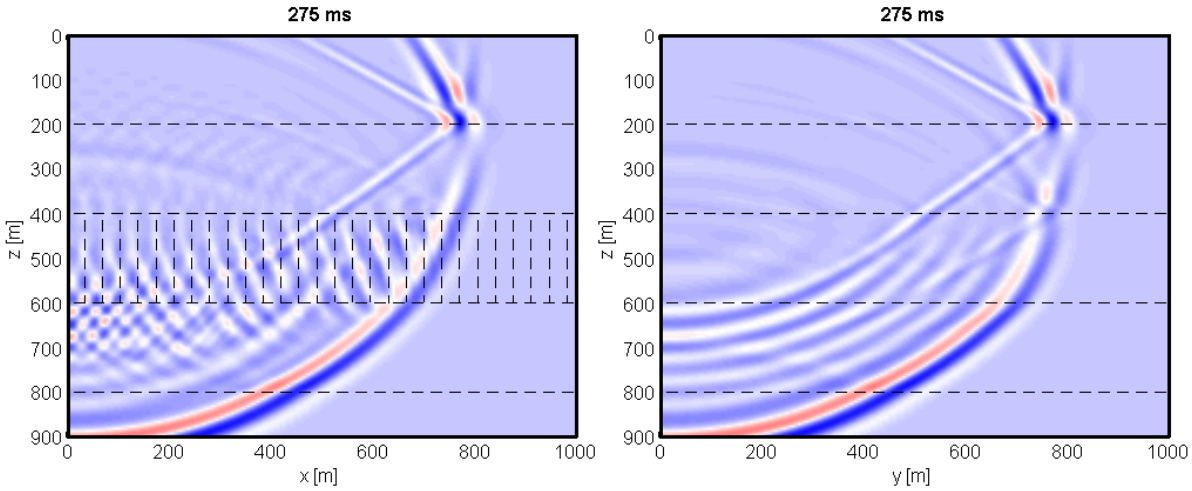

Figure 3-15: Snapshots of the vertical component (Vz) at 275 ms in the x-z (left) and y-z (right) plane. Data correspond to the 3D model with fracture spacing 35 m.

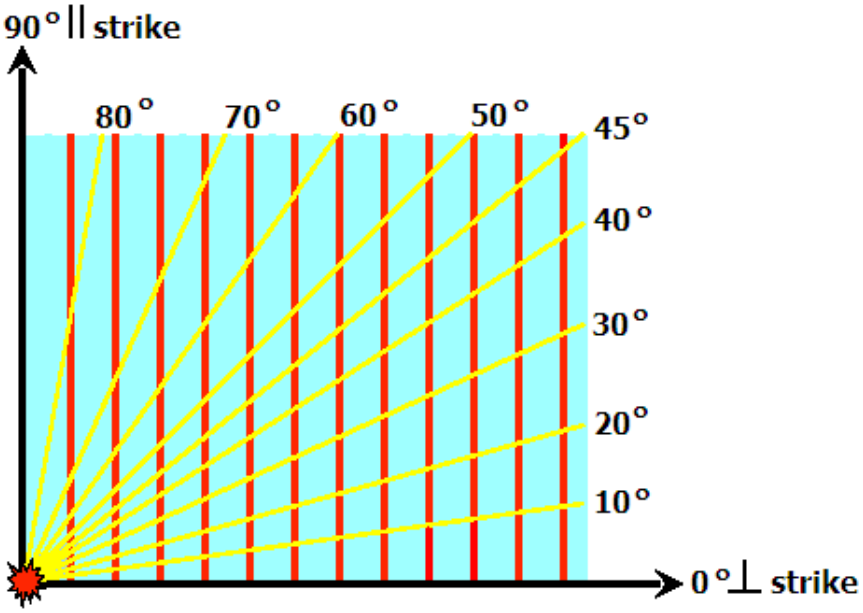

Figure 3-16: Map view of the top of the fractured layer in the 3D model with fracture spacing 35 m. Modeled data were sorted into 10-degree azimuthal gathers as indicated with the yellow lines. The azimuth numbering convention is also shown: 0° corresponds to the direction perpendicular to fracture strike (90°).

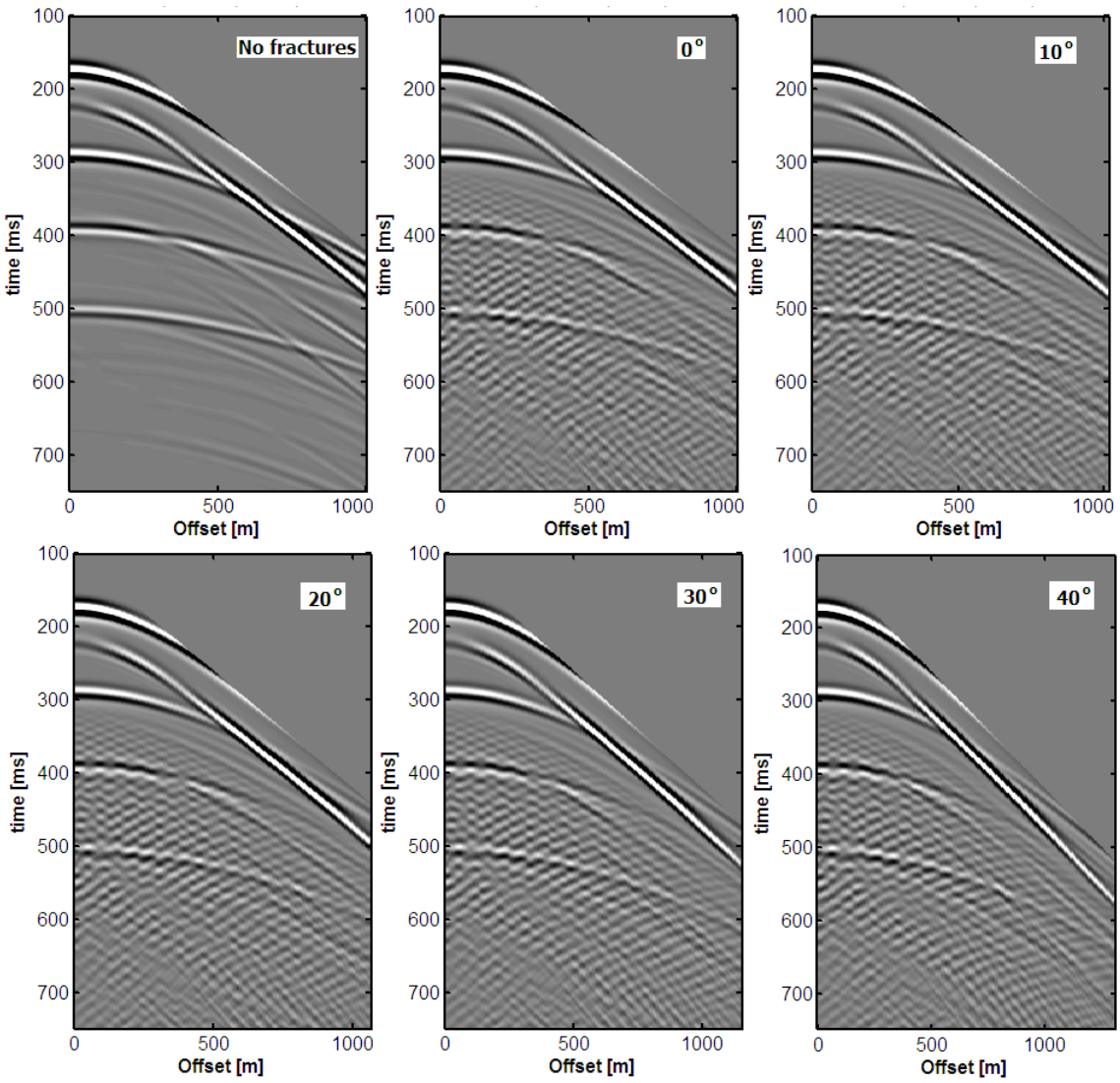

Figure 3-17: Data from the 3D model sorted by azimuth every 10°. The record at the top left displays the no-fracture model data. All records show the vertical component (Vz).

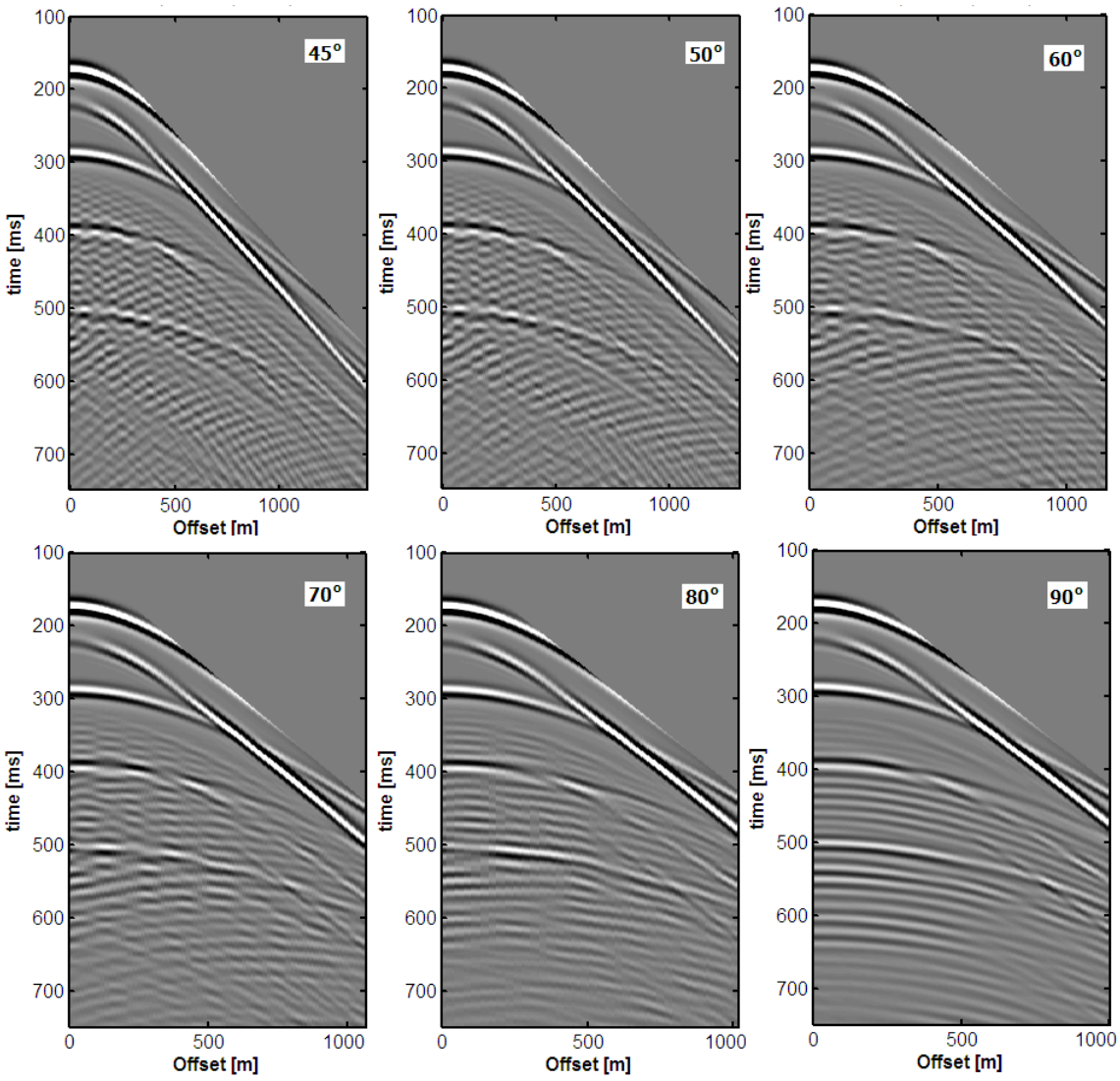

Figure 3-18: Azimuthal gathers (45° to 90°) from the 3D model.

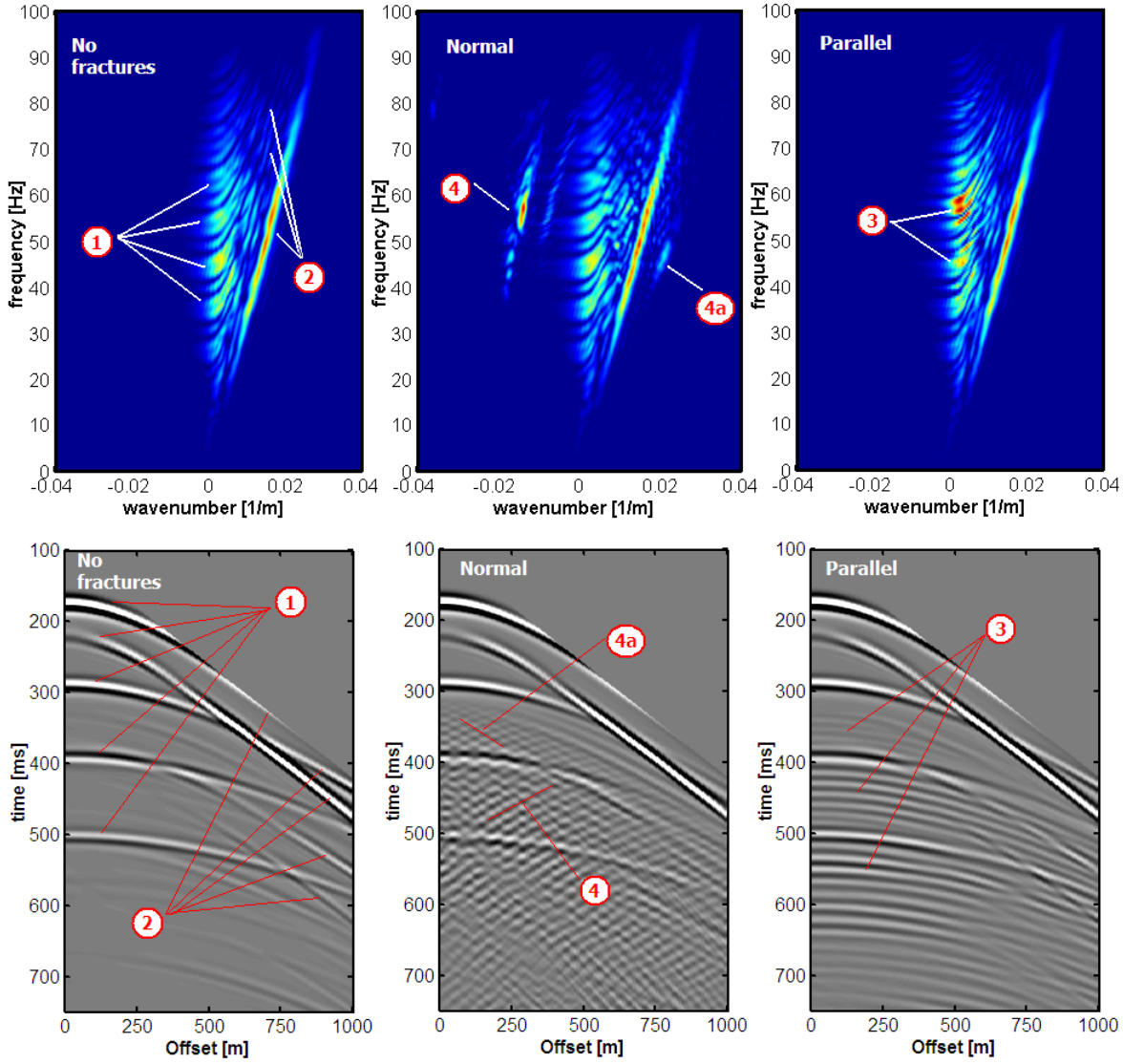

Figure 3-19: F-k spectra (top) of the modeled data (bottom). From left to right, data from a model without fractures, data sorted in the direction normal to fracture strike from the 3D model of figure 3-11 (fracture spacing is 35 m), and data sorted in the azimuth parallel to fracture strike. Numbered events are explained in the text.

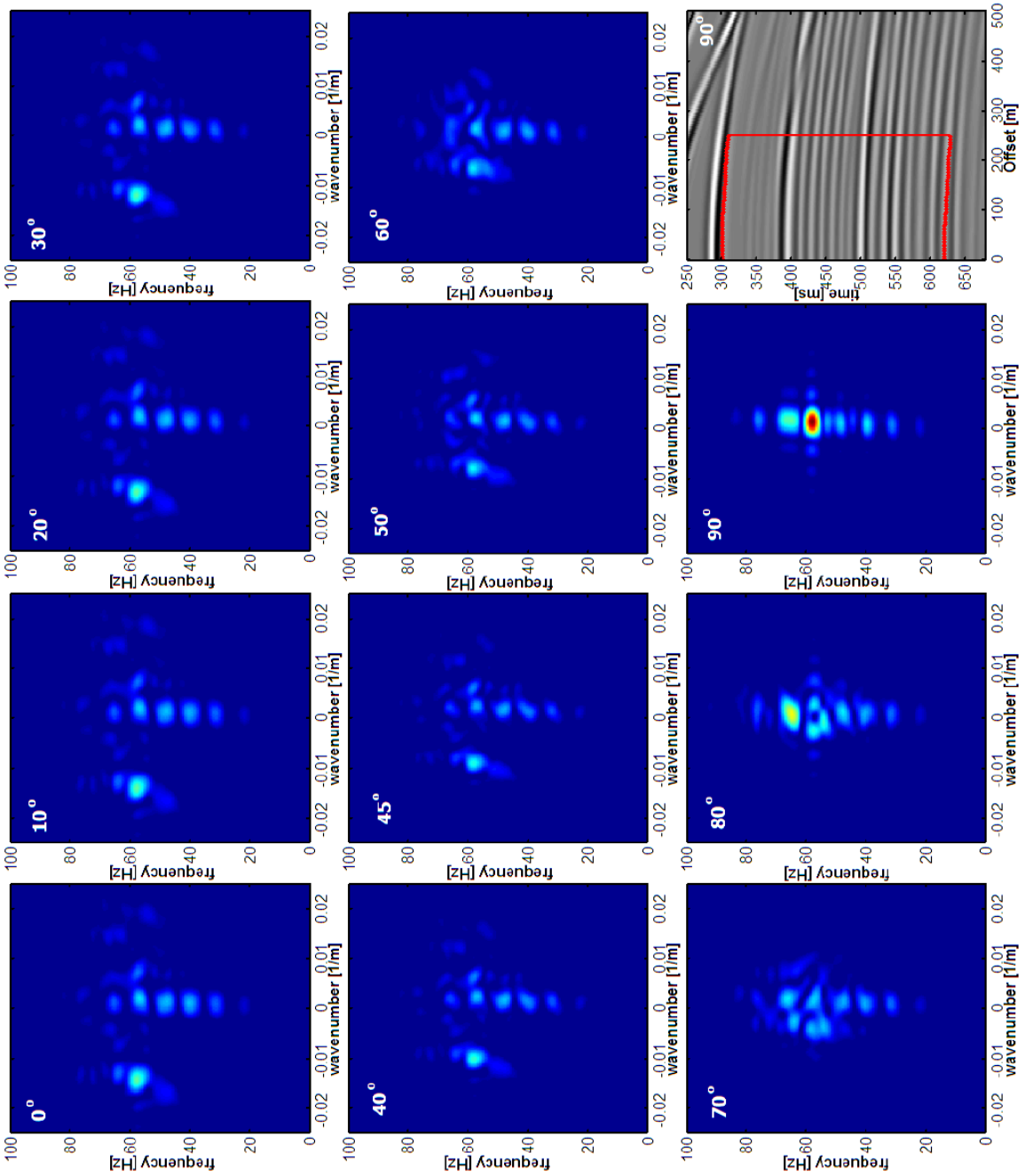

Figure 3-20: {F-k spectra of the data from the 3D model. Azimuthal gathers are depicted in figures 3-17 and 3-18. At the bottom rightmost figure the time-offset window input to the analysis is indicated over the gather at 90°.

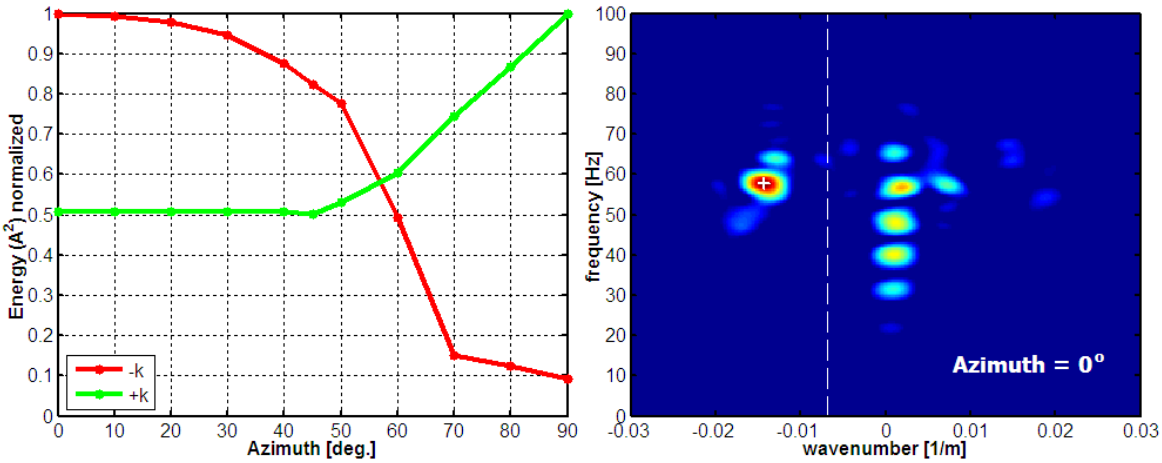

Figure 3-21: The normalized backscattered energy (E_{scatt}) is computed every 10° with equation 3.2 and plotted as a function of azimuth in the left figure (red). The green curve corresponds to the forward scattered energy, computed in the positive wavenumber interval. On the right, the *f-k* spectrum of the 0° gather (normal to fracture strike). The energy maximum in the negative wavenumber interval is indicated (white plus sign) as well as the value of k_o chosen to compute E_{scatt} (white dash line). Fracture spacing is determined from the frequency-wavenumber values of the energy peak through equation 3.3.

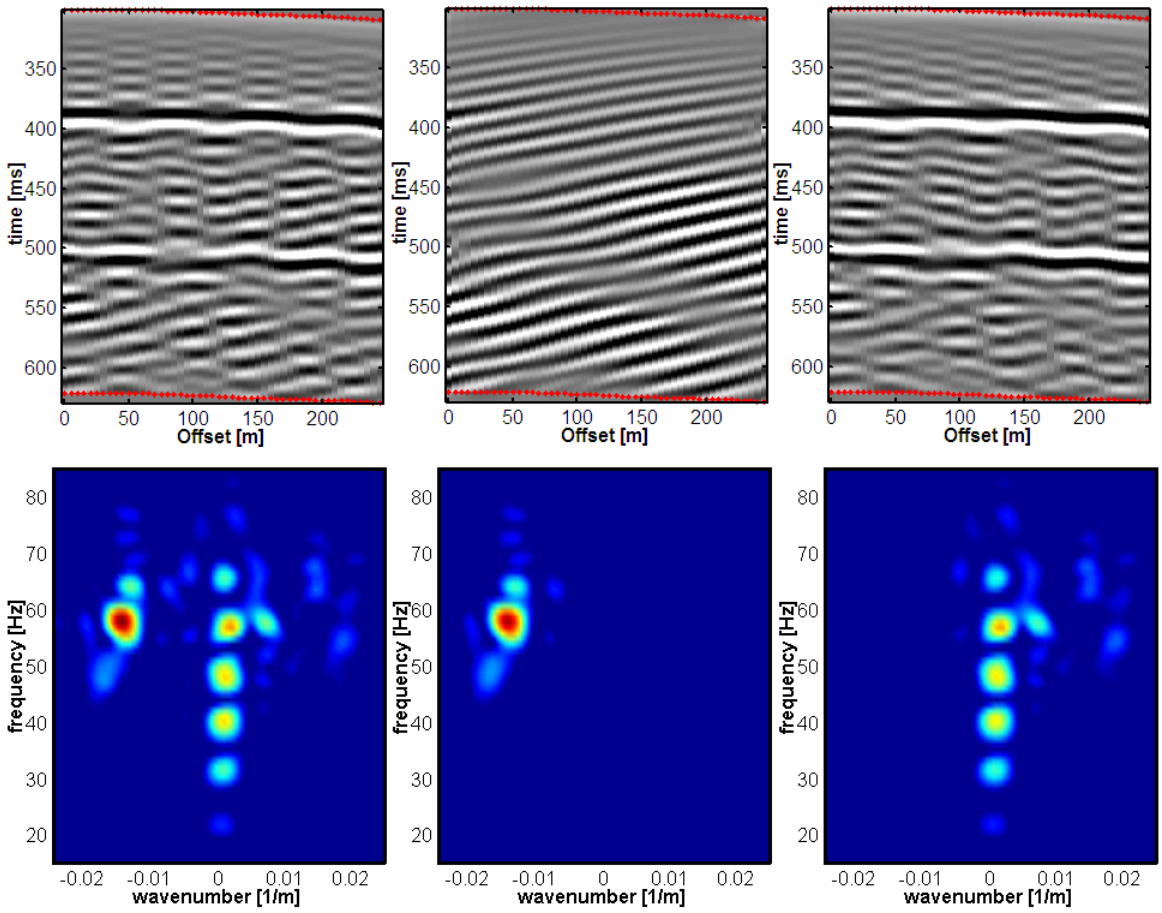

Figure 3-22: Windowed synthetic shot records showing scattered energy (top row) and their corresponding *f-k* spectra (bottom row). The first shot record (top left) is for the 0° azimuth. The middle shot record is the result of *f-k* filtering the first shot record to preserve only the backscattered energy. The right shot has had the backscattered energy removed.

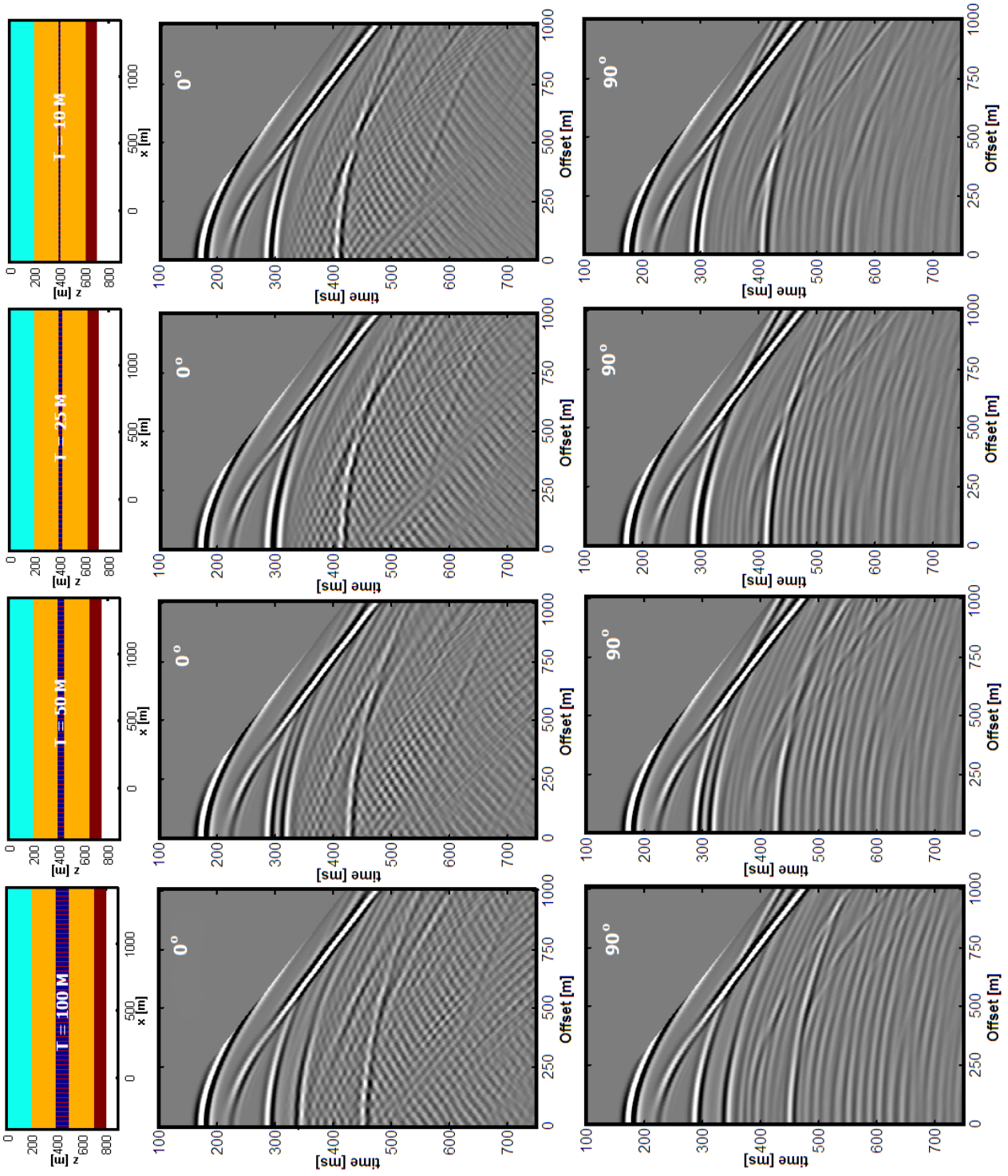

Figure 3-23: Data at 0° (top) and 90° from models which vary the fracture layer thickness. An x-z view of each 3D model is at the top most row. From left to right, thickness is: 100 m, 50 m, 25 m, and 10 m. The rest of the model parameters are as in table 3.2.

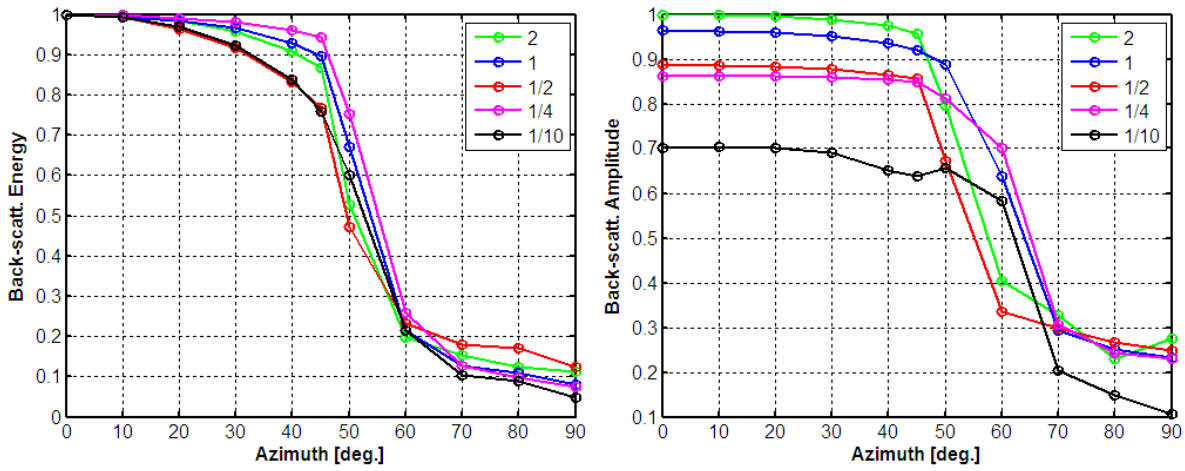

Figure 3-24: On the left, backscattered energy plotted as a function of azimuth for models in which the fracture height is reduced from 2λ to $\lambda/10$ or equivalently from 200 m to 10 m. On the right, the amplitude of the highest energy peak on the negative wavenumber interval (backscattered amplitude) is plotted as a function of azimuth for the same models).

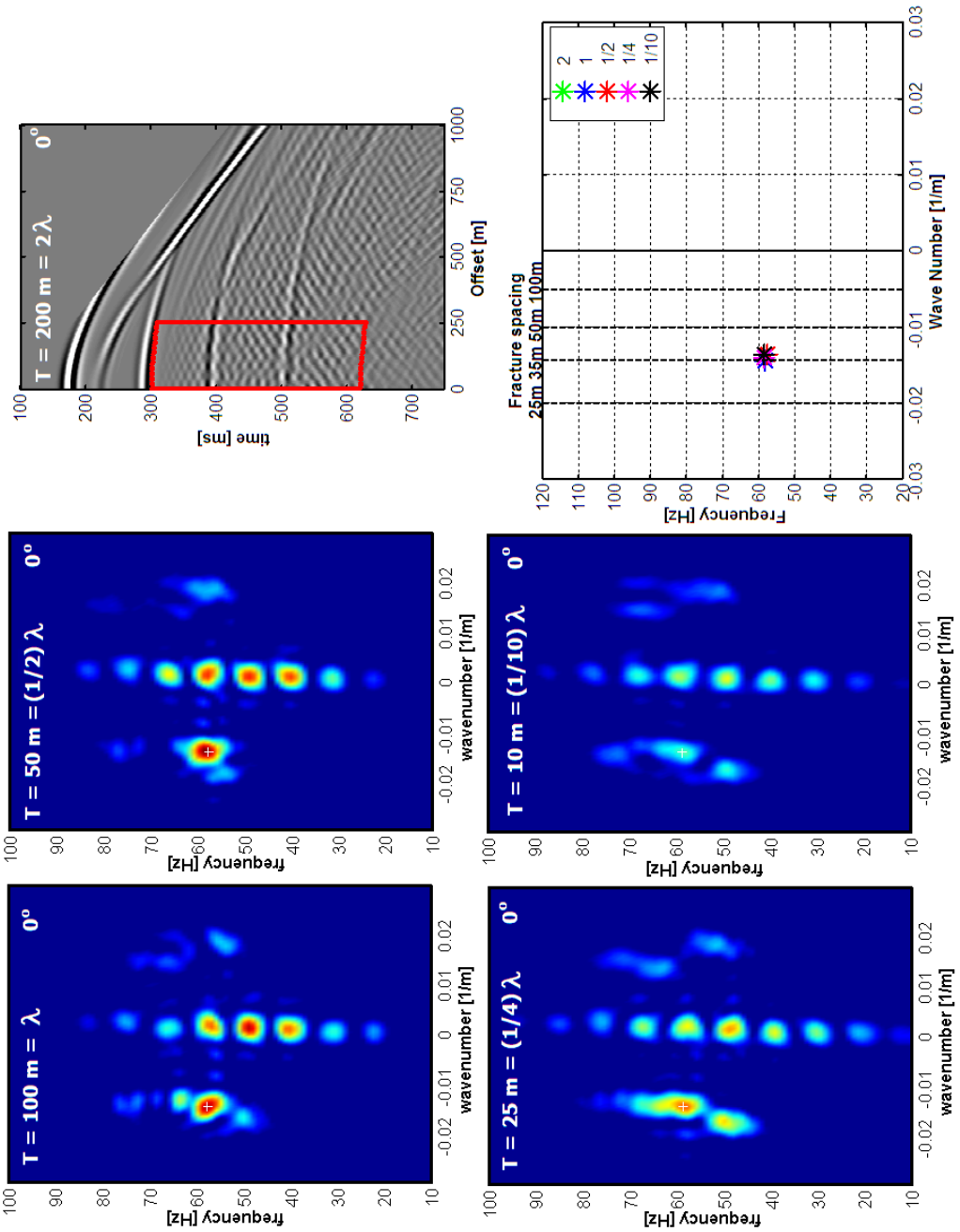

Figure 3-25: *F-k* spectra of the 0° gather from the different thickness models. From the top left plot and clockwise: model with thickness 100 m, 50 m, 25 m and 10 m. The window of data extracted for the analysis is indicated in red on the shot gather at 0° of the control model. On the spectra, energy maxima are indicated with white plus signs. At the bottom right, *f-k* components of all cases consistently estimate the fracture spacing of 35 m with great accuracy and precision.

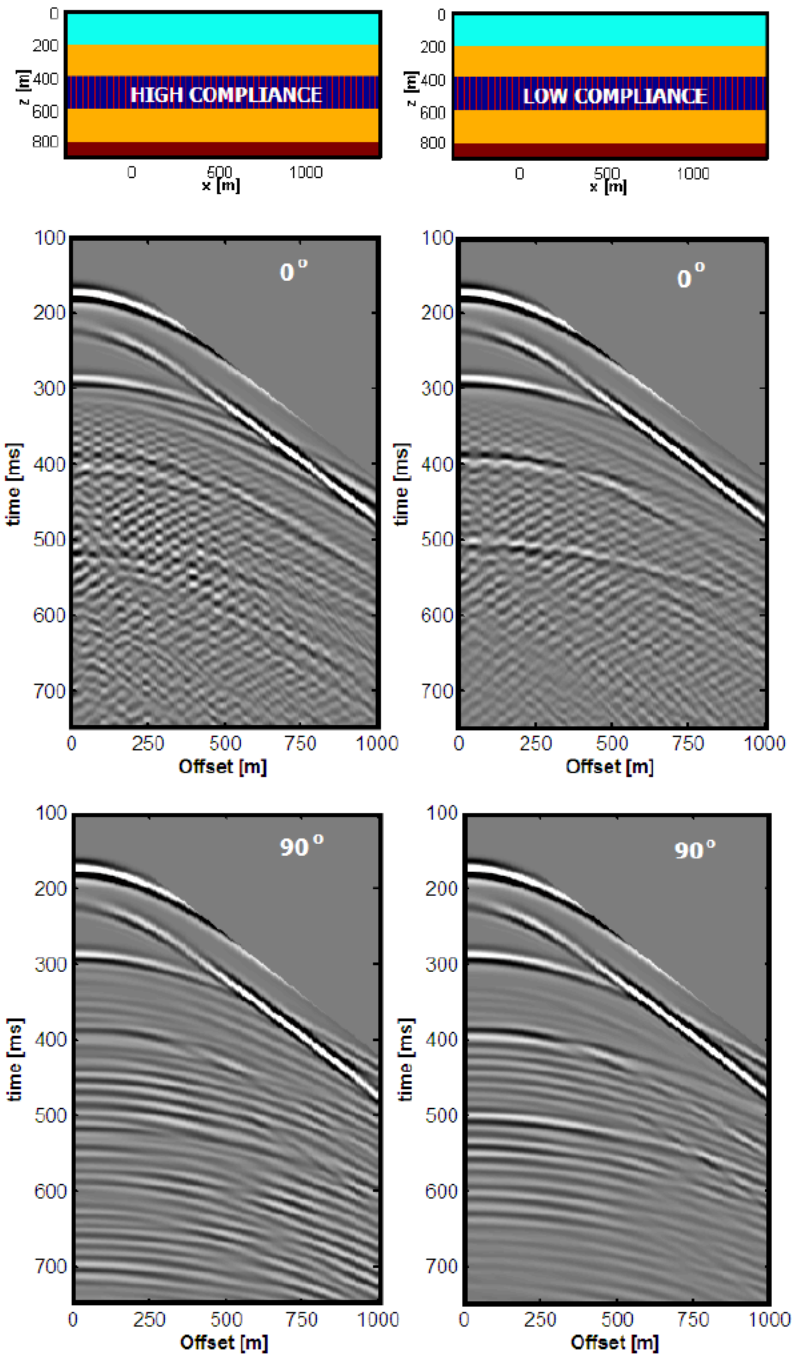

Figure 3-26: Data at 0° (top) and 90° from models which vary the fracture compliance. An x-z view of each 3D model is in the top row. From left to right, stiffness is: 8 x $10^8 Pa/m$ and 4 x $10^9 Pa/m$. The rest of the model parameters are as in table 3.2.

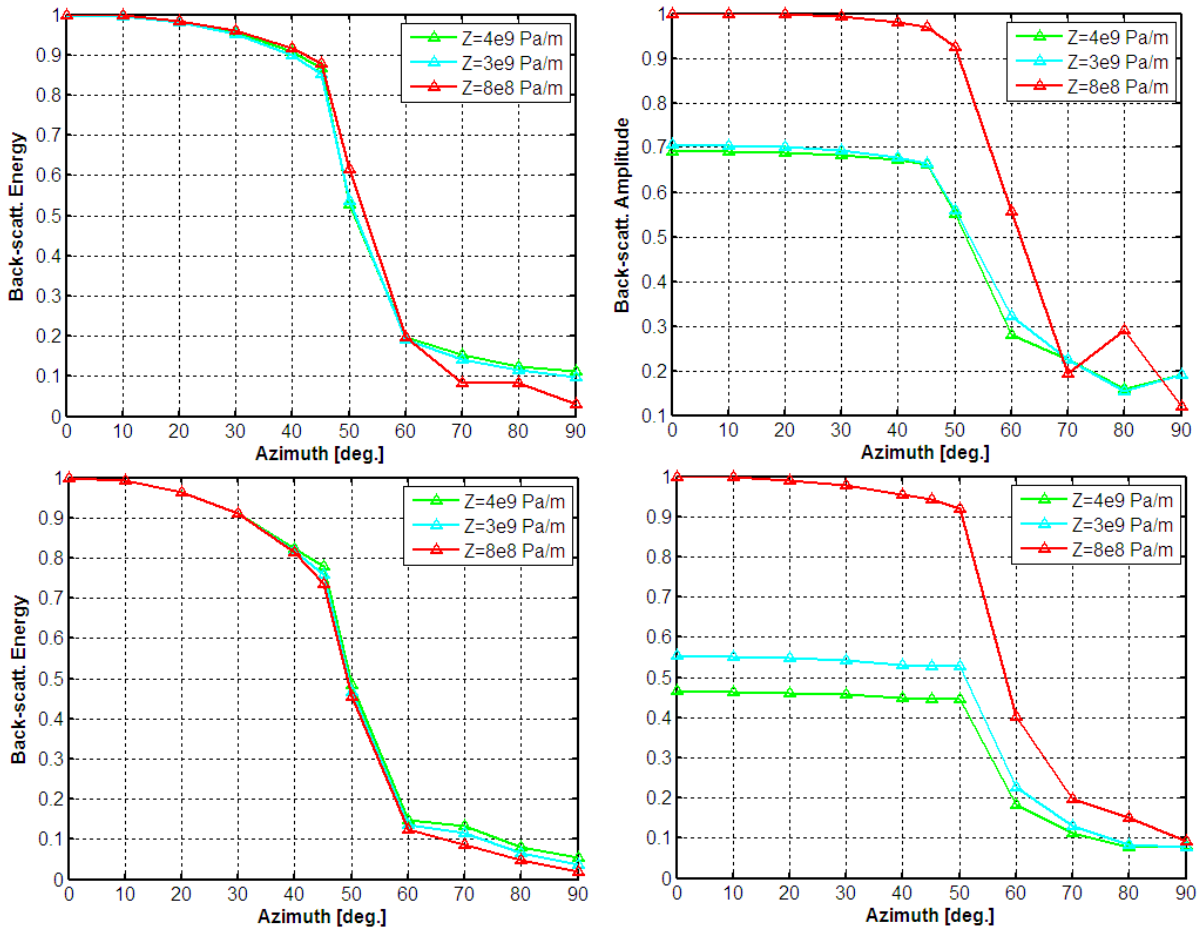

Figure 3-27: In the left column, backscattered energy is plotted as a function of azimuth for models in which the fracture stiffness is increased from 8 x $10^8 Pa/m$ to 4 x $10^9 Pa/m$. In the right column, the amplitude of the highest energy peak on the negative wavenumber interval (backscattered amplitude) is plotted as a function of azimuth for the same models. The top row uses a long analysis window and the bottom row uses a short time window.

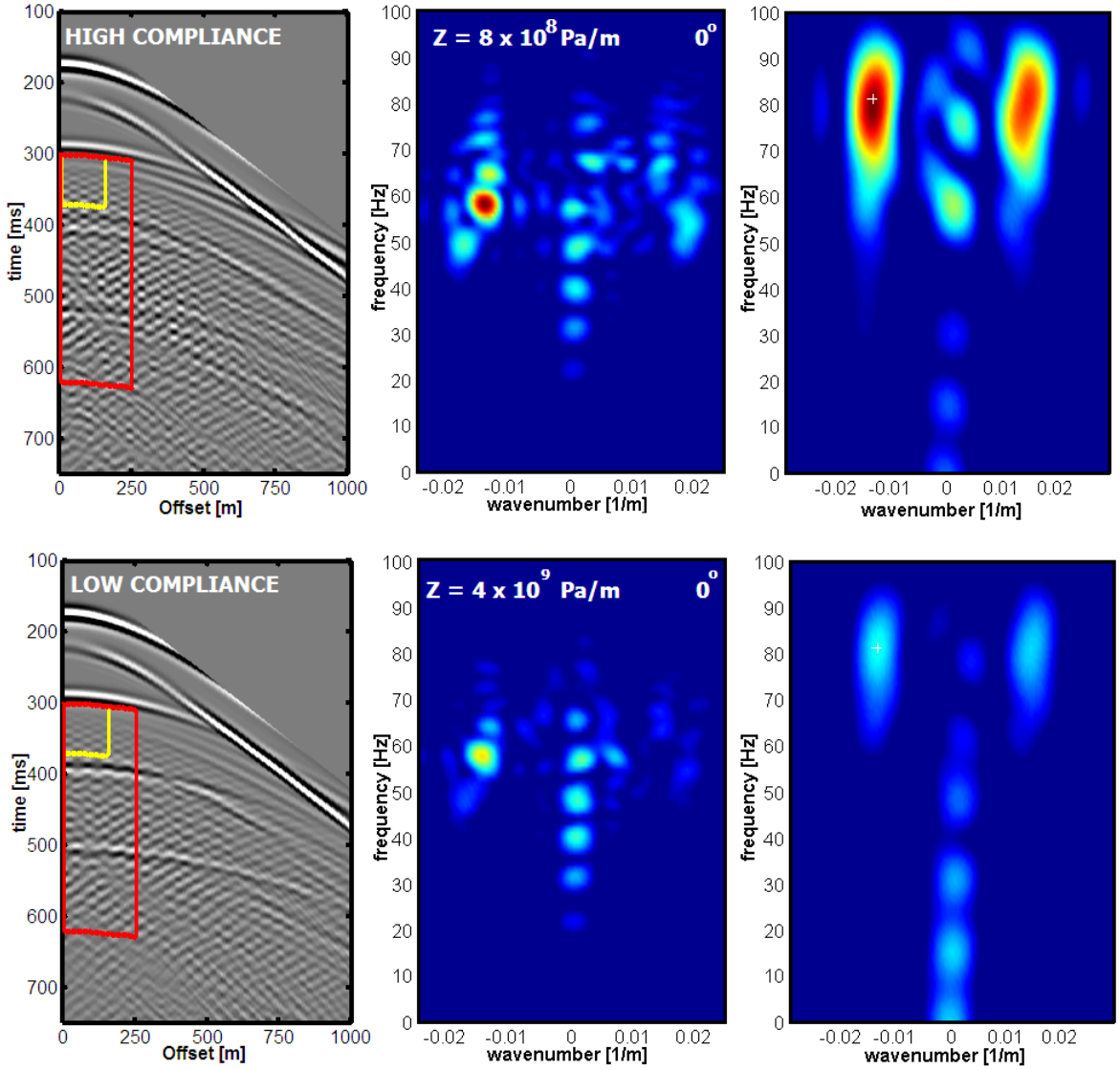

Figure 3-28: *F-k* spectra of the 0° gathers from the different fracture compliance models. In the top row, data and spectra computed in two different windows for the highly compliant fractured model. In the bottom row, equivalent figures for the control model (low compliance). The windows are indicated on the left gathers. The middle panel shows the spectrum for the larger analysis window, while the right panel shows the results for the smaller window. The energy maxima associated to the fracture backscattered component are indicated with the white + symbols.

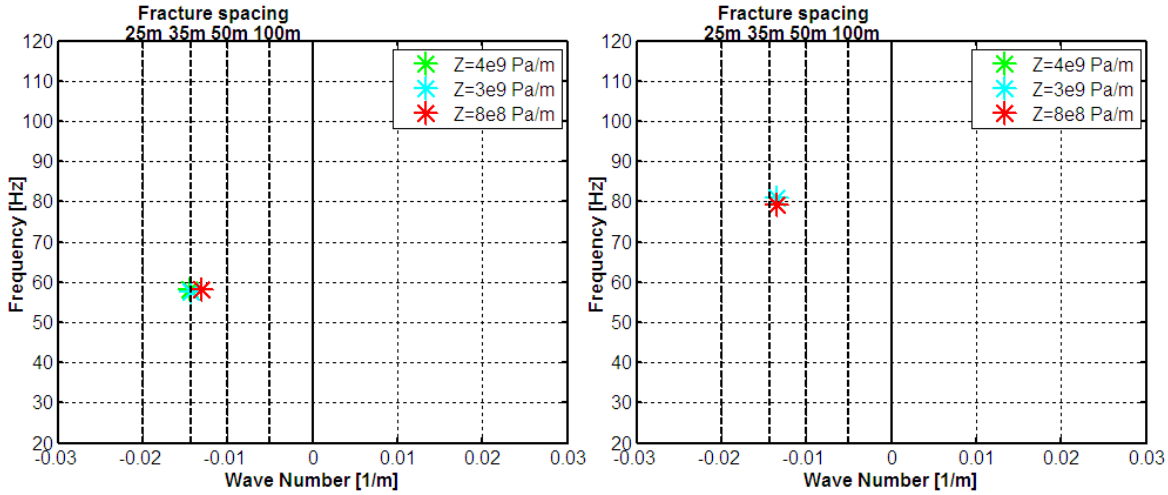

Figure 3-29: *F-k* components of the energy peak for all fracture compliance models. The left plot corresponds to the results from the long analysis. On the right, the corresponding results when the input data window is shorter.

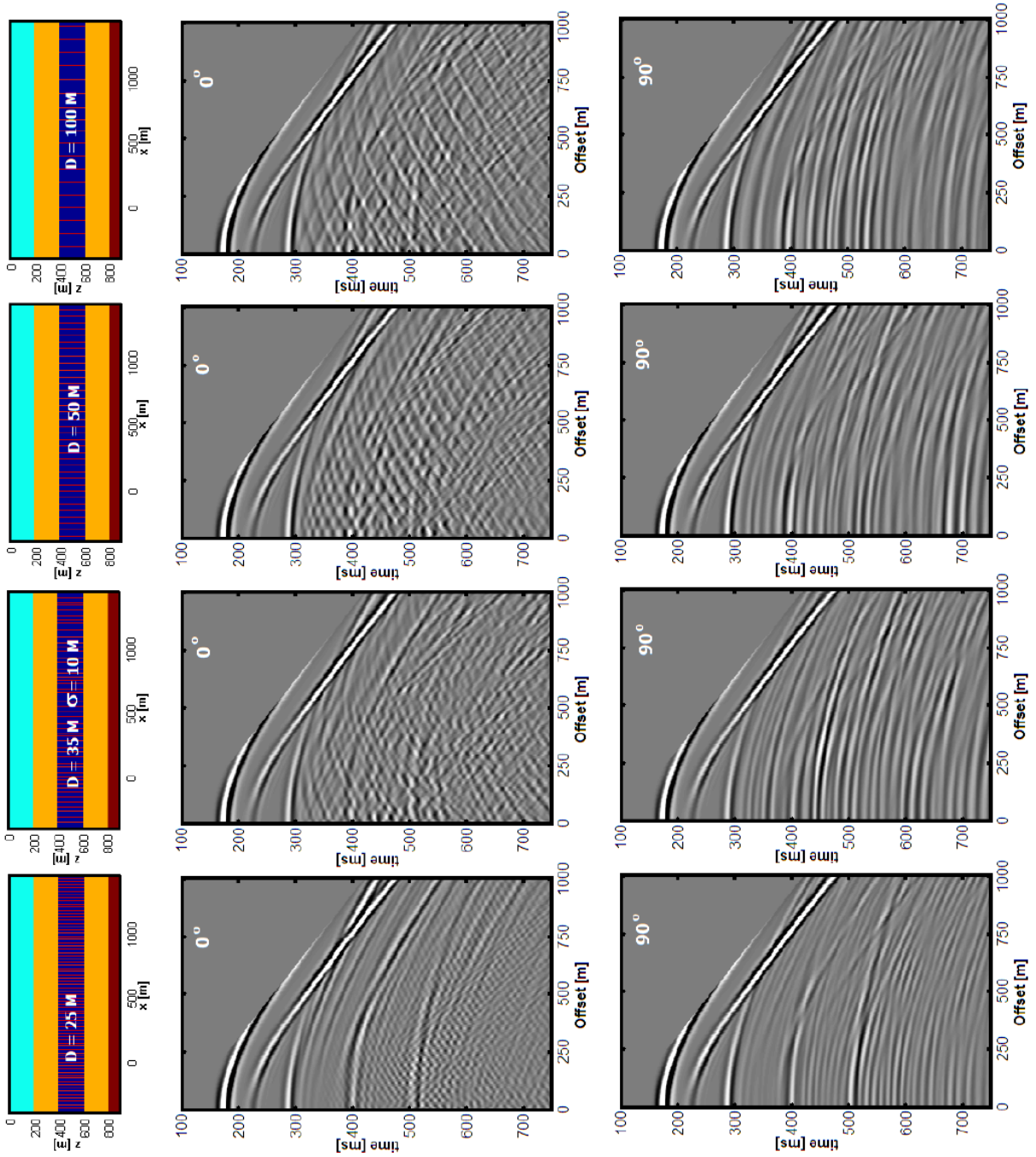

Figure 3-30: Data at 0° (top) and 90° from models which vary the fracture spacing. An x-z view of each 3D model is in the top row. From left to right, spacing is: 25 m, a pseudo-normal distribution with mean spacing 35 m and standard deviation 10 m, 50 m, and 100 m. Model parameters are as in table 3.2 except for the fracture material whose normal and tangential stiffness are 8 x 10^8 Pa/m.

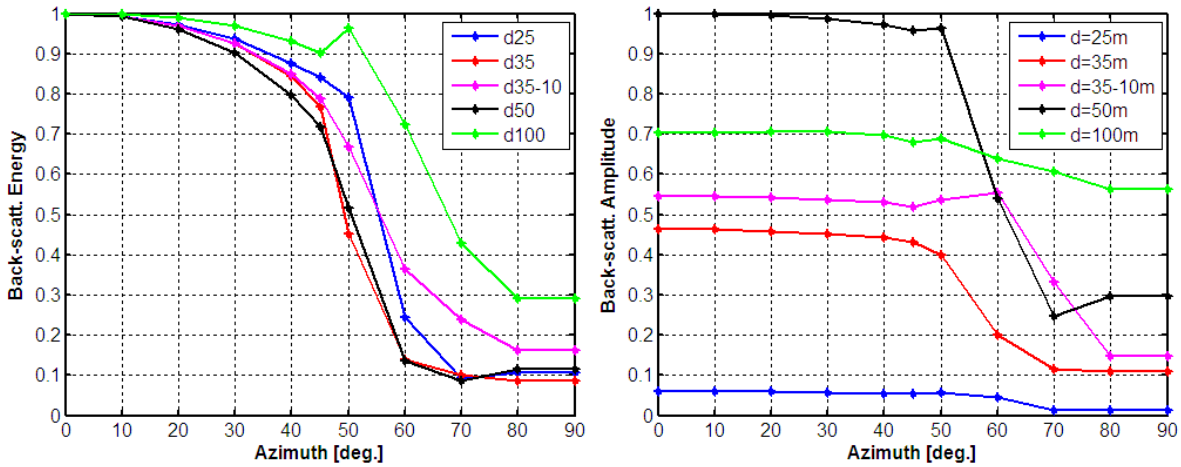

Figure 3-31: On the left, backscattered energy plotted as a function of azimuth for models in which the fracture spacing is reduced from 100 m to 25 m. On the right, the amplitude of the highest energy peak on the negative wavenumber interval (backscattered amplitude) is plotted as a function of azimuth for the same models.

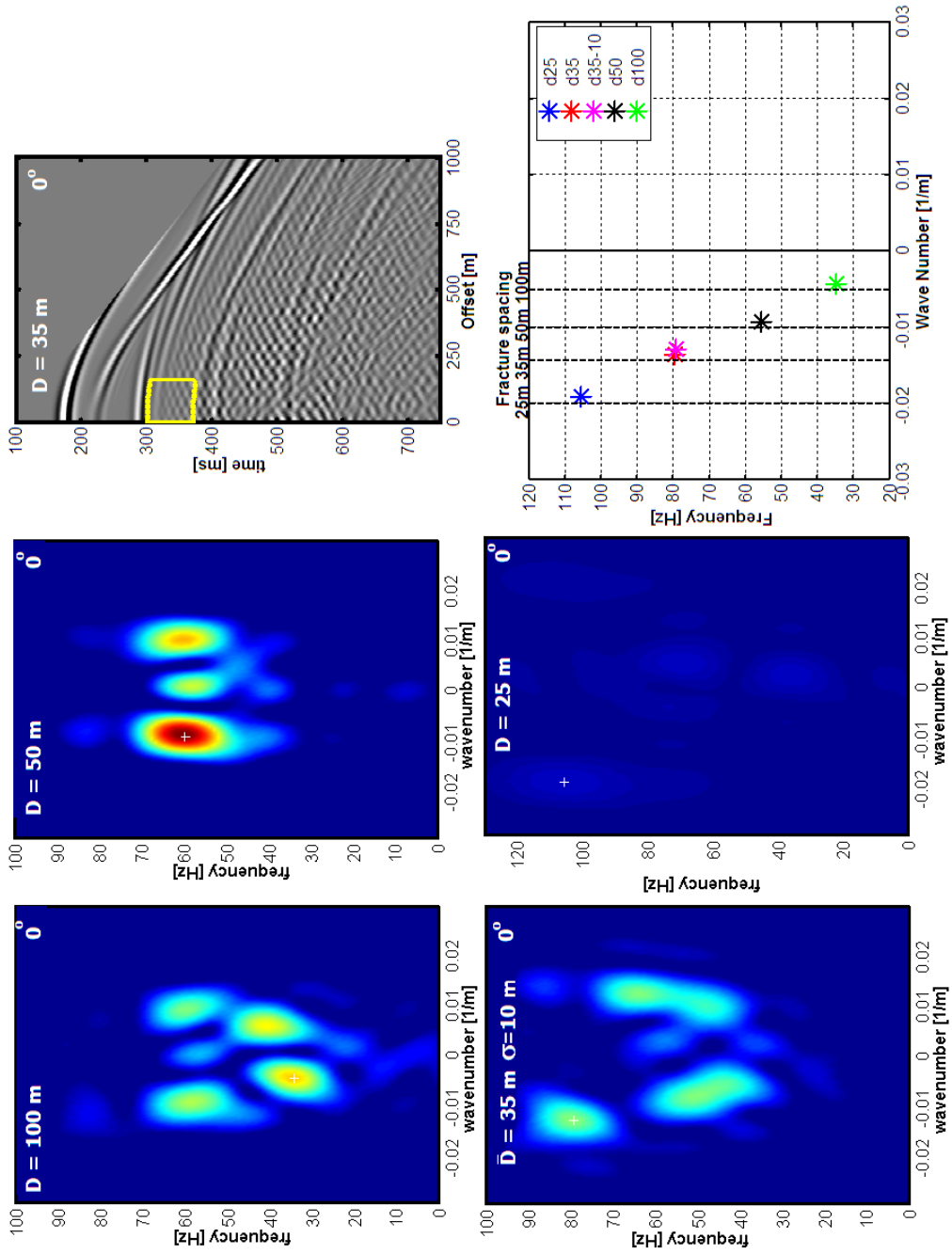

Figure 3-32: F-k spectra of the 0° gather from different spacing models. From the top left plot and clockwise the spacing is: 100 m, 50 m, a pseudo-normal distribution with mean spacing 35 m and standard deviation 10 m, and 25 m. The window of data extracted for the analysis is indicated in yellow on the shot gather at 0° of the 35 m fracture spacing model. On the spectra, energy maxima are indicated with white plus signs. At the bottom right, the peak wavenumber is related to fracture spacing though equation 3.3.

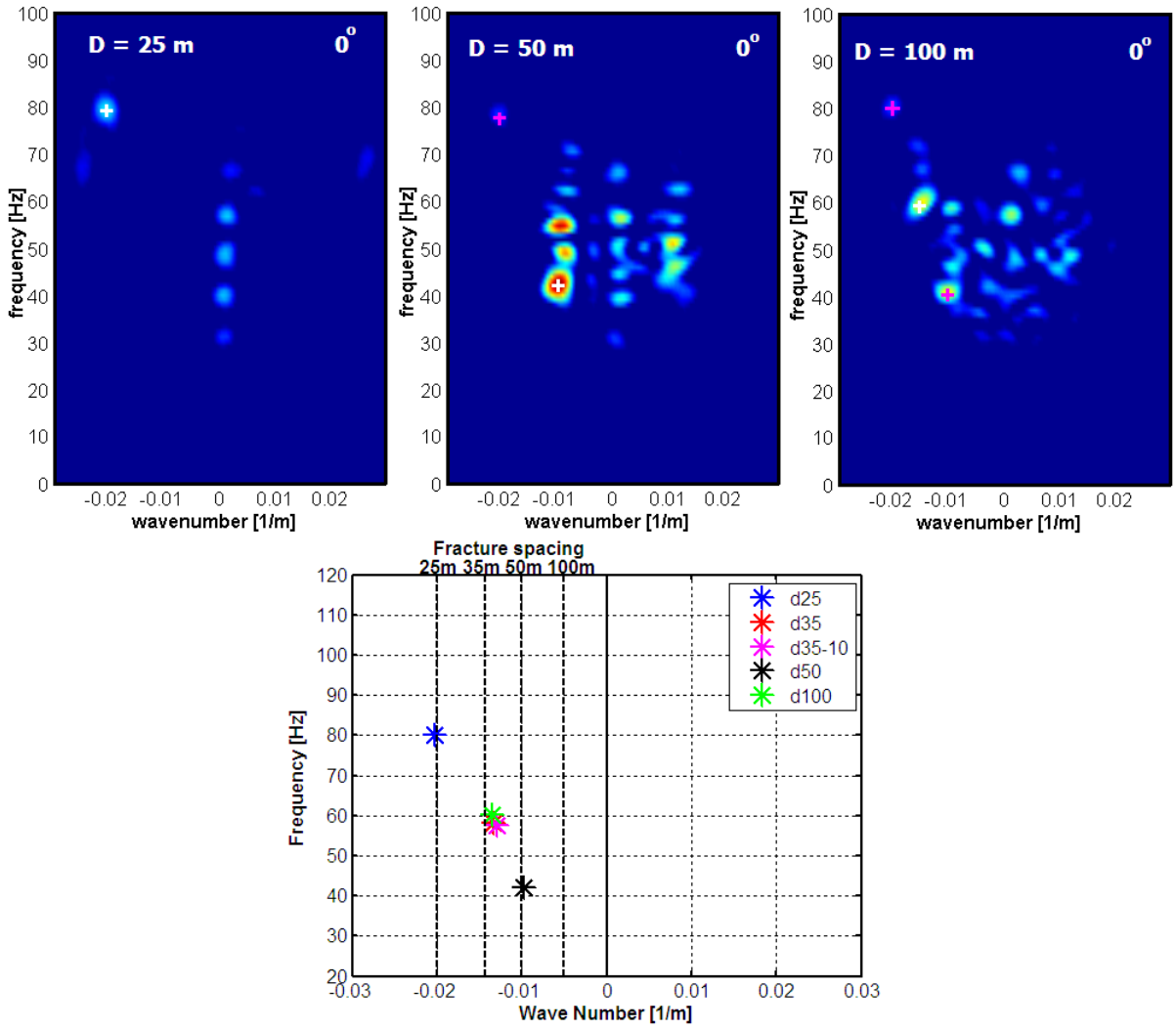

Figure 3-33: F-k spectra of the 0° gather from the 25 m, 50 m, and 100 m fracture spacing models. The analysis is performed in long time windows (indicated in red in figure 3-28. On the spectra, energy maxima are indicated with white plus signs. Other energy peaks are indicated with magenta plus signs. At the bottom, the peak f-k values are extracted for all cases and compared to fracture spacing. In the 100 m fracture spacing model the F-K technique applied in the long window fails to resolve without aliasing the dominant wavenumber and therefore it under estimates the fracture spacing.

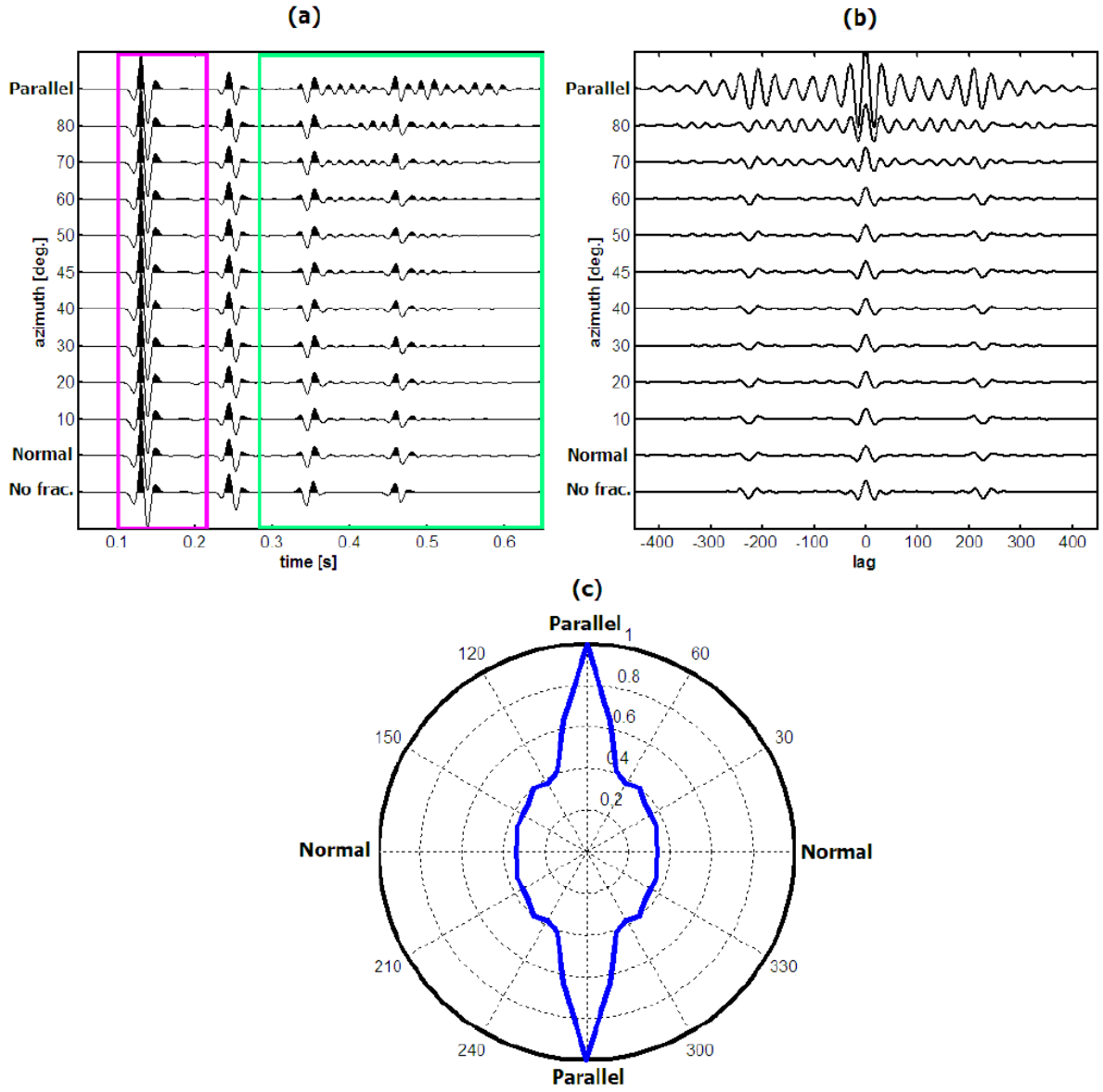

Figure 3-34: The *SI* method explained on the control model data: (a) azimuthal stacks and windows above (magenta) and below (green) the reservoir to extract input and output wavelets; (b) azimuthal transfer functions; (d) azimuthal scattering indices. In (a) and (b), the lowest trace corresponds to the no fracture case.

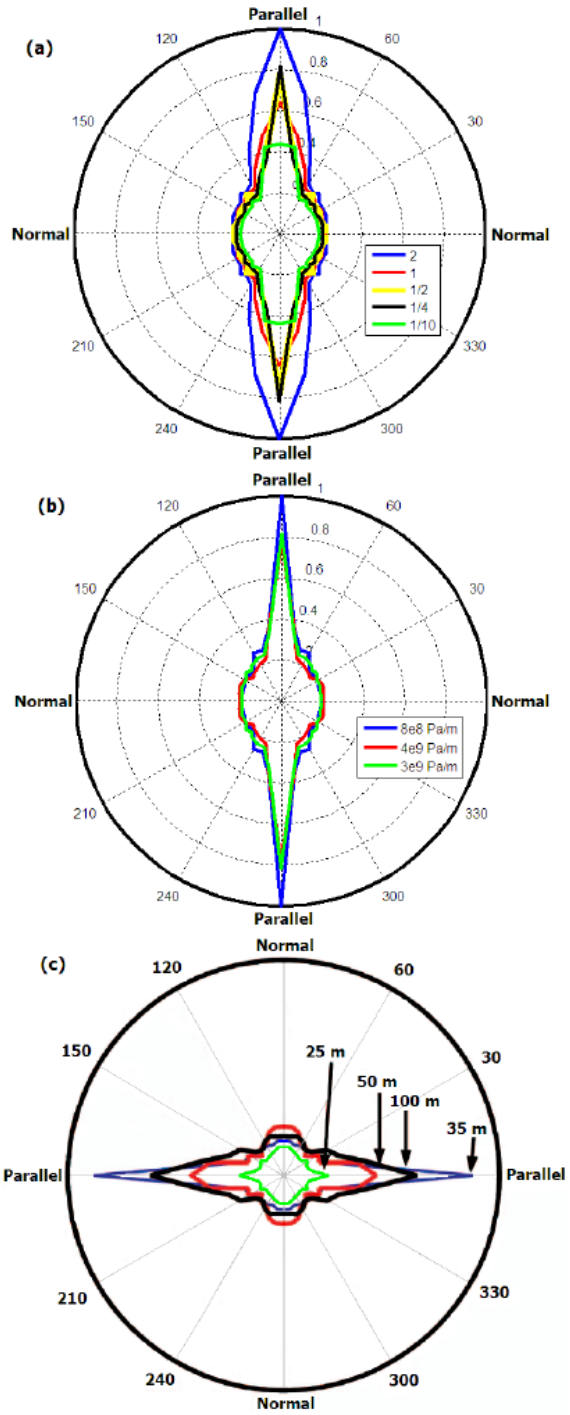

Figure 3-35: Scattering index as a function of azimuth computed for the following models: (a) models where fracture height is reduced from 2λ (control model, in blue) to $1/10\lambda$ (10 m, in green); (b) models where fracture stiffness is reduced from $4\text{x}10^9 Pa/m$ (control model, in red) to $8\text{x}10^8 Pa/m$ (in blue); and (c) models where fracture spacing is decreased from 100 m (black) to 25 m (green) (control case is in blue). Figure (c) is modified from Willis et al. (2006).

Chapter 4

The Lynx Field

The ideas and techniques developed in chapter 3 will be applied to a real reservoir case in the following chapter. In the present chapter, background information about the *Lynx* field is provided.

Knowledge of the geological setting is critical because it guides the fracture analysis. It also assists in evaluating the validity of the intrinsic assumptions of the scattering methods when applied to a particular field case. Furthermore, rock type, regional tectonics, and stress regime, among others, are key to interpreting the results of chapter 5.

First, the geographical and geological location of the Lynx area is described followed by a summary of the tectonic history and typical regional structures (section 4.2). Section 4.3 and 4.4 discuss petrophysical and stratigraphical data and the structural model of the Lynx field, respectively.

Section 4.5 collects information related to fractures in the Lynx field, either from direct observations or inferred by previous studies. The production history of Lynx, briefly described in section 4.6, clarifies the practical motivation to apply the fracture scattering techniques in order to provide a fracture map of this gas field. Finally, the current and past stress state in the Lynx and adjacent areas are discussed in section 4.7.

4.1 Location

The Lynx field is located in southwest Canada, in the foothills of the Canadian Rocky Mountains, in the Alberta Province, about 450 Km to the north of the city of Calgary and to the northwest of Grande Cache (figure 4-1).

The Lynx field is also on the western edge of the Western Canadian Sedimentary Basin (WCSB), specifically in the structural domain known as the Foothills. The Foothills cover about 40,000 mi^2 and are limited on the west by the Front Ranges of the Rocky Mountains and on the east by the Plains domain (Newson, 2001). The Plains sedimentary section extends east to igneous and metamorphic outcrops of the Canadian Shield. To the west of the Foothills and the Rocky Mountains is the Rocky Mountain Trench, a long valley that stretches from the US border to the Yukon (figure 4-2).

The Rocky Mountain trench separates the region of alloctonous rocks (plutonic, volcanic, metamorphic and granitic) from the structured belt of the WCSB in the east formed of folded and faulted sedimentary rocks (Wennekers, 2007a). To the west of the trench are found numerous metal deposits, industrial minerals, and coal, whereas the eastern area yields oil, natural gas, coal, potash, salt, gypsum, and other non-metallic products.[1] The WCSB is one of the world's most prolific hydrocarbon basins. In Alberta, natural gas production at the end of 2006 was about 130 tcf. Another 100 tcf of gas (not including coal bed methane reserves), are estimated to be still in place (Alberta Energy and Utilities Board, 2007). However, the structured belt of the WCSB is also one of the most complex structures in the world and "*future exploration will only be successful when stress and strain are understood in this area*" (Wennekers, 2007a).

The Lynx field was discovered in 1963. With the exception of few wells (e.g. well 10-28), drilling activity and commercial gas production formally started in 1998. Until today, well 6-18 has been the most prolific well in the Lynx field from the Cadotte formation (Canadian Discovery Digest, 2004). Figure 4-3 gives an idea of the type

[1] http://atlas.nrcan.gc.ca

of structures found at the reservoir level beyond the area of study, as well as the relative location of several wells. The tectonics of the region have extensively folded the southwest area, with the major axis of these folds being in the NW-SE direction. The structural folding reduces and flattens smoothly into a vast plain towards the East.

4.2 Tectonic History of the Western Canadian Sedimentary Basin

The WCSB is a foreland basin, and the adjacent Rocky Mountain Thrust and Fold Belt is a transpressional accretionary prism. Subsidence and sediment accumulation in the WCSB is linked to the origin and tectonic evolution of the Cordilleran orogenic belt and thereby to the history of the tectonic interactions between the craton and the adjacent plates. Next, a summary of such tectonic history is presented as described in Price (1994), Monger and Price (2002) and Wennekers (2007a).

1000 Ma - 540 Ma: Rifting of Rodinia and Miogeocline Formation

In the Proterozoic, about 1000 Ma, all continents were amalgamated into a supercontinent called *Rodinia*. Rifting and drifting of Rodinia started about 750 Ma. On the eastern limit of the rift along the large fragment, *Laurentia*, which included present North America, a continental shelf-slope margin was completely formed by the Early Cambrian (540 Ma). This margin eventually became the site of the present Cordillera. The adjacent ocean basin, *Panthalassa*, was the ancestor of the Pacific Ocean.

540 Ma - 175 Ma: From Passive Margin to Subduction to Collision

The passive intra-plate boundary evolved, first, into an inter-plate convergent margin by the Middle Devonian (390 Ma), and second into a collision margin by the Early Jurassic (175 Ma). At the time of subduction, there were chains of island arcs on the

ancient Pacific plate that became large land masses as the plate moved, piling them together. About 175 Ma, the first of such land masses, the Intermontane Terrane, closed in on the North American Plate but, being too buoyant to be forced downward, it was accreted to the edge of the continent. This started the collision and mountain building period known as the Nevadan orogeny.

By that time, Panthalassa had expanded and all continental fragments had amalgamated again into another supercontinent, *Pangea*, in the opposite hemisphere. Pangea's rifting, about 200 Ma, also contributed to the force driving the strong, cold North American lithosphere to collide with the oceanic plate on the west. In its movement, the North American Plate eventually overrode the trench and the subduction zone.

175 Ma - 55 Ma: Front Ranges and Foreland Basin formation

Collision between the continental margin and the Intermontane Terrane led to the development of the accretionary prism that evolved into the Rocky Mountain Thrust and Fold Belt. The prism was formed by alloctonous rocks brought by the overriding bodies and rocks scraped off the North American plate. Simultaneously, the initial phase of subsidence of the foreland basin began about 160 Ma and is correlated with the change in the style of deformation at the suture zone, from subduction to collision. However, the main event responsible for the formation of the front ranges and the subsidence of the foreland basin had taken place about 85 Ma (Late Cretaceous). This episode is known as the Laramide orogeny, and it started after a second large Terrane, the Insular Terrane, was accreted.[2] The intense compressive force of this collision folded and thrust faulted sedimentary rocks in the east to form the Rockies and the Foothills. Isostatic flexure of the North American lithosphere under the weight of the rocks that form the foreland thrust and belt completed the subsidence of the foreland basin. After the Laramide orogeny, the new continental margin was located about 500 Km oceanward with respect to the original margin.

Between Early Jurassic and Late Paleocene, the main forces acting on the accre-

[2] http://www.mountainnature.com/Geology/platetectonics.htm

tionary prism and adjacent rocks were compressive, especially in the south, and of right-lateral transpression (strike-slip) in the north. Because the collision was oblique, numerous parallel and vertical strike slip faults broke the shield and the sedimentary cover. While being deformed by shear forces, the shield was simultaneously horizontally shortened (about 160 Km) by direct compression from the east, leading to massive thrusts along which new rocks were ploughed and pushed up. This thrust the sedimentary section to great heights.

Recent Tectonics

During the Eocene, displacement between North America and the accreted terranes slowed down and finally ceased about 42 Ma. At this time, the deformation style changed, becoming primarily transtensional in the north and extensional in the south. As a consequence, subsidence of the foreland basin was followed by isostatic uplift and erosion.

Today, the western margin of the North American Plate features convergent and transform plate boundaries. From south to north, the boundary is first dominated by transform faults, as the San Andreas Fault; then it is convergent in the Cascadian subduction zone, west of which is the Juan de Fuca Plate. Moving north, the boundary again becomes a transform margin at the latitudes of the Queen Charlotte fault, west of which the Pacific Plate moves northward to descend below Alaska, along the Aleutian subduction zone. On-going tectonic activity manifests in earthquakes and volcanism along these boundaries (figure 4-4).

4.2.1 Regional Structures

Under such a complex stress environment, rocks were effectively shortened primarily by two independent mechanisms. In some cases, rocks faulted and stacked on top of each other to form structures in which the reservoir rock today is faulted repeatedly (fault bend folds). In other cases, horizontal compression created tight folds associated with thrust fault detachment (Newson, 2001). Figure 4-5 shows figures

of the geometry of these types of structures. In addition to classical compressional structures, the high topographic elevations at Paleocene time, together with more recent periods of glaciations, facilitated the formation of gravity sliding structures (Wennekers, 2007a).

Plays in the Foothills are generally part of a thin-skinned thrust system in which a basal thrust (décollement) branches into more steeply dipping thrusts to form imbricate fans (Newson, 2001; McMechan, 1999). In the basin, sediments came from the erosion of igneous-metamorphic rocks of the Canadian shield on the east, but in post-Triassic time a second source of sediments emerged on the west from the uplifted rocks (Wennekers, 2007a). Consequently, older strata in the sedimentary cover (Cambrian to Triassic) comprises primarily carbonates or sandstones, whereas the younger strata (Late Jurassic to Tertiary) comprises thick sandstone, siltstone, shale, and coal units separated by marine shale units. These shale units form multiple levels of detachment, and in between, a series of tectonic wedges have been interpreted (McMechan, 1999). Depending on the competence of the sandstones separated by these detachments, folds and faults develop, sometimes giving place to triangle zones.

In the structured belt, rollovers/leading edges of thrusts and folds are the main drilling targets. In these structures, reservoir rock is often fractured, with curvatures and relative age determining the availability of open fractures. In typical thrust-belt anticlines, because of the way the fold develops, the reservoir rock is generally fractured in multiple assemblages related to the structural position within the fold (figure 4-6). Strike-slip faults parallel with structure trends and at angles to them also add fractures and enhance reservoir quality (Wennekers, 2007b). Predicting the occurrence of such fractures is considered a difficult task in structural geology (Wennekers, 2007a). The role of fractures is also difficult to assess. In general, rocks with moderate to poor matrix become good producers, and fields in which the matrix is good may be negatively affected by fractures (Newson, 2001).

4.3 Stratigraphy and Petrophysics of the Lynx Field

The main reservoir unit in the Lynx field is the Cadotte Member of the Peace River Formation. Cadotte is a tight-gas sandstone of early Cretaceous age, at a depth of 3 Km (1.9 s). Mud logs and FTIR[3] analyses of cores show a composition dominated by a quartz pebble conglomerate with abundant chert (20-30%) and minor clays, carbonates, and siderite. Cadotte was deposited in a marine shoreline environment and exhibits an overall coarsening upward in gamma ray logs and cores, from fine grained to conglomerates, indicating a local regressive pulse. It is in this conglomerate section that Cadotte is believed to be most prolific (Canadian Discovery Digest, 2004).

In the overburden, immediately above Cadotte, lies uncomformably the Paddy Member whose lithology varies greatly in the area, including clastics, coals, and carbonates (figure 4-7). The contact Paddy-Cadotte is an erosional surface indicative of a transgression or sea-level raise (Sen et al., 2007). Paddy is overlain by the shales of the Shaftesbury Formation. Overlying this thick shale succession (more than 200 m), is the Dunvegan Formation, another prospective sandstone. The formation below Cadotte, Harmon, consists of interbedded silts and shales (Canadian Discovery Digest, 2004). Below Harmon is the Falher Formation consisting of coal bearing sands and shales. Figure 4-8 shows that the transition Paddy-Cadotte is easily identified in gamma ray logs. There, Cadotte's gamma ray reading is about 30° API, typical of its conglomerate or very clean sand face. The lithological distinction between Cadotte and Harmon is less sharp in the gamma ray logs due to the gradual decrease in grain size within Cadotte. Cadotte's thickness across the area ranges from 20 to 40 m with the shallower 15 to 20 m usually related to the coarse upper shore face (Canadian Discovery Digest, 2004).

VeritasDGC did a petrophysical analysis of Cadotte using well and mud logs from 8 wells (6-18, 6-9, 10-22, 10-28, 9-16, 9-17, 11-7 and 3-19) and core data from 2 wells (6-18 and 6-9; see figure 4-3 for wells' location). Figure 4-10 shows the distribution of P-wave log velocities at the Cadotte's depth interval for 5 of these wells. Cadotte

[3]FTIR: Fourier Transform Infrarred spectroscopy

is a fast formation with P-wave velocities varying in a wide range, from well to well, between 4000 and 6600 m/s. Such a range may be related to composition or pore geometry variability due, for example, to presence of microcracks (personal communication with Tad Smith- VeritasDGC). Paddy, on the other hand, is a soft low velocity formation. As observed in the plot on the right of figure 4-10, there is a large acoustic impedance contrast between Paddy and Cadotte. In this figure, acoustic impedance log for each well was computed from density and velocity logs and shifted to match Cadotte's top depth in all wells. In general, Cadotte's impedance is about 30% greater than the background shales (Shaftesbury).

Figure 4-9 shows that Cadotte's sandstone is tightly cemented with matrix porosities below 10%. Permeability is estimated in average around 0.1 md. The lowest water saturations observed are 20%, and possibly lower, due to the high content of chert that can cause overestimations (personal communication with Tad Smith- VeritasDGC). Such low saturations are typical of tight-gas sandstones.

Lynx's plays are considered both structural and stratigraphic. As mentioned, Cadotte's conglomerates (upper shore lithofacies) are related to productivity but the structural position of this face seems to control its local suitability as a reservoir (Canadian Discovery Digest, 2004).

4.4 Seismic Structural Interpretation

More locally, the Lynx field is located in what is known as the Kakwa area. This area is located to the east of the Muskeg Thrust which is the eastern limit of significant deformation (Sen et al., 2007). The Muskeg Thrust is a continuous west verging thrust in the Alberta Foothills. East of this thrust, folds and faults are laterally discontinuous (McMechan, 1999).

In the study area, the structural front manifests as a mixture of folds and thrusts primarily west-verging. As in other areas of the Foothills, the main driver of the deep structures (Paleozoic-Triassic carbonates) is thrust faulting. In the Upper Cretaceous formations, lithology changes to clastic systems dominated by sandstones and shales.

In here, commonly, folding happens. The variations in style are due to the large mechanical differences between sections (personal communication with Dean Sinnot and Mark Skoko, ConocoPhilllips).

A series of imbricate thrust faults have been proposed to explain Cadotte's elevation changes across the area, which deepens towards the northeast (figure 4-18). In figure 4-18 one west verging NW-SE trending thrust is located south of well 11-07. Two other thrusts, or alternatively box folds without thrust faults, could be interpreted to be located between wells 6-18 and 9-17, and at the location of well 5-21 (Canadian Discovery Digest, 2004).

Figure 4-11 shows seismic interpreted horizons corresponding to the top of the main formations over an unmigrated seismic section from the survey area. Figures 4-12, 4-13, 4-14 and 4-15 depict maps of the interpreted horizons. These interpretations were provided by ConocoPhillips. In general, NW-SE fold structures dominate the southwest area. Some reverse faults are interpreted parallel to the trend of the folds as shown in figures 4-16 and 4-17. Lynx's faults are believed to be purely reverse without a strike-slip component, at least at a local scale. Shortening along strike happens mostly through faults en èchelon (personal communication with Mark Skoko, ConocoPhillips).

The rock matrix at the main reservoirs in Lynx (Cadotte and Dunvegan) is of variable quality and, in general, fractures are believed to act as main fluid conduits because rocks are tight-gas sandstones, of extremely poor porosity and permeability. In principle this is the reason why structure is believed to be so important (to provide the fractures), however performance has been somewhat random. Flush production is very common with some wells depleting very fast, e.g. in one year the production rate typically decreases 3 to 4 times (pers. comm. Dean Sinnot- ConocoPhillips). This is in part the motivation to look for a structural model that consistently predicts the fractures.

4.5 Evidence of Fractures

Gas production in Lynx is believed to be largely controlled by fractures. Evidence of fractures in the region comes from outcrops and well data. VeritasDGC observed fractures in cores and thin sections from two wells (6-18 and 6-9), and interpreted them indirectly from resistivity and image logs in 5 wells (10-22, 11-7, 6-9, 3-19, and 6-18) and a dipole sonic log at well 11-07.

In Lynx, multiple fracture sets of variable scales and potentially different orientations are observed. VeritasDGC classifies them into three categories: large scale, small scale and micro scale. The definition of large scale fractures depends on their identification in image logs and possible separation of shallow and deep resistivity curves, which is typically considered an indication of high permeability. Large fractures are not generally seen in cores although rubble zones might be associated to these types of fractures or fault zones.

These fractures were not observed in the overburden but are present at Cadotte and formations below. For instance, figure 4-19 shows a section of the Cadotte level and below in the image log of well 6-18 where several large fractures are identified. The resistivity logs exhibit separation of the curves at the corresponding depths. Separation of resistivity curves was also observed at other wells and in the Falher zone (Sen et al., 2007).

Fracture densities estimated in the reservoir from images logs are indicated in table 4.1. Breakouts were also observed in image logs. The stress information obtained from breakouts is discussed at the end of this chapter.

Considering Lynx's velocity anisotropy, the dipole sonic log at well 11-07 agrees with image logs in that the overburden is not fractured with the exception of the Dunvegan formation where shear wave splitting is observed (figure 4-22). Anisotropy at Dunvegan is estimated around 10% while for Cadotte and below, anisotropy was somewhat lower, around 300 m/s or 6-9%. The Cadotte in this well shows fractures in the image log and separation of long and short resistivity curves (pers. comm. Tad Smith VeritasDGC). The formation below Cadotte, Harmon-Falher, shows great

anisotropy, sometimes as high as 15%.

Small scale fractures are believed to be natural although they may not contribute to flow. They are not necessarily seen in image logs but are identifiable at the core scale. A photograph of the core taken in well 6-9 is shown in figure 4-20 to exemplify the scale of these fractures. Stylolites and cementation are frequent in Lynx's core samples.

Cracks at the micro scale are not observable in cores or resolved by image logs. They are identified as discontinuities between grains observed in thin sections and SEM images.[4] Figure 4-21 shows an example from well 6-9. Cracks observed in Lynx's thin sections and SEM images are randomly distributed. The importance of microcracks rises when trying to explain the large variability of compressional velocities measured at Cadotte. Initially, velocity variations are ascribed to variations in porosity or composition, but in Lynx no correlation was found between P-wave velocity and porosity (either from logs or ultrasonic measurements in cores; pers. comm. with Tad Smith from VeritasDGC). Other possible causes could be differences in the relative angle of the wells with respect to fracturing or variations in the degree of fracturing at Cadotte. Modeling Cadotte as a pure quartz rock with 6% matrix porosity and 1% crack porosity, and assuming an effective medium theory (Kuster-Toksöz), VeritasDGC reproduced the velocity differences. Then, computing the difference at each well between a non-cracked modeled velocity and the real log, they obtained a potential indicator of crack concentration. Correlation between such an indicator and production at wells was good (table 4.1).

AVO feasibility studies carried out by ConocoPhillips suggest that although around 10% of anisotropy (HTI) could give rise to significant changes in AVO gradient, bed thickness needs to be at least 25 m to be resolved. Cadotte's thickness may prevent reliable fracture detection with an AVO technique (pers. comm. with Ethan Nowak-ConocoPhillips). Nevertheless, the final AVOA study detected an anomaly to the southwest of the survey area, approximately around well 9-17 (pers. comm. with Doug Foster- ConocoPhillips). Sen et al. (2007) show that the AVOA response at

[4]Scanning Electron Microscope

the top of the Falher Formation is unusual because of transmission effects through the shallower anisotropic Cadotte and possibly due to the presence of multiple non orthogonal vertical fractures.

4.6 Production History

In naturally fractured reservoirs low porosities are unrelated to production since permeability depends on the degree of fracturing and in some instances fracturing is even more intense in intervals of low porosities (Aguilera, 1998). There is no indication that Cadotte's thickness is related to low productivity or lack of fractures. On the contrary, outcrop and production data have historically shown that joint and fracture spacing is proportional to bed thickness in sedimentary rocks (Aguilera, 1998; Narr and Suppe, 1991).

In fractured reservoirs, productivity is expected to be maximized according to well placement relative to fractures. For instance, Nelson (2001) ranked optimum drilling paths in typical fractured asymmetric folds according to the possibility of intercepting the major number of fractures (figure 4-23). It is suggested that directional wells in flank positions (backlimb, forelimb) can produce better oil and gas rates than in the hinge.

In Lynx, the lack of correlation between high productivity and position drilled on the structure is puzzling. Successful well placement relative to structure is complicated by the fact that the reservoir thickness for most of the area is below seismic resolution and impedance contrast is weak in many areas. Notwithstanding, the interpreted structures have been drilled at their crestal position (well 9-17), on the frontlimb (wells 6-18 and 6-9), backside (wells 9-16, 3-19, 11-07 and 5-21) and on the low curvature side (wells 10-28 and 10-22).

In terms of initial production, well 6-18 is the most successful (IP=12.12 $mmcf/d$; see table 4.1). This well produced in a 2-year period about 5 bcf of gas (Canadian Discovery Digest, 2004). Despite its trajectory being similar to well 6-18, well 6-9 did not do so well (IP=0.35 $mmcf/d$). According to the most accepted structural

model of the area, well 6-18 lies close to a structural rollover where fracturing would typically enhance reservoir quality (Canadian Discovery Digest, 2004). Such assertion is partly supported by the observation of fractures in cores and image logs in well 6-18 as described in section 4.5.

Wells 9-16, 9-17 and 3-19 are good producers with IP of 10.85, 9.75 and 3.32 $mmcf/d$ respectively, but well 11-07 also aiming to cross fractures in the backlimb, produced minor gas (IP=0.14 $mmcf/d$). Well 10-22 had geomechanical problems and became a minor gas producer with an IP of 0.2 $mmcf/d$. It currently produces from Dunvegan. Well 5-21 was abandoned since it did not find Cadotte.

10-28 was one of the first wells, drilled about 20 years ago. Although it crosses Cadotte, it produces only from Dunvegan. It is believed to produce from fractures and matrix (pers. comm. with Dean Sinnot- ConocoPhillips). It has produced 20 bcf of gas and today's rate is still 1 $mmcf/d$ (Canadian Discovery Digest, 2004, average rate of 11.4 $mmcf/d$ until October 2004). Under the assumption that natural fractures in this field are primarily vertical, vertical wells do not stand the same probability of success than directional wells; however 10-28 has been a successful producer from Dunvegan.

Production from fractured reservoirs is not only optimized by well position relative to structure. The completion method, degree of mineralization of the fractures, and current stress regime which defines the aperture of fractures are also key factors to consider. Particularly, we believe that stress controls the distribution of open large scale fractures or joints that have the greatest impact in enhancing fluid flow. This thesis intends to determine orientation distribution and spacing of large fractures in Lynx. It contributes to the understanding of the variation of stress across this area and hopes to increase the probability of success of future prospects.

4.7 In-Situ and Regional Stress

The general assumption that one principal stress is vertical and the other two are horizontal is valid in the WCSB where topography is relatively low. Even at the

edge of the Foothills, where some relief may exist, the deflection of stress axes will be minimal below a few hundred meters (Bell et al., 1994).

In recent years, there has been an increased interest in mapping in-situ stress in the WCSB and particularly in the Alberta Province. Such an interest is mainly related to experimental evidence that minimum in-situ stress magnitude could be a meaningful indicator of coal bed methane permeability (Bell, 2006, e.g). Knowledge of in-situ stress in coal beds is also desirable to better plan and control activities of CO_2 sequestration either for environmental benefit or to enhance methane recovery (Hawkes et al., 2005).

As a consequence, a great number of stress measurements exist today in the basin. Contemporary stress orientation has been determined primarily through well breakouts and less often using other techniques such as overcoring, induced fractures and anelastic strain recovery. Horizontal in-situ stress magnitudes, on the other hand, are generally more difficult to measure and therefore data are less available. Only overcoring, micro and mini fracture tests are considered accurate methods to obtain minimum stress magnitude. However, several methods to estimate it from leak-off tests and fracture breakdown pressures have been applied in the WCSB increasing considerably the dataset of stress magnitudes in this area.

Maximum Horizontal Stress Orientation

The first compilation of stress data was presented by Bell and Babcock (1986). Most of the orientation estimations in this compilation are derived from well breakouts (154 locations). Stress orientation in another 7 locations was derived from other methods. Stress magnitudes ($SHmax$, $Shmin$ and Sv) were obtained in 9 locations. The majority of the estimations in the 1986 dataset has been incorporated, verified and ranked in the most recent version of the World Stress Map (WSM) (Reinecker et al., 2005). $SHmax$ azimuth derived from focal mechanisms of few earthquakes are added in the WSM database. In 1994, a second compilation of stress data was published (Bell et al., 1994) adding 21 stress orientation data points from well breakouts and increasing the locations with control of stress magnitude to 62. More recently, Bell and

Bachu (2003) reported 10 new breakout locations. The additional stress orientation information, not included in the WSM database, is integrated and mapped in figure 4-24 by means of the software CASMI provided by the World Stress Map Project (Reinecker et al., 2005). Additional data points are reproduced in table 4.2.

As illustrated in figure 4-24, the NE-SW trend of the maximum horizontal stress, perpendicular to the Mesozoic deformation front, is very persistent. Breakout data also indicate that there is little variation of this orientation with depth, rock type or age (Bell et al., 1994). Open tectonic fractures in Lynx are therefore expected to bear this NE-SW trend, in other words, fractures sub-parallel to $SHmax$ are expected to be more resistant to closure. In fact, dominant fracture axis in Cretaceous coal seams in Alberta measured in shallow coal mines gives orientation aligned within 20 degrees of the trajectories of $SHmax$ (Bell and Bachu, 2003). In other places of the Foothills, however, exceptions of this trend have been observed with open fractures running parallel to fold axes (NW-SE) (Bell et al., 1994).

In the Lynx field, breakouts were observed in image logs at wells 3-19, 10-22, 6-09, 6-18, and 11-07, indicating that the horizontal stresses are unequal also in this zone of the Foothills. The orientation of $SHmax$, inferred from well breakouts is consistent at NE-SW and NNE-SSW (figure 4-25). Maximum horizontal stress orientation from the wells in Lynx are also included in table 4.2 and in figure 4-24.

Vertical Stress

Numerous density logs in the area have been analyzed and there is a good agreement in that the gradient of vertical stress for Cretaceous rocks varies between 23-24.7 kPa/m in the Foothills and is around 20.1 kPa/m closer to the Canadian shield to the northeast (Bell and Bachu, 2003; Hawkes et al., 2005). Figure 4-26 shows the calculation of vertical stress from the density log of a particular well in Lynx (well 9-16). Extrapolation of the density trend to the surface is necessary because these logs are rarely run in the whole well section. Consequently, estimations of vertical stress will vary depending on the way this extrapolation is done.

At Cadotte's depth, Sv gradient in well 9-16 is about 24.3 kPa/m. Sv magnitude

at Cadotte in this well varies between 64.7 and 67.9 MPa depending on the choice of density at the surface. Comparing the vertical stress estimations of 5 wells in Lynx (table 4.3), the average vertical stress gradient is 24 kPa/m- similar to the rest of the Foothills and close to the lithostatic gradient (1 psi/ft). Sv magnitude at Cadotte varies among Lynx's wells between 64.7 and 83 MPa.

Minimum and Maximum Stress Magnitudes

Few measurements of fracture closure pressure exists in the area but they have been integrated with adjusted leak-off and fracture breakdown stress tests to provide estimations of $Shmin$. Comparisons with the vertical stress show that the minimum in-situ stress is horizontal for most of the WCSB (Bell, 2006). Exceptions are reported at shallow depths (above 600 m), for example in northeastern Alberta, and in the Wapiti area in the Foothills (southeast of Lynx) where Sv is the smallest stress or is very close to $Shmin$ (Bell et al., 1994).

Based on the premise that $Shmin$ is the minimum stress in central and southern Alberta, comprehensive maps of $Shmin$ gradient and magnitude, at specific formation depths, have been compiled. Bell and Bachu (2003) found gradients of $Shmin$ between 15 and 20 kPa/m for Upper Cretaceous-Tertiary rocks, and similar (13-20 kPa/m) for a Lower Cretaceous formation. Bell (2006) mapped $Shmin$ for the Upper Cretaceous 'Bell River' formation where gradient varies between 12 and 22 kPa/m. Hawkes et al. (2005) included stress information inferred in acid-gas injection sites in Alberta and obtained average $Shmin$ gradients of 17 kPa/m at shallow depths and about 13 kPa/m below 1000 m.

The definition of a unique stress regime in WCSB is difficult given the lack of maximum horizontal stress measurements. Based on few direct measurements in shallow sites and rough estimations from hydraulic fracturing tests, Bell and Babcock (1986) distinguish three regimes according to depth: a thrust regime with $SHmax$ the greatest stress and Sv the minimum stress above 350 m; a strike slip regime with Sv the intermediate stress between 350 and 2500 m; and a normal fault regime with Sv the greatest stress below 2500 m. The same paper gives an example of a

Falher sandstone around 2050 m (in a location southeast of Lynx), that shows a ratio $SHmax/Shmin$ of 1.6 with $Shmin$ about 40 MPa, Sv about 51 MPa, and pore pressure of 15.2 MPa. In general, a $SHmax/Shmin$ ratio between 1.3 and 1.6 is suggested above 2500 m or so. Bell et al. (1994) prefer to divide the regime type according to regions in the WCSB and assign a strike slip regime to the deep western flank (close to Lynx), and a normal fault regime to the east basin in Saskatchewan. Hawkes et al. (2005) states that the intermediate stress in the basin is $SHmax$ and the difference between $Shmin$ and Sv is in average 30% at depth.

Although most of the fields in the Foothills share similar tectonic origin and the forces responsible for the formation of major structures were of regional scale, extrapolating the studies described above to infer in-situ stress in other areas has to be carried out carefully. There are practically no data points of minimum stress gradient west of the Laramide deformation front and therefore the validity of the reported gradients at the exact location of Lynx (practically on that edge), is questionable. Local differences are bound to exist primarily because of overburden changes along and across the belt and basin, i.e., reservoir depth changes. Perturbation of the regional stress field is also likely to occur in fields undergoing production where pressure conditions are changing.

No measurement or estimation of horizontal stress magnitudes has been published for the Lynx field. However, the high vertical stress gradient at Cadotte's depth obtained from Lynx's well logs, suggests that also in this field Sv should be the greatest principal stress, therefore $SHmax$ is likely to be the intermediate stress. The most important implication of the stress regime for the fracture characterization discussed in next chapter is that giving the strong indication that $Shmin$ is the minimum stress at reservoir depths in Lynx, fractures are expected to be vertical and therefore comply with this constraint imposed by the fracture scattering methods applied here. Only at shallow depths of the WCSB, where the minimum stress may be vertical, fractures would be horizontal.

Paleostresses

With the emplacement of the alloctonon in the west, the maximum stress in the Rocky Mountains, Foothills, and probably in the basin, was horizontal, parallel to bedding, at the time of collision, i.e., thrust faulting stress regime (Newson, 2001). Since the topography was at least 3 miles higher than today, overburden pressures are believed to have been also higher. This is supported by anomalously high velocities of shale sections in some areas of the Foothills in comparison to their counterparts in the Plains which give rise to overpressured zones (Wennekers, 2007a). These zones are interpreted as areas where the column has not had enough time to structurally relax.

Whether stresses have changed in the geological history of the basin is addressed in several papers. Bell and Babcock (1986) note the similarity between the principal stress orientations in the basin and the direction of overthrust faulting in the Foothills and Rocky Mountains, and interpret that $SHmax$ has been NE-SW for at least 100 million years, since the Laramide orogeny. Regarding the lateral variations of the vertical and minimum stresses observed, Bell and Bachu (2003) argue that these are a reflection of the level of tectonic stress caused by past orogenic processes. Vertical stress gradient and magnitude decrease away from the edge of the Foothills to the east, consistent with the model of the foreland basin loading from the west. $Shmin$ stress gradient exhibits some lineaments parallel to the Rocky Mountain front.

4.8 Summary

The Lynx field is located in the foothills of the Canadian Rocky Mountains, a classic foreland fold-thrust belt. Tectonics have reshaped this area extensively. The Laramide orogeny in the late Mesozoic was defining in the formation of the Front Ranges and the Foothills. Such a complex tectonic environment gave rise to fold and thrust structures like imbricate thrusts, detachment folds and duplexes. In Lynx, structures are primarily of the fault-bend-fold type. Folds and reverse faults trending NW-SE have been interpreted to the southwest of the area of study. In these folds,

intense fracturing develops as evidenced in cores and well logs. Structures in Lynx seem to be fractured at different scales. However, prediction of the fractured areas to optimize production and development of this field has been difficult. Well breakouts are also observed in Lynx's wells. Inferred orientation of $SHmax$ coincides with regional in-situ stress estimations collected across western Canada. High vertical stress gradients obtained from density logs in Lynx suggest that Sv is the largest principal stress, in agreement with other areas of the Foothills. As a consequence, open fractures are expected to be vertical at reservoir depths and preferentially oriented NE-SW, that is, parallel to $SHmax$.

WELL	IP $[mmcf/d]$	FD background [#/m]	FD enhanced [#/m]	FD productive [#/m]	Crack indicator [%]
6-18	12.12	0.17	0.19	0.23	NA
9-17	10.85	NA	NA	NA	13.9
9-16	9.75	NA	NA	NA	11.8
3-19	3.32	1.17	none	0.32	18.2
6-9	0.35	0.7	0.04	0.11	13.7
10-22	0.2	2.28	1.4	0.14	NA
11-7	0.14	2.11	0.29	0.18	5.7

Table 4.1: Initial Production (IP), density of fractures interpreted in image logs (FD) and indicator of crack intensity obtained by VeritasDGC in Lynx's wells. Classification of fractures as productive enhanced or background follows an internal criteria; loosely speaking, productive refers to fractures coincident with gas shows and/or drilling mud losses; enhanced refers to fractures aligned with regional maximum stress and therefore prone to be open; and background corresponds to fractures at high angles to the maximum stress direction, hence, prone to closure (pers. comm. Ethan Nowak- ConocoPhillips).

WELL/Location	LON [deg.]	LAT [deg.]	$SHmax$ Azimuth [deg.]	Type	Source
01-04-05-9W2	-101.151	49.351	36.2	BO	[1]
09-13-05-13W2	-103.622	49.388	37.4	BO	[1]
13-15-05-25W2	-105.298	49.391	136.5	BO	[1]
C3-05-066-10W2	-103.327	49.442	121	BO	[1]
10-11-10-17W4	-112.204	9.81	154.5	BO	[1]
13-25-10-16W4	-112.057	49.857	158.4	BO	[1]
08-02-11-16W4	-112.078	49.879	145.5	BO	[1]
09-01-12-29W4	-113.83	49.97	146.6	BO	[1]
14-36-12-18W4	-112.339	50.047	167.3	BO	[1]
07-35-18-21W4	-112.786	50.563	178.23	BO	[1]
06-11-19-3W4	-110.391	50.593	152.8	BO	[1]
16-10-21-3W4	-110.331	50.774	165.6	BO	[1]
8-11-36-21W4	-112.888	52.077	153.7	BO	[1]
06-25-40-14W5	-115.888	52.47	157.4	BO	[1]
06-36-49-23W5	-117.235	53.267	137.1	BO	[1]
14-22-50-11W4	-111.532	53.332	146.4	BO	[1]
11-28-55-6W4	-110.838	53.783	146.3	BO	[1]
14-09-58-24W4	-113.515	54.005	148.3	BO	[1]
06-13-63-8W4	-110.79	54.449	141.8	BO	[1]
06-27-65-5W4	-110.676	54.653	144.8	BO	[1]
2B-11-67-8W6	-119.097	54.779	134	BO	[1]
2B-14-67-8W6	-119.097	54.797	131	BO	[1]
10A-03-73-23W6	-110.835	55.296	131.1	BO	[1]
13-26-80-22W4	-113.343	55.969	139.5	BO	[1]
07-24-83-7W4	-110.989	56.213	123.5	BO	[1]
10-23-83-7W4	-110.989	56.213	150	BO	[1]
07-18-109-7W6	-119.154	58.463	13	BO	[1]
B-45-A-94-P-14	-121.059	59.785	149	BO	[1]
CANMORE	-115.351	51.072	60.5	OC	[2]
KIPP MINE	-112.977	49.768	80	OC	[2]
3-8-12-12W2	-103.611	49.977	70.5	HF	[1]
2B-11-67-8W6	-103.383	54.779	37.7	SEVERAL	[1]
C9-12-6-11W2	-103.383	49.491	59	ANEL.STRAIN	[1]
10-28-28-24W3	-109.316	51.426	52	MICROSEIS	[1]
12-21-34-28W4	-113.923	51.935	48	BO	[3]
16-23-62-20W5	-116.879	54.383	57.1	BO	[3]
06-08-29-24W4	-113.348	51.465	40.2	BO	[3]
02-29-20-20W4	-112.737	50.719	55.2	BO	[3]
07-26-21-11W4	-111.421	50.81	40.1	BO	[3]
05-22-59-04W4	-110.527	54.113	42	BO	[3]
02-29-59-22W5	-117.26	54.124	45.2	BO	[3]
06-28-68-24W5	-117.601	54.914	26.8	BO	[3]
06-22-69-06W6	-118.83	54.987	33.4	BO	[3]
04-36-69-11W5	-115.549	55.012	26.4	BO	[3]
11-07-61-9W6	-119.346	54.259	25	BO	Lynx-COP
6-18-61-9W6	-119.341	54.274	45	BO	Lynx-COP
6-09-61-9W6	-119.291	54.259	30	BO	Lynx-COP
3-19-61-9W6	-119.342	54.285	10	BO	Lynx-COP
10-22-61-9W6	-119.259	54.298	28	BO	Lynx-COP

Table 4.2: Maximum horizontal stress orientation in western Canada. Stress information not incorporated in the World Stress Map (Reinecker et al., 2005). [1]: Bell et al. (1994); [2]: Bell and Babcock (1986); [3]: Bell and Bachu (2003). Well identification follows the Alberta Township System. BO: breakouts; HF: hydraulic fracture; OC: overcoring.

WELL	Sv gradient $[kPa/m]$	Sv [MPa]
3-19	24.3 - 25	73.08 - 74.91
9-16	23.4 - 24.5	64.7 - 67.9
9-17	23.3 - 24.5	65.8 - 69.4
10-22	24 - 24.9	80 - 83
10-28	23 - 24.3	77.8 - 82.1

Table 4.3: Vertical stress in the Lynx Field. Minimum and maximum values correspond to limiting density gradients used to extrapolate the density logs to the surface.

Figure 4-1: Location of the Lynx field (from: http://atlas.nrcan.gc.ca/).

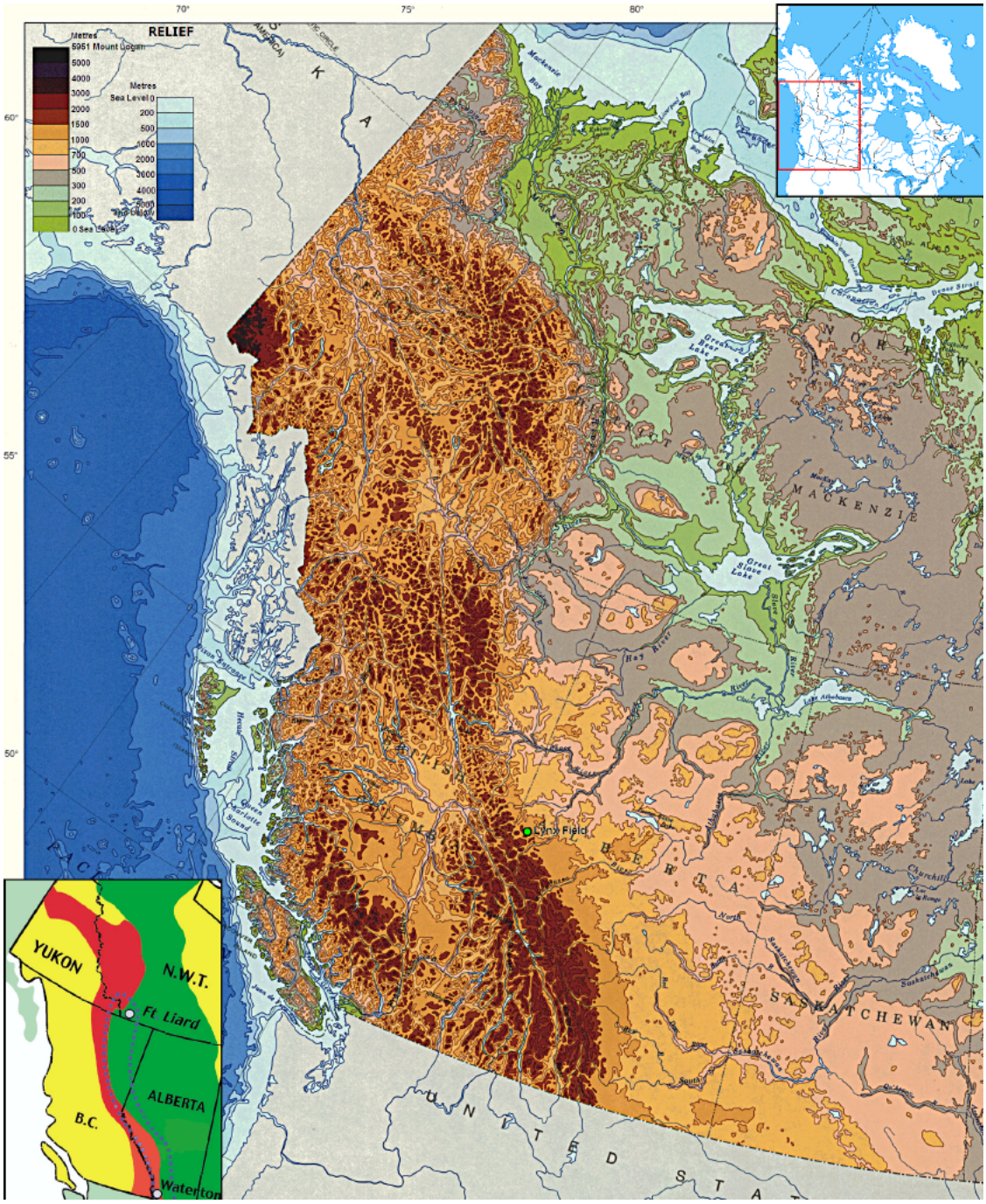

Figure 4-2: Relief map of western Canada (from http://atlas.nrcan.gc.ca/). The Lynx field is in the Foothills of the Canadian Rocky Mountains. In the inset figure, Foothills' area is enclosed by blue dots, the Rocky Mountain Fold and Thrust Belt is in red and the WCSB is in green. Inset figure is modified from Newson (2001).

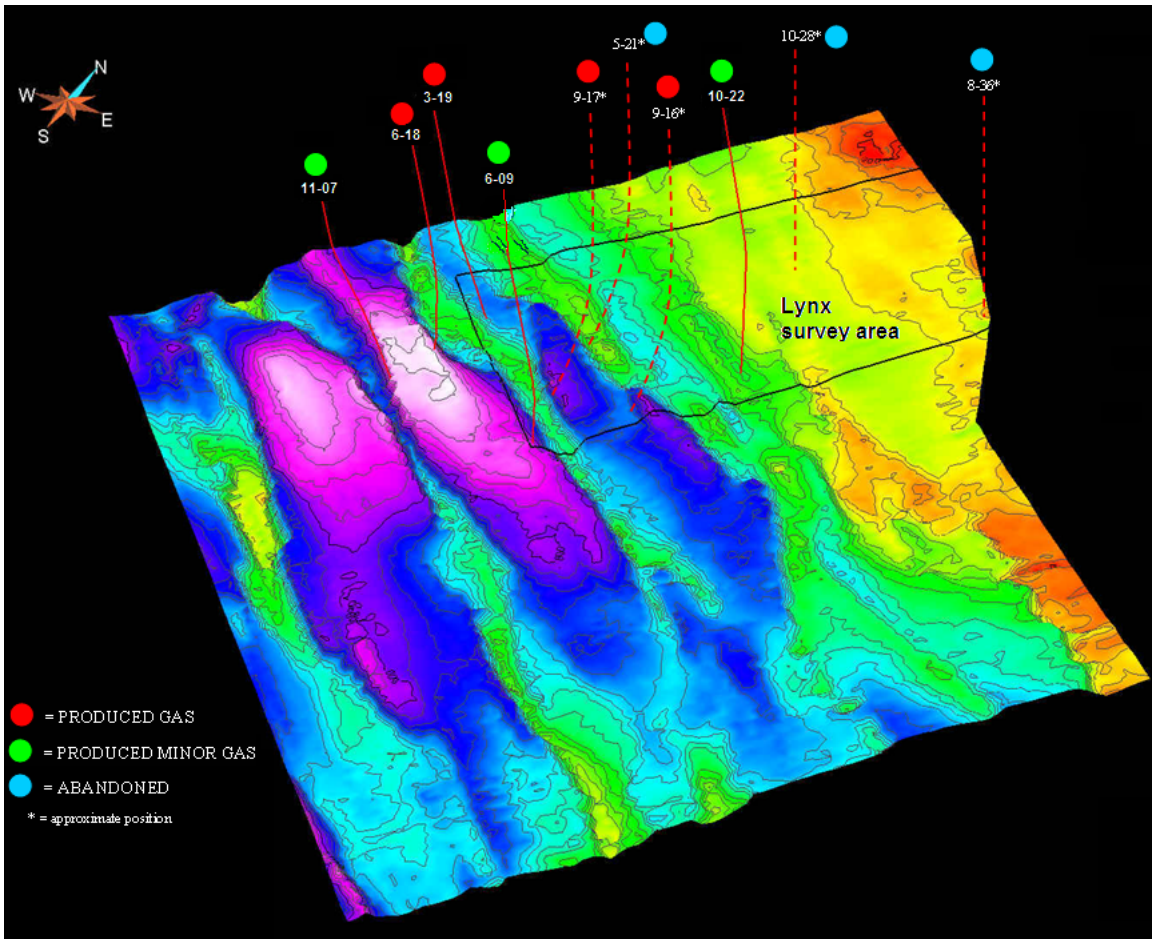

Figure 4-3: Structural time map of main reservoir in Lynx and well locations referred in the text. Courtesy of Tad Smith (VeritasDGC).

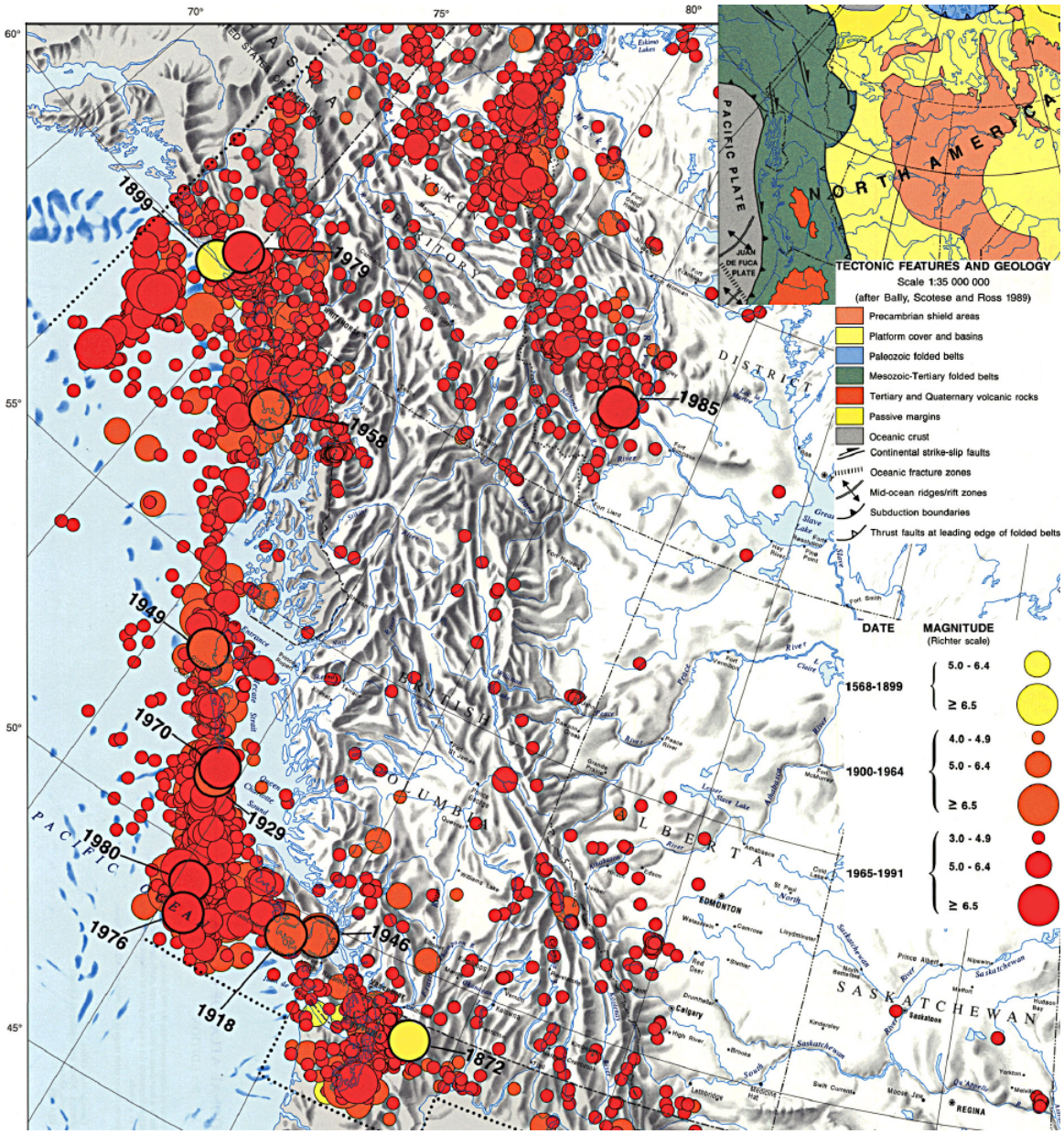

Figure 4-4: Western Canada seismicity (from http://atlas.nrcan.gc.ca/). In the inset figure, tectonic and geology of the North American plate.

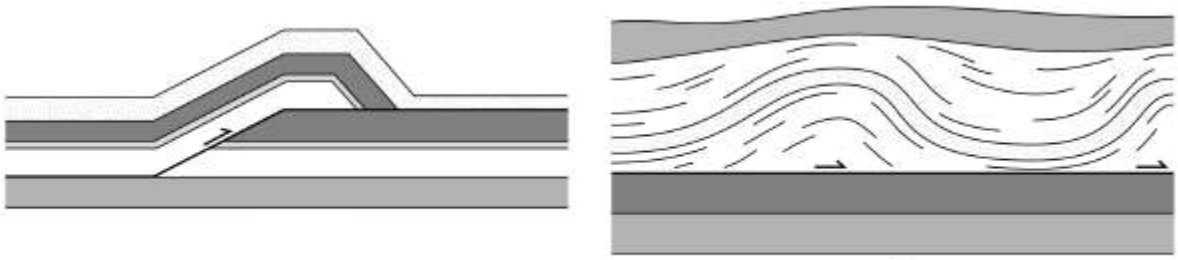

Figure 4-5: Idealized fault-bend-fold structure (left) and detachment fold (right). After van der Pluijm and Marshak (2004).

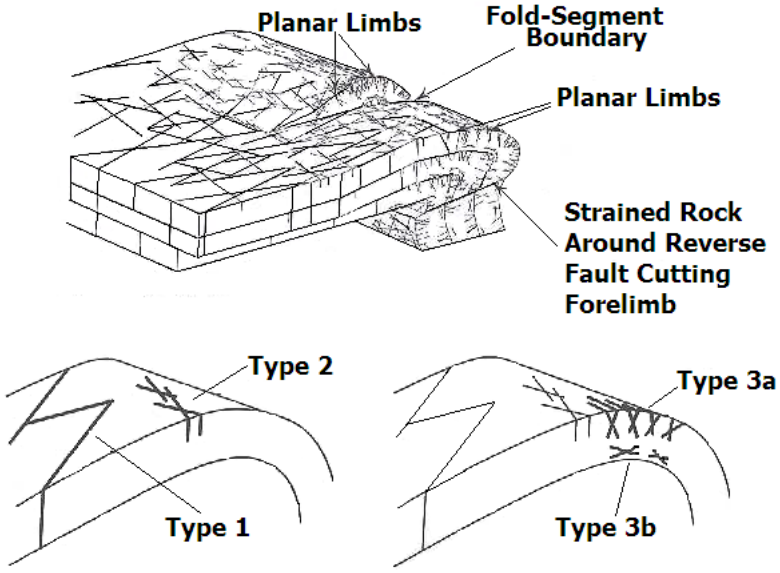

Figure 4-6: Typical truncation anticline (top) and diagram of fold-related fracture patterns (bottom). After Lewis and Couples (1993). Types 1 and 2 are normal to layering. Type 3a is associated to layer elongation. Type 3b is associated to layer contraction.

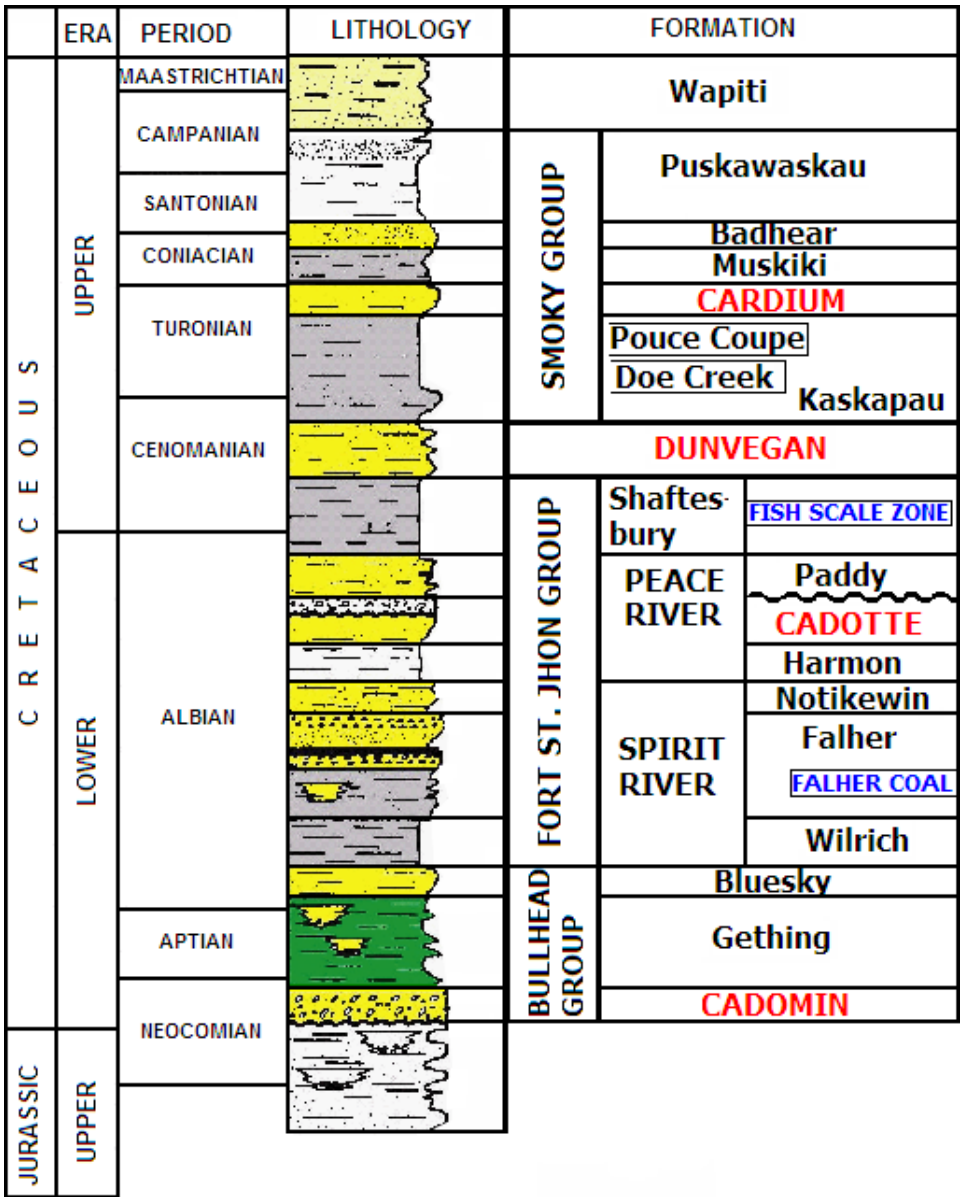

Figure 4-7: Stratigraphic column in the Lynx area. Modified from Canadian Discovery Digest (2004).

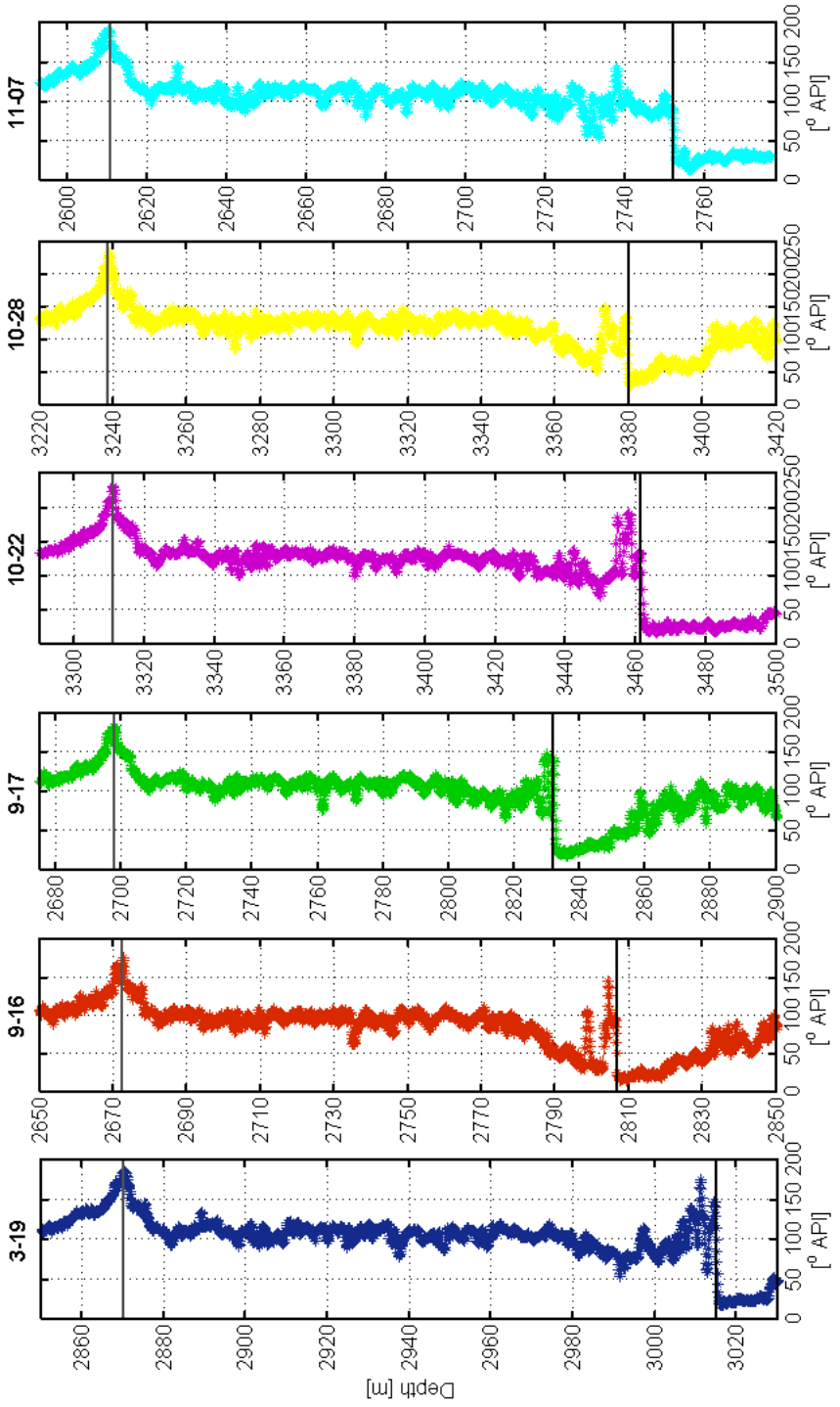

Figure 4-8: Gamma ray log of wells 3-19 (blue), 9-16 (red), 9-17 (green), 10-22 (yellow), 10-28 (purple), and 11-07 (cyan). Gamma ray increases at the shaly "Base of Fish Scales" (gray line), which is a regional marker. Top of Cadotte is identified as a decrease in gamma ray reading (black line). Cadotte's thickness varies from well to well.

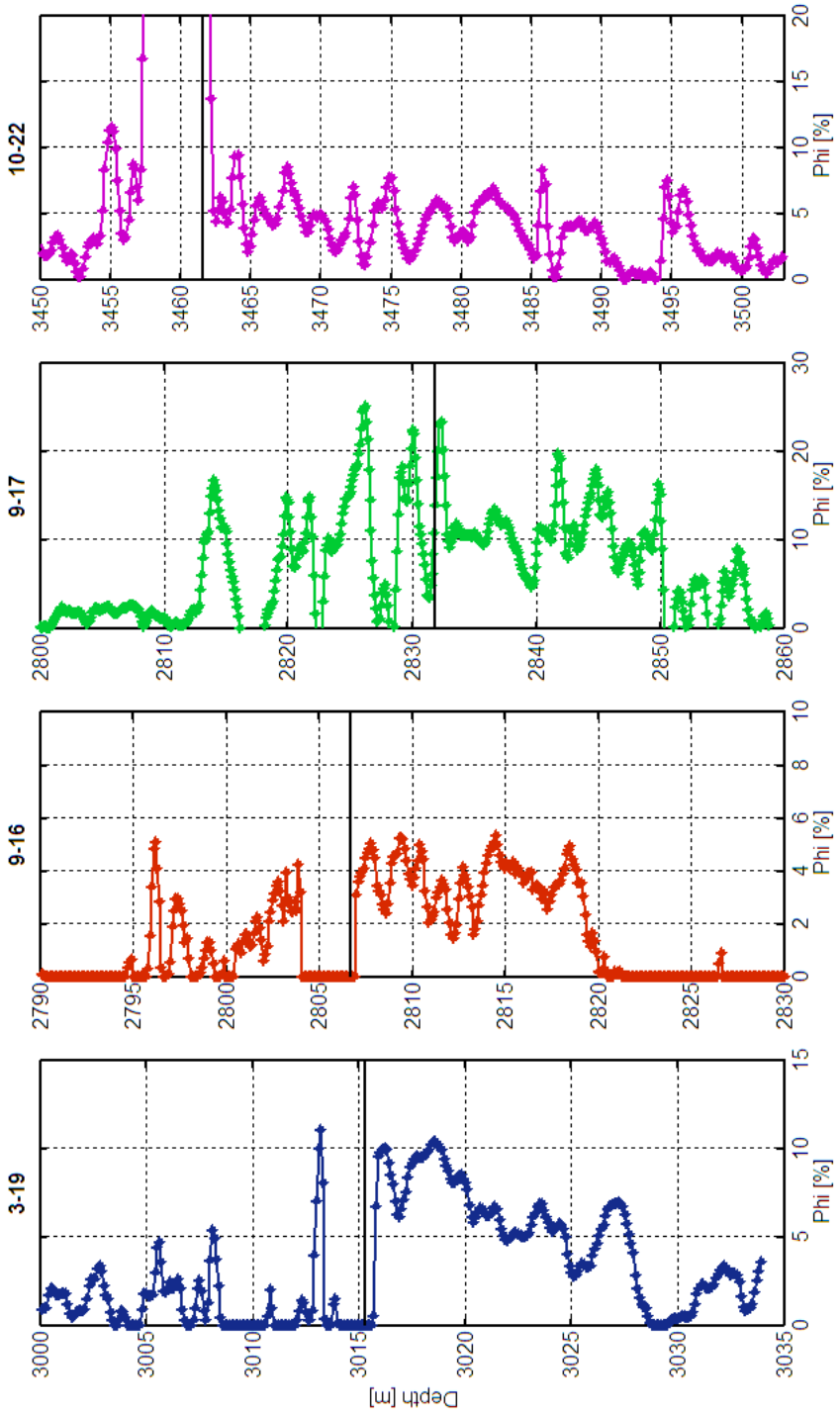

Figure 4-9: Porosity logs of wells 3-19, 9-16, 9-17 and 10-22. Top of Cadotte formation is indicated.

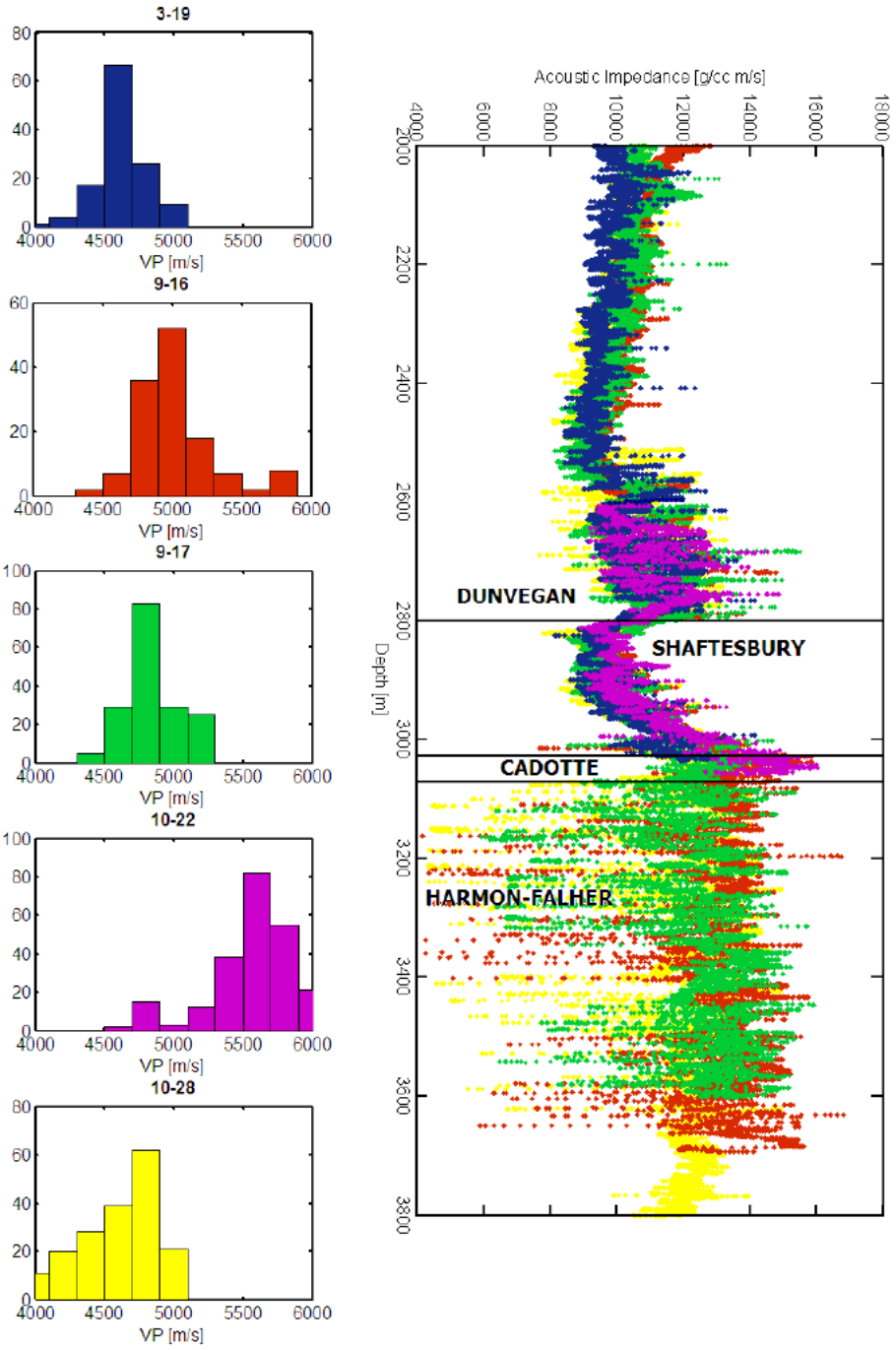

Figure 4-10: On the left, P-wave velocity variation in the depth interval of the Cadotte formation at 5 wells. On the right, acoustic impedance logs computed from density and velocity logs and shifted to align all wells at Cadotte's depth. The color code is as in the histograms on the left.

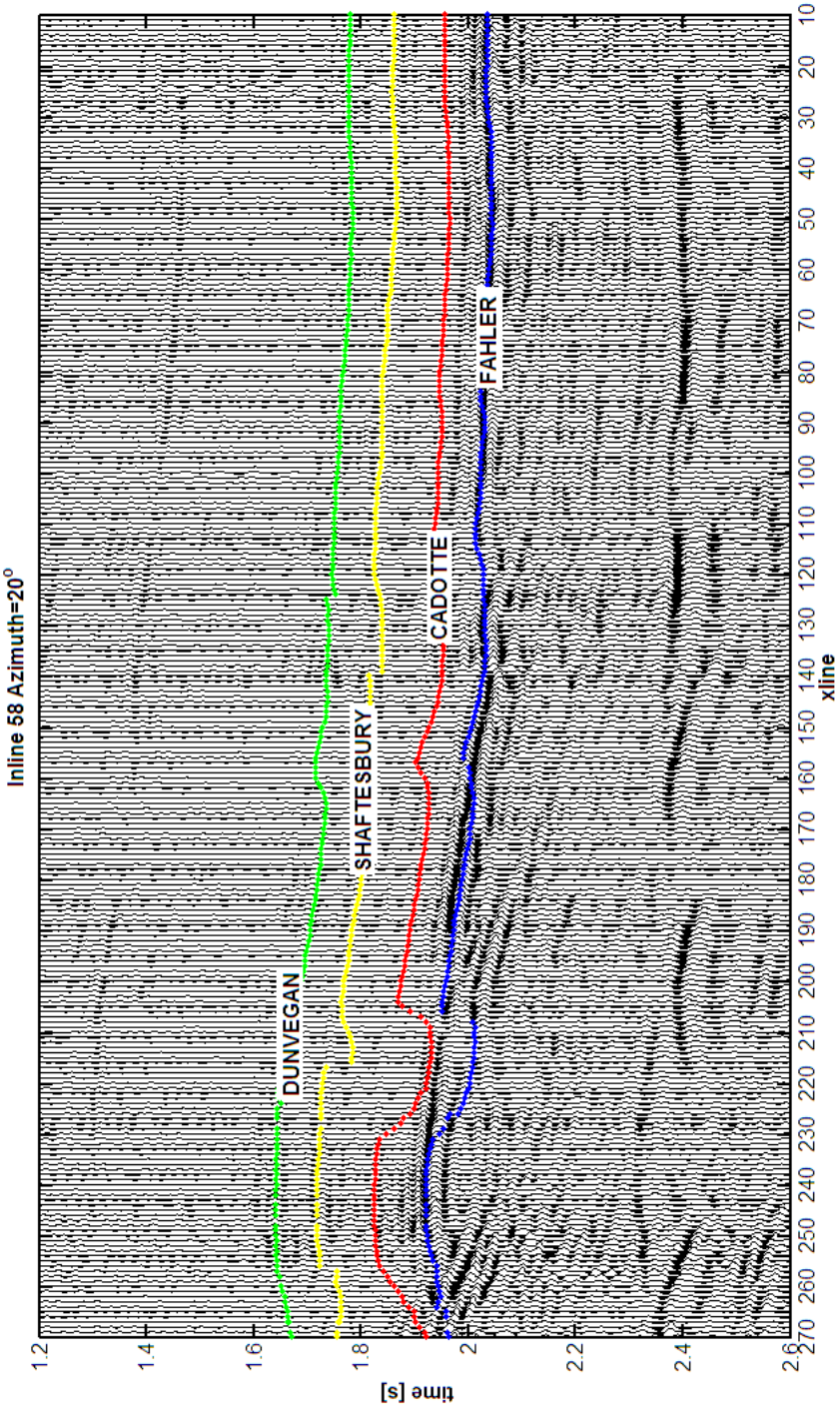

Figure 4-11: Seismic inline 58 and interpreted horizons corresponding to the top of formations: Dunvegan (green), Shaftesbury (yellow), Cadotte (red) and Falher (blue).

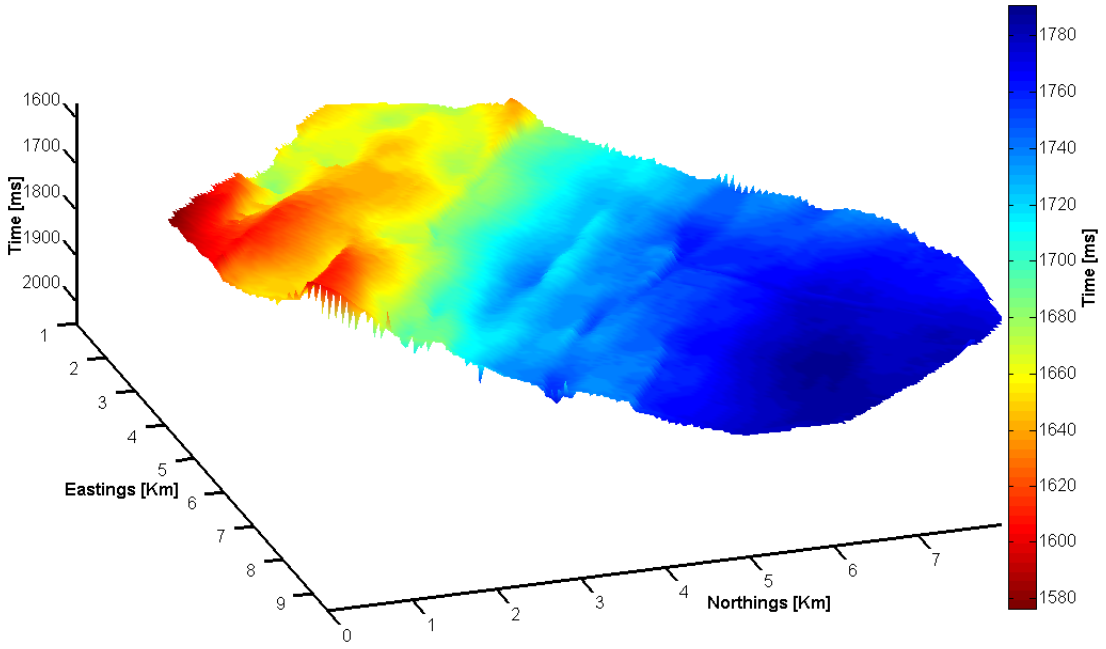

Figure 4-12: Time horizon at the top of the Dunvegan formation.

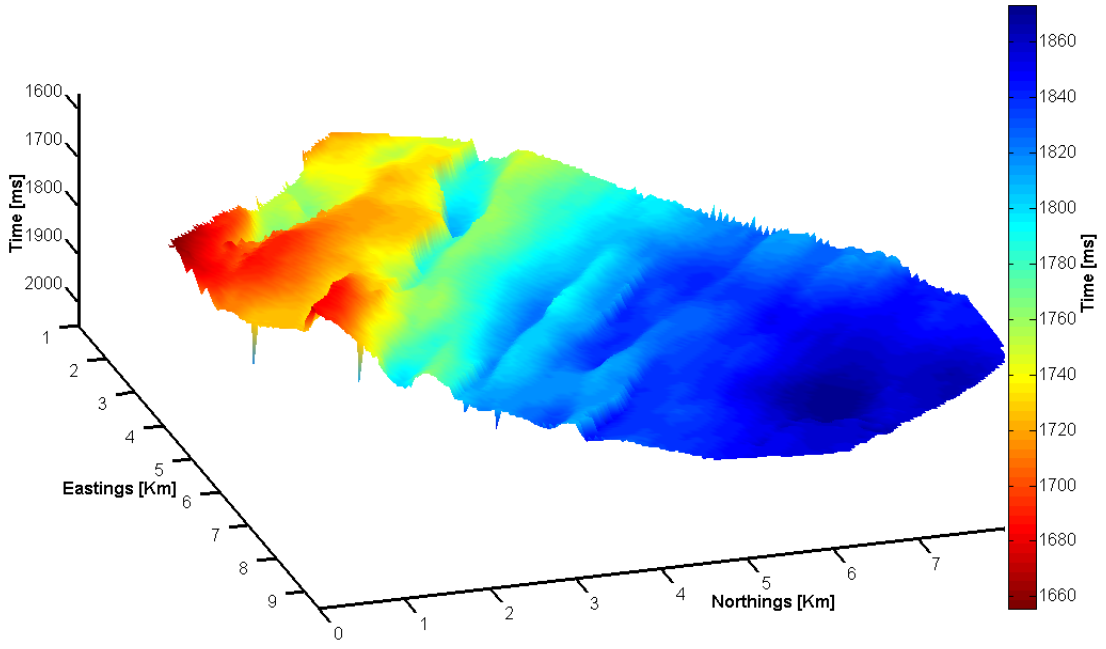

Figure 4-13: Time horizon at the top of the Shaftesbury formation.

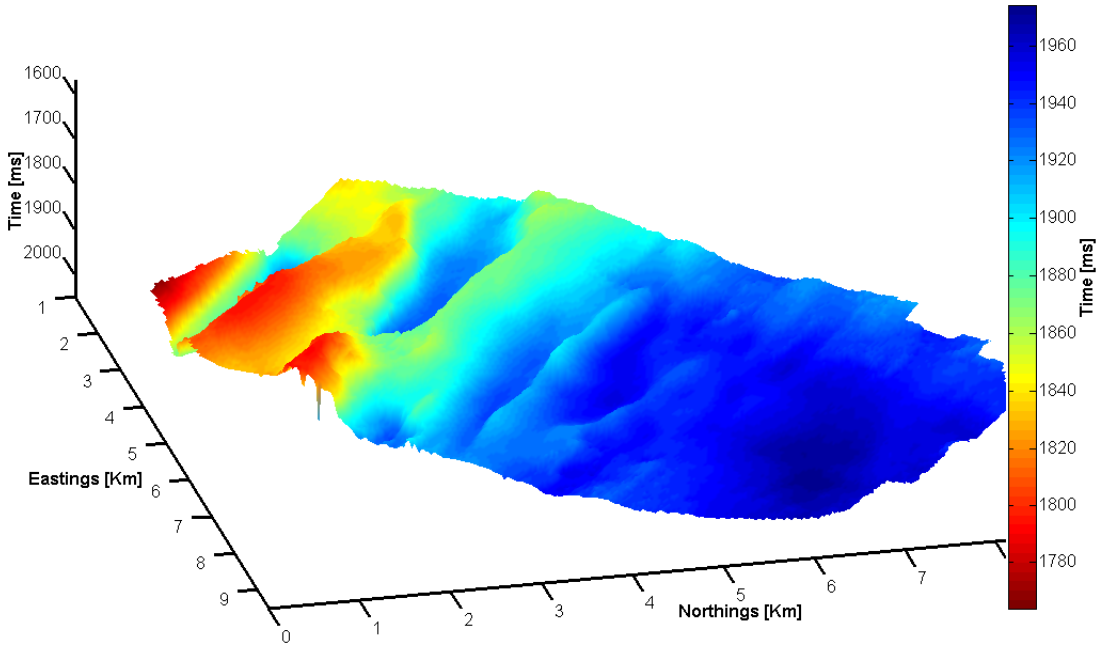

Figure 4-14: Time horizon at the top of the Cadotte formation.

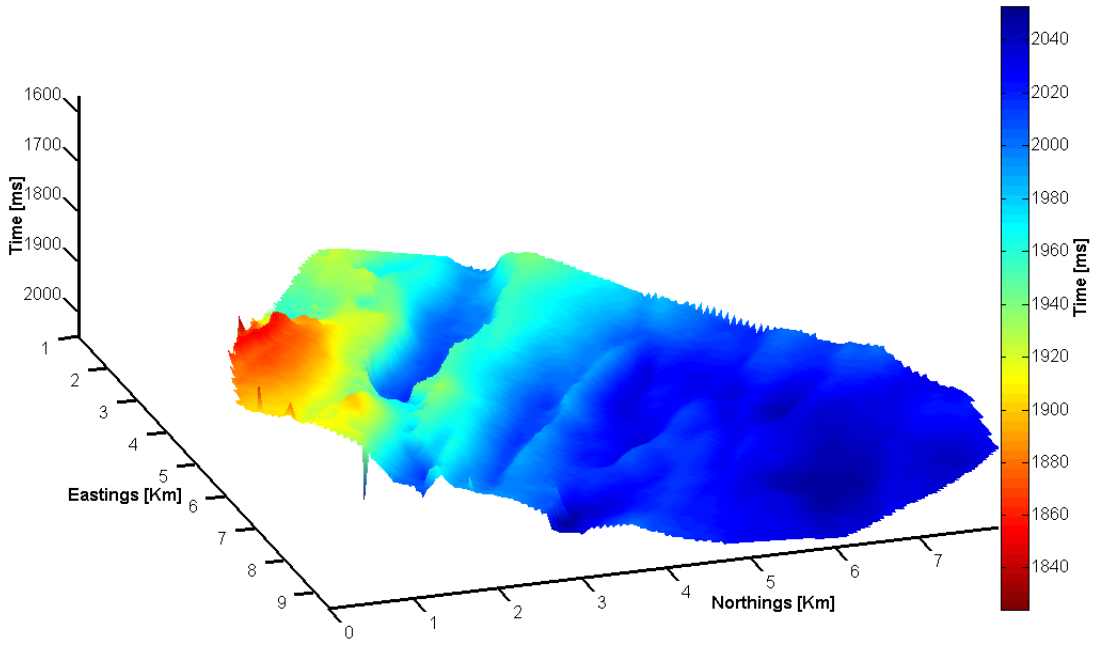

Figure 4-15: Time horizon at the top of the Falher formation.

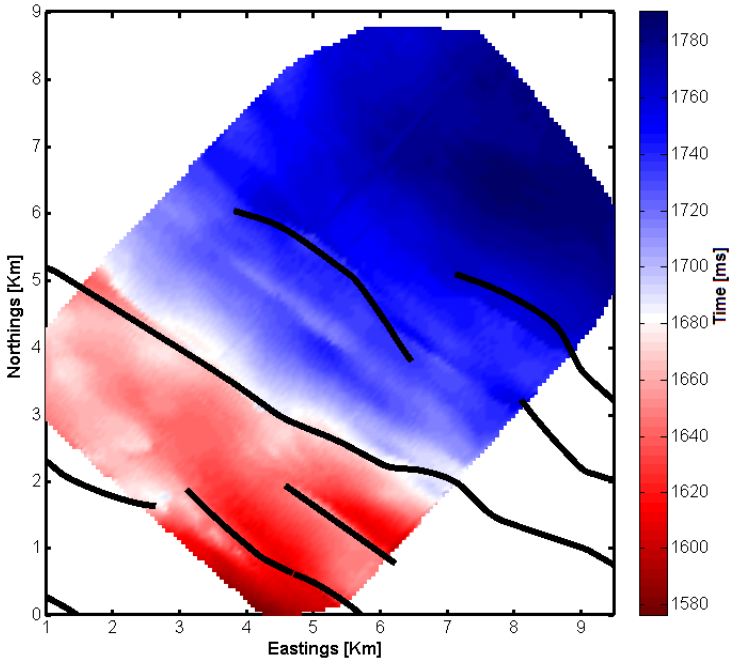

Figure 4-16: Interpreted faults over time horizon of the Dunvegan.

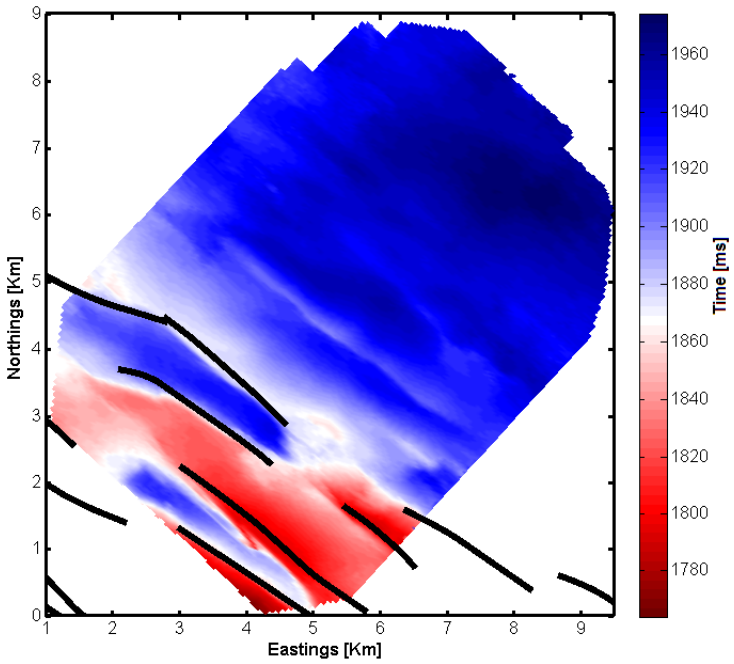

Figure 4-17: Interpreted faults over time horizon of the Cadotte.

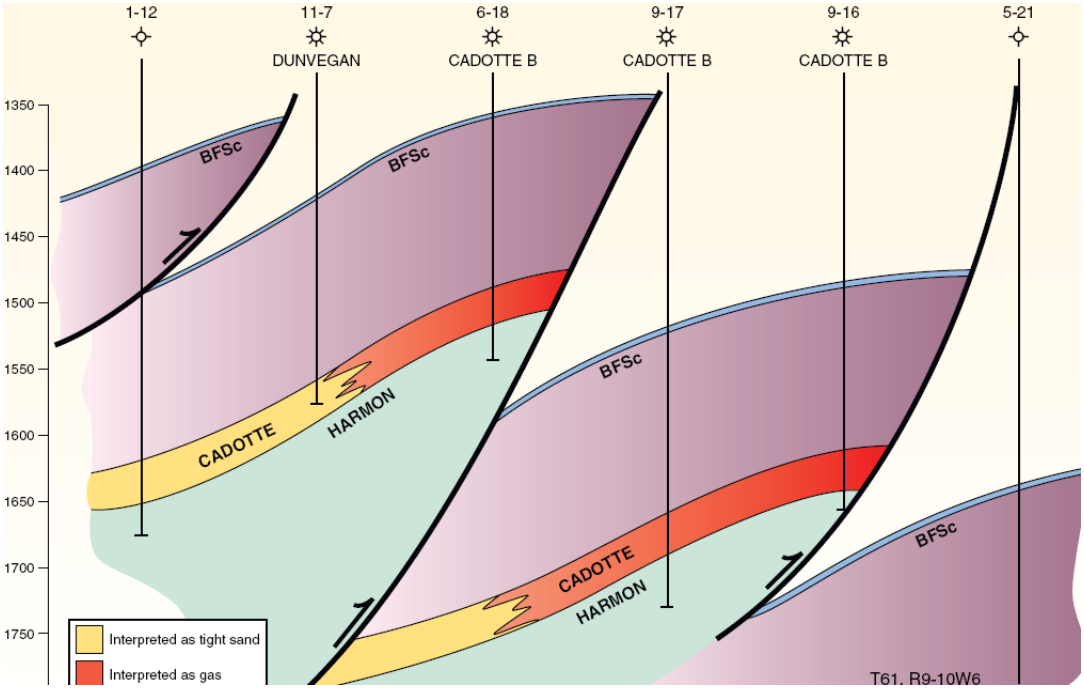

Figure 4-18: Schematic structural cross-section in Lynx. After Canadian Discovery Digest (2004).

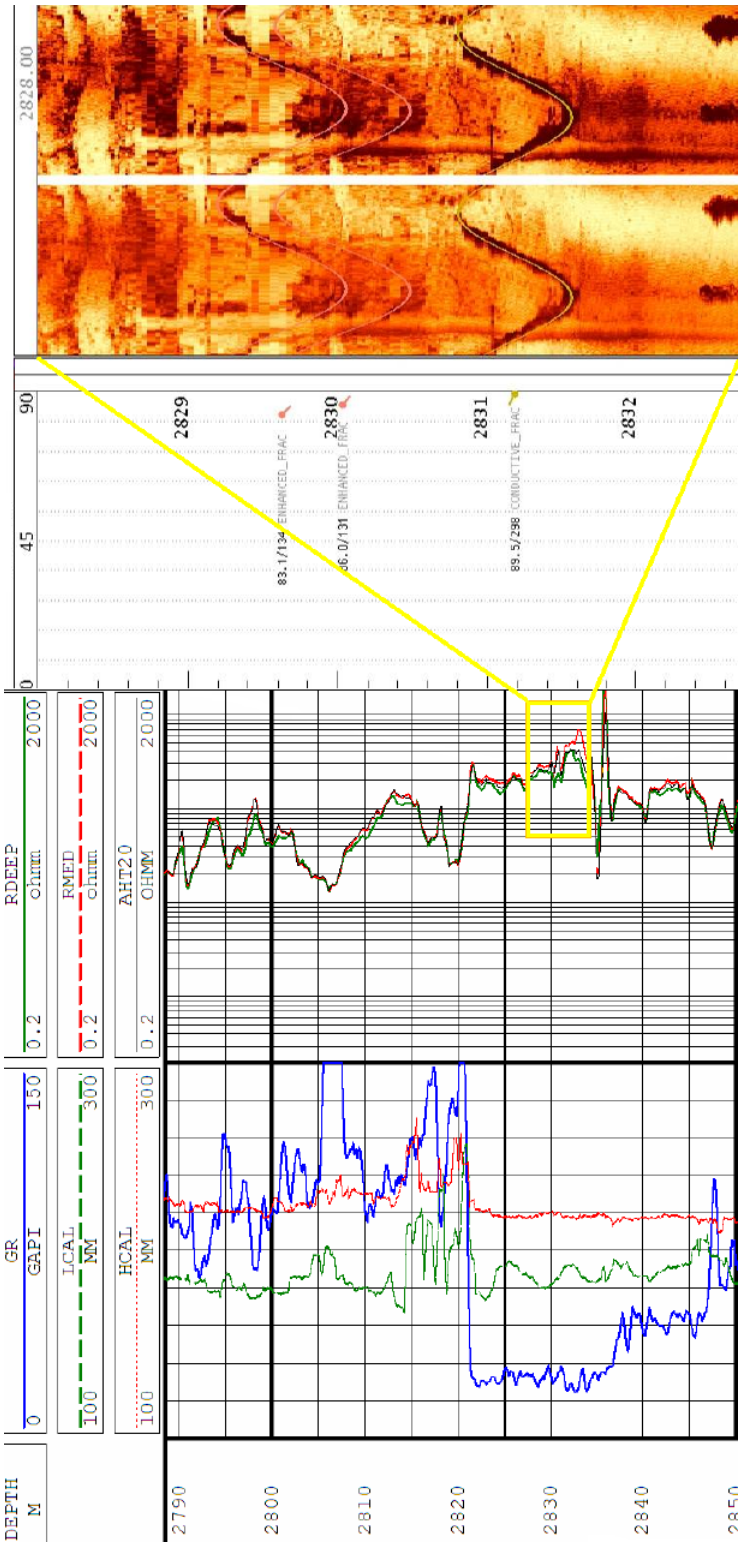

Figure 4-19: Logs' section in well 6-18. From left to right: gamma ray, resistivity, and FMS (formation microscanner) image around the Cadotte. Courtesy of Tad Smith (VeritasDGC).

Figure 4-20: Example of core samples taken in well 6-09. Courtesy of Tad Smith (VeritasDGC).

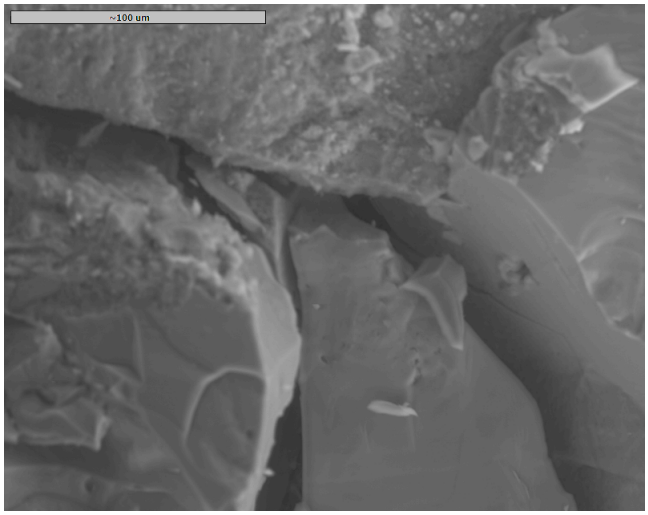

Figure 4-21: Scanning electron microscope (SEM) image of a rock sample from well 6-09. Courtesy of Tad Smith (VeritasDGC).

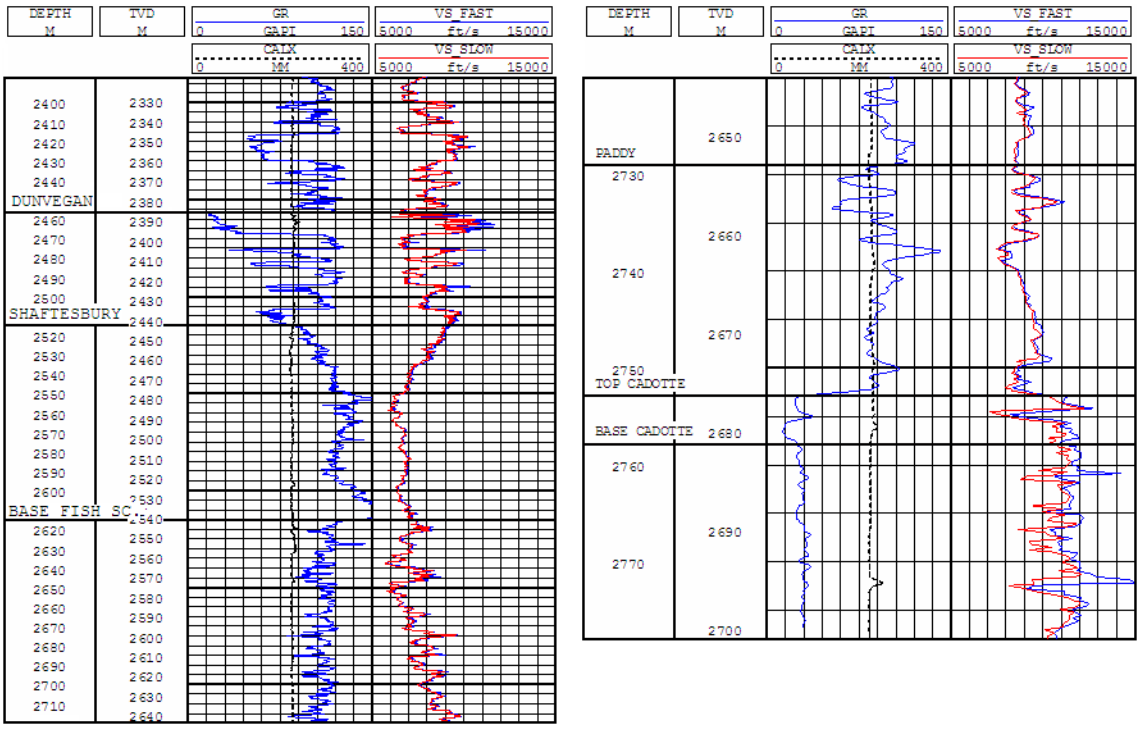

Figure 4-22: Fast and slow shear wave velocity in well 11-07. Courtesy of Tad Smith (VeritasDGC).

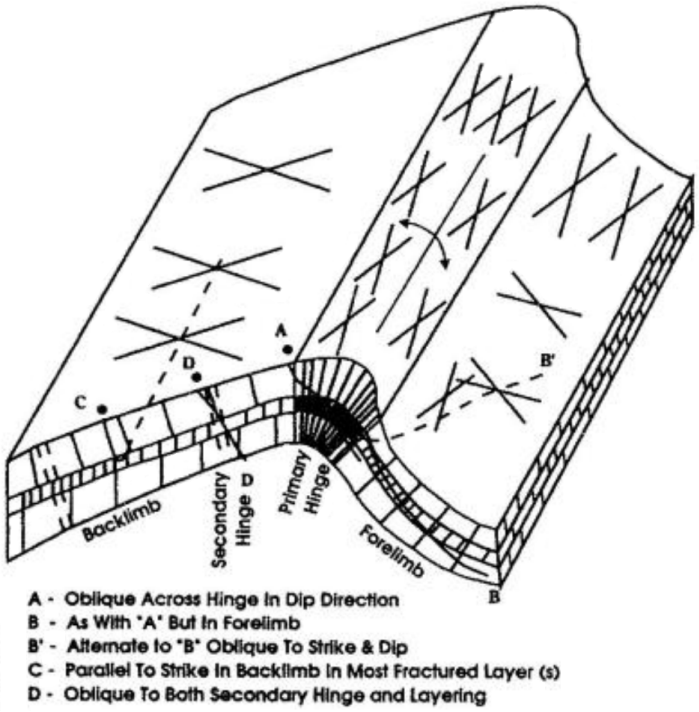

Figure 4-23: Optimal well paths in fractured folds. After Nelson (2001).

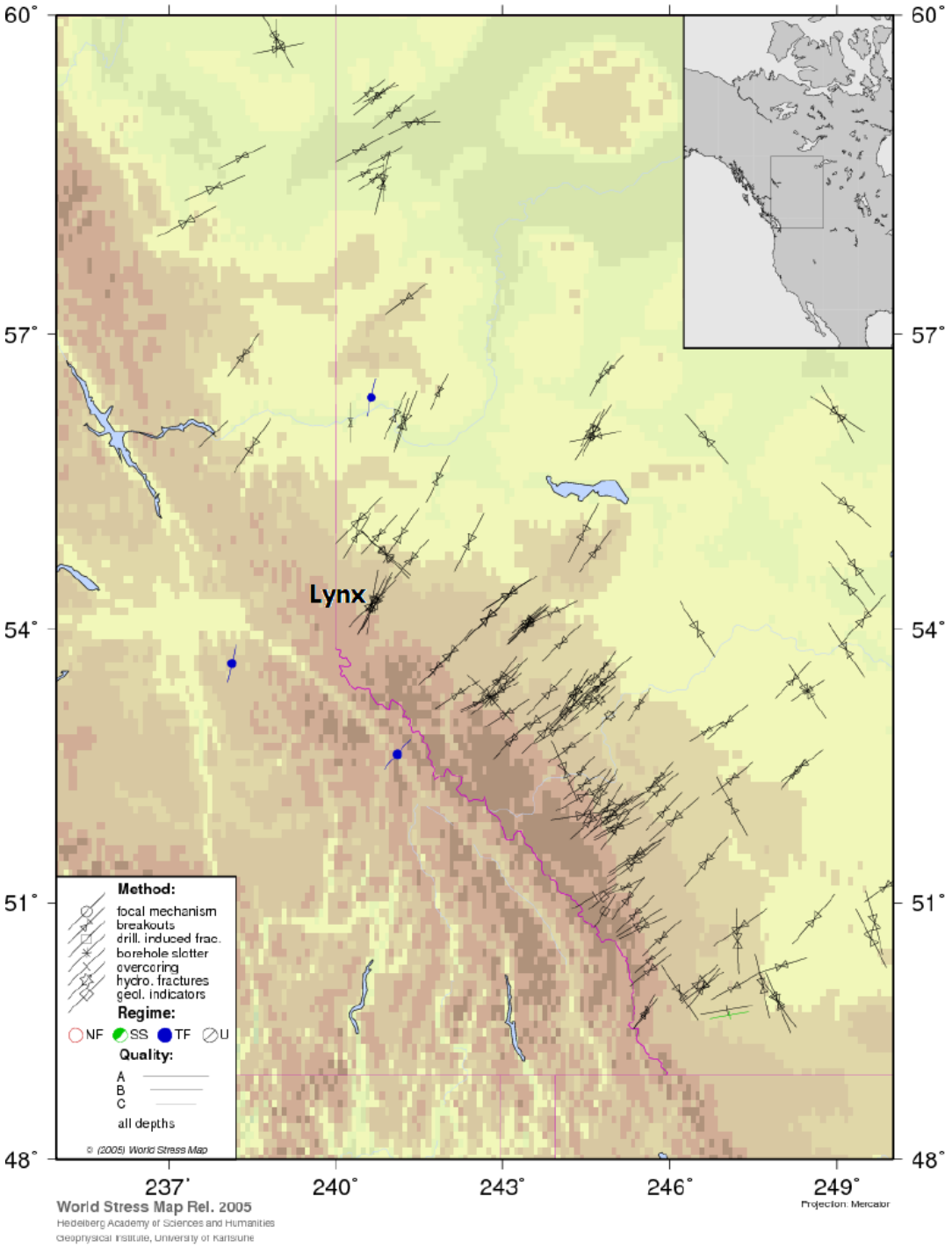

Figure 4-24: Orientation of maximum horizontal stress in the Western Canada Sedimentary Basin and in the area of the Lynx field. This map is different from the current World Stress Map because it includes more recently reported stress orientations in the WCSB, and particularly in the Alberta Province.

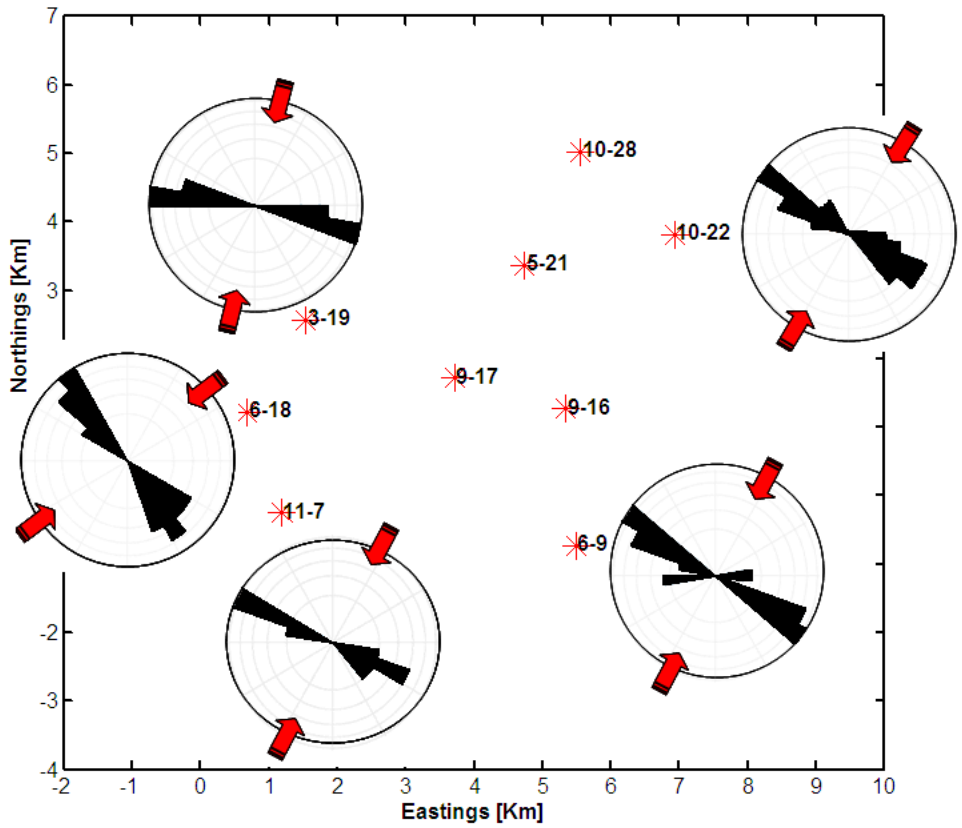

Figure 4-25: Breakout data in 5 wells of Lynx indicate the azimuth of $Shmin$. The orientation of $SHmax$ is inferred (red arrows).

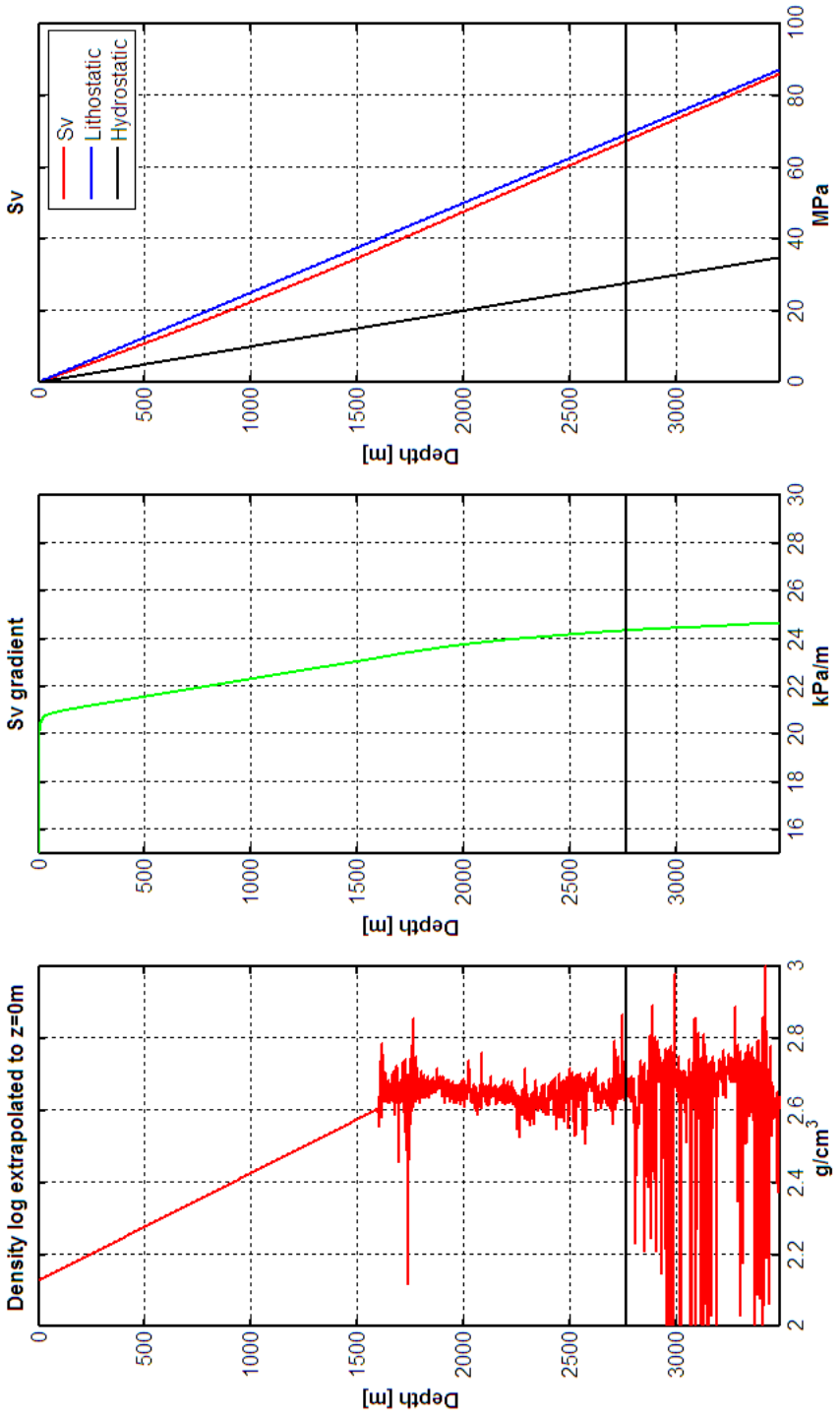

Figure 4-26: From left to right: density log in well 9-16 extrapolated to the surface; Sv gradient; and Sv estimated.

Chapter 5

Estimation of Fracture Properties in the Lynx field

In this chapter, we analyze scattered energy from the Lynx field in the frequency-wave number domain aiming to estimate the orientation and mean spacing of fracture corridors. In chapter 3, it was shown that waves propagating through fracture corridors scatter energy. The orientation of shot records relative to fracture strike determines the spectral character of these scattered waves. Based on those observations, the F-K method was developed as a tool to estimate fracture parameters.

The present chapter evaluates the applicability of the F-K method to real reservoir situations and assesses the limitations and advantages of the technique when applied to field data. The exercise is in itself a method to better understand, adjust and improve the F-K technique.

The Lynx field was amply described in chapter 4. In that chapter, it was established that Lynx is a gas field in western Canada with a complex tectonic history that resulted in the formation of fold and thrust structures. Production history, regional stress field, reservoir rock properties, and direct evidence of fractures, from petrophysical and surficial observations, indicate that future development of this field depends on the possibility of obtaining a better image of primary fluid flow channels and small faults which might be defining reservoir compartmentalization. Conventional seismic data attributes have been of little help in the interpretation of minor

faults and ultimately in the consistent prediction of successful well locations. The mechanical behavior and the lithological composition of the main reservoirs, Cadotte and Dunvegan, suggest that fracture corridors may be present in this field.

The *F-K* method makes use of surface seismic data, thus, appropriate pre-processing is necessary and relevant. Such a task is challenged by the acquisition geometry of seismic surveys, signal to noise ratio and presence of dipping structures. Section 5.1 details the processing sequence designed for Lynx's seismic data in preparation for the fracture characterization. In this section, emphasis is placed on the treatment of acquisition footprint because of its potential negative impact on the performance of the fracture scattering methods here applied.

Section 5.2 is the core of this chapter since it presents the results obtained from the *F-K* method, namely, fracture orientation and spacing of the main reservoirs of the Lynx field. A measure of confidence in the results, as well as a potential tool to derive relative stiffness based on spectral amplitudes are explained at the end of the section.

The Scattering Index methodology (Willis et al., 2006) is also applied to the same data, after creating appropriate azimuth stacks. A modified version of the Scattering Index method is created and applied for the first time to a stacked volume using all azimuths. These results are shown in section 5.3. The Scattering Index technique has higher spatial resolution to map fracture distribution, intensity and orientation, and therefore complements the spectral method. A comparison in terms of fracture orientations and distribution derived from both methods is included in the same section. Other practical aspects of the *F-K* and Scattering Index methods are discussed in appendix C.

Finally, section 5.5 builds a case for the connection between the fracture estimations and stress, and other information about fractures available in the area as described in chapter 4. The in-situ stress values derived from well logs in the Lynx field, and extracted from the World Stress Map and other reported studies of the area, are utilized to partially validate our results and detect anomalous stress areas which may be indicators of recent faulting or weak zones.

5.1 Data Preparation for Fracture Analysis

The seismic data used in the present study were acquired in 2000 by VeritasDGC and comprise about 110 Km^2. The survey area covers the northeast part of the Lynx field. Shot lines were oriented N42°W and receiver lines were oriented in the perpendicular direction (figure 5-1). The orthogonal acquisition pattern produced a relatively uniform azimuth distribution and high fold coverage at low and mid offsets. Figure 5-2 depicts the survey's fold where each yellow dot represents one or more traces recorded at the corresponding azimuth and offset. Receivers were spaced apart in the field about 60 m, receiver lines were spaced around 400 m, and the shot lines were about 480 m apart.

VeritasDGC processed these data in 2001 and the final migrated cubes were interpreted by ConocoPhillips. The interpreted horizons guide the fracture analysis as will be explained below. Later in 2004, VeritasDGC, ConocoPhillips, and ERL (Dr. Mark Willis), worked together in designing a processing sequence appropriate for the fracture analysis in this study. The accepted sequence included: gain recovery, coherent noise attenuation, surface consistent deconvolution, all statics, and azimuthal anisotropic moveout.

Great care was taken to ensure that the scattered signals were preserved throughout the preprocessing sequence. Bin borrowing, or flexing, which is a commonly used process to artificially increase fold by borrowing traces from neighboring common midpoint gathers, was not allowed during this stage. The use of trace mixing processes was also limited. In particular, common multitrace filters and typical processes, like migration, were left out because their effect on the scattering signal, which, while not fully tested, is suspected of potentially reducing the scattered signal.

As a result, the seismic data for this study have an apparent lower signal to noise ratio than the conventional final processed seismic data volume (see for example the stack shown in figure 4-11). Thus, the methods applied in this study attempt to extract fracture parameters from the portion of the signal that conventional processing steps may suppress since they identify it as noise.

The data were sorted into the CMP domain, for the *SI* method, and into the SHOT domain, for the *F-K* method. Afterwards, each dataset is sorted into azimuthal gathers. The azimuthal gathers are further stacked in the *SI* method. Sorting the data appropriately is a key process to obtain reliable results. We next give the motivation and details of the azimuthal sorting of the Lynx data as well as other characteristics of the data.

5.1.1 Acquisition Footprint, Fold, and Azimuthal Binning

In general, no seismic survey produces perfectly homogeneous fold. For land surveys, like this Lynx field survey, the fold homogeneity is additionally affected by skips and offsets at rivers, towns, terrain accidents, and other obstacles that prevent a regular deployment of sources and receivers. The finite length of the source and receiver arrays makes the sampling of offsets and azimuths typically irregular. Geological structures in the subsurface that are narrow with respect to cable length or have a preferential strike, steeply dipping structure, and/or large velocity contrast (e.g., salt domes), can all affect the true, in contrast to nominal, azimuthal distribution of offsets. This is caused by the resulting shadow zones in the path of propagated waves. Even if locally the earth's surface is flat and the acquisition geometry is perfectly regular, the distribution of sources and receivers may leave an imprint on the data, known as *acquisition footprint*. This footprint degrades seismic quality, by introducing bright spots (areas with good data quality) and dim spots (areas with no data or low quality), especially at near offsets where it is most noticeable, and at early times on the traces. This effect is usually easy to see on time slices (i.e. a 2D display showing a single time sample for all traces) of the data volume.

The acquisition footprint of the data influences the performance of the *F-K* and the *SI* methods. If a particular azimuth is under sampled by having low fold, the amount of scattered energy may be over estimated. This is because the scattered energy will not cancel out for the *SI* method or will be aliased for the *F-K* method. Thus if there is a significant variation in fold, the change in the scattered energy measured as a function of azimuth may not be representative of the actual scattered

energy. Without some correction, the final fracture orientation maps may be biased toward azimuths with lower fold.

Concerning the *F-K* method, irregular offset sampling could lead to aliasing of forward and backscattered events as shown in figure 5-3. At the top left figure, the SHOT gather in the direction normal to fractures has offsets sampled every 5 m. The gather in the middle-column has a source-receiver distance which is not constant thereby mimicking a case of low fold. The clear scattered events on the original gather are distorted on the decimated gather. The lack of continuity observed on the decimated data results in an aliased and complicated *f-k* spectrum which over estimates the energy in positive wavenumbers and diffuses the energy in the negative wavenumbers. Infilling the gather with blank traces (top right) to try to compensate for the missing offsets, correctly positions each trace with its proper offset. However, the resulting spectrum exhibits an interesting periodicity in the wavenumber direction (lower right figure 5-3). This introduces more energy in both halves of the wavenumber spectra which obscures the location and distribution of the actual scattered energy (shown in the bottom left spectrum). Attempting to locate and characterize the scattered energy in the low fold spectra would likely over estimate the amount of energy for both positive and negative wavenumber spectra. Noise, present in field data, would likely exacerbate this effect.

The *SI* method relies on the constructive stacking of scattered events parallel to fractures and the destructive stacking in the normal direction. The amount of scattered energy found by this method in the direction parallel to the fracture strike is mostly insensitive to variations in fold. However, if the acquisition footprint reduces the number of traces in the non-parallel azimuths, the scattered energy will not be attenuated as much. This means that the amount of scattered energy measured in the non-parallel directions will increase and thus will decrease the prominence of the scattering index value in the parallel direction. In this case, it is likely that the scattering index analysis would report little azimuth variation in scattered energy and therefore, no detectable fractures. This is illustrated in figure 5-4. The top left panel in figure 5-4 shows a synthetic gather with full fold in the normal direction. Below it

is shown the scattering index for all azimuths. The top right panel shows the same record which has been randomly decimated. Blank traces have been inserted into this gather to preserve the offsets for the display, but were not used in the analysis. Below it is shown the corresponding full analysis for all azimuths. Note that the scattering index value for the parallel direction (90°) has not changed, but all other azimuths have larger values. Thus this CMP would have been labeled as having no significant amount of fractures.

Another possibility might be for the fold to be low only in one azimuth. In this case, since the scattered energy would not be attenuated, this azimuth might compete with the actual parallel direction and show a possible secondary set of fractures at the low fold azimuth, or an incorrect fracture azimuth in the worst case. That one low fold azimuth might bias the resulting fracture maps toward this direction.

In field data, there is one more aspect to consider with respect to the variation in fold affecting the *SI* method. Stacking of high fold data effectively attenuates random noise. If the resultant fold in the azimuthal gathers is too low or if fold is too different among gathers, random noise and not fracture scattering signals might dominate the variation of scattering index with azimuth.

In Lynx, despite the large extent of the source and receiver arrays, angular fold is not uniform. The most regular offset distribution occurs in the direction of the receiver lines. The acquisition footprint is anticipated to affect the fracture analysis and, therefore, a first step of the fracture study consists in binning the data appropriately.

In an ideal survey, the traces could be sorted into any number of azimuth ranges and the fold and offset ranges would be uniform. However, for every actual field data set we seek an optimal sorting of traces into azimuthal gathers which attempts to maximize the resolution in azimuth while keeping the fold uniform and adequate. Therefore, the factors to be determined are: (1) the minimum azimuth increment which determines the angular resolution; (2) the minimum and maximum numbers of traces in each azimuth gather which determines the variation in fold; (3) the distance between traces in a gather which controls the sampling and aliasing of information within each gather; and, (4) the amount of traces shared or borrowed between az-

imuth ranges to equalize the fold. These requirements are interrelated. For instance, choosing a specific azimuth increment sets the number of traces in a CMP or SHOT azimuth gather. Limiting offsets within a range as required by both, the *F-K* and *SI* method, further reduces this number. Azimuthal resolution of fracture orientation often has to be sacrificed in order to obtain a more homogeneous offset distribution.

Azimuthal CMP Gathers

In order to get the optimal azimuth gathers for both the *F-K* and *SI* methods, the SHOT records and CMP gathers of Lynx are analyzed separately. Starting with the CMP gathers several combinations of azimuth increment and degrees of overlap between azimuth sectors (or ranges) were tried, and the distribution of offsets and the number of traces common in consecutive azimuthal gathers were checked in every case. We define this process of gathering the traces into separate azimuth ranges as "sectorization." Azimuth widths of 10°, 15° and 20°, were tested with no azimuthal overlap and with respective overlaps of 10°, 15° and 20°. Another test of the 20° azimuth range was run for a 10° overlap. The white dots in figure 5-5 show the CMP map locations that have at least 5 fold for all azimuthal components after gathering into azimuths ranges of: 10° with an overlap of 10° (top left), 15° with an overlap of 15° (top right), and 20° with an overlap of 20° (bottom). Decreasing the azimuth increment reduces the number of CMPs in the survey that pass the test of having relatively uniform fold characteristics for all azimuths. Of course, if more traces are added by increasing the width of the overlapping area, the fold is increased at the expense of trace mixing (borrowing) between the azimuth gathers. Tests of the signal to noise after stacking suggested that a minimum fold of 5 is required to obtain significant results. In several test locations, it was found that the level of noise in stacks with less than 5 traces was too high to determine a preferential azimuth of scattering or, in other words, to yield a significantly higher scattering index at a particular azimuth with respect to the other azimuths.

In summary, to avoid possible acquisition footprint issues and insure the largest possible area coverage, the optimal sorting of Lynx data was 20° wide azimuthal

groups with an overlap of 20°. This makes the total width of each azimuth gather to be 40°. The fracture analysis was carried out only in gathers where "full" azimuthal fold was found; where full fold means that the resultant gather contains at least 5 traces between 0 and 4000 m. The offset distribution in each azimuthal gather was checked for uniformity, neglecting those CMPs in which the required 5 traces are all grouped at a particular offset interval or if the coverage of offsets is too different from azimuth to azimuth. The process of fold regularization is illustrated in figure 5-6. The folds of two CMP gathers (located in the survey as shown in the right panel of figure 5-7) are shown. The colored dots represent the azimuth-offset components of every trace in the CMPs. CMP 1398 (in the top two panels) is at the edge of the survey and therefore has very few traces with practically none recorded at azimuths greater than 100°. In contrast, CMP 16155 (bottom two panels) is located in the center of the survey and has a better coverage of offsets at all azimuths. The azimuthal binning of CMP 1398 (top right) is unable to regularize the fold due to the lack of traces. However, the azimuthal binning of CMP 16155 yields gathers with many more than 5 traces relatively which are very well distributed in the offset interval of interest.

Sorting the data in this way resulted in about 50% of the survey satisfying the criteria above. Fracture calculations at those gathers are considered to be reliable and free of footprint biases. However, the minimum 5 traces requirement can be relaxed in order to extend the map area with information about fractures. For example, if azimuthal gathers with at least 1 trace in all azimuths are accepted, the survey data for SI analysis increases to about 75% of the original dataset (figure 5-9).

Azimuthal SHOT Records

The azimuthal sort of SHOT records was initially chosen to be the same as for the CMP gathers: traces were grouped into 20° azimuth sectors with an overlap of 20°. However, this choice of azimuth increment may not be sufficient to obtain a wide enough distribution of offsets in all the azimuthal gathers for most of the survey's SHOT records.

The fold distribution of an example SHOT gather (22132) is shown in the upper

panel of figure 5-8. Yellow dots indicate that the SHOT contains a trace recorded at the corresponding offset and azimuth. Unlike the CMP gathers, sectorization in this case includes the supplementary azimuths from 180 to 360°. The shot position is shown on the map in figure 5-7. For offsets between 480 and 3000 m and at 220° azimuth, this SHOT has about 4 times the fold found at 20 or 100°. The fold distribution is obviously not uniform and even after sorting the data into 20° azimuthal records (middle panel), some azimuths appear much under sampled in comparison to others (e.g. 120° vs. 220°).

In addition, the distinction of forward and backscattered events in the *F-K* method is directly affected by offset coverage and 5 traces (the requirement imposed on CMP gathers) is too low of a requirement in the SHOT domain. I found that a minimum of 25 traces in each azimuthal component was the practical limit to make the *f-k* spectrum utilizable. Utilizable means that the *f-k* spectrum does not contain significant spectral aliasing and extra smearing as it was described above.

In the SHOT domain, we limited the offset analysis window between 480 and 3000 m to avoid ground roll residuals at near offsets and converted waves at far offsets. In order to gather at least 25 traces in this offset range, up to 4 neighboring SHOT records had to be combined. *Supershots* were formed in this way. In figure 5-8 (bottom), it can be noted that the supershot formed combining SHOT 22132 and neighbors has an improved fold in most of the azimuthal components. In the improved azimuths the receiver distance has been regularized to 60 m. However, some azimuthal components will not enter the fracture processing because they resulted with less than 25 traces or the offset differentials were too different from the nominal receiver spacing. In the case of supershot 22132 the disregarded azimuths are 20° to 120°, and 180°. A minimum of 10 out of 18 azimuthal gathers was required to process a particular supershot. In total, 159 supershots passed the criteria. These constitute the input data for the *F-K* analysis (figure 5-10).

The acquisition for Lynx is well tailored to the present study because it was designed to have high fold multiazimuth data. In contrast, other surveys may not be designed with this purpose and have unequal fold.

5.1.2 Frequency Filter

The raw data features a non-flat amplitude spectrum. The observation is evident in the SHOT record plotted in figure 5-11 where only 3 receiver lines are shown. A band-pass zero-phase filter is applied to the raw data to attenuate frequencies below 5 Hz and above 55 Hz. Besides this, the pre-processed gathers were not treated before entering the fracture analysis. As depicted in figure 5-11, low frequency ground roll residuals and high-frequency noise have been attenuated after filtering.

5.2 Fracture-Oriented Processing: The *F-K* Method

The mechanics of the *F-K* technique to characterize fracture corridors was designed and explained in chapter 3. In this section, the method is applied to the Lynx field to demonstrate how the analysis is performed in practice. We will compare the extracted fracture maps with the results of the *SI* method.

F-K analyses are performed in a time window for each azimuth record below the interpreted horizons for Dunvegan and Cadotte. Time window for the analysis extends about 0.45 s from the top of reservoirs Dunvegan and Cadotte (figure 5-12). These two reservoirs are fairly close together and the respective analysis windows overlap. It seems like it would be difficult to separate these two sets of scattering signal. However, the moveout appears different and characteristic in each case (see appendix C).

Data are also windowed in offset. Far offsets are omitted to avoid converted waves, refractions and mute artifacts. Near offsets are also omitted because of likely contamination with air waves and ground roll (figure C-1). The chosen offset window spans between 480 m and 3000 m. Our analysis is limited to SHOT records that have acceptable fold resulting in a total of 159 supershots as shown in the map of figure 5-10.

Following the procedure described in section 3.4 for determining fractures orientation and spacing, 2D Fourier transforms are computed for 18 azimuthal gathers in every supershot. This is performed for both Dunvegan and Cadotte levels.

5.2.1 Determination of Fractures Orientation and Spacing

Once the data are in the frequency-wavenumber domain, one can proceed to detect the direction normal to fractures. In the synthetic data analysis, such determination was based on the behavior of the sum of negative wavenumber energy with azimuth (equation 3.2). The backscattered energy (E_{scatt}) is expected to be maximized when data are collected perpendicularly to fracture strike. In the field data case, the backscattered energy function was computed in two wavenumber intervals. The first is a small interval that extends from the Nyquist value of -0.0083 $1/m$ to -0.0029 $1/m$. The second window is larger and extends between the Nyquist value and -0.0017 $1/m$. The choice of these two windows is based upon the *f-k* resolution which is discussed in appendix C.

Another metric to detect the direction normal to fractures is the maximum *f-k* spectral amplitude, *Aneg*. This is the peak value in the frequency-wavenumber spectrum in the same wavenumber intervals as above (figure 5-14). *Aneg* is expected to be the largest in the direction normal to fractures. It is easier to compare all azimuthal maximum amplitudes if this quantity is normalized. Normalization can be done in several ways; one possibility, for example, is to normalize between the maximum and minimum of the maximum spectral amplitudes in the full *f-k* space of all azimuthal spectra ($Anorm1$, equation 5.1). Another normalization, $Anorm2$, is obtained simply dividing by the maximum spectral amplitude of all azimuths (equation 5.2). Both types of normalizations are useful in the final selection of the normal to fracture direction as will be explained next.

$$Anorm1_i = \frac{Aneg_i - Amin}{Amax - Amin} \tag{5.1}$$

$$Anorm2_i = \frac{Aneg_i}{Amax} \tag{5.2}$$

where,

$$\begin{aligned} Aneg_i &= max(A_i|_{-k_N}^{-k_o}) \\ Amax &= max(max(A_i|_{-k_N}^{k_N})) \\ Amin &= min(max(A_i|_{-k_N}^{k_N})) \end{aligned}$$

A denotes spectral amplitude; the index i indicates the azimuth number, from 1 to 18; k_o is either -0.0029 $1/m$, for the small range, or -0.0017 $1/m$ for the large range; and k_N refers to the Nyquist wavenumber. In the first normalization scheme, $Anorm1$ varies between -1 and 1. Large positive values indicate large relative backscattering. Larger negative values indicate less scattering.

The determination of fracture orientation using the *F-K* method is implemented as a three-step process: (1) identification of typical bounds; (2) automatic determination of fracture orientation and spacing; and (3) quality control.

In the first step of the procedure the typical bounds of the backscattered *f-k* response is determined at several test locations. Typical characteristics, such as, amplitudes, frequencies, and wavenumbers, of the backscattered waves are determined. For Lynx data, I analyzed about 15% of the supershots in this step for each reservoir. The peak frequency in the negative wavenumber interval ranged between 20 and 55 Hz. The backscattered waves typically had spectral amplitudes ($Anorm2$) higher than 0.3.

Such typical bounds are utilized in the second step in which determination of fracture orientation based on the backscattered energy function is performed automatically to all input supershots. The azimuth at which the backscattered energy function reaches a maximum is output as the initial estimate of the normal to the fracture azimuth for the particular location.

Fracture Spacing

Identification of the backscattered events in the frequency-wavenumber domain in the normal direction to fractures is followed by the computation of fracture spacing. The

fracture spacing is related to the peak wavenumber by equation 3.3.

To exemplify the analysis, the typical procedure applied to a supershot's azimuthal gathers at the Cadotte level is illustrated in figures 5-15 and 5-16. Supershot locations used in this example and others in this section are shown on the map in figure 5-13. At the top of figure 5-15, the variation of backscattered energy with azimuth in both bounded regions is depicted. Despite the oscillation of the backscattered energy function, a clear maximum is reached at 300°. At this azimuth the backscattered waves have the lowest negative apparent velocity. In the middle and bottom plots, $Anorm1$ and $Anorm2$ exhibit a similar behavior as the backscattered energy. With either normalization, the global maximum also occurs at 300°. The maximum amplitudes satisfy the two criteria: $Anorm1$ is greater than 0.3, and $Anorm2$ is positive. All metrics indicate with relative high confidence that 300° is the direction normal to fractures and therefore the fracture strike is inferred to be 90° away, at 40°.

Figure 5-16 shows the azimuthal gathers at 300°, normal to fractures, and 40°, parallel to fractures, together with their corresponding *f-k* spectrum. In this example, backscattered waves can be identified by direct inspection on the time-offset data. Unlike the 300° gather, the 40° gather exhibits only forward scattered events with similar moveout to the strong reflector at approximately 2.025 s. Events in this gather look flat because NMO has been applied (see appendix C for an explanation about the effects of NMO on the *F-K* analysis). The differences in character between both directions are more evident in the Fourier domain. As predicted by the models, energy is more compact in the *f-k* space in the direction of fractures. The *f-k* spectrum of the normal component of supershot 30136 has an energy maximum in the negative wave number region at about 40 Hz and -0.0029 $1/m$, hence the estimated fracture spacing is 172 m at this location.

Backscattered energy can be filtered out for further processing using a *f-k* pass-reject filter, as shown in figure 5-17. The backscattered component identified in the *f-k* spectrum of figure 5-16 has been filtered out (lower left) of the 300° gather (top). The difference of these two gathers corresponds to the forward scattered component (lower right) which, as in the models, is less prominent.

In both horizons analyzed, Cadotte and Dunvegan, areas were found to be isotropic or non-fractured. In these areas, energy in the negative wavenumber space is on the order of the noise at all azimuths and there is not one direction where backscattered waves are particularly dominant. As an example, figure 5-18 shows the variation of backscattered energy with azimuth for supershot 28129 at the Cadotte. Although energy maximizes at 140° and 300°, the peak amplitudes are very low, with $Anorm2$ smaller than 0.3 and $Anorm1$ negative. The largest amplitude in the negative wavenumber range is found at 140° at 43 Hz and -0.0018 $1/m$ which corresponds to a fracture spacing of 280 m. Such a large fracture spacing is consistent with the fact that the f-k response does not change significantly with azimuth. Cadotte is not likely to be fractured at this location or if fractured, fractures should be sparse. Figure 5-19 demonstrates the similarity of the spectral character of several azimuthal gathers.

Quality Control

The third step of the F-K analysis is for quality control. Because the azimuthal sorting was carried out in 18 sectors (20° each), covering 0 to 360°, it is possible that the backscattered energy exhibit two peaks, ideally 180° apart. In addition, because the backscattered energy is computed in two bounded regions, sometimes several local maxima are identified. In other words, backscattered energy can be multi-peaked. Frequency and amplitude components are used to ultimately choose the azimuth with the global maximum. Therefore, in the third step, every shot is checked independently using the results from the second step as a guide, and adding the maximum amplitude metric. For Lynx data, about 40% of the shots needed to be repicked in the third iteration due to two main causes:

1. Noise in the data that made the automatic determination of fracture orientation ambiguous. Some of the causes for this ambiguity are discussed in appendix C with the most important one being the contamination with unmigrated diffractions given that the data were not migrated (section C.5).

2. A frequency and/or amplitude component out of acceptable range. Acceptable values are: $Anorm1$ should be positive and $Anorm2$ should be above 0.3; peak frequency should be consistent with the trends observed in the locations around. In these cases, the supplementary azimuth, or an azimuth 20° away, may exhibit better frequency and amplitude values; thus, the azimuth corresponding to the normal to fractures' direction is repicked.

Under the assumptions that only one fracture set with a predominant direction exists, and that all azimuthal gathers have a similar signal to noise ratio, the backscattered energy should in theory reach a maximum every 180°. This case is exemplified in figure 5-20. At the location of supershot 34125, the energy function peaks at 140° and again at 300-320°, which are 180° away. These azimuths indicate the direction normal to fractures. The middle plot shows the variation of maximum spectral amplitude normalized by the maximum of all azimuthal spectra in the full wavenumber axis ($Anorm2$). $Anorm2$ at 140 and 300°, irrespective of the wavenumber range, is larger than 0.3, however the lower plot shows that the 140° peak amplitude is very weak (negative $Anorm1$).

In figure 5-21, the *f-k* spectrum of the azimuthal records at the normal and parallel direction are shown for the 34125 location. The *f-k* spectrum of the azimuth normal to fractures of supershot 34125 exhibits an energy maximum in the negative wavenumber axis at about 33 Hz and -0.0074 $1/m$, hence the estimated fracture spacing is approximately 67 m at this location.

In some instances, when the backscattered energy function peaks at two azimuths, the direction normal to fractures is decided based on the frequency trend. In figure 5-22, backscattered energy at the location of SHOT 34146 reaches a clear maximum at 340°, however, the corresponding peak frequency at this azimuth is greater than 50 Hz whereas the backscattered component in locations around appear at much lower frequencies. Supershot 34146 is located near the edge of the accepted fold region and, in fact, only 15 out of 18 azimuthal gathers comply with the fold requirement, thus the backscattered energy function has been interpolated at these angles. Perhaps this is the reason why the backscattered component 180° away, at 120°, fits better

the behavior of frequency in this area. Such azimuth is chosen as the direction normal to fractures in spite of it having a lower peak amplitude than the value at 340°. In figure 5-23, it can be noted that the backscattered energy off the fracture corridors at the location 34146 has a predominant frequency of 37 Hz and wavenumber -0.0081 $1/m$ from which fracture spacing is estimated in 61 m.

Fractures Orientation and Spacing Maps

Determination of fracture orientation following the F-K technique is carried out for all supershots. The results for the Cadotte and Dunvegan levels are presented in figures 5-24 and 5-25. In these figures, fracture orientation is indicated with red vectors whose length is proportional to peak amplitude normalized with equation 5.2. At the Lynx field, the preferential fracture strike coincides approximately with the regional maximum stress orientation, that is, in the N-E direction. In other words, backscattered signals off fracture corridors in the reservoirs are stronger in the N-W direction. Departures from this trend are more evident at the Dunvegan reservoir.

At the normal to fractures f-k spectrum, identification of the backscattered component dominant wavenumber leads to estimation of fracture spacing. Values obtained at all supershot locations are mapped in figures 5-26 and 5-27. At Cadotte, fracture spacing is relatively regular across the western part of the survey, varying between 60 m and 120 m approximately. On the eastern part, fractures of seismic scale become more sparse or non existent. This interpretation is consistent with the structural behavior of Cadotte. Distribution of fractured areas at the Dunvegan is somewhat different than at the Cadotte. Non-fractured areas (or less dense fractured areas) are more extensive at the Dunvegan, probably because also at this formation, structure is less steep. Areas with closer fractures are restricted to the most western and northern region of the survey. Differences in fracture distribution in depth suggests that fracture corridors mapped may be confined to each reservoir layer.

Amplitude and Frequency Maps

The fracture spacing maps shown in figures 5-26 and 5-27 are derived from the peak wavenumbers. Peak frequency and amplitude also carry useful information although their interpretation in terms of fracture properties is less clear.

Already in figures 5-24 and 5-25 the amplitude dimension is exposed. Length of quivers represents amplitude values and, in principle, might be used as a measure of confidence in the results. The *F-K* method will be less accurate in estimating fracture spacing and orientation from backscattered signals that are weak. Figures 5-28 and 5-29 show maps of peak amplitudes, $Anorm1$, for Cadotte and Dunvegan. Values have been clipped below zero to indicate areas with low amplitude in black. High amplitude regions are shown in bright yellow. In these maps, the eastern region of Cadotte and Dunvegan seem more prone to have lower amplitudes, as well as the northern part of Dunvegan. The spatial trend suggests that amplitudes may be indicative of geological features besides being useful to measure accuracy of the results. In chapter 3, based on synthetic models, it was concluded that backscattered signal amplitude is sensitive to fracture stiffness, thickness, and spacing; therefore, the amplitude maps may be showing a combination of variations of these properties across the Lynx field. According to these maps, more compliant fractures would be located on the west whereas fractures on the east would be stiffer. Cadotte's thickness would decrease towards the east. The relationship between fracture spacing and amplitude, as explained in section 3.5, depends on the scattering resolution limit. At this point, only a relative sense of stiffness or thickness variation can be provided. More research is needed on this topic but the results are encouraging in that peak amplitude could be a potential estimator of fracture stiffness and/or reservoir thickness.

Frequency maps at the Cadotte and Dunvegan level are depicted in figures 5-30 and 5-31. If it is assumed that all backscattering is being generated at the same formation and it is only attributed to fracture corridors of varying spacing and stiffness, backscattered waves' frequency is not expected to vary greatly spatially. Frequency varies between 25 and 50 Hz and is, in general, lower at the Cadotte than at the Dun-

vegan. The modeling experiences described in chapter 3, suggest that frequency is not sensitive to changes in stiffness or fracture vertical length. Frequency changes with fracture spacing since it is related to the apparent velocity of backscattered waves. However, comparison of these frequency maps with fracture spacing maps obtained from peak wavenumbers hints about sensitivity differences between frequency and wavenumber to detect fracture spacing.

5.3 Comparison with the Scattering Index Method

Another method to describe fractured reservoirs is the Scattering Index (SI) method. The Scattering Index method was explained in section 3.6. A complete description of this method and an application to a field dataset are presented in Willis et al. (2006). The SI method produces maps at the reservoir level of scattered energy associated to the presence of fracture corridors.

In this methodology, transfer functions of the fractured zone are estimated for a number of azimuths. Transfer functions are computed in three steps: (1) extraction of a wavelet from a time window above the reservoir; (2) extraction of a wavelet from a time window below the reservoir; and (3) deconvolution of the upper wavelet from the lower wavelet. Transfer functions reverberate and are less temporally compact in the azimuth parallel to fractures. The scattering index is a number that measures how much a transfer function oscillates. When compared azimuthally, the largest SI value yields the direction of fractures.

The Scattering Index method is performed in the CMP domain as opposed to the F-K method which is applied in the SHOT domain. Other practical differences of the methods include the length of the analysis time window. In the SI method the analysis is performed locally, around the horizon of interest, whereas in the F-K method the input data correspond to the relatively long coda arriving after the reflector generated by the top of the reservoir (figure 5-32).

In the computation of azimuthal stacks, offsets were limited between 0 and 4000 m. This range is slightly larger than the offset interval analyzed with the F-K method.

For the *SI* method, the data were sorted into azimuthal gathers every 20° with an overlap of 20°, as explained in section 5.1.

The Scattering Index method is applied to the Lynx field, post-stack and pre-stack, and the results are compared with the *F-K* method. The post-stack data are created by stacking all azimuthal stacks. In this case, only one trace per bin is inverted. In contrast, in the pre-stack version of the *SI* method several azimuthal stacks are treated per CMP or bin.

The Scattering Index method was applied to a total of four lithologic intervals: Dunvegan, Shaftesbury, Cadotte and Falher. The limitations and advantages of both methods are revised in section 5.4 in order to understand how these two techniques should be integrated to provide a more complete picture of reservoir fractures.

5.3.1 *SI* Post-Stack: Fractures Distribution and Intensity

The impulse response of the fractured reservoir can be estimated for both pre-stack and post-stack data. In all previous studies, the *SI* method has been applied to azimuthally stacked data. In this thesis, we apply the Scattering Index concept for the first time on post-stack data. The value of this approach is that it can be used as an initial and quick evaluation of the intensity of fracturing in an interval of interest. Practically any 3D seismic data volume could be processed with this technique. Once the data are stacked, the azimuth information is lost and the method can only indicate the relative amount of scattering from one location to the next. The detection of fractured areas would depend on the azimuthal fold. If there is adequate fold in the fracture direction, the scattered energy would remain in the final stack. If there is not enough fold in the fracture strike azimuth, the final stack will not contain the scattered energy; thus, fractures would be undetected.

Following the method, an input and output wavelet are computed in time windows above and below the horizon interval. Figure 5-33 shows these time windows for the Dunvegan, Shaftesbury, Cadotte, and Falher horizons plotted over the seismic section of inline 64. Given the short traveltime difference between the reflectors, the analysis windows overlap. Window lengths were selected after several tests performed for the

Cadotte level.

Figures 5-34 to 5-37 show normalized scattering indices at the Dunvegan, Shaftesbury, Cadotte, and Falher levels computed post-stack. Each of these maps is normalized independently so that differences in seismic trace amplitudes do not influence their interpretation. Scattering Index values are shown in three colors: black, gray and white. The cutoff levels for these three colors are indicated in the inset histograms. High values of *SI* are rendered as black areas. These areas possibly contain more intense fracturing. Alternatively, the fractures may be more tuned to seismic wavelengths in these areas. White areas correspond to either low values of *SI* or low fold areas that were left out of the analysis. Gray areas indicate intermediate values of *SI*.

The distribution of zones of high scattering changes between the Dunvegan, Cadotte, Shaftesbury, and Falher maps. The shallower, less folded formations (Dunvegan and Shaftesbury) appear less fractured on the west side of the survey than in the center and east parts. On the Cadotte and Falher maps greater scattering is shown on the west side of the survey. The structural folding in this region is mostly confined to the Cadotte. This is echoed by the intense fracturing observed on the *SI* map (figure 5-36).

As an example of the procedure, figure 5-38 shows a comparison of transfer functions computed for all horizons at CMP 16525. The location of the CMP is shown in figure 5-13. The transfer function associated with the Cadotte time level exhibits amplitudes an order of magnitude larger but, more importantly, reverberates longer in time than the corresponding transfer functions for Shaftesbury and Dunvegan. As a consequence, the scattering index computed up to lag 0.4 ms using equation 3.5 is 0.6 for the Cadotte and around 0.1 for the upper horizons.

5.3.2 *SI* Pre-Stack: Fractures Distribution, Intensity and Orientation

In this section we apply the scattering index method to a collection of azimuth stacks at each CMP. For the Lynx data set, 9 azimuth stacks were created as described above. For every horizon and for every CMP bin, 9 transfer functions and the corresponding 9 scattering indices are generated. These 9 *SI* values correspond to azimuthal groups centered at 20°, 40°, 60°, 80°, 100°, 120°, 140°, 160°, and 180° measured from geographical North in a clockwise sense.

As an example, figure 5-39 shows the *SI* processing steps for CMP 10460 (whose location is depicted in figure 5-13): (1) azimuthal stacks every 20° (top), (2) transfer functions obtained from the *SI* analysis around Cadotte (middle), and (3) corresponding scattering indices (bottom figure). For this CMP, the scattering index is 70% higher in the 40° azimuth than 90° away.

We determine the azimuth at which the scattering index has its maximum value for each CMP bin location. We also compute the difference between the maximum and minimum scattering index in the bin. Figures 5-40 to 5-43 show maps of the direction with the maximum scattering index values for the Dunvegan, Shaftesbury, Cadotte and Falher horizons. The colors indicate the extracted fracture azimuth directions. White bins indicate that the scattering index is not particularly dominant in any direction. For simplicity, only CMPS with maximum *SI* difference above a certain threshold (red line on the inset histograms) are displayed. This threshold was adjusted to test the match of the spatial correlation of high scattering regions in the post-stack maps. White bins also correspond to CMPs that had less fold than what was required (at least 5 traces with different offsets in all 9 azimuths).

A strong correlation is observed between these maps and their post-stack counterparts. The distribution of areas of high scattering varies spatially and with depth (or time). Similarly, the preferred orientation of fractures varies across the surveyed area in the different formations. This suggests that the in-situ stress field is not homogeneous or consistent with the regional stress field everywhere.

Upscaled Maps

To more easily look for trends in the scattering index maps we upscale the results in two ways: (1) grouping the extracted scattering index directions into larger, 45° bins, and (2) modal smoothing which assigns to each CMP the most common fracture direction in a small area (120 m x 120 m) surrounding it.

The new maps are shown in figures 5-44 and 5-45 for the Dunvegan and Cadotte levels respectively. The original maps had 9 fracture directions but after upscaling (by grouping) there are only four directions: N-S (green), E-W (yellow), NE-SW (red) or NW-SE (blue). In a similar way, the original maps showed directions for each CMP but after the modal smoothing, only consistent directions in 4 times the original bin size are preserved.

From these upscaled maps we see that at the Cadotte level, fracture strikes are preferentially due North or North-East (green and red). Some other areas exhibit fractures oriented normal to this N-NE predominant trend (yellow and blue). Fracture strikes NW-SE are more common at the Dunvegan. At this shallower level, orientations are in general less homogeneous than in the Cadotte unit. This suggests that the difference between maximum and minimum horizontal stress may be less pronounced in the overburden.

Fractures and Structure

An alternative way of displaying the *SI* results is shown using quivers in figures 5-46 and 5-47. Fracture orientations represented with vectors are superimposed on the Dunvegan and Cadotte time topography along with faults interpreted from migrated sections (provided by Dean Sinnott- ConocoPhillips). The length of each quiver represents the scattering intensity. The direction of each quiver shows the fracture strike.

These figures reveal NW-SE trending areas of intense fracturing interspaced by quiet areas. The orientation of the highly fractured bands aligns with the main structural trends, i.e. fold axes and strike of faults. Some correlation between fault strike

and fracture orientation can be found locally with directions parallel or orthogonal to the NW-SE trend. The bands of intense fracturing and rapid variation of fracture direction mapped with the *SI* method, could be used as a guide to interpret faults and locate new prospects. Changes of fracture orientation are known to occur in the proximity of faults or in places where the topography of the reservoir changes abruptly (Yale, 2003). As discussed in chapter 4, the high resolution imaging of structures and the interpretation of faults are complicated because Cadotte has weak reflectivity and is thin (below seismic resolution).[1] Our results provide additional insight about the structure and the stress field at the Cadotte and other horizons.

Histogram Maps and In Situ Stress

To simplify the identification of fracture trends, fracture orientations at the Cadotte and Dunvegan are histogrammed in areas of 500 x 500 m and shown as rose diagrams in figures 5-48 and 5-49. Only fracture directions (not intensity) are shown in this plot. The histograms are useful to identify locations where the fracture or stress direction is rotated from the regional stress direction expected for the area. For instance, in these figures histograms have been plotted in red when the most frequent direction is orthogonal to the regional $SHmax$, that is, between 100° and 140° azimuth. The rose histogram type of plot will be especially useful to make comparisons with the *F-K* results in the following section.

There are no acquisition footprint artifacts noticeable on these maps. The post-stack results are also useful to test the performance of the data binning explained in section 5.1. In a different experience applying the *SI* method to field data, it was observed that strong footprint can contaminate the results (Grandi et al., 2006). In that case, data re-sorting was not possible and geostatistical techniques were used to filter the fracture maps. In this case, because great care was taken to assure that CMPs/SHOTs analyzed had similar fold in azimuth and offset, *SI* maps do not show acquisition geometry or binning print; on the contrary, the distribution of

[1] A discussion about the implications of Cadotte thickness for the fracture processing is presented in appendix C

high-fracture areas seems to be related to geological structures.

5.4 Integration of Fracture Information from the *SI* and *F-K* Methods

In the integration of fracture descriptions obtained from the *F-K* and *SI* methods, the issue of the difference in resolution needs to be considered. The *SI* method operates in the CMP domain and in a time window around the reservoir. It measures fractures in an area about the size of the bin (60 x 60 m for Lynx). The *F-K* method operates in the SHOT domain and therefore probes reflection points covering multiple CMPs. It is easier to compare the results of these methods if the *SI* method is upscaled to the same resolution as the FK method.

An upscaled and histogrammed version of the *SI* fracture orientations found at the Cadotte level is shown in figure 5-50. The blue rose diagrams were computed in a radius of 500 m around the supershot locations to match the measurement resolution of the *F-K* analyses. Figure 5-51 depicts fracture orientations obtained from both methods at the Cadotte level. The red quivers show the orientation of fractures from the *F-K* method, and the blue quivers show the upscaled equivalents from the *SI* method. The blue *SI* quivers indicate the most frequent direction in the histograms shown in figure 5-50.

We decompose this figure in three cases: (1) where the results are similar; (2) where they are orthogonal; and (3) where the *SI* shows great variability in the local region of the supershot point.

Figure 5-52 highlights the locations where both methods yield similar orientations. Figure 5-53 highlights the locations where the *SI* method provides a distinct direction that is orthogonal, or at a high angle, to the *F-K* result. Figure 5-54 highlights the locations where the *SI* histogram shows great variability of fracture orientations not matching the *F-K* orientation.

Local differences as in the latter case may be related to the sensitivity of the *SI*

method to variations of fracture orientation that the *F-K* method misses given its averaging effect. In the former situation, differences could be attributed to presence of fractures in the overburden (see appendix C). Figures 5-55 and 5-56 show the comparison of both methods at the Dunvegan level.

5.5 Fracture Corridors, Cracks, and Stress

We compare the fracture information here derived with other types of fracture and stress data measured at 5 well locations of Lynx. In particular, we can compare our results with: (1) image logs at wells 10-22 and 3-19; (2) VeritasDGC's crack indicator calculated from wells 3-19, 9-16 and 9-17 (section 4.5); and (3) production data available of wells 10-22, 3-19, 9-17, and 9-16 (section 4.6). The image logs contain information about breakouts ($SHmax$ azimuth can be inferred), and orientation and density of cracks in the immediate vicinity of the borehole. The fracture and breakout interpretations obtained from image logs were provided by ConocoPhillips. The crack indicator is an estimation of crack concentration that may explain the velocity differences of the Cadotte from well to well. This estimation was based on an effective medium theory that assumes cracks are diluted in the rock. Our results using the *F-K* and *SI* correspond to fractures at the seismic scale (fracture corridors). Table 5.1 summarizes all the information.

Only well 10-28 falls in the high-fold *SI* maps shown above. Well 10-28 is a producer from Dunvegan. At this well, no image logs or cores are available. In order to make comparisons with other wells that have additional information about fractures we have to include lower fold bins. Figures 5-57 and 5-58 show color (smoothed) and quiver maps for the Cadotte when the requirement of minimum fold is relaxed (shown in figure 5-9). These maps provide information about fractures in a wider area of the survey but its utilization is cautioned. With this more extensive covering, information about fractures can be collected around wells 9-17, 9-16, 10-22, and 3-19. 3-19 is at the farthest location with respect to the high fold area thus comparisons with data from this well would be the least reliable. 10-22 is quite close to the high fold area.

With the exception of well 10-28, all the wells are deviated (directional wells).

Given the strong scale differences among the data shown in table 5.1, we make the following comparisons only in a qualitative sense:

- The *SI* and *F-K* method agree in their determinations of fracture orientation at wells 10-28 and 10-22. The predominant orientation of cracks observed in the image log of well 10-22 also agrees with the orientations derived with the seismic methods. However, $SHmax$ inferred from breakouts in this well (10-22) is orthogonal to the orientation of fractures and cracks. In this case, the fracture orientation matches the direction of the main axis of the folds (NW-SE). The *F-K* method predicts a relative large fracture spacing at this location (160 m) which may explain the relative low IP of this well and the relative low fracture density measured from the image log (0.18 $\#/m$). In addition, well 10-22 is deviated in the N-S direction which appears to be at an acute angle with respect to the orientation of fractures. This well may have had a better performace if it had crossed Cadotte in a NE-SW direction.

- The fracture directions derived from the scattering methods at the location of well 9-16 are similar. At this location, fractures are oriented NNE-SSW according to the *SI*, and NE-SW according to the *F-K* method. The initial production of this well (9.75 $mmcf/d$) and the crack concentration (11.8%) represent intermediate values with respect to the other wells. In the same way, fracture spacing at this location which is about 100 m, corresponds to a relative intermediate value as observed in the map of figure 5-26. This well may be producing from the matrix since fractures are expected to run parallel to the actual direction of the well which lowered the chance of crossing them.

- The *SI* and *F-K* methods disagree about the predominat orientation of fractures at the locations of wells 3-19 and 9-17. $SHmax$ azimuth is similar to the orientation of fractures obtained with the *F-K* method at the location of well 3-19. However, the image log of this well suggests that cracks are oriented similarly to the orientation of fractures obtained with the *SI* method. The

disagreement between the fracture scattering methods and the observations in well 3-19 may be related to the fold issues explained above. The disagreement of the *F-K* and *SI* results in well 9-17 may be related to the proximity of a fault (see figure 5-58). However, the location of well 9-17 shows a tight fracture set (70 m fracture spacing) and in this case the initial production was much higher (10.85 $mmcf/d$).

WELL	10-28	10-22	3-19	9-16	9-17
IP $[mmcf/d]$	NA	0.2	3.32	9.75	10.85
FD (productive) [#/m]	NA	0.18	0.32	NA	NA
FO (productive)	NA	NW-SE	WNW-ESE	NA	NA
Crack indicator [%]	NA	NA	18.2	11.8	13.9
$SHmax$ (BO)	NA	NE-SW	NNE-SSW	NA	NA
FO (SI)	NE-SW	NW-SE	NW-SE	NNE-SSW	NW-SE
FO (F-K)	NE-SW	NW-SE	NE-SW	NE-SW	NE-SW
FS [m]	66	160	64	100	70

Table 5.1: Orientation and spacing of fracture corridors, density and orientation of cracks, and $SHmax$ orientation in wells of Lynx. IP: Initial Production; FD (productive): Fracture Density interpreted in image logs; FO (productive): Fracture Orientation interpreted in image logs; Crack indicator: crack concentration percentage obtained by VeritasDGC (section 4.5); $SHmax$ (BO): azimuth of $SHmax$ inferred from breakouts (section 4.7); FO (SI): Fracture Orientation obtained with the SI method; FO (F-K): Fracture Orientation obtained with the F-K method; FS: Fracture Spacing obtained with the F-K method.

5.6 Summary

We applied two methods to describe fracture corridors in the Lynx field. In general, fracture orientations obtained from the Scattering Index method and the F-K analysis technique agree quite well across the survey. The dominant fracture direction coincides with the regional maximum horizontal stress orientation (NE-SW) and departures from this trend have been identified as stress-perturbed areas, possibly related to recent faulting or weak areas. Resolution of fracture orientation in the field is limited to 20° due to data azimuth fold.

Disagreements in fracture orientation obtained from both methods have been explained based on differences in resolution, the limitation of the *F-K* method to separate fracture response at the resevoir from the overburden, and differences in noise sensitivity between the two techniques. The *SI* method provides a higher resolution map showing local variations of fracture orientations. The spectral method complements the fracture description providing an estimation of fracture spacing. In Lynx, the fracture processing results provide additional, more detailed information about the reservoir to aid in its seismic interpretation.

The *SI* method can be applied post-stack to obtain a map of fracture distribution or intensity of the reservoir. It is a quick tool to evaluate large survey areas and it could be incorporated as a feasibility process in the regular data processing sequence to early detect areas of interest. The more detailed fracture processing using the *F-K* method and the pre-stack *SI* can then be applied to the highly fractured areas.

It has been found that relative fracture stiffness might be extracted from the spectral amplitudes of backscattered waves but a quantitative estimation would require a better understanding of attenuation phenomena in fractured media. It also remains for future projects to study the effects on the scattering energy of specific seismic data processes, as for example, seismic migration, and to develop an optimal processing sequence that preserves scattering energy.

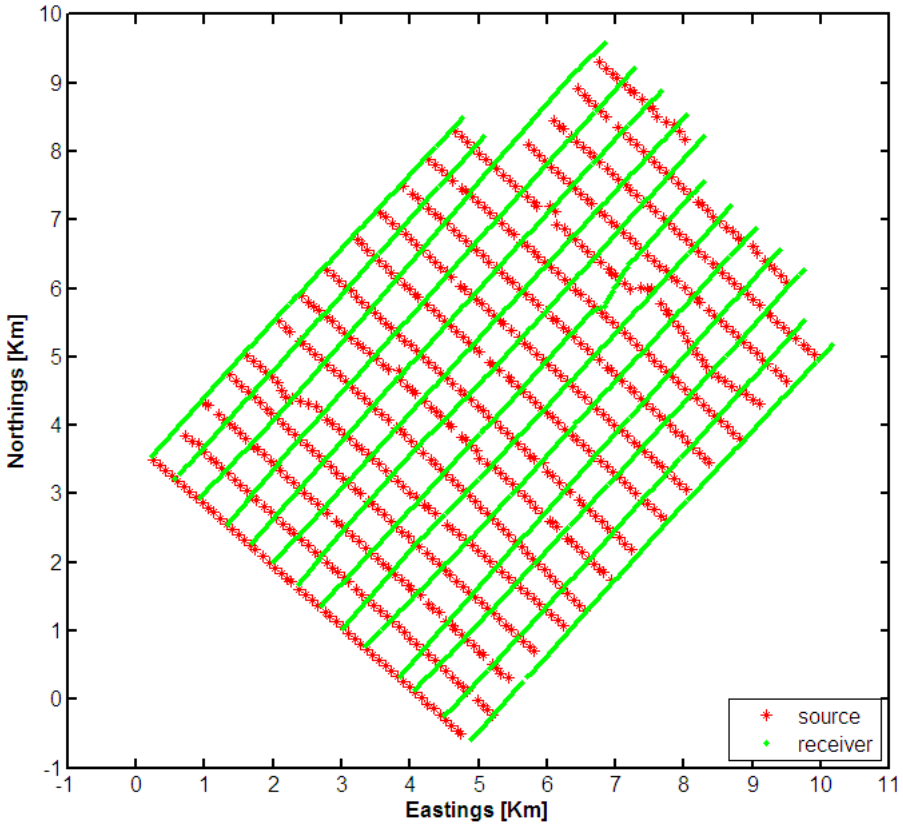

Figure 5-1: Lynx field 3D seismic survey.

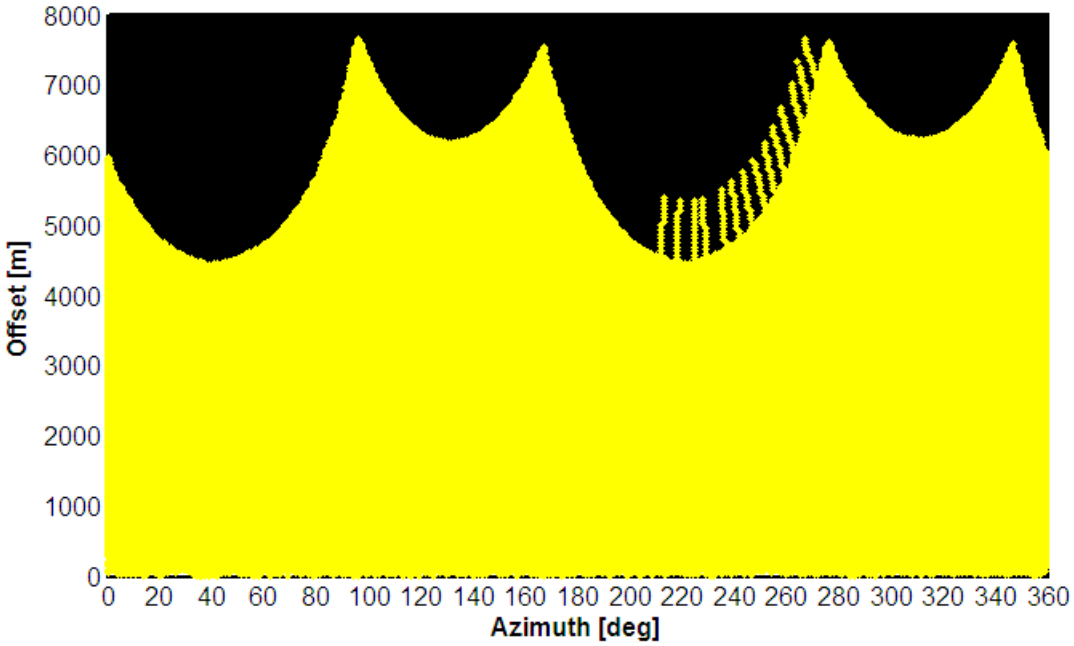

Figure 5-2: Offset vs. azimuth fold of the Lynx field 3D seismic survey. Yellow marks indicate that at the corresponding offset-azimuth value, fold is at least 1.

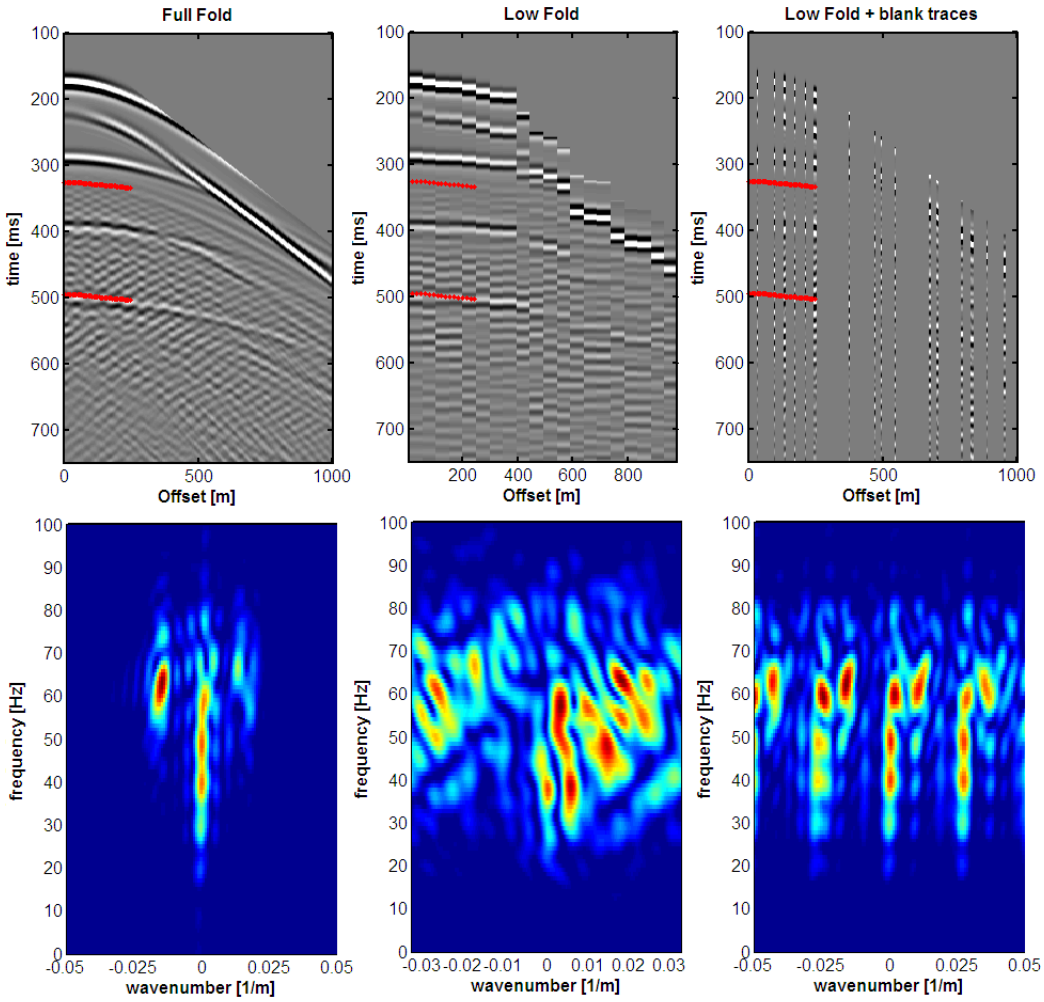

Figure 5-3: At the top, synthetic azimuthal gathers for the 5-layer fractured model described in section 3.2 at the direction normal to fractures. On the left, offsets in the record are regularly spaced every 5 m. Offsets in the middle record have been decimated irregularly. The shot record on the right have blank traces to fill up missing offsets. The bottom row plots display corresponding *f-k* spectra.

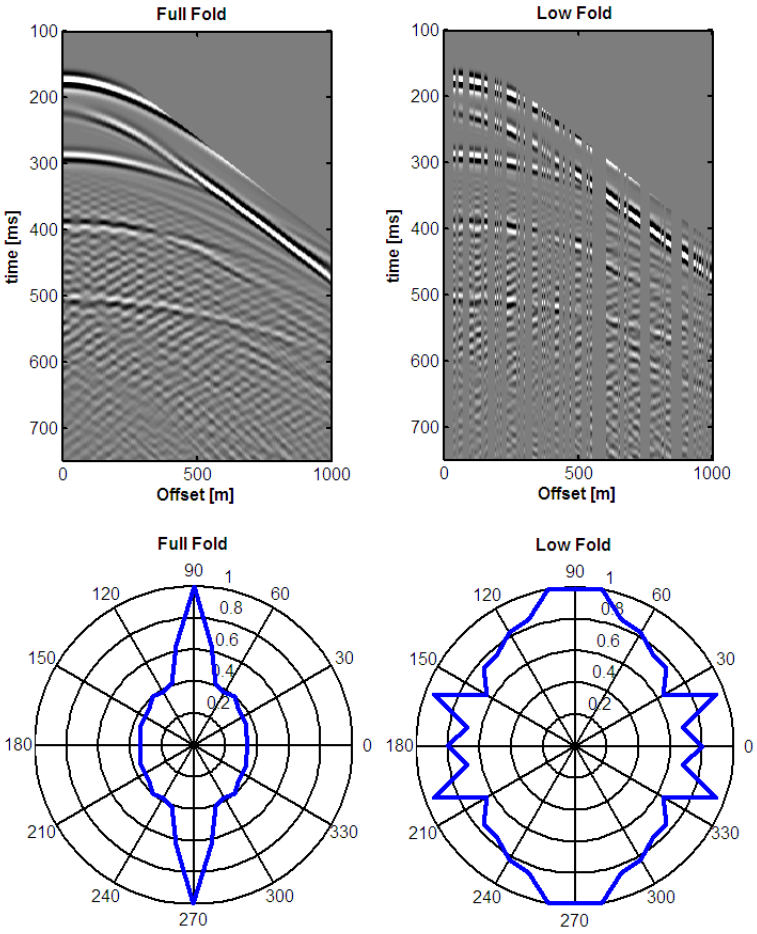

Figure 5-4: At the top, synthetic records of the 5-layer fractured model described in section 3.2 normal to fractures. On the right, offset distribution is irregular. Other azimuthal records have irregular fold as well (not shown). At the bottom, azimuthal variation of scattering index for the respective cases. Scattering index should maximize at the fracture direction (90°) in both cases, however fold irregularities challenge the performance of the *SI* method.

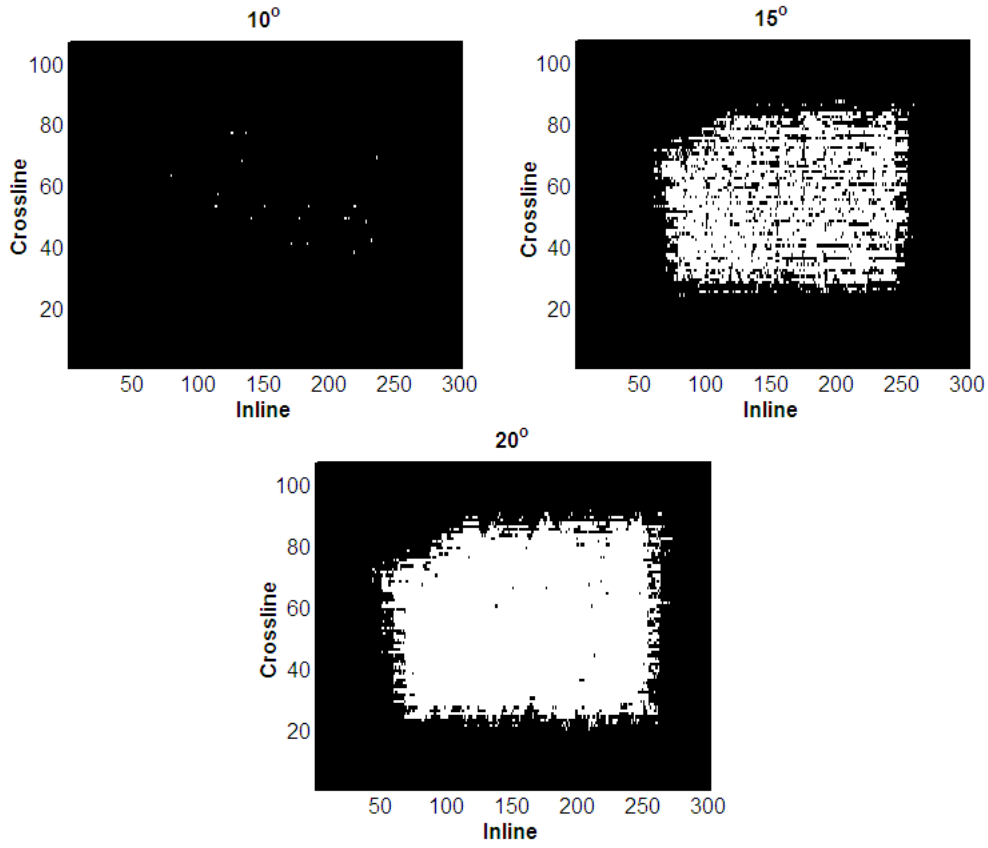

Figure 5-5: Lynx's data are sorted in azimuth in three different ways and coverage of high-fold data is compared. At the top left, CMP locations with at least 5 traces in each and all azimuthal gathers, formed every 10° with an overlap of 10°, are plotted in white. At the top right, the number of CMP locations with the same fold increases when data are sorted into 15° azimuthal gathers. Better coverage of high-fold data is obtained if data are sorted into 20° gathers with an overlap of 20° (bottom plot).

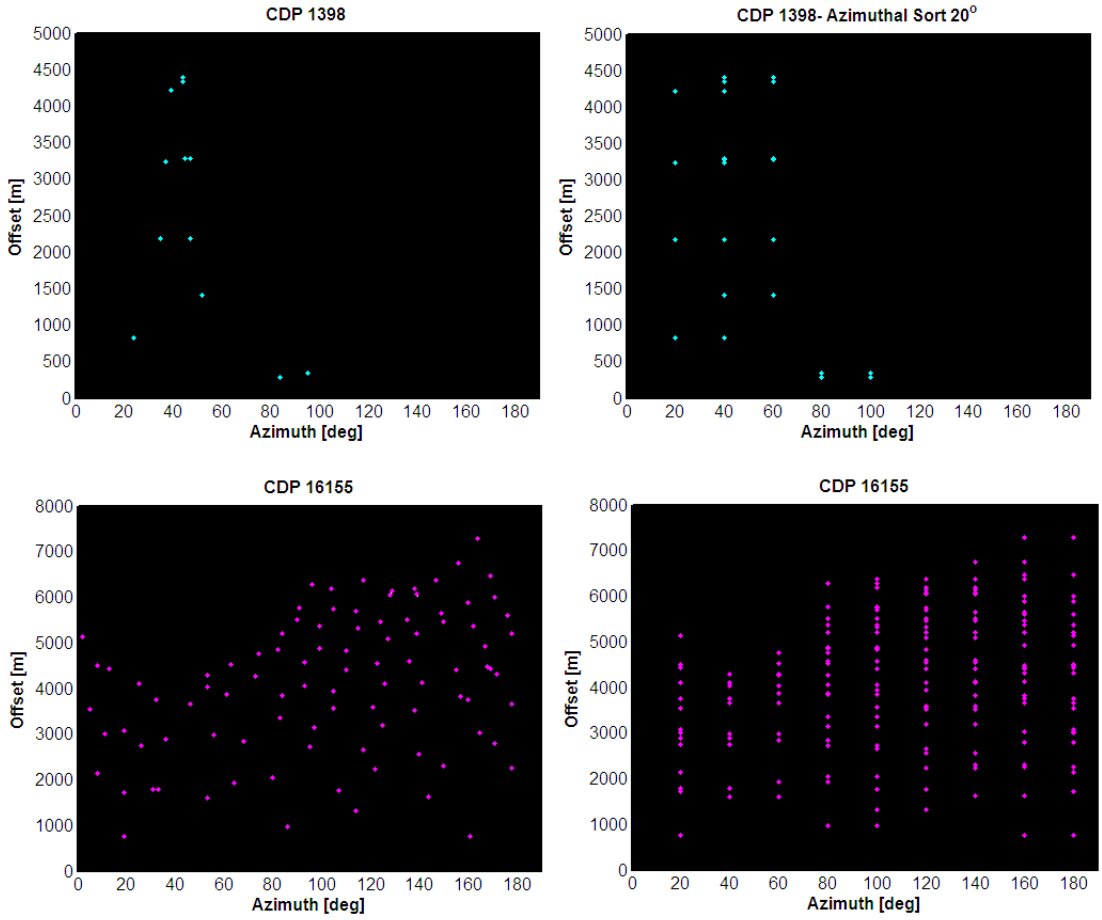

Figure 5-6: Offset-azimuth fold of CMP 1398 (top left) and CMP 16155 (bottom left) before and after regularization. CMP 1398 is on the edge of the survey and CMP 16155 is at the center as depicted in figure 5-7. Colored marks in all plots indicate fold is 1. The fold plots on the right show fold distribution of the same CMPs after sorting the data into 20° azimuthal gathers with an overlap of 20°.

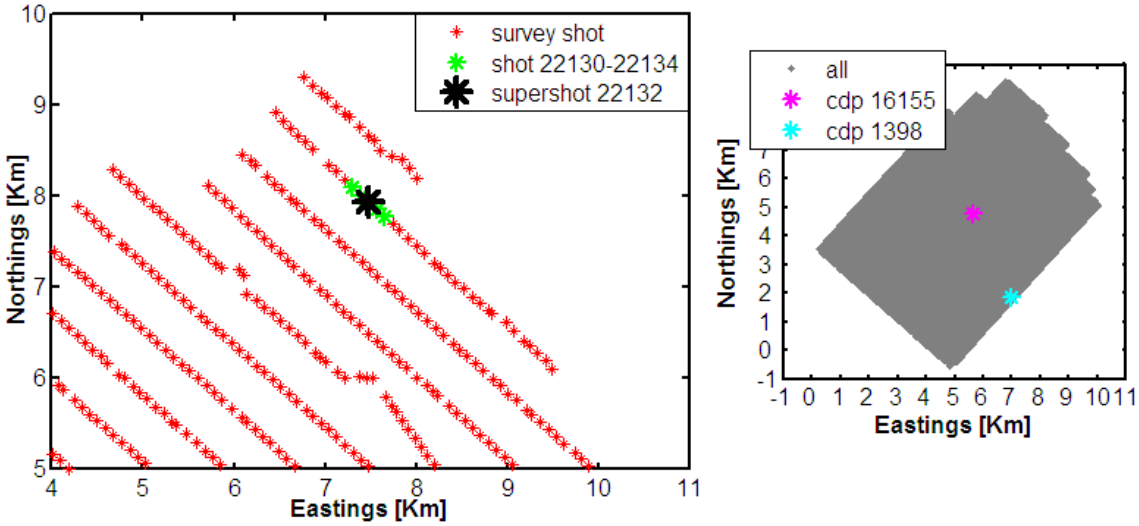

Figure 5-7: Supershot 22132 is formed by combining 4 shots around. Supershot 22132 is on the east of the survey (left plot). On the right, the location of CMPs 16155 and 1398 are highlighted over the CMP map of the Lynx survey.

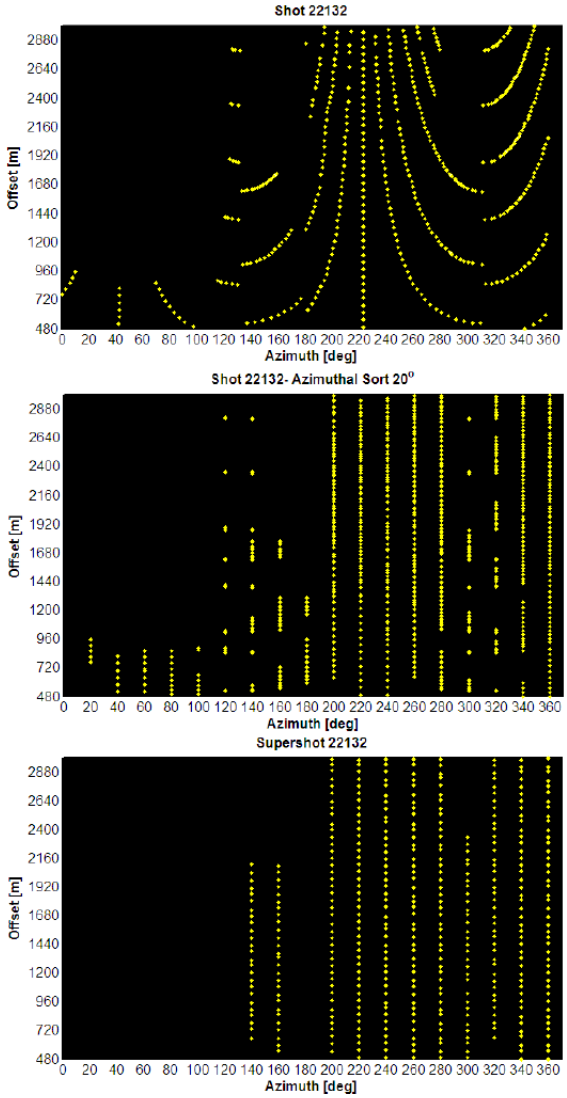

Figure 5-8: Fold Regularization of shot 22132. Yellow marks in all plots indicate fold is 1. At the top, original offset-azimuth fold of shot 22132. Shot 22132 is sorted in azimuthal records every 20° with an overlap of 20°. Fold after sectorization is irregular (middle). At the bottom, offset-azimuth fold for the supershot formed combining 22132 with neighbor shots to regularize the distribution of offsets at most azimuths. Location of shot 22132 is indicated in figure 5-7.

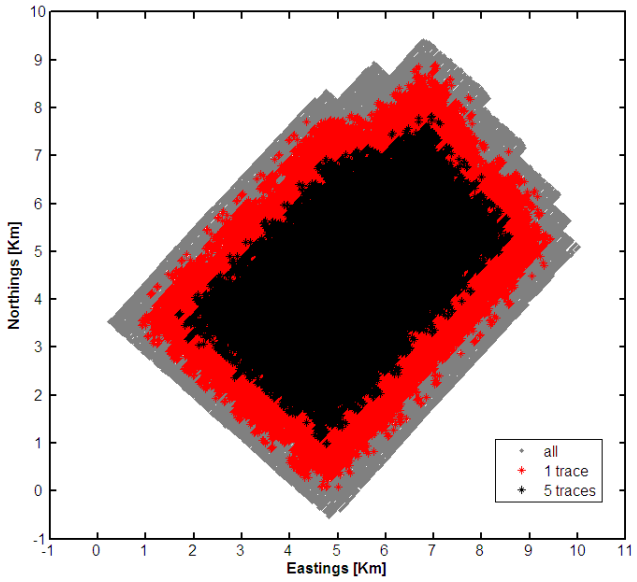

Figure 5-9: CMP map of Lynx's survey (gray). CMPs with at least 1 trace in each and all 20° azimuthal gathers are shown in red. Data processed with the *SI* technique are shown in black corresponding to CMPs with at least 5 traces in all azimuthal gathers (high-fold).

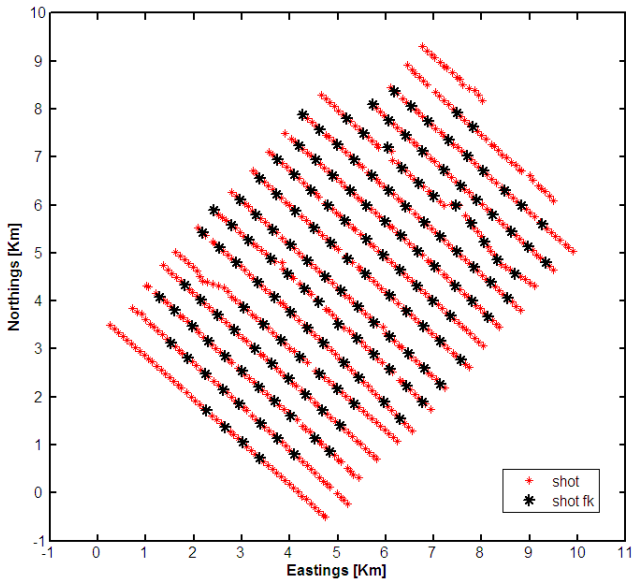

Figure 5-10: Map of supershot locations (black stars) to be processed with the *F-K* technique. One supershot is formed by combining approximately 4 shot records of the original Lynx survey (red stars).

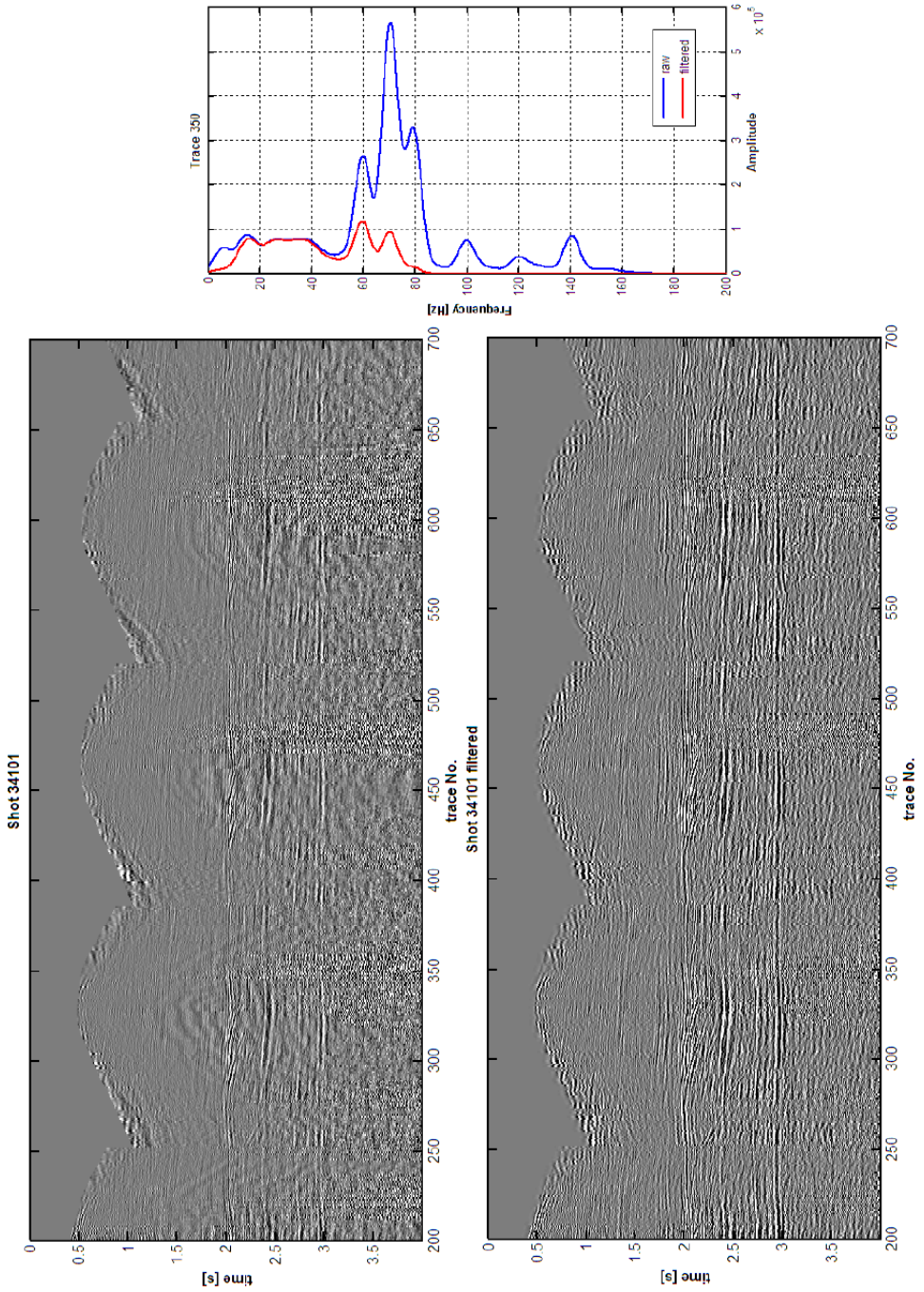

Figure 5-11: Lynx's data are filtered in frequency before the fracture processing. Three receiver lines of SHOT 34101's time-offset data are shown at the top (see figure 5-13 for location). Note the high-frequency noise especially at later times. At the bottom, high-frequencies have been filtered out. On the far right, the amplitude spectrum of an example trace is shown before and after filtering.

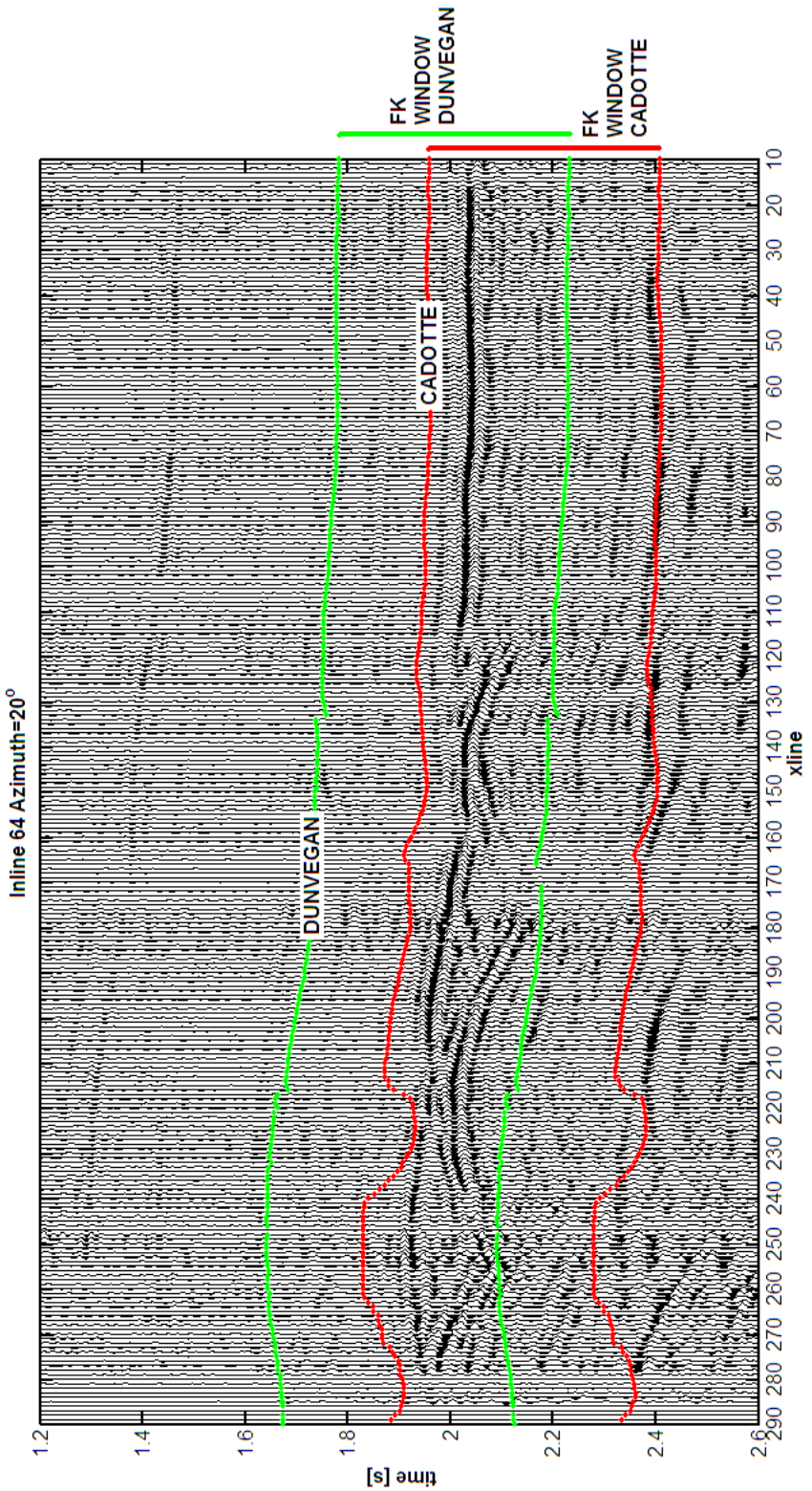

Figure 5-12: Time windows of F-K analysis for the Dunvegan (green) and Cadotte (red) horizons.

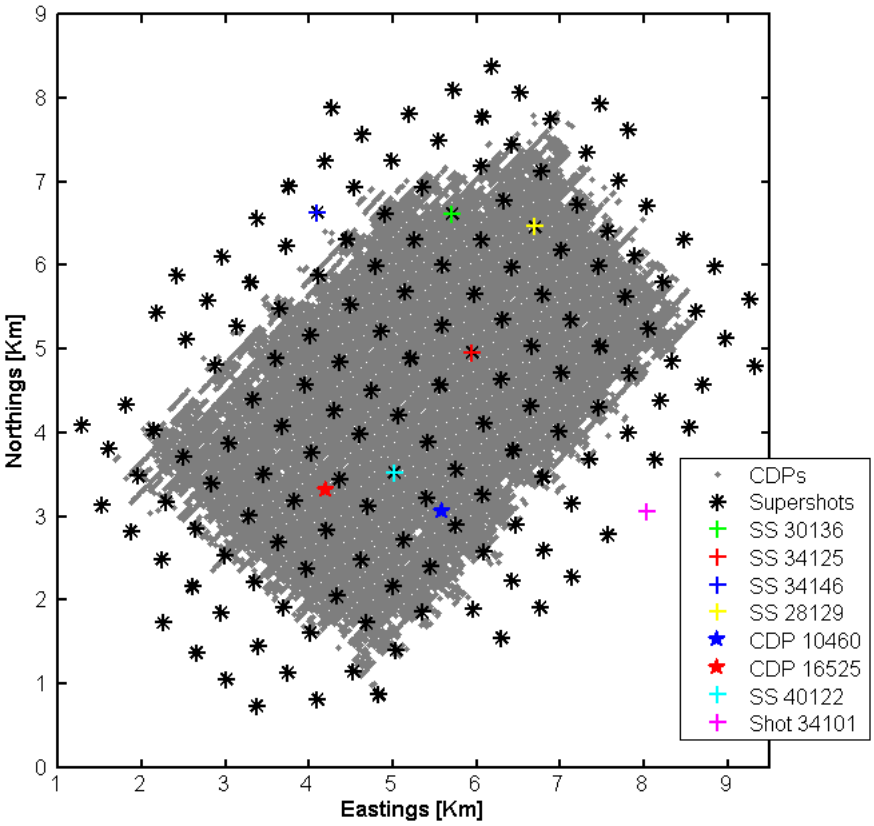

Figure 5-13: Supershot and CMP locations referred in the text.

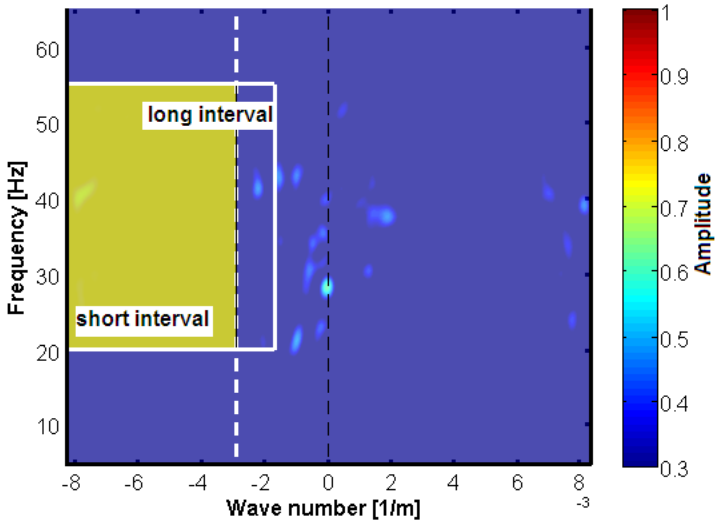

Figure 5-14: Frequency, wavenumber, and amplitude bounds to search backscattered waves in the *f-k* domain. Two intervals in the negative wave number interval are investigated: a short range from the Nyquist wave number until to -0.0029 $1/m$ and a longer interval extending up to -0.0017 $1/m$.

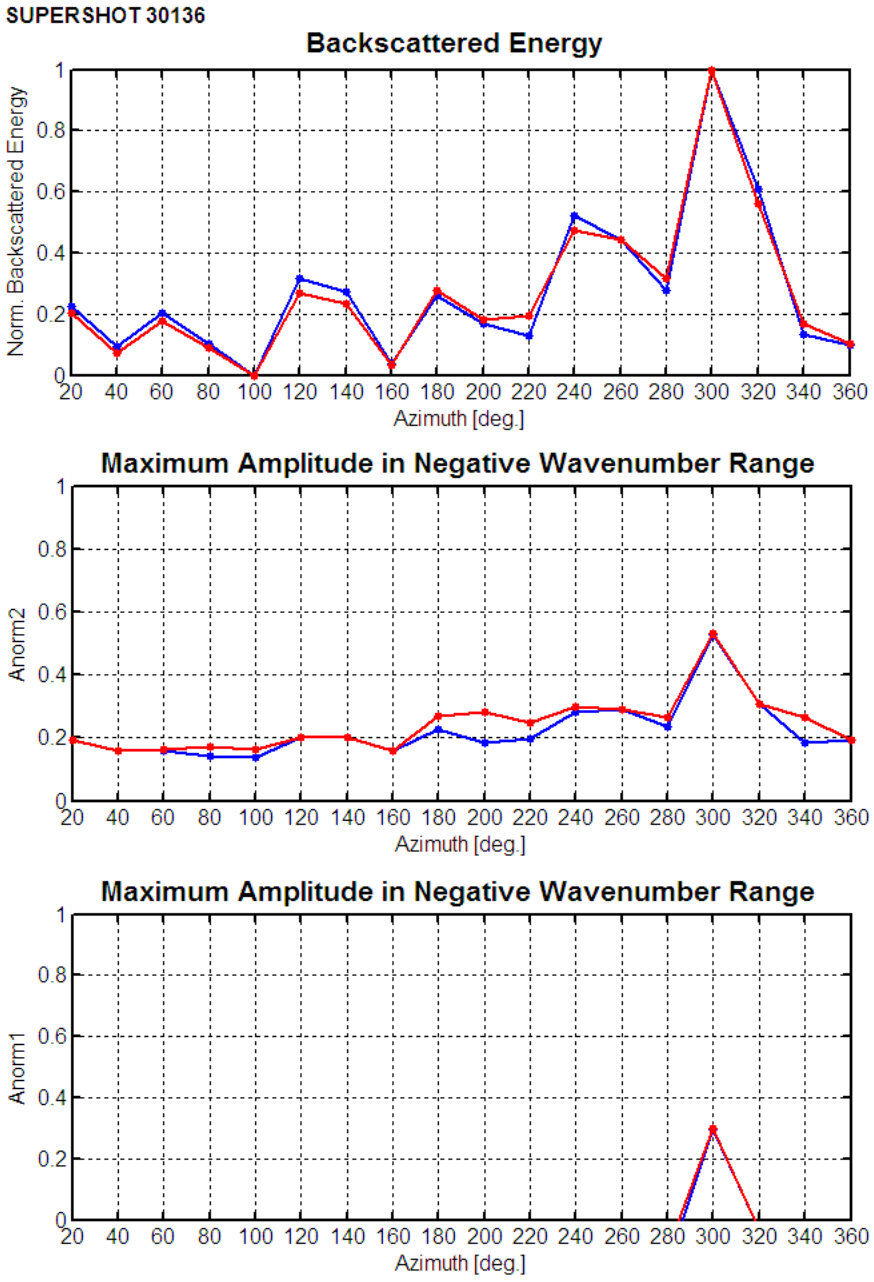

Figure 5-15: Supershot 30136 backscattered energy (top) and maximum amplitude functions (middle plot $Anorm2$ and lower plot $Anorm1$). Function values in short wave number range are displayed in blue and in red for the long wave number range.

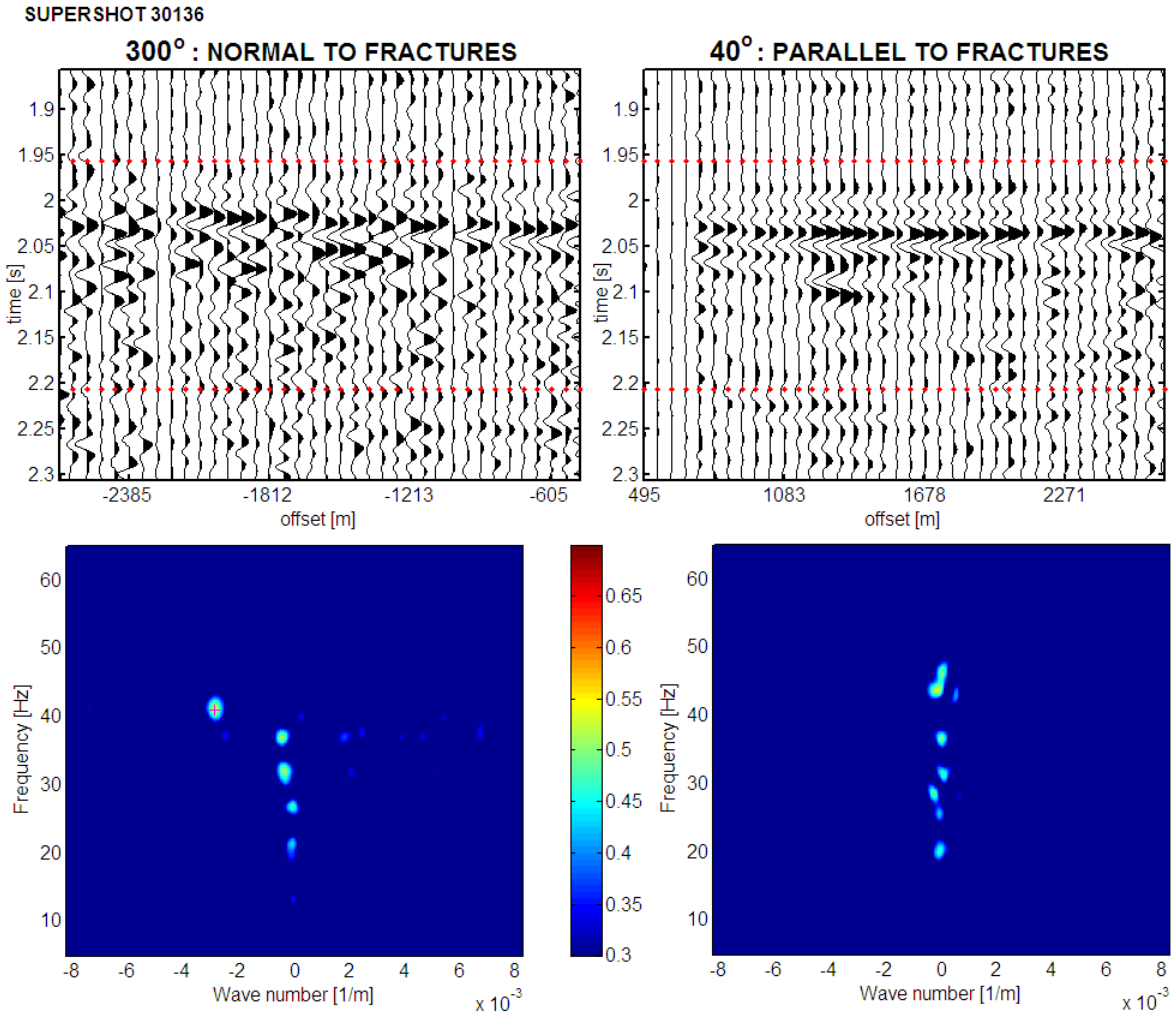

Figure 5-16: 300 and 40° azimuthal gathers (perpendicular and parallel to fracture strike), at the location of supershot 30136. Cadotte's time and the window length taken in the *f-k* analysis are indicated in red. Below, *f-k* spectra of the same gathers. Amplitude has been normalized using equation 5.2. Peak amplitude picked as the backscattered *f-k* component off fractures is indicated with a magenta (+) sign.

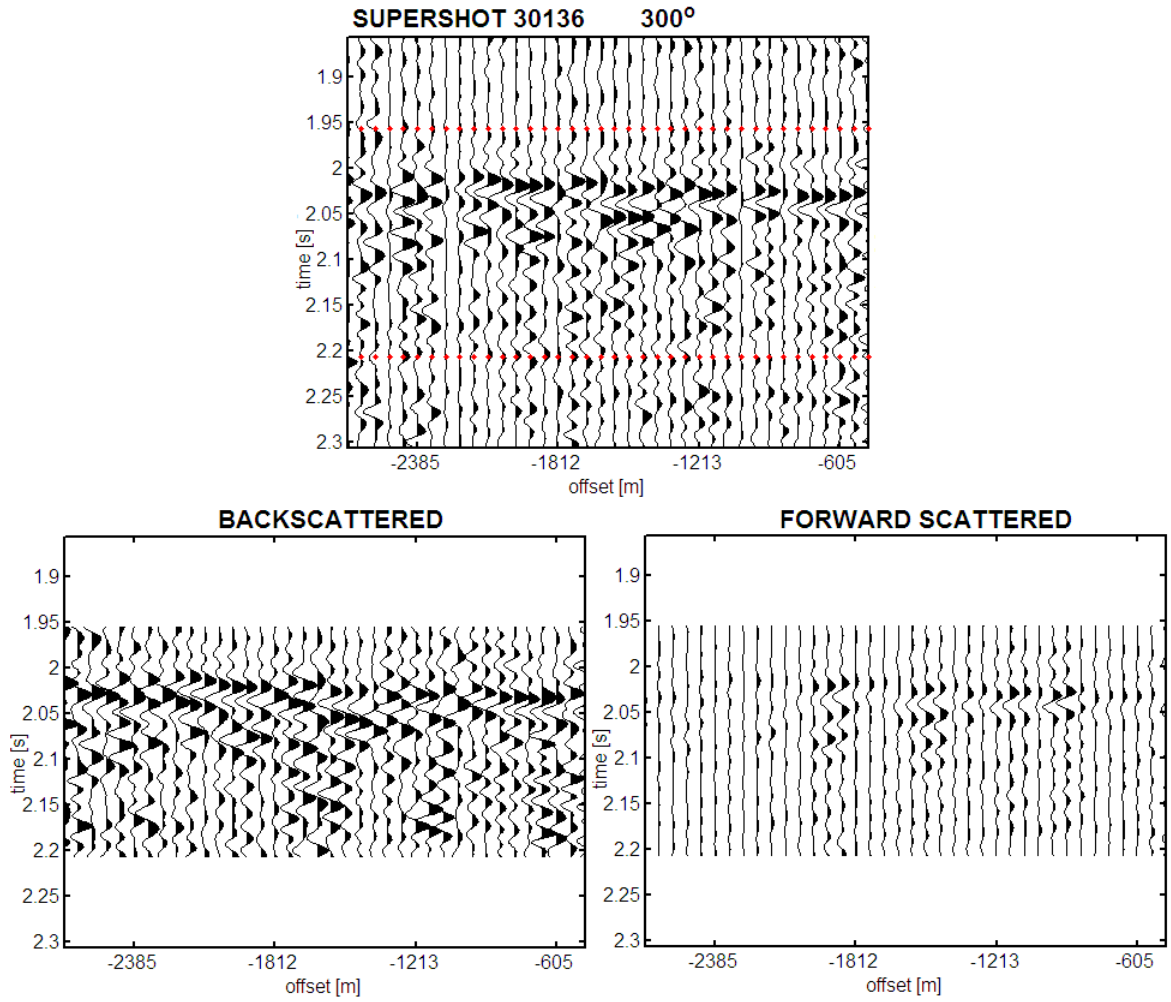

Figure 5-17: A *f-k* pass-reject filter is applied to the time-offset 300° azimuthal gather, which corresponds to the direction normal to fracture strike at the location of supershot 30136. Negative f-k region is filtered out to isolate the backscattered component (lower left) from the forward scattered waves (lower right).

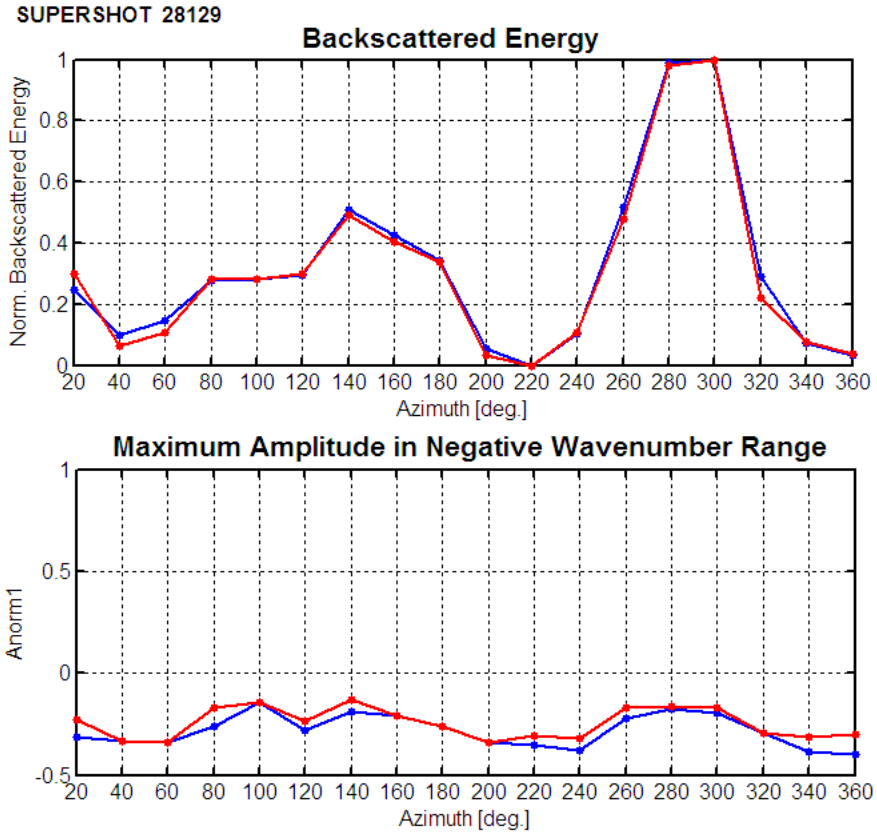

Figure 5-18: At the top, backscattered energy function vs. azimuth computed for supershot 28129 in the short wave number region (blue) and in the long wave number region (red). At the middle and lower plots the variation of peak amplitude with azimuth is shown after normalizing using equations 5.2 and 5.1.

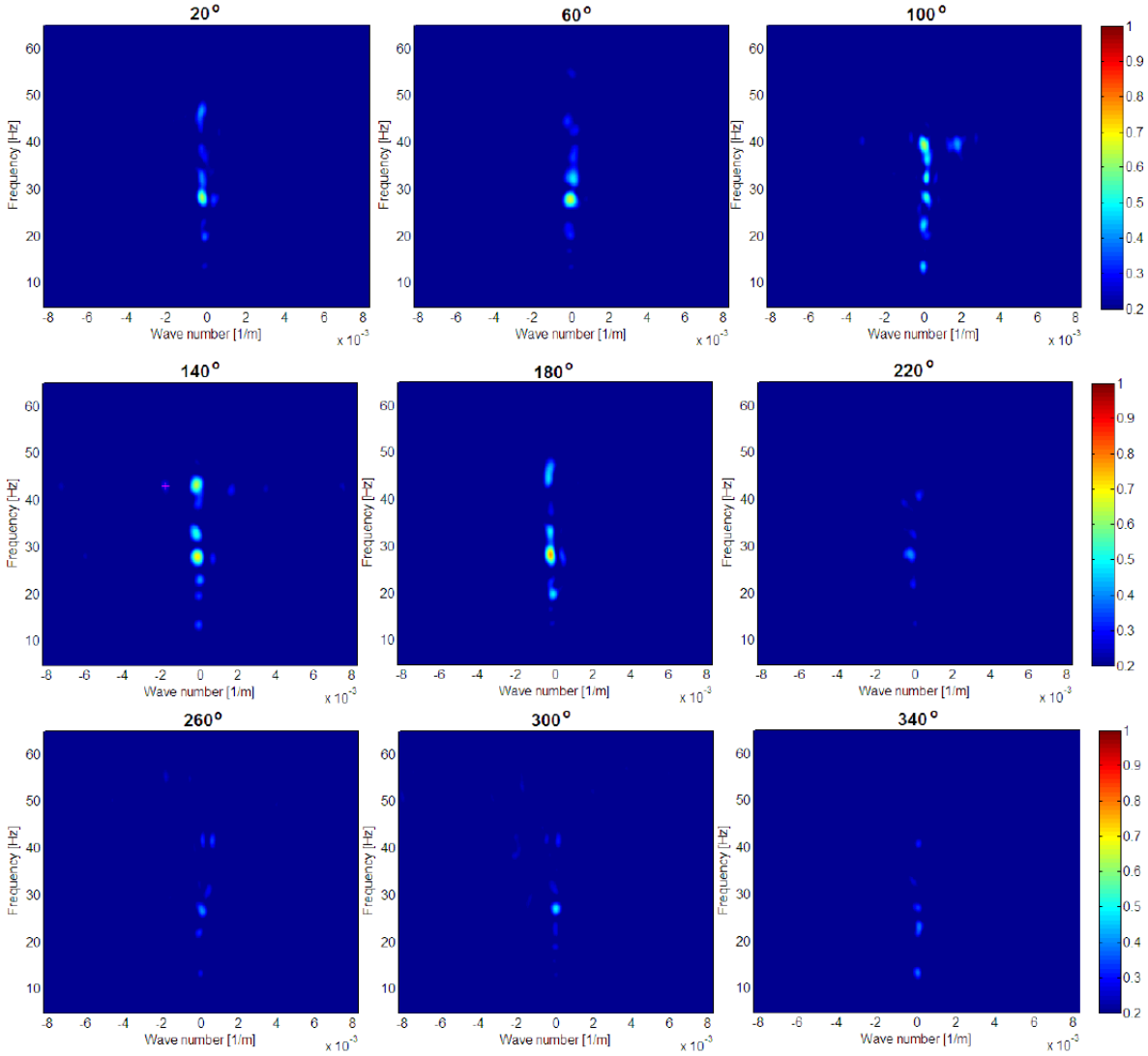

Figure 5-19: *F-k* amplitude spectra of azimuthal gathers of supershot 28129 computed at Cadotte's level. Distribution of energy is very similar at all azimuths. A dim peak amplitude in the negative wavenumber space is picked at 140° (magenta + sign).

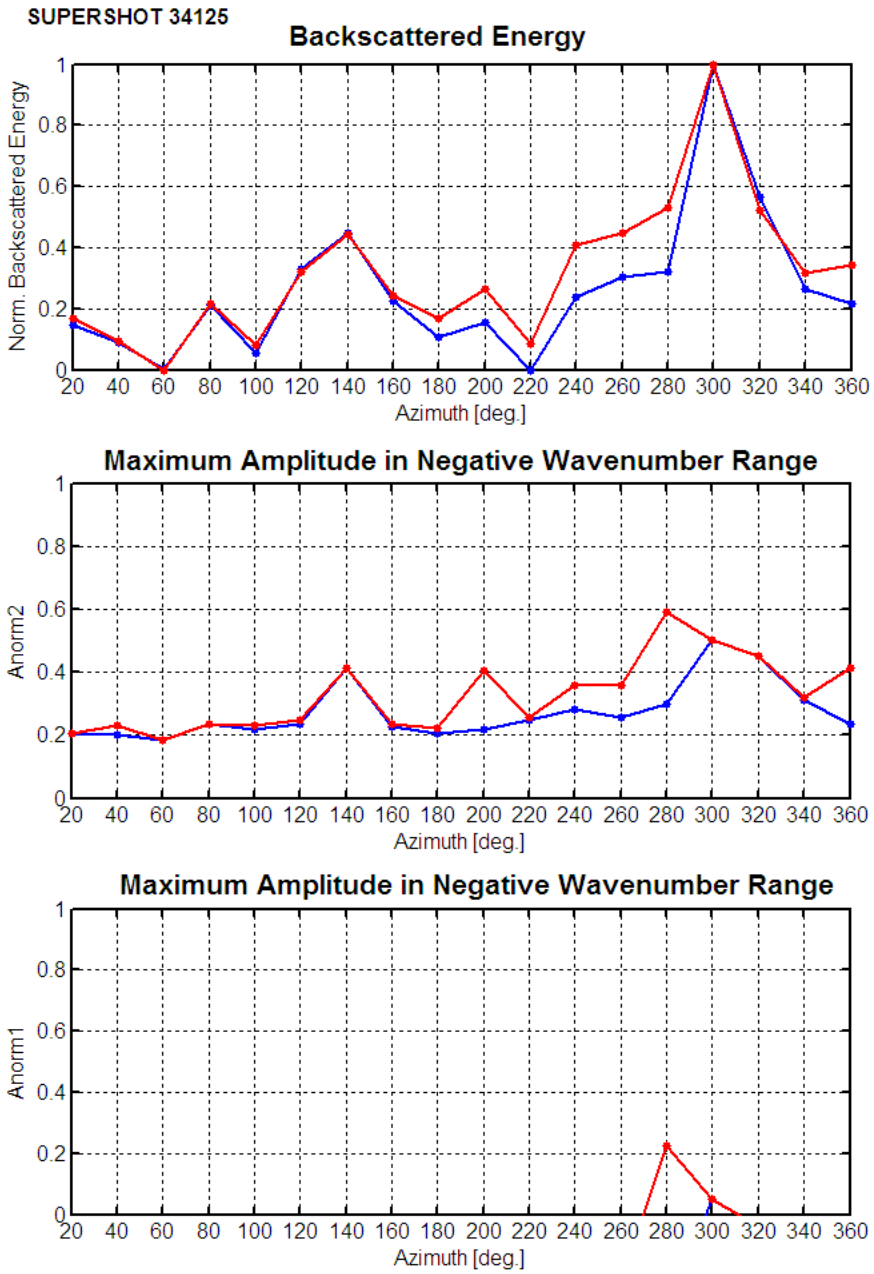

Figure 5-20: Backscattered energy vs. azimuth for supershot 34125 (top). Short wave number region is plotted in blue and long wave number region in red. Middle and lower plots correspond to the variation of peak amplitude in the negative wavenumber regions with azimuth normalized in two different ways.

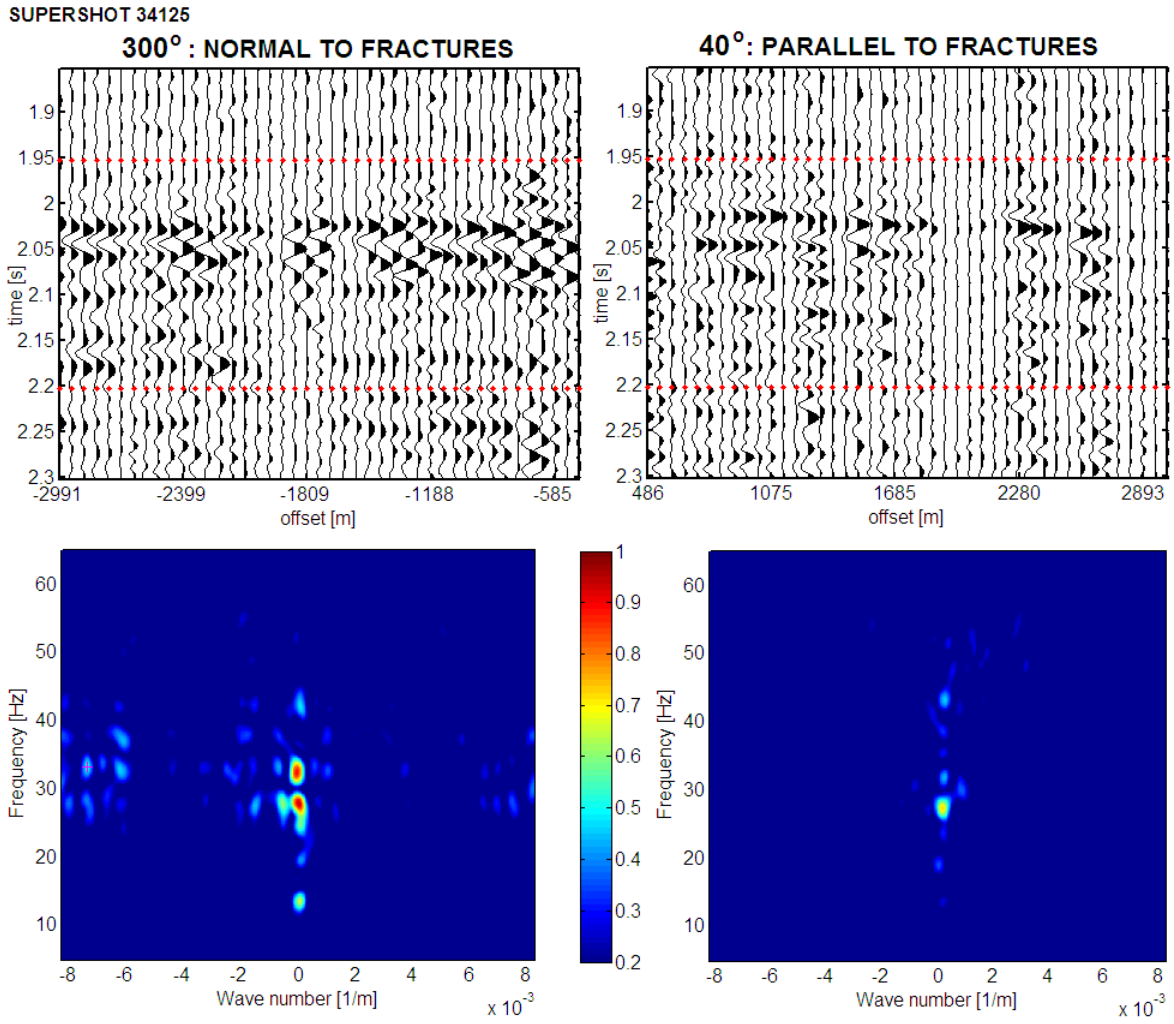

Figure 5-21: 300 and 40° azimuthal gathers, which correspond to the directions perpendicular and parallel to fracture strike at the location of supershot 34125. Cadotte's time and the window length taken in the F-K analysis are indicated in red. Below, f-k spectra of the same gathers. Amplitude has been normalized using equation 5.2. Peak amplitude picked as the backscattered f-k component off fractures at this location is indicated with a magenta (+) sign.

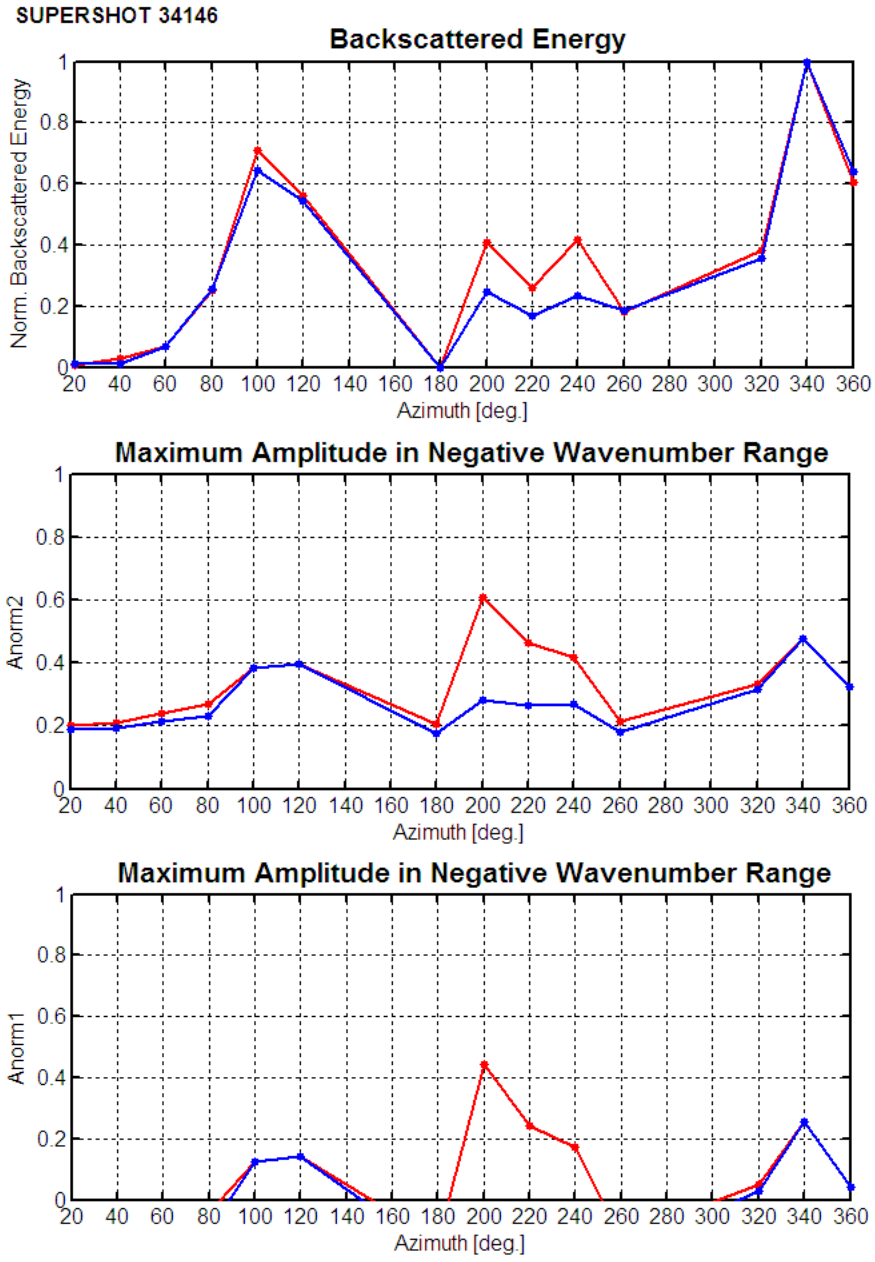

Figure 5-22: At the top, backscattered energy function vs. azimuth computed for supershot 34146 in the short wave number region (blue) and in the long wave number region (red). At the middle and lower plots the variation of peak amplitude with azimuth is shown after normalizing using equations 5.2 and 5.1.

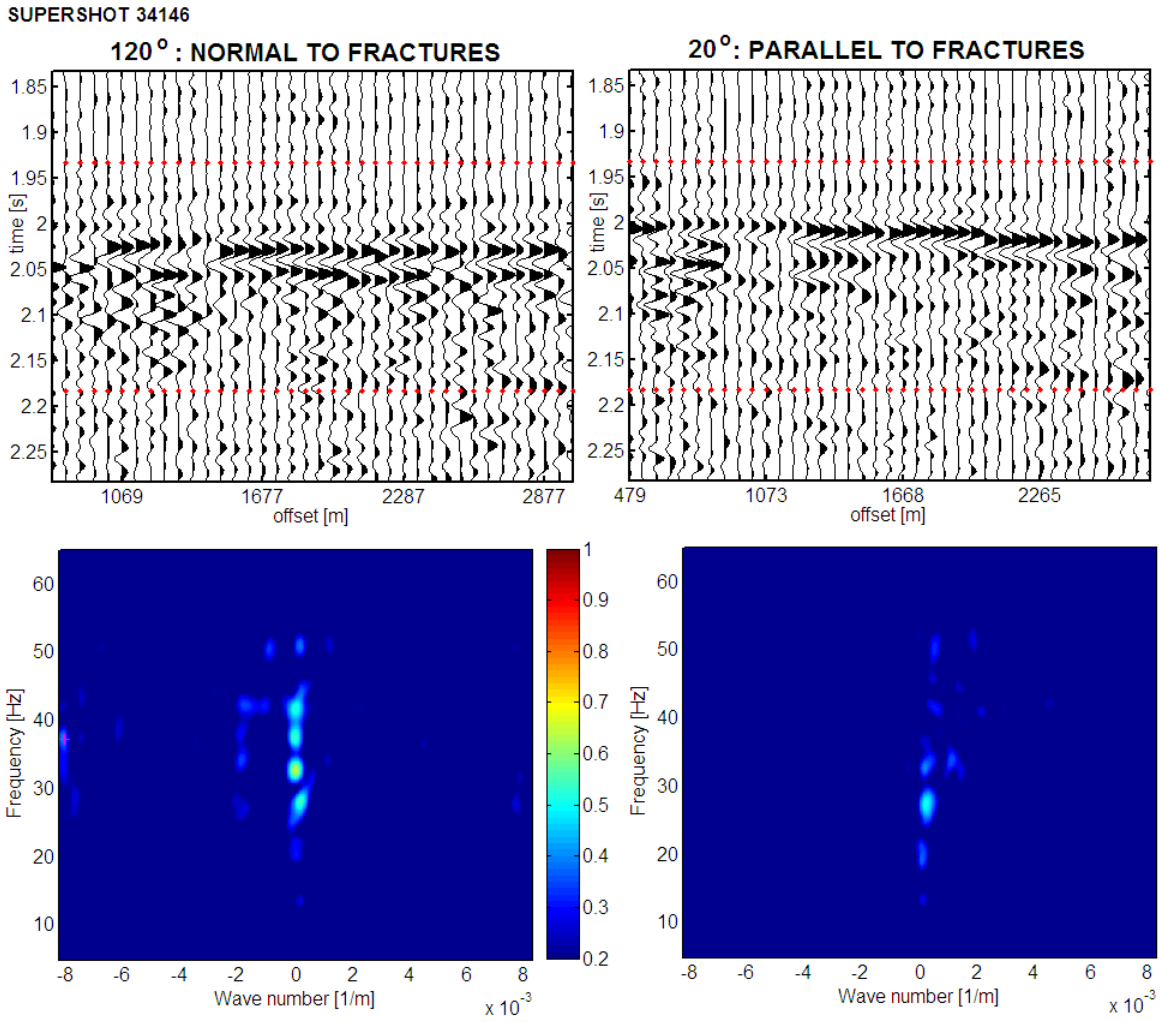

Figure 5-23: 120 and 20° azimuthal gathers (the directions perpendicular and parallel to fracture strike) at the location of supershot 34146. Cadotte's time and the window length taken in the *F-K* analysis are indicated in red. Below, *f-k* spectra of the same gathers. Amplitude has been normalized using equation 5.2. Peak amplitude picked as the backscattered *f-k* component off fractures at this location is indicated with a magenta (+) sign.

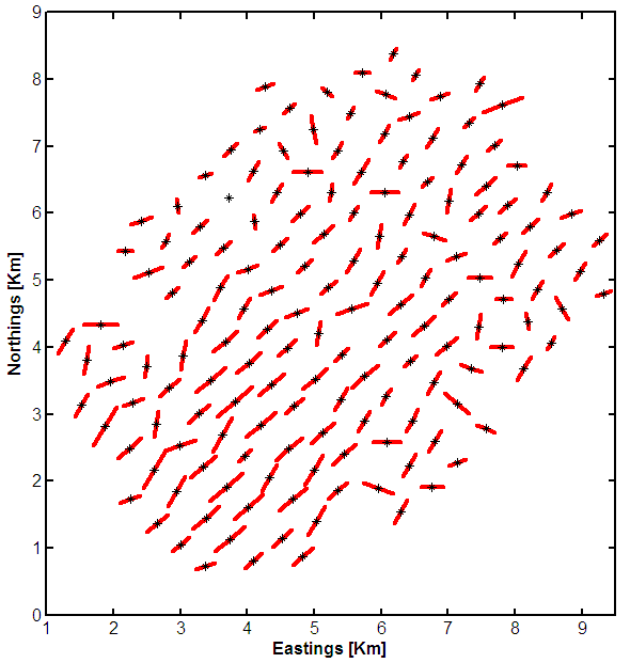

Figure 5-24: Fracture orientation map at the Cadotte from the *F-K* method. Supershot locations are indicated with black stars. Vector's length is proportional to peak amplitude.

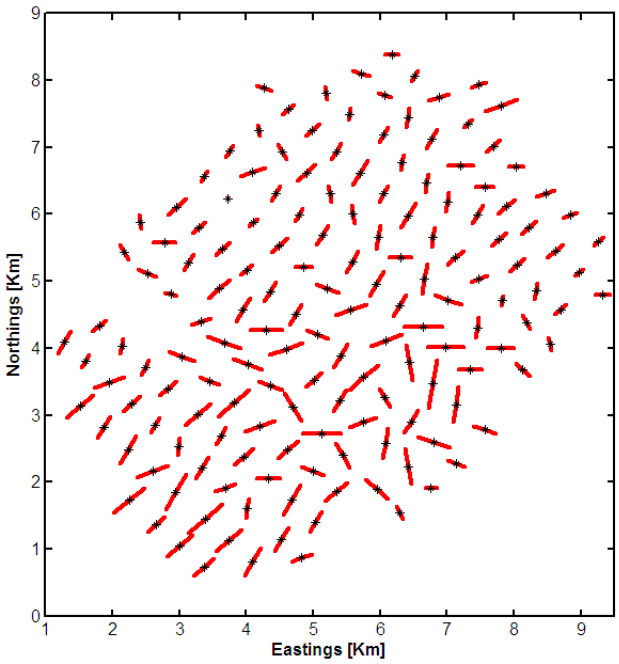

Figure 5-25: Fracture orientation map at the Dunvegan from the *F-K* method. Supershot locations are indicated with black stars. Vector's length is proportional to peak amplitude.

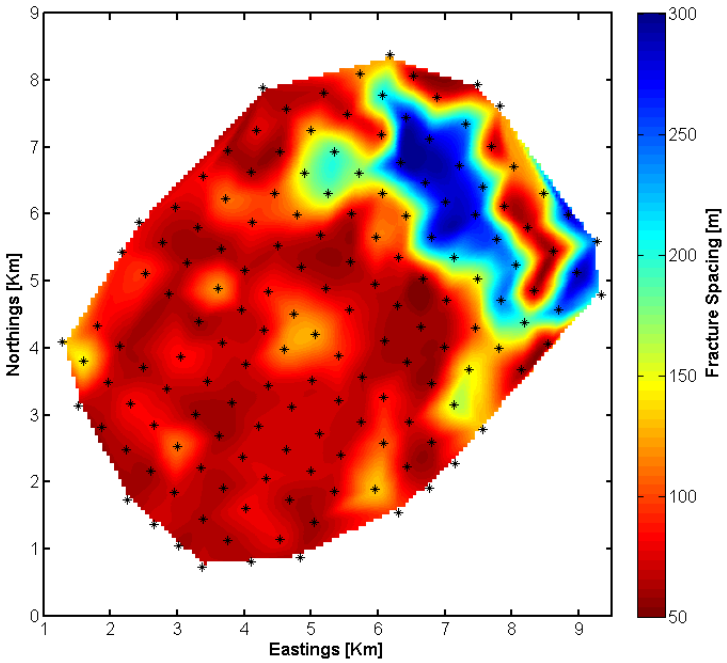

Figure 5-26: Fracture spacing map at the Cadotte (F-K method). Supershot locations are indicated with black stars.

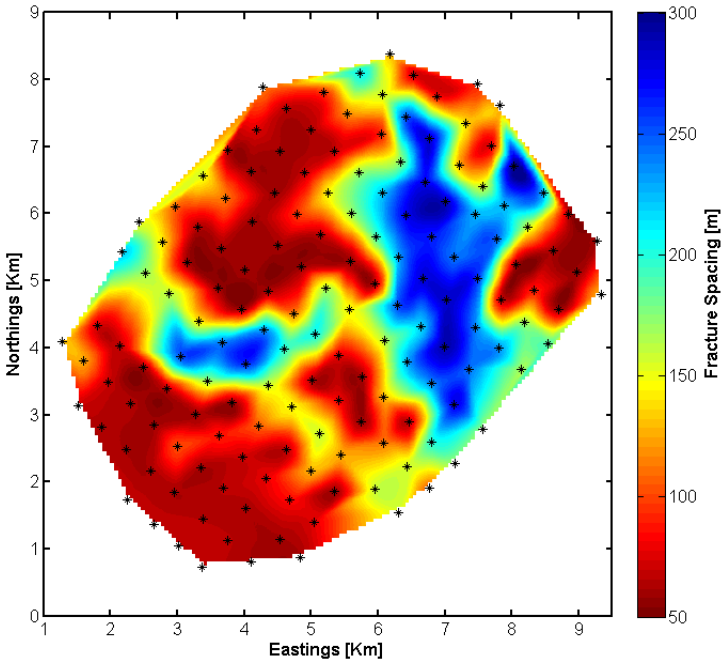

Figure 5-27: Fracture spacing map at the Dunvegan (F-K method). Supershot locations are indicated with black stars.

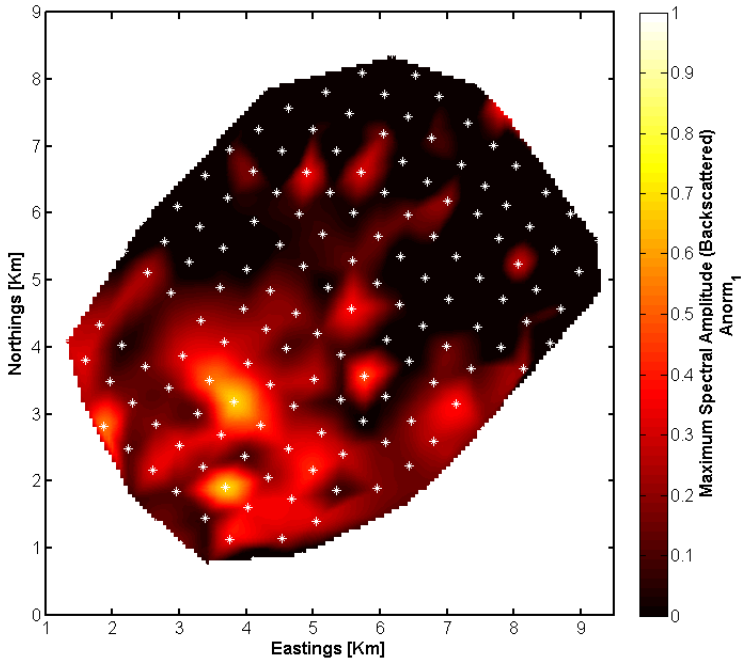

Figure 5-28: Amplitude map of backscattered waves at the Cadotte (F-K method). Amplitude has been normalized using equation 5.1. Supershot locations are indicated with white stars.

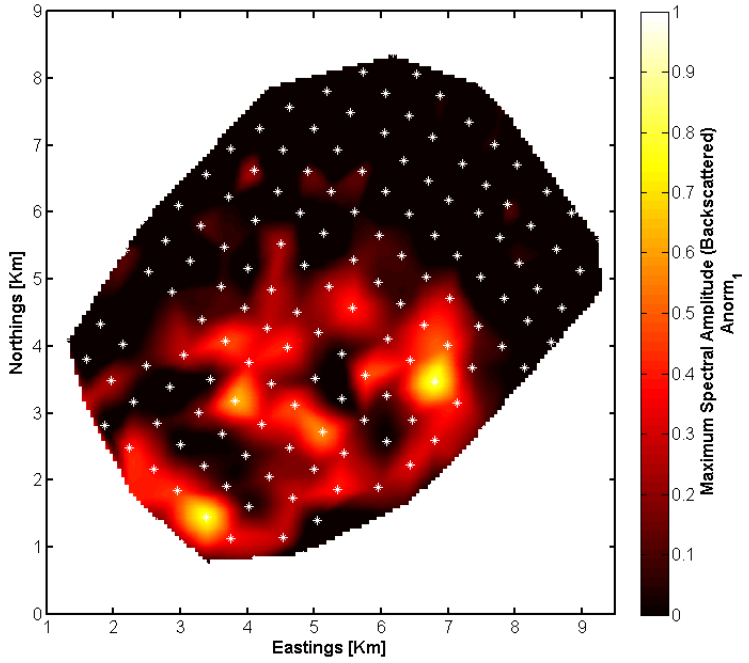

Figure 5-29: Amplitude map of backscattered waves at the Dunvegan (F-K method). Amplitude has been normalized using equation 5.1. Supershot locations are indicated with white stars.

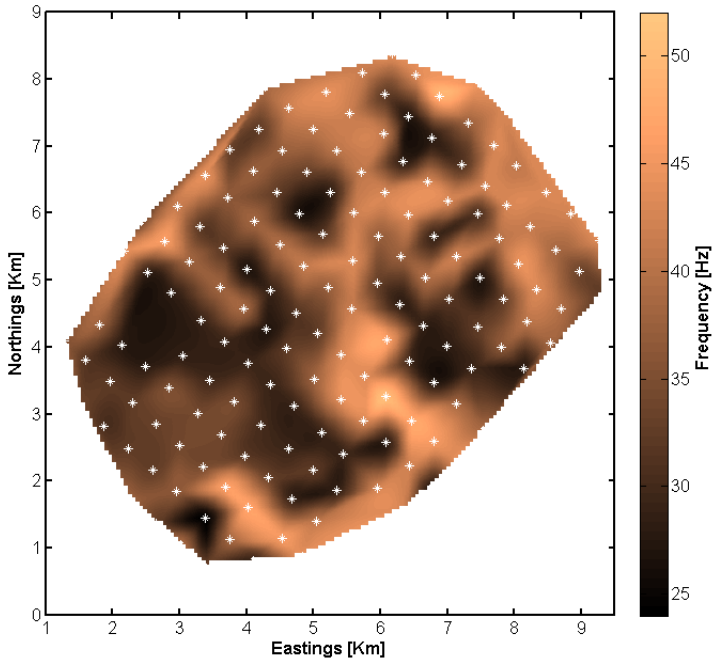

Figure 5-30: Frequency map of backscattered waves at the Cadotte (F-K method). Supershot locations are indicated with white stars.

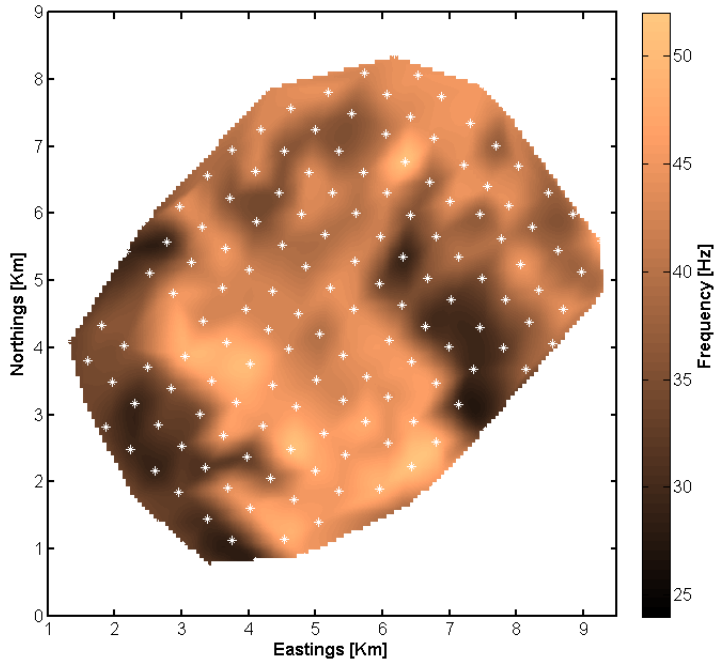

Figure 5-31: Frequency map of backscattered waves at the Dunvegan (F-K method). Supershot locations are indicated with white stars.

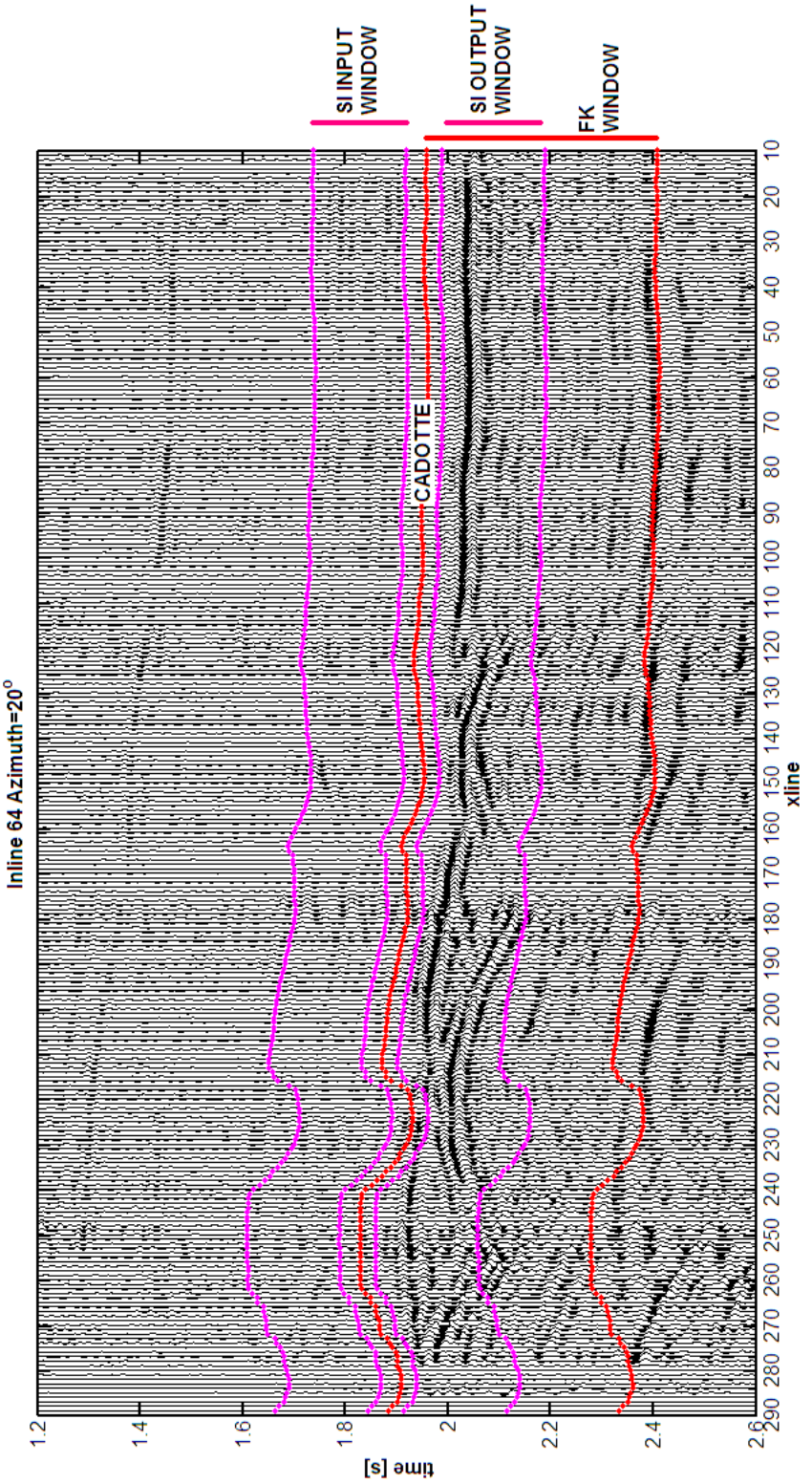

Figure 5-32: Comparison between window length used for the F-K analysis and the SI method.

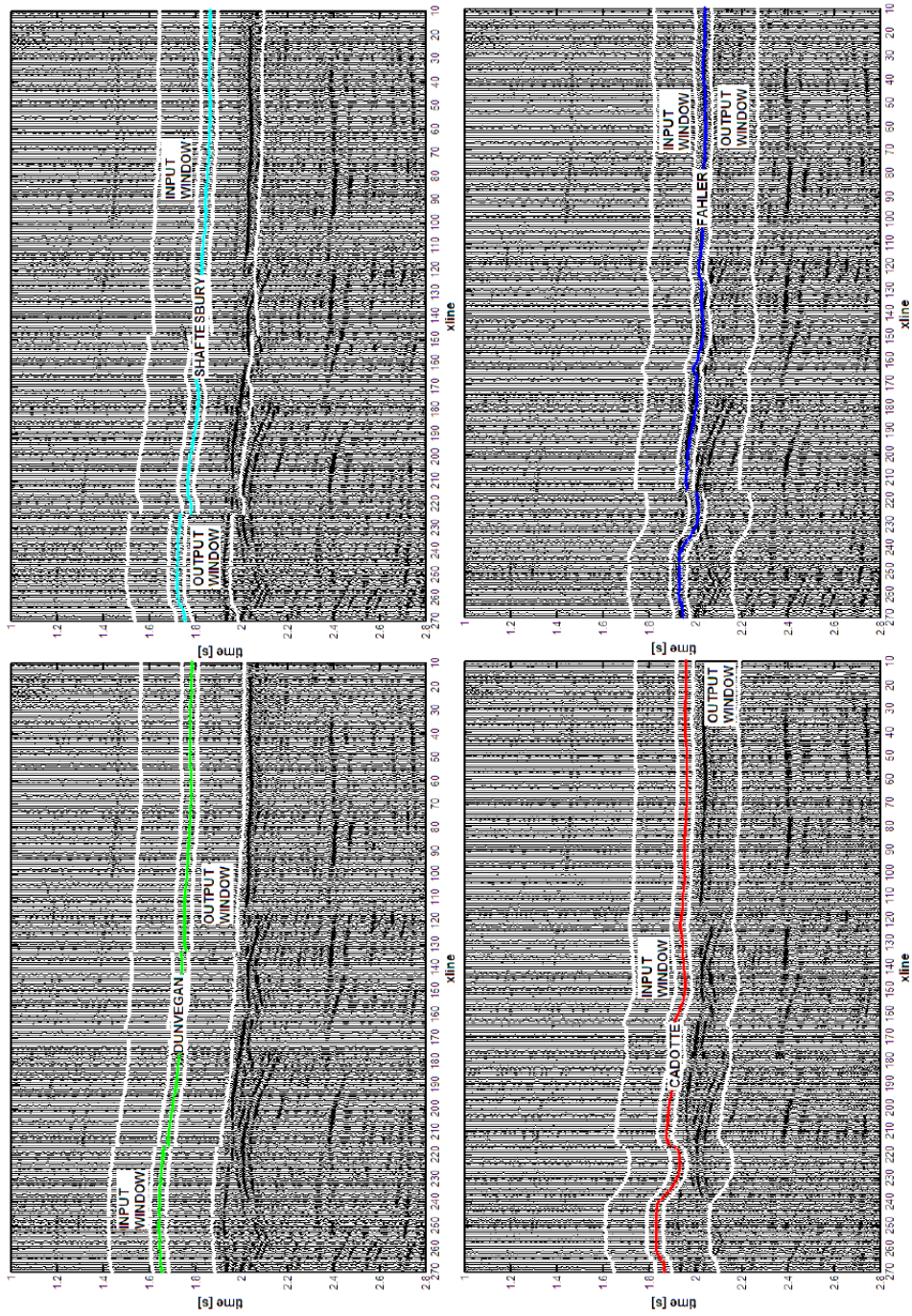

Figure 5-33: Inline 64 of Lynx survey and seismic interpretation of time horizons corresponding to the top of Dunvegan (upper left, green), Shaftesbury (upper right, cyan), Cadotte (lower left, red) and Falher (lower right, blue). The time windows to extract input and output wavelets for each horizon analyzed are indicated in white.

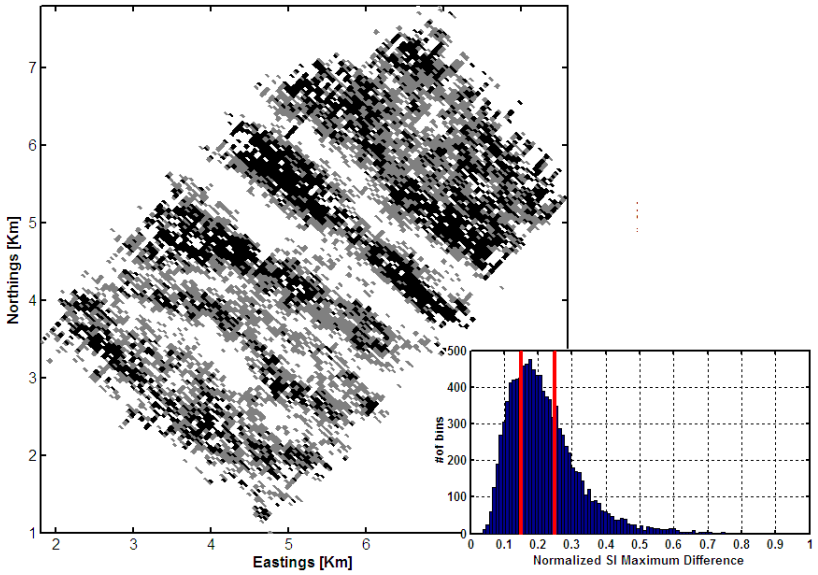

Figure 5-34: Map of fracture distribution and intensity at Dunvegan. Black, gray and white areas show decreasing levels of post-stack scattering indices following the thresholds of *SI* values identified in the inset histogram.

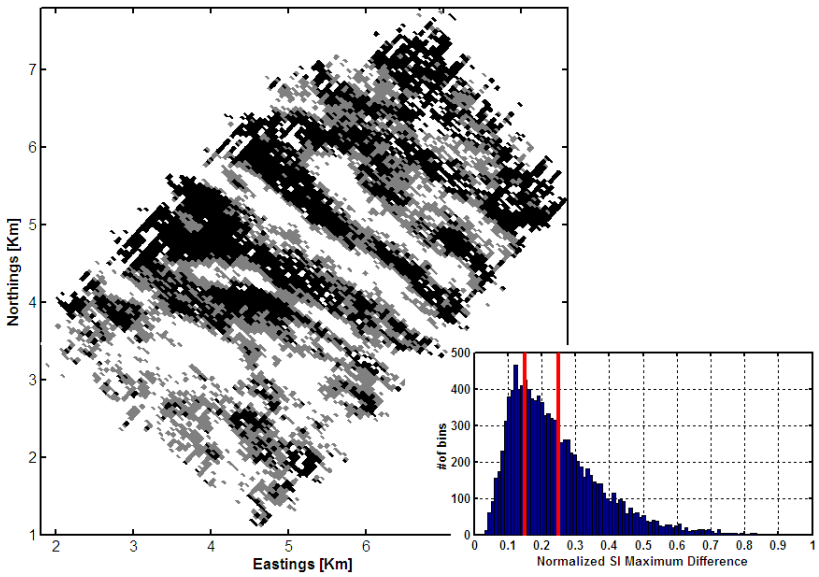

Figure 5-35: Map of fracture distribution and intensity at the level of the Shaftesbury horizon obtained from the *SI* method post-stack. Black, gray and white areas show decreasing levels of scattering indices following the thresholds indicated in the inset histogram.

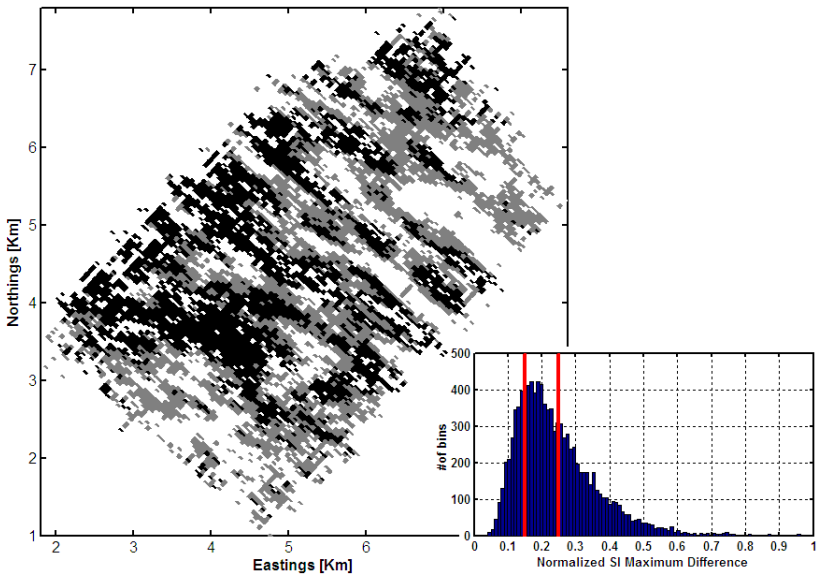

Figure 5-36: Map of fracture distribution and intensity at Cadotte computed with the *SI* method post-stack. In the inset, histogram of normalized scattering indices. Red lines indicate thresholds used to distinguish levels of *SI* intensity in the map. The level at lowest *SI* determines the transition between white and gray areas and the level at largest *SI* marks the transition between gray and black areas.

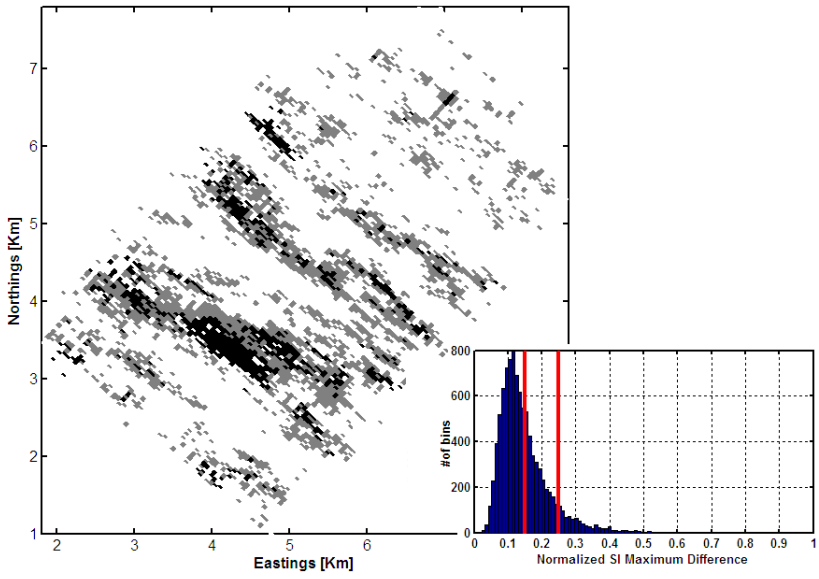

Figure 5-37: Map of fracture distribution and intensity at Falher. In the inset, histogram of normalized scattering indices computed post-stack. Red lines indicate thresholds used to distinguish levels of *SI* intensity in the map. The lowest level determines the transition between white and gray areas and the largest marks the transition between gray and black areas.

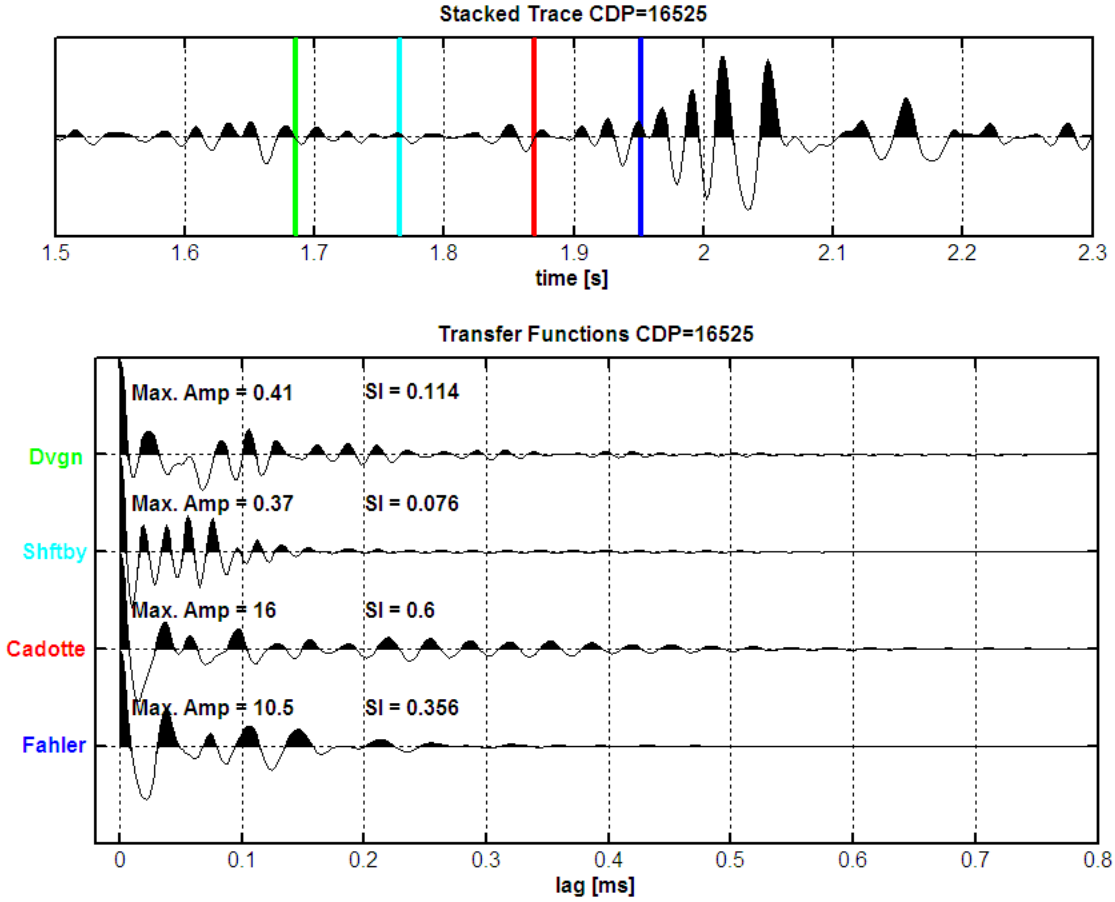

Figure 5-38: *SI* post-stack analysis of CMP 16525. At the top, the stacked trace (all azimuths and offsets 0-4000 m) for this CMP and time location of horizons; at the bottom, tranfer functions computed for the Dunvegan, Shaftesbury, Cadotte and Falher time levels. Amplitude maxima and scattering indices are indicated.

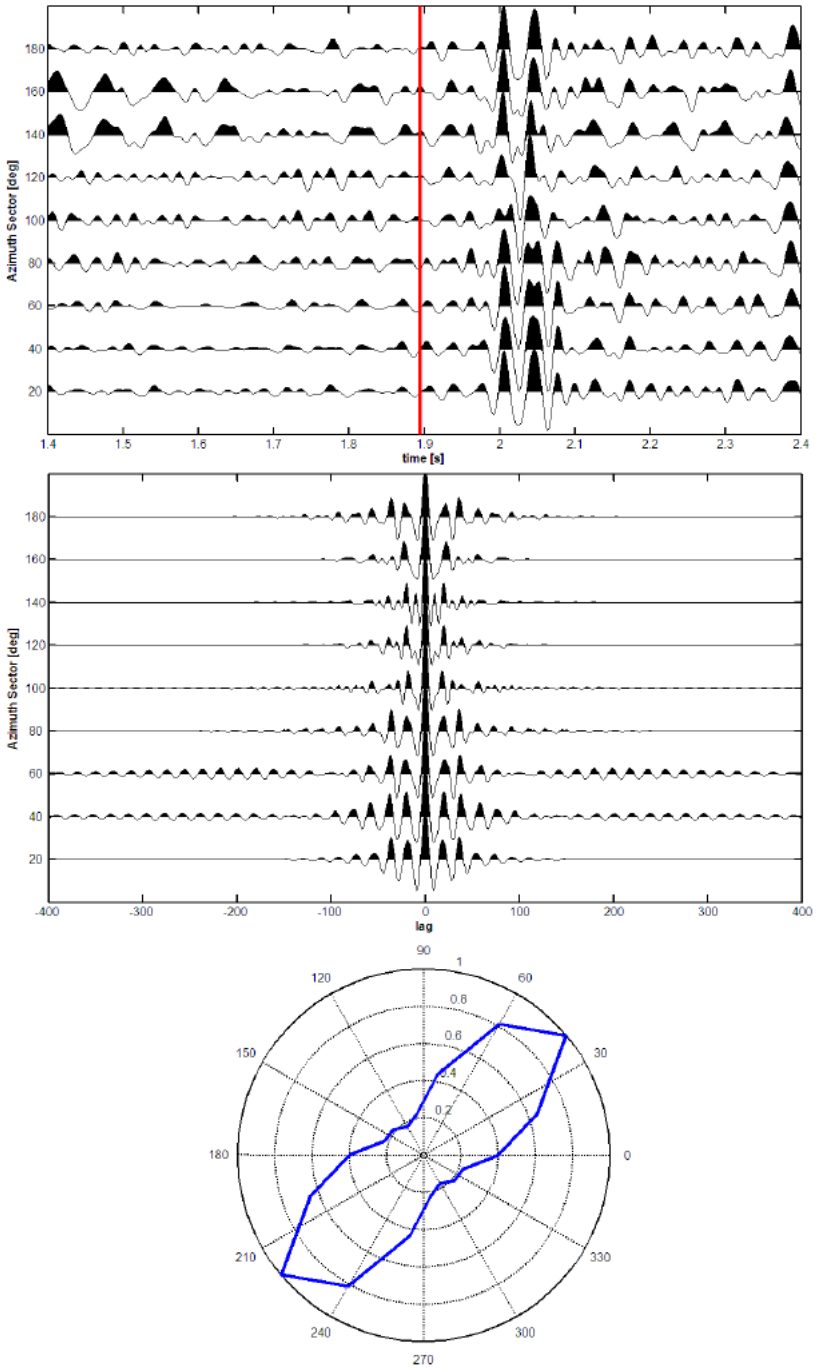

Figure 5-39: *SI* pre-stack analysis at CMP 10460 for the top of Cadotte: azimuthal stacks every 20° (top), the time location of Cadotte and the start of the upper window and end of the lower window are indicated in red; azimuthal tranfer functions (middle); corresponding scattering indices plotted as a function of angle (bottom).

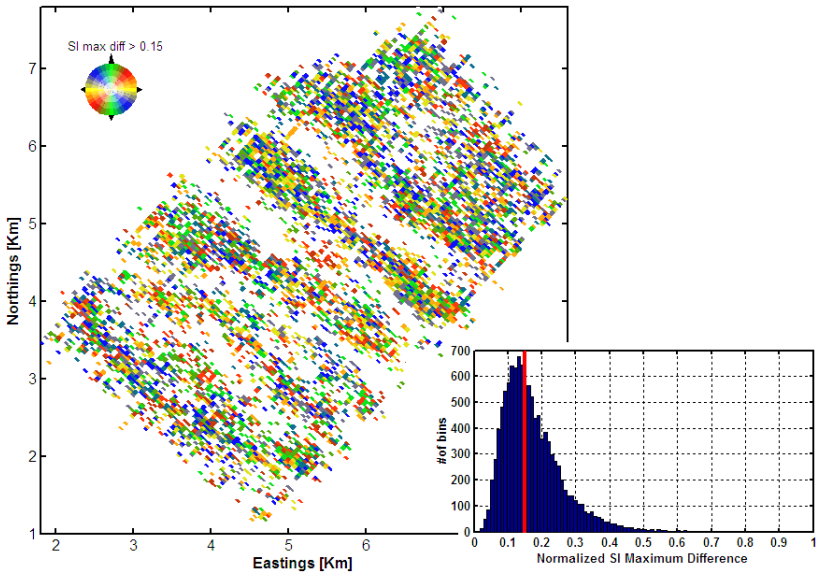

Figure 5-40: Map of fracture distribution, intensity and orientation at Dunvegan. Colors represent azimuth of fracture strike measured as in the color scale. Colored pixels indicate that maximum scattering index is above the threshold shown in the histogram.

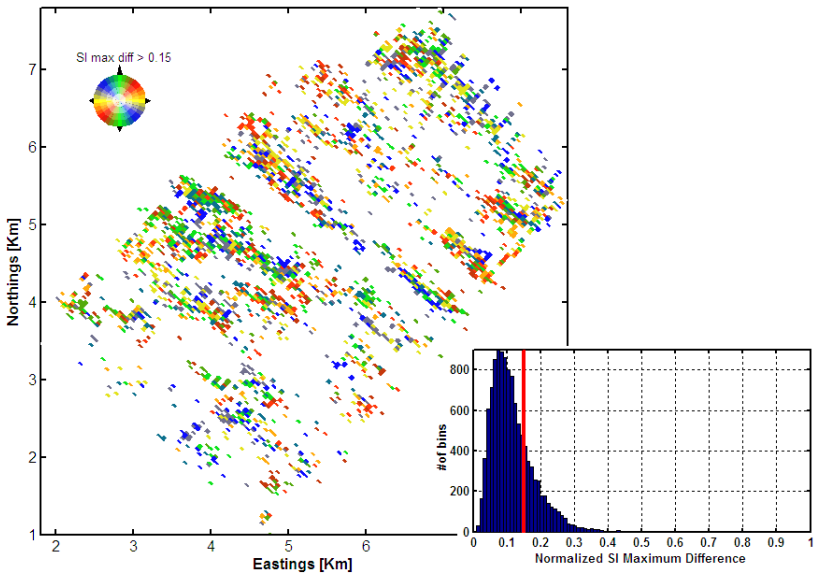

Figure 5-41: Map of fracture distribution, intensity and orientation at Shaftesbury. Red line indicates threshold used to highlight highest values of *SI* intensity in the map. Colors represent azimuth of fracture strike measured as in the color scale.

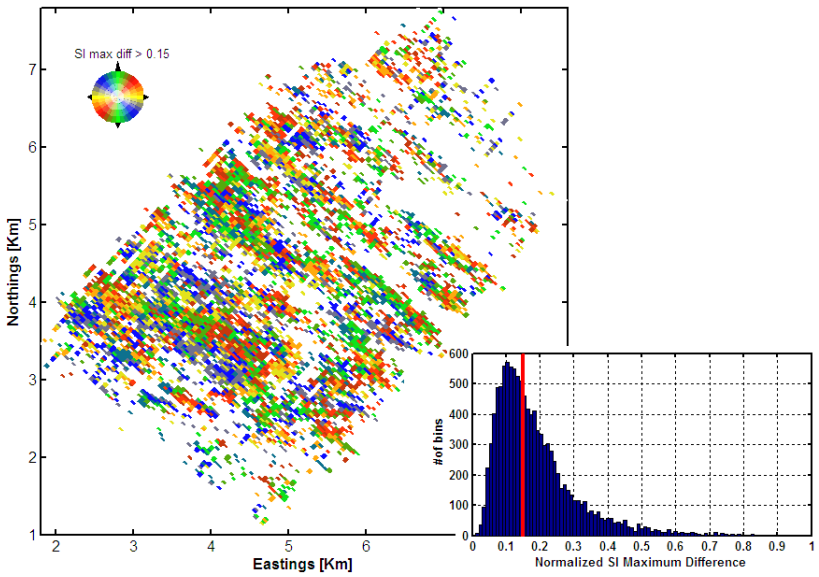

Figure 5-42: Map of fracture distribution, intensity and orientation at Cadotte. Colors represent azimuth of fracture strike measured as in the color scale. The inset figure is a histogram of the *SI* maximum differences normalized. Data have been thresholded below the red line.

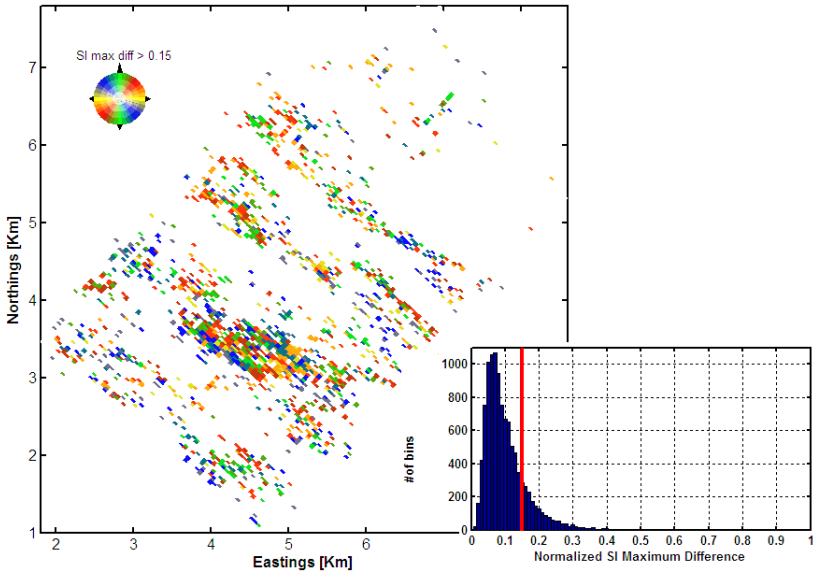

Figure 5-43: Map of fracture distribution, intensity and orientation at Falher. Colors represent azimuth of fracture strike measured as in the color scale. The inset figure is a histogram of the *SI* maximum differences normalized. Data have been thresholded below the red line.

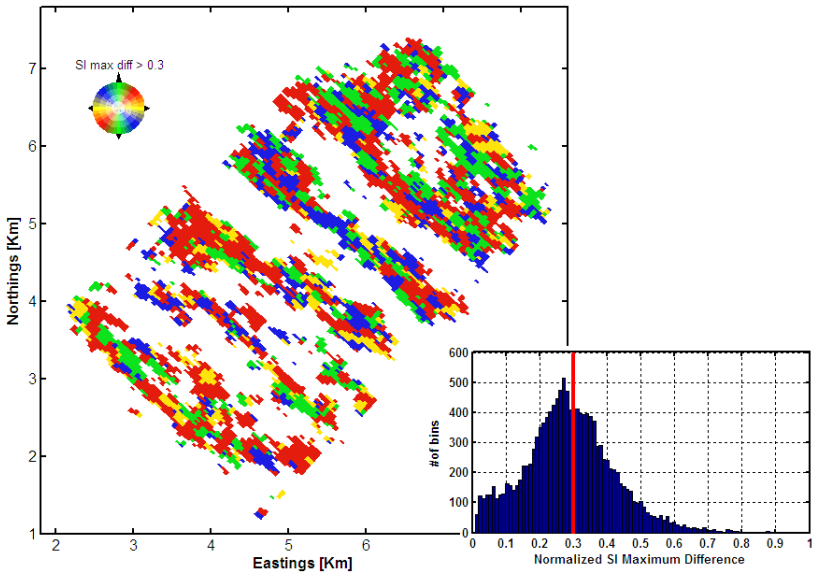

Figure 5-44: Map of fracture distribution, intensity and orientation at Dunvegan after a smoothing filter. Colors represent most common azimuth of fracture strike in a bin of 120 x 120 m. Intensity is displayed with grades of color following the thresholds indicated on the *SI* histogram in the inset figure.

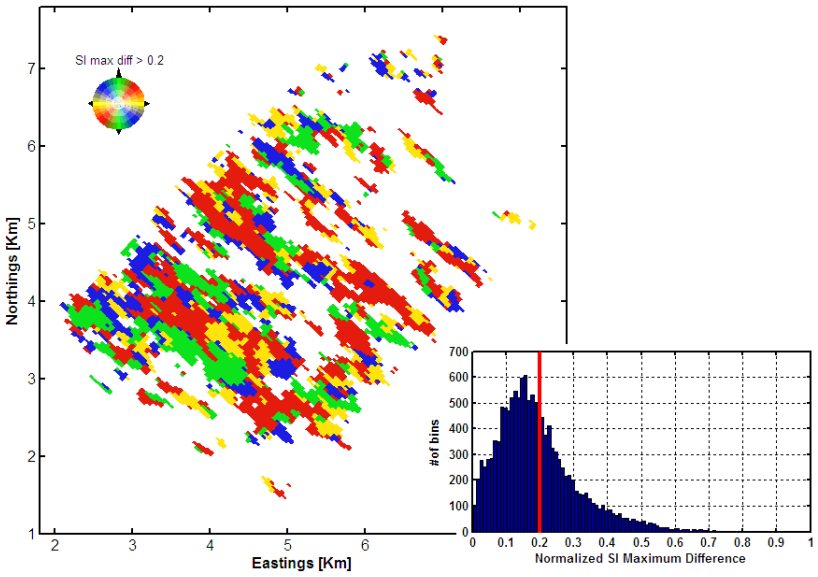

Figure 5-45: Smoothed map of fracture distribution, intensity and orientation at Cadotte. Colors represent most common azimuth of fracture strike in a bin of 120 x 120 m. Intensity is displayed with grades of color following the thresholds indicated on the *SI* histogram in the inset figure.

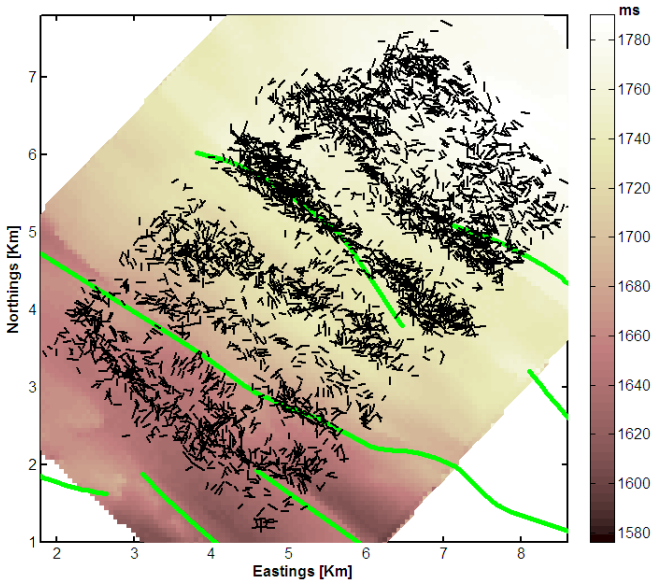

Figure 5-46: Map of fracture distribution, orientation and intensity obtained with the *SI* method at the top of Dunvegan. Quivers' length represents the *SI* magnitude and their orientation indicates fracture strike. Fracture information is plotted over the horizon time topography and fault traces interpreted from seismic data. Data was thresholded for scattering indices lower than 0.2.

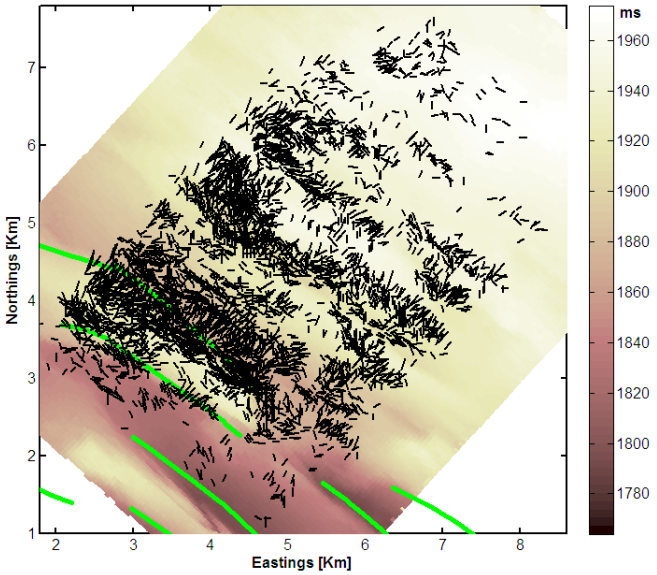

Figure 5-47: Map of fracture distribution, orientation and intensity obtained with the *SI* method at the top of Cadotte. Quivers' length represents *SI* magnitude and their orientation indicates fracture strike. Fracture information is plotted over the horizon time topography and fault traces interpreted from seismic data. Data was thresholded for scattering indices lower than 0.2.

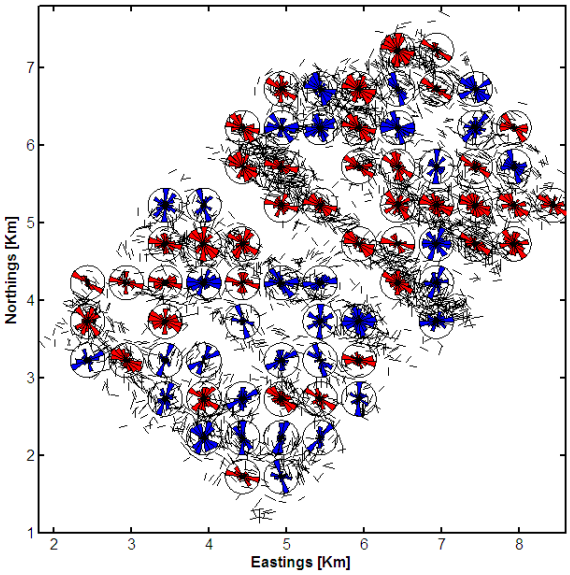

Figure 5-48: Fracture orientations obtained with the *SI* method at the Dunvegan. Orientations are histogrammed in a radius of 500 m. Histograms are plotted in red when the most frequent direction is 100-140°, that is, orthogonal to the regional $Shmax$.

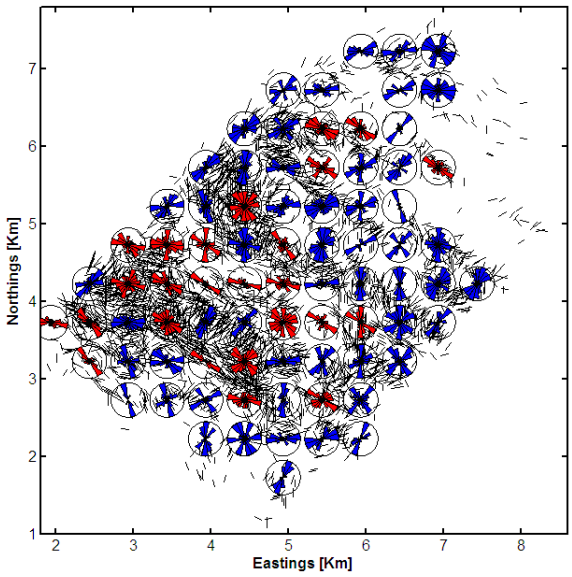

Figure 5-49: Fracture orientations obtained with the *SI* method at the Cadotte. Orientations are histogrammed in a radius of 500 m. Histograms are plotted in red when the most frequent direction is 100-140°, that is, orthogonal to the regional $Shmax$.

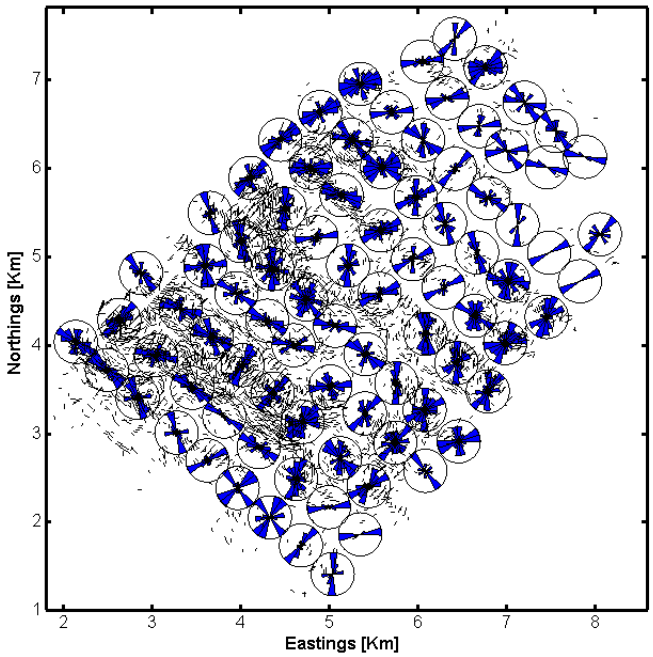

Figure 5-50: Fracture orientations at the Cadotte from the *SI* method are upscaled to match the resolution of the *F-K* method. Orientations are histogrammed in 500 m around the supershot locations.

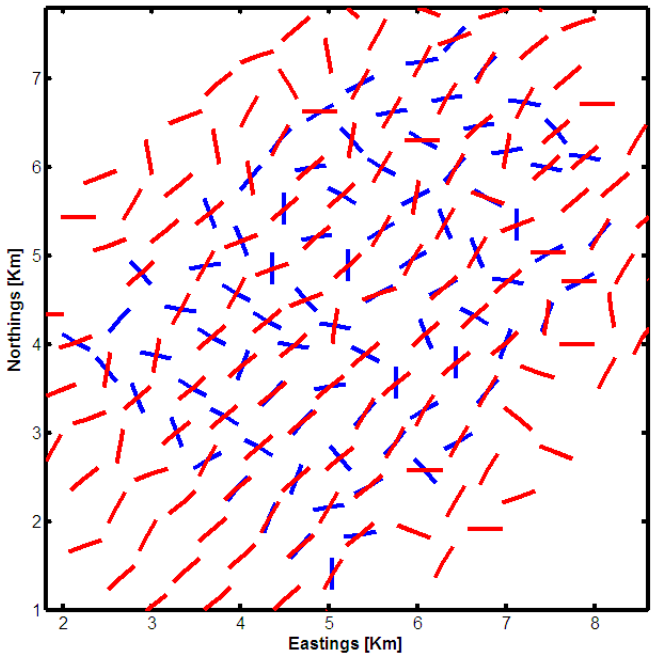

Figure 5-51: Comparison of fracture orientations from the *SI* (blue) and the *F-K* method (red) at the Cadotte. Fracture directions from the *SI* method correspond to the most common orientation found in the histograms displayed in figure 5-50.

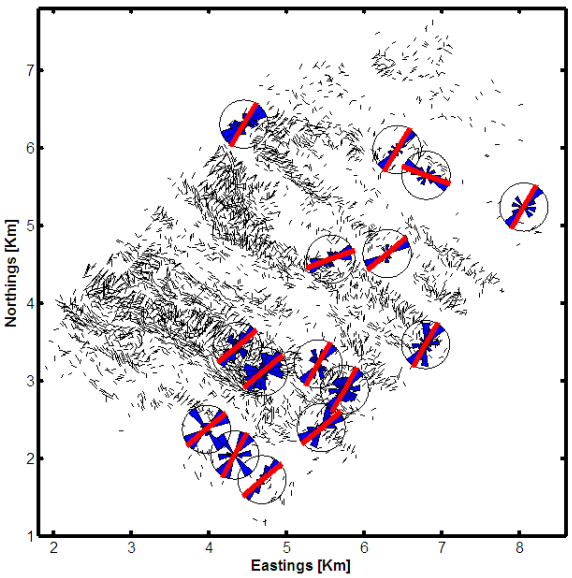

Figure 5-52: Some of the locations where fracture orientation from the upscaled *SI* method (blue histograms) coincide with the orientations obtained with the *F-K* method (red quivers).

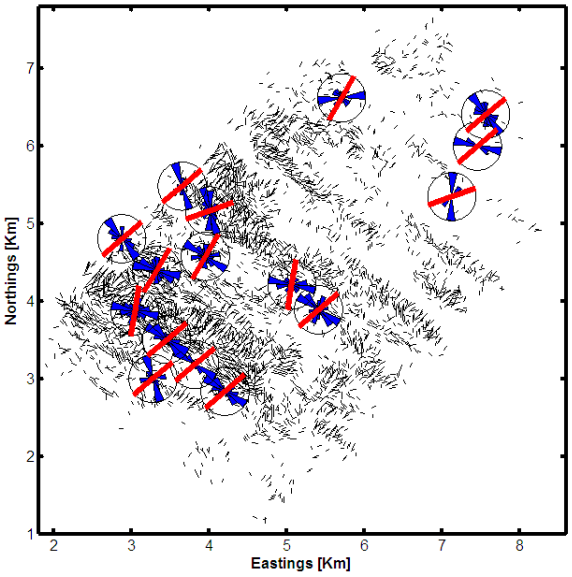

Figure 5-53: Some of the locations where fracture orientation from the upscaled *SI* method (blue histograms) do not coincide with the orientations obtained with the *F-K* method (red quivers). Fracture strike estimated from both methods at these locations are about 90° away.

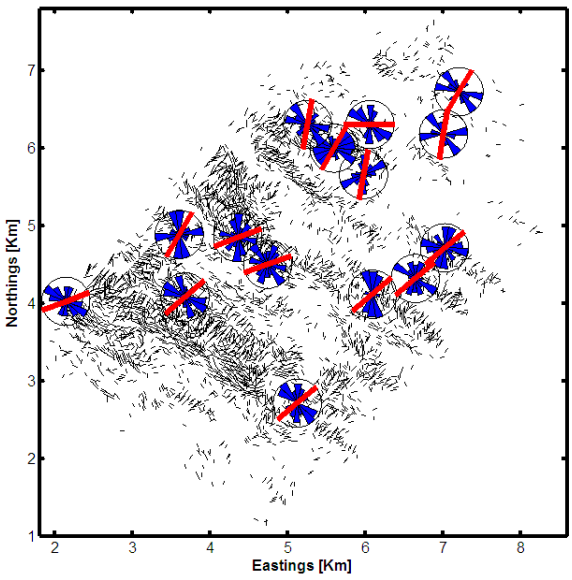

Figure 5-54: Some of the locations where fracture orientation from the upscaled *SI* method (blue histograms) do not coincide with the orientations obtained with the *F-K* method (red quivers), but fracture strike estimated from the *SI* method shows significant variation in 500 m around the supershot locations.

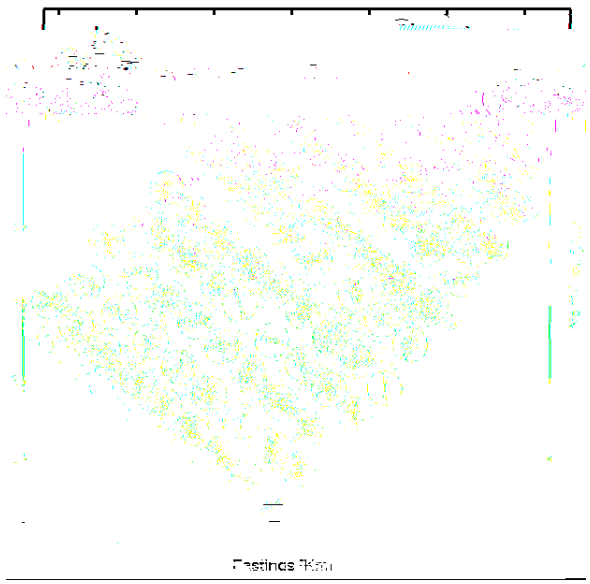

Figure 5-55: Fracture orientations at the Dunvegan from the *SI* method are upscaled to match the resolution of the *F-K* method. Orientations are histogrammed in 500 m around the supershot locations

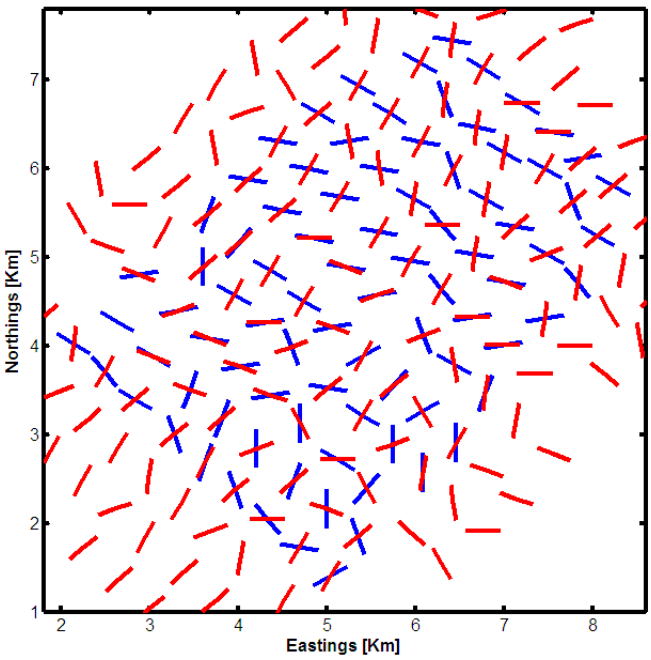

Figure 5-56: Comparison of fracture orientations from the *SI* (blue) and the *F-K* method (red) at the Dunvegan. Fracture directions from the *SI* method correspond to the most common orientation found in the histograms displayed in figure 5-55.

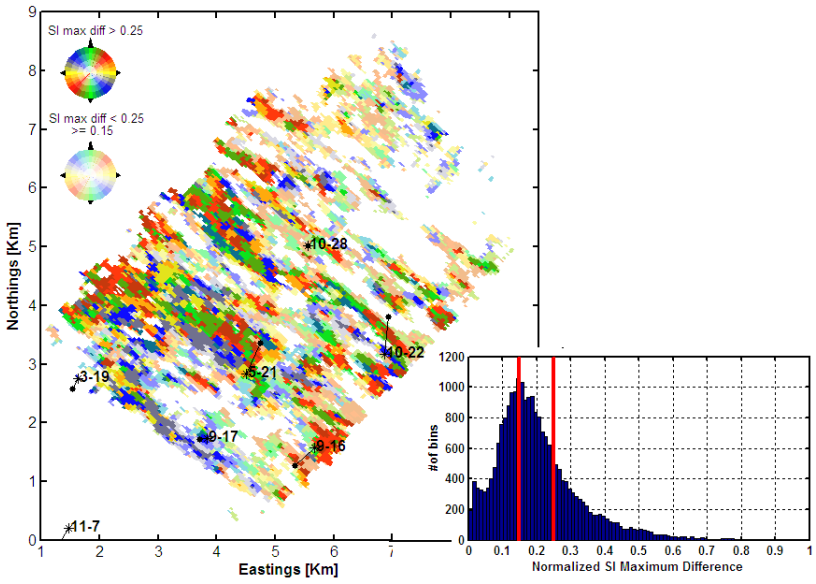

Figure 5-57: Map of fracture distribution, intensity and orientation at Cadotte with colors representing azimuth of fracture strike and color grades the level of intensity or magnitude of *SI*. The histogram in the inset shows these levels. Well locations are indicated. Stars represent well location at Cadotte's depth and solid dots the surface locations.

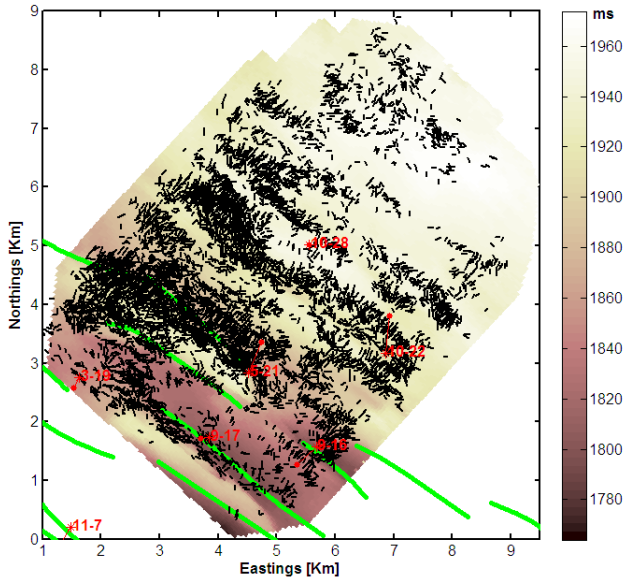

Figure 5-58: Map of fracture distribution, intensity and orientation at Cadotte with vectors representing *SI* intensity (length) and fracture strike (direction). Well locations are indicated with stars to represent location at Cadotte's depth, and solid dots, the surface locations.

Chapter 6

Conclusions

In this thesis we address the problem of determining in situ stress and fracture properties. The methods used include borehole breakouts, flexural wave crossovers, regional kinematical models of stress distribution, and fracture analyses of seismic data. The methods are based upon two fundamentally different aspects: (1) the scale of the regions they describe and the resolution of the data type; and (2) the relationship between the in situ stress field and the properties of fractures. For instance, the anisotropy of flexural waves measured with cross-dipole logs in chapter 2 is induced by the stress field. The direction of propagation of fast waves in the far field is interpreted as the orientation of maximum horizontal stress. Whether this anisotropy is associated with the presence of fractures or not has to be resolved through direct observations, for example, in image logs. However, the techniques explored in that chapter are able to tell, first, if the stress field anisotropy around the borehole is strong enough to give place to fracturing, and second, which would be the preferential orientation of such fractures. This information, combined with knowledge of the mechanical properties of the rocks around the well could then give a better diagnosis about the presence of fractures at different depths. Inference of regional fracture properties from borehole data, however, suffers from the lack of sufficient coverage (information) between wells. Moreover, it is desirable that fracture detection and stress distribution be performed before drilling. Therefore, in chapters 3 and 5, the problem of detecting and characterizing stress and fractures in the reservoir is ap-

proached differently, that is, using surface seismic data. In this case, the reservoir is assumed fractured and the distribution, orientation and spacing of these fractures reveal the local variations of the stress field.

The work presented in this thesis lead us to the following conclusions:

- The agreement of the in-situ stress orientation determined with the borehole methods strongly suggests that the integration of these techniques should be used for practical applications. The orientation of the horizontal stresses at a well location derived from flexural wave crossovers agrees with the orientation derived from breakouts observed at the borehole wall. This agreement verifies that dipole logs are a record of the stress distribution around the well. Moreover, the study suggests that the combined analysis of in situ stress from dipmeter data and sonic data compensates the limitations of both methods. The reliability of the dipmeter data is reduced if breakouts are present along with other kinds of borehole instability that obscures the measurements (e.g. washouts, key sets). The reliability of the sonic data is particularly reduced if the formation is fast and strongly anisotropic. Combining both methods yields a more complete depth profile of in situ stress since breakouts, or crossovers, do not generally occur everywhere in the well section. Breakouts are indicators of stress anisotropy after the rocks have failed, whereas crossovers reveal the conditions of pre-failure stress.

- The agreement between borehole methods and the regional scale model implies suitability of the regional model despite its simplifications. The orientation of the horizontal stresses derived from well data at a particular intraplate location agrees with models of stress distribution driven by the motion of the tectonic plates around the region of the well. A range of possible $SHmax$ azimuths is obtained by varying the relative plate velocities according to different global models of present-day plate motions. Although the stress model is a simplified representation of the processes driving the interaction of plates, the plane elasticity approximation and the pure kinematical approach seem to account for

the most important forces responsible to yield the stress field at a particular orientation.

- The consistency across scales (of stress orientation) implies the strength of the tectonic stress which in turn agrees with the stress magnitude estimations. The agreement of the results from the regional scale stress model and the more deterministic methods using borehole data suggests that the in situ stress in the region of study is particularly consistent. This consistency may be related to the fact that the location is near the plate boundary (approximately 120 Km). However, according to Yale (2003) this behavior is characteristic of areas of high tectonic stress (high differential horizontal stress). Our estimations of stress magnitudes support the interpretation of this region as an area of high tectonic stress in which local variations with respect to the regional stress field are not likely to occur (except maybe in the vicinity of faults). The consistency across scales observed in northeast Venezuela has to be generalized carefully because other areas may feature a less anisotropic stress field. With each method, stress orientations are determined within an uncertainty range. Breakouts yield the most constrained results, followed by crossovers, then regional models, and then earthquake focal mechanisms which give the least constrained stress orientations. The uncertainty range for each method is related to the scale of the measurement.

- Horizontal stress magnitudes can be estimated directly from the data without assuming empirical models or conditions of isotropicity that are often unrealistic. Reasonable values of horizontal stress magnitudes can be estimated directly from the well logs in two ways: (1) comparing stress distribution around the borehole (model) with the actual deformations (breakouts) observed at a particular depth; and (2) comparing the anisotropy observed with laboratory measurements of shear velocity in rock samples (ideally, from the formations probed). These two, relatively simple, and independent procedures provide well constrained magnitudes of $Shmin$ and $SHmax$. In the case studied in

chapter 2, estimations using both methodologies are consistent. The results obtained with either approach are data-driven unlike commonly used empirical relationships that depend on estimations of vertical stress, pore pressure, Poisson ratio, friction coefficient or assumptions of isotropicity that may not apply here.

- Our discrete fracture modeling approach reproduces the first order effects of seismic scale fractures on the propagation of waves. The numerical models presented in this thesis and others (e.g. Willis et al., 2006; Daley et al., 2002; Vlastos et al., 2003) simplify the wave phenomena that takes place in the presence of fractures with dimensions similar to the seismic wavelengths. The wavefield generated by multiple fracture sets consists of a complicated interaction of diffracted and guided waves. The discrete fracture modeling approach assumed in this thesis (Coates and Schoenberg, 1995) appears to reproduce most of the wave phenomena that have been observed in previous laboratory experiments and analytical solutions. The reverberating tails of P and S waves (coda waves) are recognized as scattering off the fractures. The amplitude of these waves can be large enough to disrupt the primary reflected signals and thus be measurable.

- Analysis of our discrete fracture modeling results show that the fractures impart distinct and identifiable spectral characteristics which can be used to extract fracture properties. The spectral response of the fracture scattering changes with azimuth. The azimuthal differences in the data spectrum are described in terms of velocity and distribution of energy. Energy appears spread out (slower velocities) in the *f-k* spectrum of a windowed gather in the direction normal to fracture strike whereas it appears confined around small wavenumbers (fast velocities) for records oriented with fracture strike. The azimuthal differences are enhanced in the 2D Fourier domain, similarly to what happens when transfer functions are computed from azimuthal stacks in the *SI* method. The main advantage of the spectral domain is that it conveniently provides a way of separating out signals exclusively related to fractures. The reason behind this is

that unlike the primary energy, a large component of the fracture scattering (the backscattered waves) maps to negative wavenumbers in the *f-k* spectrum. In theory, the backscattered energy dominates the negative wavenumber-positive frequency quadrant. In practice (chapter 5), noise, aliasing and unmigrated diffraction tails from high-angle dipping structures can all reduce the effective isolation of backscattered energy.

- We developed an effective new method to extract fracture properties- the *F-K* method. Based on the spectral characteristics of the fracture scattering, we propose two quantities (backscattered energy and maximum spectral amplitude in the negative wavenumber domain) as discriminators of fracture orientation. A simple relationship between dominant wavenumber and fracture spacing is found. This is the *F-K* method, a new strategy to extract fracture properties from seismic data. The application of the method to the Lynx field dataset in chapter 5 has helped us to make the method practical and determine its limitations and advantages upon field data.

- The sensitivity study shows that the backscattered dominant wavenumber, backscattered energy, and maximum *SI* azimuth are robust. Spectral amplitudes and *SI* values have a response tuned to thickness, spacing, and compliance of the fractures. The model-based sensitivity of the scattering spectral response (spectral amplitude, frequency and wavenumber), and scattering indices to fracture properties (thickness, spacing and stiffness) provides a basis for confidence in the robustness of the *F-K* and *SI* methods in a wide range of reservoir configurations. The study also opened up the possibility of extracting other fractures properties, like stiffness and reservoir thickness, using the information contained in the spectral amplitudes and in the relative values of scattering index. Fractures in thin bed reservoirs and of low compliance contrast generate a reduced fracture signal with respect to tall, highly-compliant fractures. Fracture spacing has a tuning effect on the amplitudes. The amplitude reduction exhibits itself as less energetic peaks in the *f-k* spectrum and decreases the maximum

difference of scattering indices computed in each CMP bin. An important conclusion of this modeling study is that the backscattered energy is always the largest perpendicularly to fracture strike. The dominant wavenumber is found to be practically insensitive to fracture thickness or compliance. Similarly, the *SI* reaches a maximum value parallel to fractures independent of the fracture properties. In practice (chapter 5), we related the spectral amplitude variations across the survey area to uncertainties in the *F-K* method, and to the intensity of fracturing in the *SI* method.

- The uneven fold and acquisition footprint issues must be estimated and removed from fracture analyses. The application of the *F-K* and *SI* methods to the field data in chapter 5 reveals that irregular fold caused from the acquisition design specifications creates missing traces within SHOT and/or CMP gathers and an irregular number (including a complete omission) of traces in each azimuth gather. If the fracture estimation is performed on data with irregular fold, aliasing artifacts obscure the true fracture characteristics. The bias introduced by this footprint can be remedied by treating early in the processing flow the irregular fold issues. We proposed a homogenization of the fold which controls trace mixing while keeping a reasonable azimuth resolution. Then, the recommendation is to apply the fracture processing techniques only in gathers that satisfy a minimum fold requirement. In this way, the resultant fracture maps reflect only the reliable information without any fold biases.

- The *SI* method can be applied to (nearly) conventionally processed, post-stack data. Heretofore, this method was only applicable to surveys designed to collect high fold in many azimuths. Using the method on conventionally designed surveys expands the number of 3D seismic surveys that can be used for fracture analysis by this simple method. The *SI* method can be applied to post-stack data (with no azimuthal differentiation) in order to obtain a map of fracture distribution or fracture intensity in the reservoir. It is a quick tool to evaluate large survey areas and it could be incorporated as a feasibility process in the

regular data processing sequence for early possible detection of fractured areas of interest. The more detailed fracture processing using the *F-K* method and the pre-stack *SI* can then be applied as more complete data are acquired and interest in the area warrants.

- The *F-K* and *SI* methods have different spatial resolutions and benefit from being interpreted together. Application of the *F-K* and *SI* methods to the Lynx data taught us that the resolution of these methods is different. The *F-K* method yields smoother results due in part to the fact that the procedure is applied in the SHOT domain. In general, it is advantageous that the *F-K* method is applicable in the field geometry because very little other processing may be necessary. However, unlike CMP gathers, the subsurface image points vary from trace to trace in SHOT gathers. As a consequence, an intrinsic assumption of the *F-K* method is that the fracture properties sought should be relatively invariant in space and depth. The *SI* method has higher resolution and allows the inversion of fracture properties at every CMP bin. In order to compare the results of these two methods we had to deal with the resolution differences. We upscaled the *SI* fracture orientation map. The orientation of fractures determined from the *F-K* and the *SI*-upscaled methods is consistent. Fractures appear to be aligned with the regional maximum stress $SHmax$. We propose three possible causes for the local differences: (1) the higher resolution of the *SI* method may be affected by smaller scale variations in ambient noise; (2) fractures in the overburden are oriented differently than in the reservoir and the *F-K* method may give a result which is overprinted by the shallower fracture orientations; and/or (3) any minor faults present causing the local fracture orientations to become erratic might not be resolved by the *F-K* method.

6.1 Contributions

In this thesis, a significant effort has been dedicated to develop practical methods to determine stress magnitudes and fracture properties. We have often approached these

problems from a modeling viewpoint; however, all the research has been ultimately tested in field data.

Efforts have been focused on four main aspects: (1) the determination of stress magnitudes; (2) the integration of multiscale in situ stress information; (3) the understanding of the seismic wave propagation in fractured reservoirs; and (4) the development of strategies to extract fracture properties from seismic data. The most important contributions of this work are:

1. We derived two independent methodologies to determine horizontal stress magnitudes from borehole data. These are particularly useful because methods to obtain magnitudes of $SHmax$ are scarce.

2. We developed the F-K method aiming to extract fracture properties from surface seismic data. Extracting this fracture information from the coda waves is a relatively new research area. The F-K method is a systematic way of detecting fractures and estimating their orientation and mean spacing from 3D field data.

3. We proposed and tested the application of the SI method to post-stack data to extend the practical applicability of the fracture scattering processing to virtually all seismic surveys.

4. We recognized the effects of acquisition footprint on the fracture maps obtained from the scattering processing and proposed a strategy to mitigate them.

6.2 Future Work

Certain processes taking place in the borehole environment are known to be transient, like near-borehole fluid invasion, mudcake build-up, shales swelling, and fracture propagation. Our modeling approach to estimate stress magnitudes strongly relies on the assumption of linear elasticity, and the validity of a particular failure criterion (Mohr-Coulomb). A generalization of the approach could be achieved building more realistic constitutive equations into the calculation. Another way of determining stress magnitudes could be carried out by matching the observed crossover frequency with the

modeled response of a stressed medium. The crossover frequency is a function of the radial distance at which the formation is undisturbed by the borehole presence under a particular far field stress; thereby the thickness of such zone should be an indirect measurement of the stress field intensity.

The characterization of fracture corridors can be further advanced in the following directions:

- To extract other properties, e.g. fracture stiffness, from the scattering signal. For this purpose, the spectral amplitude, the response at intermediate azimuths, other recorded components, and other fracture waves like guided waves may be analyzed. Transforms other than the Fourier transform (tau-p, Karhunen-Loeve or eigenimages, wavelet transforms) may generate higher resolution maps and perform better separations of the fracturing in the reservoir from the overburden.

- To deepen our understanding of the wave interaction that takes place in fracture systems. More realistic modeling techniques need to be developed, for example, to take into account the role of fluids in the fractures. The modeling studies have to be calibrated with laboratory experiments. Future models should also simulate the behavior of multiple fracture sets with different orientations, and fracturing of limited extension.

- To validate the information extracted about fractures. At this point the estimations of fractured properties from seismic data have only been validated with well breakouts, image logs and resistivity logs. These data provide fracture information in the near field of the borehole which is probably associated with cracks at the subseismic scale. To supplement these analyses, the scattering extraction methods could be applied to borehole seismic data or crosswell tomography surveys. The frequency of these types of data is higher than that of surface seismic but the correlation with fractures at the seismic scale might be more consistent.

Important questions remain to be addressed, particularly regarding the connection

between fractures and in situ stress. For instance, can we be confident that the stresses responsible for the fracturing in a reservoir correspond to the present-day stresses?

Appendix A

Formulation of Stress-Strain Problems

When a layer of rock, buried at certain depth, is subjected to a stress field, the displacements and displacement gradients are sufficiently small for the theory of linear elasticity to be valid. The equations of motion, or equilibrium, can be considered to be satisfied in the undeformed reference configuration. We choose the Lagrangian description of motion to express the global conservation laws. Because of the fixed material viewpoint, the conservation of mass is automatically satisfied (Reddy, 1993).

Using conservation of momentum, the Cauchy's equations of motion are obtained (Malvern, 1969). In vectorial notation,

$$\nabla T + f = \rho \frac{\partial u}{\partial t}, \tag{A.1}$$

where u is the velocity, ρ is the density of the material, f represents the body forces per unit volume and T is the stress tensor:

$$T = \begin{bmatrix} \sigma_x & \tau_{xy} & \tau_{xz} \\ \tau_{yx} & \sigma_y & \tau_{yz} \\ \tau_{zx} & \tau_{zy} & \sigma_z \end{bmatrix} \tag{A.2}$$

In the special case of static equilibrium, the acceleration $\frac{\partial u}{\partial t}$ is zero and equation

A.1 reduces to:

$$\nabla T + f = 0 \tag{A.3}$$

In general, $T_{ij} = T_{ji}$, and there are only six independent unknown stress components instead of nine. However, the 3 equations A.1 are not enough to solve for the stresses, and constitutive equations have to be used. The stress-strain relations describe the ideal macroscopic behavior of the material under consideration. For an ideal elastic solid, the constitutive equations are known as Hooke's law :

$$T = C\epsilon, \tag{A.4}$$

where C is a fourth-rank tensor and ϵ is the strain tensor,

$$\epsilon = \begin{bmatrix} \epsilon_x & \gamma_{xy} & \gamma_{xz} \\ \gamma_{yx} & \epsilon_y & \gamma_{yz} \\ \gamma_{zx} & \gamma_{zy} & \epsilon_z \end{bmatrix} \tag{A.5}$$

In the most general case, C contains 81 elastic constants or modulii, however, provided T and ϵ are symmetric, C can be reduced to 36 constants.

By definition, the strains are related to the displacements, $\bar{u}$ = (u,v,w), as:

$$\begin{aligned} \epsilon_x &= \tfrac{\partial u}{\partial x}; & \epsilon_{xy} &= \frac{\gamma_{xy}}{2} = \frac{1}{2}\left(\frac{\partial u}{\partial y} + \frac{\partial v}{\partial x}\right) \\ \epsilon_y &= \tfrac{\partial v}{\partial y}; & \epsilon_{yz} &= \frac{\gamma_{yz}}{2} = \frac{1}{2}\left(\frac{\partial v}{\partial z} + \frac{\partial w}{\partial y}\right) \\ \epsilon_z &= \tfrac{\partial w}{\partial z}; & \epsilon_{zx} &= \frac{\gamma_{zx}}{2} = \frac{1}{2}\left(\frac{\partial w}{\partial x} + \frac{\partial u}{\partial z}\right) \end{aligned} \tag{A.6}$$

For an elastic isotropic material, the coefficients of C can be expressed in terms of only two elastic modulii. Usually, these are either the Lamé constants, λ and μ, the Young's modulus E and Poisson ratio ν, or the bulk modulus K and the shear modulus G. The bulk modulus is a measure of the fractional volume change when the pressure is increased by δP. It is obtained through isotropic compression experiments. Most frequently, uniaxial compression is simpler to perform, in which case, it is the

Young's modulus that it is measured. By definition, $E = \sigma_{zz}/\epsilon_{zz}$. On the other hand, the deformations that take place in the transverse direction are described by the Poisson ratio: $\nu = -\epsilon_{yy}/\epsilon_{zz}$ (Gueguen and Palciauskas, 1994).

Using the Young's modulus (E), and the Poisson's ration (ν), Hooke's law reduces to:

$$\begin{aligned}
\sigma_x &= \tfrac{E}{1+\nu}\left(\epsilon_x + \tfrac{\nu}{1-2\nu}(\epsilon_x+\epsilon_y+\epsilon_z)\right); \quad \tau_{xy} = \frac{E}{2(1+\nu)}\gamma_{xy} \\
\sigma_y &= \tfrac{E}{1+\nu}\left(\epsilon_y + \tfrac{\nu}{1-2\nu}(\epsilon_x+\epsilon_y+\epsilon_z)\right); \quad \tau_{yz} = \frac{E}{2(1+\nu)}\gamma_{yz} \\
\sigma_z &= \tfrac{E}{1+\nu}\left(\epsilon_z + \tfrac{\nu}{1-2\nu}(\epsilon_x+\epsilon_y+\epsilon_z)\right); \quad \tau_{zx} = \frac{E}{2(1+\nu}\gamma_{zx}
\end{aligned} \tag{A.7}$$

Finally, substituting equation A.6 in A.7 and equation A.7 in A.3, Navier's displacement equations of motion are obtained:

$$-\nabla C \nabla u = f \tag{A.8}$$

where,

$$C = \begin{bmatrix}
(\lambda+2\mu) & \lambda & \lambda & 0 & 0 & 0 \\
\lambda & (\lambda+2\mu) & \lambda & 0 & 0 & 0 \\
\lambda & \lambda & (\lambda+2\mu) & 0 & 0 & 0 \\
0 & 0 & 0 & \mu & 0 & 0 \\
0 & 0 & 0 & 0 & \mu & 0 \\
0 & 0 & 0 & 0 & 0 & \mu
\end{bmatrix} \tag{A.9}$$

and λ and μ in terms of E and ν are:

$$\begin{aligned}
\lambda &= \frac{E\nu}{(1+\nu)(1-2\nu)} \\
\mu &= \frac{E}{2(1+\nu)}
\end{aligned} \tag{A.10}$$

Once the derivatives of the displacements have been obtained, all strain and stress components can be derived.

A.1 Plane Elasticity

The three-dimensional elasticity problem can be simplified under certain assumptions concerning the loading. For example, if the body is a linear elastic solid whose thickness is very large in comparison with the size of its cross-section, the problem can be considered to be a plane strain problem. On the other hand, if the thickness is small compared with the area of the cross-section, the problem can be approximate as a plane stress problem. In both cases, the body forces, if any, cannot have components in the z-direction and the applied boundary forces must be uniformily distributed across the thickness. No loads can be applied on the parallel planes bounding the top and bottom surfaces for the former approximation to be valid (Malvern, 1969).

In modeling the deformations around the borehole, plane strain is an appropriate 2D approximation. Therefore, we assume no displacements take place in the z-direction (borehole axis) and the displacements in x and y directions are functions of x and y but not z. Then,

$$\epsilon_z = \gamma_{yz} = \gamma_{zx} = 0 \tag{A.11}$$

and in eq.A.8 $u = (u, v)$ (only two dependent variables).

Therefore, the condition for plane strain is:

$$\epsilon_z = \gamma_{yz} = \gamma_{zx} = 0 \tag{A.12}$$

where ϵ_z is the normal strain in the z-direction and γ_{yz} and γ_{zx} are shear strains.

Before deriving the finite element model associated to this problem (appendix B), it is useful to rewrite the governing equations under the assumptions of plane strain, and the boundary conditions, using an appropriate notation. First, the equations of motion,

$$\begin{aligned} \frac{\partial \sigma_x}{\partial x} + \frac{\partial \sigma_{xy}}{\partial y} &= 0 \\ \frac{\partial \sigma_{xy}}{\partial x} + \frac{\partial \sigma_y}{\partial y} &= 0 \end{aligned} \tag{A.13}$$

ignoring any body forces and assuming the displacements are constants in time.

Then, we need constitutives relations. In this case (linear elasticity),

$$\begin{bmatrix} \sigma_x \\ \sigma_y \\ \sigma_{xy} \end{bmatrix} = \begin{bmatrix} c_{11} & c_{12} & 0 \\ c_{12} & c_{22} & 0 \\ 0 & 0 & c_{66} \end{bmatrix} \begin{bmatrix} \epsilon_x \\ \epsilon_y \\ \gamma_{xy} \end{bmatrix} \tag{A.14}$$

where the matrix of elastic constants has been reduced first using the symmetry of the stress and strain tensors, from 81 to 36 constants, further to 21 assuming a strain-energy function exists (hence, $c_{ij} = c_{ji}$) (Malvern, 1969), and finally to 9, making the material principal directions to coincide with the coordinate axes (x, y, z) used to describe the problem. The latter correspond to a medium with 3 orthogonal planes of symmetry, named orthotropic; an isotropic material is also orthotropic but the opposite is not true.

The 4 constants different from zero in A.14 result from imposing the assumptions of plane elasticity, however the distinction between one type or the other will be given by the values these elastic constants take. For the plane strain case and an isotropic material (constants reduce to 3, only 2 independents),

$$\begin{aligned} c_{11} &= c_{22} = c_1 = \frac{E(1-\nu)}{(1+\nu)(1-2\nu)} \\ c_{12} &= c_2 = \frac{\nu E}{1-\nu-2\nu^2} \\ c_{66} &= c_3 = \frac{E}{2(1+\nu)} \end{aligned} \tag{A.15}$$

or, in terms of the Lamé constants, λ and μ,

$$\begin{aligned} c_1 &= \lambda + 2\mu \\ c_2 &= \lambda \\ c_3 &= \mu \end{aligned} \tag{A.16}$$

Substituting A.14 in A.13 and using the definitions in A.6 one can obtain the

actual equations being solved which are in terms of the displacement components u and v:

$$\begin{aligned} -c_1\frac{\partial^2 u}{\partial x^2} - c_3\frac{\partial^2 u}{\partial y^2} - (c_2+c_3)\frac{\partial^2 v}{\partial x \partial y} &= 0 \\ -c_3\frac{\partial^2 v}{\partial x^2} - c_1\frac{\partial^2 v}{\partial y^2} - (c_2+c_3)\frac{\partial^2 u}{\partial x \partial y} &= 0 \end{aligned} \tag{A.17}$$

In order to solve the problem numerically, boundary conditions have to be specified. In general, they can be expressed as (Reddy, 1993),

Natural Boundary Condtions, on Γ_2:

$$\begin{aligned} t_x &= \sigma_x n_x + \sigma_{xy} n_y = (c_1\frac{\partial u}{\partial x} + c_2\frac{\partial v}{\partial y})n_x + c_3(\frac{\partial u}{\partial y} + \frac{\partial v}{\partial x})n_y \\ t_y &= \sigma_{xy} n_x + \sigma_y n_y = c_3(\frac{\partial u}{\partial y} + \frac{\partial v}{\partial x})n_x + (c_2\frac{\partial u}{\partial x} + c_1\frac{\partial v}{\partial y})n_y \end{aligned} \tag{A.18}$$

Essential Boundary Conditions, on Γ_1:

$$\begin{aligned} u &= \hat{u} \\ v &= \hat{v} \end{aligned} \tag{A.19}$$

where Γ_1 and Γ_2 refer to disjoint portions of the boundary that do not overlap (except for a small number of discrete points). Γ_1 and Γ_2 together constitute the boundary Γ of the whole region, and on each, normal vectors can have different directions. In the natural boundary conditions, (n_x, n_y) are the components (or direction cosines) of the unit normal vector on the boundary Γ, $(\hat{n} = n_x\hat{i} + n_y\hat{j} = \cos\alpha\hat{i} + \sin\alpha\hat{j})$. A particular region border can be subdivided in as many boundaries as needed.

Appendix B

Finite Element Formulation of Stress-Strain Problems

This appendix includes a brief overview of the fundamental concepts and assumptions of the finite element method. Later, it presents the weak formulation and the finite element model associated to the in situ stress modeling.

B.1 Finite Element Method

The finite element method is a special case of a class of numerical methods grouped under the name of variational methods. In the solution of a differential equation by a variational method, the equation is put into an equivalent weighted-integral form and the approximate solution over the domain is assumed to be a linear combination of appropriately chosen approximation functions and undetermined coefficients. These coefficients are calculated such that the integral statement is satisfied (Reddy, 1993). In general, all variational methods (Galerkin, Rayleigh-Ritz etc) are difficult to implement because they do not provide a systematic procedure for the derivation of the approximation functions.

To overcome this disadvantage, in the finite element method any geometrically complex domain is represented as a collection of simpler subregions, called finite elements, over which the solution can be assumed continuous and therefore, be rep-

resented by a linear combination of, for example, algebraic polynomials. The connection with the variational methods comes with the fact that the coefficients in these algebraic relations are computed from satisfying the governing equations in a weighted-integral sense over each element. The coefficients correspond to the values of the approximate solution at the nodes.

The method involves three-step approximations: (1) the finite element discretization of the domain; (2) the representation of the solution over each element as a linear combination of nodal values and approximation functions; and (3) the element equations assembled assuming continuity of the physical quantities.

The approximate solution in the finite element method is of the form:

$$u_N \approx \sum_{j=1}^{N} c_j \phi_j + \phi_0 \tag{B.1}$$

where c_j are the coefficients and ϕ_j the approximation functions, in this case, algebraic polynomials. N represents the number of terms taken in the approximation and j its index. If the approximate solution B.1, is directly substituted into the original differential equation, there may not be enough linearly independent algebraic equations to derive c_j, this is where the variational methods are needed.

Basically, the variational principles allow the construction of the weak form of the given differential equation. A weak form is a weighted-integral statement of a differential equation in which the differentiation is distributed among the dependent variable and the weight function (Reddy, 1993). Furthermore, in this form, the natural boundary conditions are included, therefore the problem is reduced to require the approximate solution to satisfy only the essential boundary conditions.

The main advantage of using the weak form is clear from its definition: if the differentiation is distributed between the approximate solution and the weight function, the resulting integral form will require weaker continuity conditions on the approximation functions.

To illustrate the construction of the weak form, we will make use of the generalized

differential equation of one dependent and one independent variable:

$$-\frac{d}{dx}[a(x)\frac{du}{dx}] = q(x) \tag{B.2}$$

for $0 \leq x \leq L$, and subject to the boundary conditions:

$$\begin{aligned} u(0) &= u_0 \\ \left[a\frac{du}{dx}\right]_{x=L} &= Q_0 \end{aligned} \tag{B.3}$$

a and q are functions of the coordinate x, and u_0 and Q_0 are known values.

First, we rewrite B.2 in its weighted-integral sense:

$$\int_0^L w[-\frac{d}{dx}(a\frac{du}{dx}) - q]\, dx = 0 \tag{B.4}$$

When u in this equation is replaced by B.1, the expression in the square brackets is not zero, therefore, the form B.4 is a statement that the error due to the approximation of the solution is zero in a weighted-integral sense.

Choosing N functions w allows to find N equations for c_j. So far, w, the weight functions, are required to be nonzero and integrables.

The trading of differentiability from the dependent variable to the weight function, is only possible to perform if it leads to boundary terms physically meaningful (Reddy, 1993). For instance, in the case of displacements, it will be shown later that the boundary terms represent the forces.

Integrating the first term of B.4 by parts leads to,

$$0 = \int_0^L (\frac{dw}{dx}a\frac{du}{dx} - wq)\, dx - [wa\frac{du}{dx}]_0^L \tag{B.5}$$

Coefficients of the weight function and its derivatives in the boundary term are named secondary variables and their specification on the boundaries constitute the natural boundary conditions, as opposed to the weight function itself, (called primary variable) whose specifications on the boundaries correspond to essential boundary con-

ditions. Following these definitions and observing the boundary term in B.5, the first equation in B.3 is of the essential type while the second boundary condition is a natural one.

The boundary conditions B.3 are now imposed on the weak form resulting in,

$$0 = \int_0^L (a\frac{dw}{dx}\frac{du}{dx} - wq)\, dx - w(L)Q_0 \tag{B.6}$$

which is the weak form equivalent to the original differential equation B.2 and the bounday conditions B.3.

Once the weak form of the differential equation is built, the next step is to compute the approximate solution over a typical finite element.There are several variational methods depending on the choice of the integral statement and weight functions. In the following, the Rayleigh-Ritz method will be used to find the approximate solution on each finite element. The particularity of this method is that the choice of weight functions is restricted to the approximation functions, that is, $w = \phi_j$.

Let us denote the finite element solution over element Ω^e by U^e an algebraic polynomial that is required to be: (1) complete, that is, it has to include all lower-order terms up to the highest order used to capture all possible states (constant, linear and so on); (2) continuous over the element and differentiable as required by the weak form, in this case, at least once; (3) it should be an interpolant of the primary variables at the nodes of the finite element.

The degree of the approximation is inversely related to the error in the approximation. For the moment, let us assume a quadratic approximation of the form:

$$U^e(x) = a + bx + cx^2 \tag{B.7}$$

which requires three nodes in order to rewrite U^e in terms of the nodal values

(u_1^e, u_2^e, u_3^e). Thus,

$$\begin{aligned} u_1^e &= U^e(x_1^e) = a + bx_1^e + c(x_1^e)^2 \\ u_2^e &= U^e(x_2^e) = a + bx_2^e + c(x_2^e)^2 \\ u_3^e &= U^e(x_3^e) = a + bx_3^e + c(x_3^e)^2 \end{aligned} \tag{B.8}$$

and the coefficients a, b, c can be obtained. Notice however, that these are not the coefficients of the general approximate solution, they correspond to the solution over the particular element e.

Solving for a, b and c and substituting in B.7:

$$U^e = \sum_{j=1}^{3} \psi_j^e(x) u_j^e \tag{B.9}$$

where ψ_j^e are the quadratic Lagrange interpolation functions (Reddy, 1993),

$$\begin{aligned} \psi_j^e(x) &= \frac{1}{\sum_{i=1}^{3} \alpha_i^e}(\alpha_i^e + \beta_i^e x + \gamma_i^e x^2) \\ \alpha_i^e &= x_j^e (x_k^e)^2 - x_k^e (x_j^e)^2 \\ \beta_i^e &= (x_j^e)^2 - (x_k^e)^2 \\ \gamma_i^e &= -(x_j^e - x_k^e) \end{aligned} \tag{B.10}$$

the subscripts here permute in natural order: for $i = 1$, $j = 2$ $k = 3$; for $i = 2$, $j = 3$ $k = 1$, for $i = 3$, $j = 1$ $k = 2$.

The function ψ_i^e is equal to 1 at node i and zero at the other nodes.

Finally, the approximate solution over each element has to be substituted into the weak form B.6 and following the Rayleigh-Ritz procedure, w is chosen as the functions ψ_j^e. n (number of elements) equations are obtained which in matrix notation can be written as

$$[K^e][u^e] = [f^e] + [Q^e] \tag{B.11}$$

where $[K^e]$ is the coefficient matrix, (nxn), acting on u_i^e, the nodal values; $[f^e]$ is

a column vector of size $nx1$ and $[Q_i^e]$ contains the former boundary term. For the equation B.2,

$$\begin{aligned} K_{ij}^e &= \int_0^L (a\frac{d\psi_i^e}{dx}\frac{d\psi_j^e}{dx})\,dx \\ f_i^e &= \int_0^L q\psi_i^e\ ,dx \\ Q_i^e &= \sum_{j=1}^{n} \psi_j^e(x_i^e)Q_j^e \end{aligned} \tag{B.12}$$

In the system B.11, there are $2n$ unknowns namely u_i^e and Q_i^e. The assembly of the element equations, this is, collecting all the elements and taking into account the common nodes between them, and the imposition of the boundary conditions, reduce the number of unknowns to n as long as the problem is well-posed.

Equations B.11 describe the finite element model whose solution correspond to the approximate solution in the global domain of the original equation.

B.2 The Weak Form

Following the procedure described in section B.1, the weak form of equations 2.6 subject to boundary conditions A.18 and A.19 is derived. As mentioned before, the domain is discretized into finite elements. Next, we multiply each of the equations in 2.6 by a weight function, w_1 and w_2 respectively, and integrate over the domain of one element Ω^e,

$$\begin{aligned} \int_{\Omega^e} w_1 \left(-c_1\frac{\partial^2 u}{\partial x^2} - c_3\frac{\partial^2 u}{\partial y^2} - (c_2+c_3)\frac{\partial^2 v}{\partial x \partial y}\right) dxdy &= 0 \\ \int_{\Omega^e} w_2 \left(-c_3\frac{\partial^2 v}{\partial x^2} - c_1\frac{\partial^2 v}{\partial y^2} - (c_2+c_3)\frac{\partial^2 u}{\partial x \partial y}\right) dxdy &= 0 \end{aligned} \tag{B.13}$$

Integrating by parts to trade the differentiation equally between the weight function and the dependent variables,

$$0 = \int_{\Omega^e} \left[\frac{\partial w_1}{\partial x}(c_1 \frac{\partial u}{\partial x} + c_2 \frac{\partial v}{\partial y}) + c_3 \frac{\partial w_1}{\partial y}(\frac{\partial u}{\partial y} + \frac{\partial v}{\partial x}) \right] dxdy \\ - \oint_{\Gamma^e} w_1 \left[(c_1 \frac{\partial u}{\partial x} + c_2 \frac{\partial v}{\partial y}) n_x + c_3 (\frac{\partial u}{\partial y} + \frac{\partial v}{\partial x}) n_y \right] ds \quad \text{(B.14)}$$

$$0 = \int_{\Omega^e} \left[\frac{\partial w_2}{\partial y}(c_2 \frac{\partial u}{\partial x} + c_1 \frac{\partial v}{\partial y}) + c_3 \frac{\partial w_2}{\partial x}(\frac{\partial u}{\partial y} + \frac{\partial v}{\partial x}) \right] dxdy \\ - \oint_{\Gamma^e} w_2 \left[(c_2 \frac{\partial u}{\partial x} + c_1 \frac{\partial v}{\partial y}) n_y + c_3 (\frac{\partial u}{\partial y} + \frac{\partial v}{\partial x}) n_x \right] ds$$

where ds is the arclength of an infinitesimal line element along the boundary. From B.13 to B.14 each term was developed separetly and then common terms were grouped. For instance, the first term $\int w_1 \left(-\frac{\partial}{\partial x} c_1 \frac{\partial u}{\partial x}\right) dxdy$ can be rewritten as $\int w_1 \frac{\partial F_1}{\partial x} dxdx$ with $F_1 = -c_1 \frac{\partial u}{\partial x}$. By properties of the derivative of a sum:

$$\int \frac{\partial}{\partial x}(w_1 F_1)\, dxdy = \int \frac{\partial w_1}{\partial x} F_1\, dxdy + \int w_1 \frac{\partial F_1}{\partial x}\, dxdy \quad \text{(B.15)}$$

where the second term in the RHS correspond to the first term in the first equation of B.13. Thus,

$$\int w_1 \frac{\partial F_1}{\partial x}\, dxdy = \int \frac{\partial}{\partial x}(w_1 F_1)\, dxdy - \int \frac{\partial w_1}{\partial x} F_1\, dxdy \quad \text{(B.16)}$$

On the other hand, the volume integral in B.15 can be rewritten in terms of a surface integral by the divergence theorem,

$$\int \frac{\partial}{\partial x}(w_1 F_1)\, dxdy = \oint w_1 F_1 n_x\, ds \quad \text{(B.17)}$$

hence,

$$\int w_1 \frac{\partial F_1}{\partial x}\, dxdy = \oint w_1 F_1 n_x\, ds - \int \frac{\partial w_1}{\partial x} F_1\, dxdy \quad \text{(B.18)}$$

The terms in square brackets in B.14, corresponding to the boundary integrals, constitute the second variables, while the weight functions w_1 and w_2 are the first variations of u and v respectively. Substituting the natural boundary conditions A.18 in B.14, the final weak form is given by:

$$\begin{aligned} 0 &= \int_{\Omega^e} \left[\frac{\partial w_1}{\partial x}(c_1 \frac{\partial u}{\partial x} + c_2 \frac{\partial v}{\partial y} + c_3 \frac{\partial w_1}{\partial y}(\frac{\partial u}{\partial y} + \frac{\partial v}{\partial x}) \right] dxdy - \oint_{\Gamma^e} w_1 t_x \, ds \\ 0 &= \int_{\Omega^e} \left[\frac{\partial w_2}{\partial y}(c_2 \frac{\partial u}{\partial x} + c_1 \frac{\partial v}{\partial y} + c_3 \frac{\partial w_2}{\partial x}(\frac{\partial u}{\partial y} + \frac{\partial v}{\partial x}) \right] dxdy - \oint_{\Gamma^e} w_2 t_y \, ds \end{aligned} \tag{B.19}$$

B.3 Finite Element Model

The functions u and v in B.19 can be approximated over the domain of the element Ω^e by the Lagrange family of interpolation fuctions, in particular for linear triangular elements (Reddy, 1993):

$$\begin{aligned} u &\approx \sum_{j=1}^{3} u_j^e \psi_j^e(x,y) \\ v &\approx \sum_{j=1}^{3} u_j^e \psi_j^e(x,y) \end{aligned} \tag{B.20}$$

where $j = 1, 2, 3$ represents the node of the element. Any other element could have been chosen here ($n > 3$), but these are the simplest ones. In this case, the problem has two degrees of freedom per node (u_j^e, v_j^e) and a total of six nodal displacements per element (fig. B-1).

Next, we substitute approximations B.20 in the weak form B.19. The weight functions are chosen as ψ_i^e. The resulting algebraic relations can be written in matrix form as:

$$\begin{bmatrix} [K^{11}] & [K^{12}] \\ [K^{12}]^T & [K^{22}] \end{bmatrix}^e \begin{bmatrix} [u]^e \\ [v]^e \end{bmatrix} = \begin{bmatrix} [F^1]^e \\ [F^2]^e \end{bmatrix} \tag{B.21}$$

where

$$K_{ij}^{11} = \int (c_1 \frac{\partial \psi_i}{\partial x} \frac{\partial \psi_j}{\partial x} + c_3 \frac{\partial \psi_i}{\partial y} \frac{\partial \psi_j}{\partial y}) \, dxdy \tag{B.22}$$

$$K_{ij}^{12} = K_{ij}^{21} = \int (c_2 \frac{\partial \psi_i}{\partial x}\frac{\partial \psi_j}{\partial y} + c_3 \frac{\partial \psi_i}{\partial y}\frac{\partial \psi_j}{\partial x})\, dxdy \tag{B.23}$$

$$K_{ij}^{22} = \int (c_3 \frac{\partial \psi_i}{\partial x}\frac{\partial \psi_j}{\partial x} + c_1 \frac{\partial \psi_i}{\partial y}\frac{\partial \psi_j}{\partial y})\, dxdy \tag{B.24}$$

and

$$F_i^1 = \oint \psi_i t_x \, ds \tag{B.25}$$

$$F_i^2 = \oint \psi_i t_y \, ds \tag{B.26}$$

where t_x and t_y are the natural boundary conditions as for example in A.18. Equations B.21 are obtained for each element. ψ_i^e has the form

$$\psi_i^e = \frac{1}{2A_e}(\alpha_i^e + \beta_i^e x + \gamma_i^e y) \tag{B.27}$$

where A_e is the area of the triangular element.

In practice, a matrix of correspondence between the global and the local (each element) nodes is built. This matrix determines the assembly of the final stiffness matrix K and F. For instance, if the first global node corresponds to the first node of element 1 and also the first node of element 2 (fig. B-2), $K_{11} = K_{11}^1 + K_{11}^2$ where the superscripts refer to the element number.

After assembly all the elements, the finite element model is complete:

$$\left[\ K\ \right] = \left[\ \bar{u}\ \right] \left[\ F\ \right] \tag{B.28}$$

where $[K]$ has size nxn with n the number of global nodes and $[F]$ and $[\bar{u}]$ are vectors of length $2n$.

The solution of equations B.28 can be computed inverting the matrix $[K]$ as long as it is positive definite. Usually, the stiffness matrix does not have an inverse, however, after imposing the essential conditions on u and v, some rows and columns of $[K]$ can

be "pinned" and the system is reduced to one with solution,

$$\left[\begin{array}{c} \bar{u}^* \end{array} \right] = \left[\begin{array}{c} K^* \end{array} \right]^{-1} \left[\begin{array}{c} F^* \end{array} \right] \tag{B.29}$$

where the vector $[\bar{u}^*]$ contains the approximate solution of u and v at each global node except those already specified from the essential boundary conditions. It has then $2n - b$ unknowns with b the specified degrees of freedom.

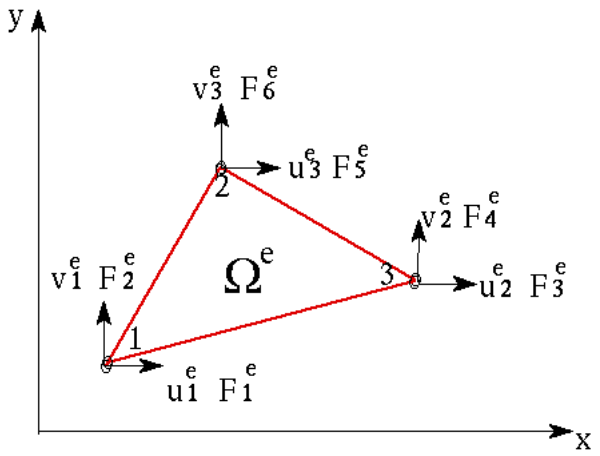

Figure B-1: The figure shows the notation used in system B.21 for one particular triangular element. Modified from Reddy (1993)

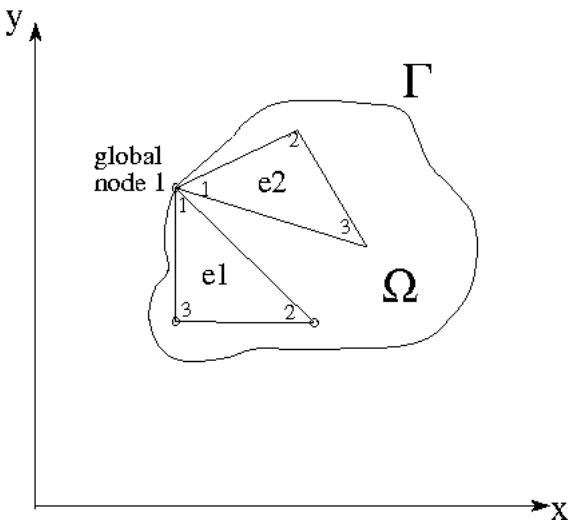

Figure B-2: Two elements of the discretization of Ω whose first node coincide with the global node 1, hence, both contribute to the assembled equation for this node

Appendix C

Practical Aspects of the Fracture Scattering Processing

In this appendix particular challenges of the Lynx field and practical aspects of the *F-K* and *SI* methods are discussed. The methods need to be adjusted when applied to field data because they are fundamentally different from the modeled data based on which the methods were derived. Similarly, data manipulation is often required to make them fit to be input in the fracture processing. Although most of the issues concern typical seismic datasets acquired and processed with today standard technology, some of the limitations of the methods are specifically related to the Lynx field.

C.1 Over and Under Printing

In the synthetic data of chapter 3 the choice of a time window was of little relevance because fractures were modeled only in the "reservoir" layer. The definition of a time window to perform the *F-K* analysis becomes more critical in field cases. If the reservoir is not properly isolated, fracture-related signal may be contaminated with the effects of near surface scatterers or overlying fractured layers of no interest (over printing). Being a differential technique, the *SI* method is insensitive to fractures in the overburden or in formations below the fractured reservoir.

To test over printing effects in the *F-K* method we built and analyzed models of two consecutive fractured layers with different fracture spacing. Orientations of fractures in both layers were the same in one model and orthogonal in another model. The results (not shown) suggest that the bias in the determination of fracture orientation in the deeper layer depends on whether the fractures above are similarly oriented or not. If fracture orientations across depth are different, some destructive interference may occur; thus, normal and parallel orientations may become indistinguishable. However, when fractures are oriented similarly in depth, the fracture scattering changes as a function of time, in amplitude and moveout. These differences appear to be sufficient to resolve the fracture orientation (and spacing) as long as the analysis windows are selected close to each reservoir. If the analysis is localized in this way, fracture scattering coming from each reservoir is dominant in the corresponding window.

Fractures below the target reservoir (under printing) are less harmful to the *F-K* method because their signals will be delayed with respect to the ones from the reservoir.

C.2 Coherent and Random Noise

Ideally, coherent noise including ground roll, air phase, and side or backscattering due to the presence of irregularities near the surface or other topographic features, are removed previous to the fracture analysis. Residuals can be dangerous because linear noise can map in the negative wavenumber space together with the backscattered energy off the fractures. On the other hand, if noise removal filters are too strong, fracture scattering signal may be damaged.

The first step in the *F-K* method consists on the definition of the time and offset window in which the analysis will be carried out. Converted waves, mute artifacts, and residuals of direct arrivals, control the far offset limit of the input data. In field data, and especially in land data where ground roll is present, offsets have to be limited also at the near field. This is the reason why *f-k* transforms of Lynx data are

computed in the offset interval 480 m to 3000 m.

Figure C-1 shows an example of how the F-K method can be corrupted by the ground roll. The analysis is performed in two offset windows: a long window including the near offsets (cyan window and top f-k spectrum), and a shorter window excluding the near offsets (red window - bottom spectrum). High wavenumber components of the ground roll are aliased in the first case mapping into the negative wavenumber space along with other backscattered events. The wrapping adds energy to the negative wavenumber quadrant, biasing the distribution of energy with azimuth according not only to the presence of aligned fractures but to variations of ground roll components with azimuth. At a particular azimuth, like the one in the figure, the algorithm fails to detect the energy peak related to the backscattered waves from fractures. Instead, maximum energy appears at a lower frequency and a small negative wavenumber which corresponds to the ground roll backscattered component. Limiting the offset window leaves out the ground roll and therefore only backscattered signal from fractures dominates the negative wavenumber spectrum (bottom).

Random noise in the SHOT gathers could affect significantly the F-K analysis if the noise has similar frequencies to the backscattered signal. For the SI method, non-stationary noise can be harmful because it would not be deconvolved effectively thus mixing with signal related to the presence of fractures. In general, the SI method is expected to be more sensitive to noise than the F-K method because of resolution differences between these two techniques. The averaging effect of analyzing fracture properties in such an extensive area as the one covered by supershots, simultaneously acts on the noise.

C.3 Wavenumber Resolution

The survey's receiver distance is the most critical parameter to decide whether the F-K method is applicable or not to a particular dataset. In the best case scenario of regular offset distribution in each azimuthal gather, receiver distance or offset sampling rate determines the Nyquist wavenumber and therefore the minimum fracture spacing to

be resolved without aliasing. If the fracture spacing is much less than the receiver distance, the *F-K* method will not be able to detect it.

In Lynx, receivers were spaced 60 m. Such distance is characteristic in nowadays surveys. The seismic frequency bandwidth at the reservoir level ranges between 20 and 50 Hz. This implies that dominant wavelengths are expected to be greater than 90 m, hence recoverable fracture spacings will be tuned to such a value. Fracture corridors with spacing less than 60 m are hard to recover since their signal will be aliased. If fractures are separated slightly less than 60 m, the corresponding wavenumber will be wrapped into the positive k-axis and therefore could become indistinguishable from forward scattered events. If the fracture spacing is much less than 60 m the corresponding wavenumber may fall again into the negative wavenumber space but at an erroneous wavenumber-frequency component. In this case, the *F-K* method will provide an inaccurate estimation of fracture spacing.

The resolution of large fracture spacing (in comparison to dominant wavelengths) is also limited. As the wavenumber approaches zero (fracture spacing increases), the bias of the *F-K* method increases (Dainty and Toksöz, 1990; Dainty and Harris, 1989). This happens because of the constant sampling in wavenumber and frequency intrinsic to the Fourier transform. The 100 m fracture spacing model case in section 3.5 illustrates this problem.

C.4 NMO

Normal moveout has been applied to Lynx's data. NMO is necessary to stack the CMP azimuthal gathers input to the *SI* method. NMO however, can introduce a small bias to the *F-K* results.

Figure C-2 shows the effects of NMO on the *F-K* analysis. Synthetic data in this figure correspond to the fracture model described in section 3.2.4. After NMO (top right), backscattered waves appear with faster apparent velocities. In the Fourier domain, this translates into a slight shift of the *f-k* peak energy of the backscattered waves towards lower frequency-wavenumber. This causes a small over estimation of

fracture spacing. NMO velocities are usually selected to correct primary events, but if velocities are too large and forward scattering waves are over corrected, energy in the negative wavenumber domain could be disrupted.

C.5 High-Angle Structures and Migration

The individual and collective effects on the scattering signal of certain filters and processes need to be studied further. Since scattering energy is generally treated as noise, applying certain processes can potentially attenuate it. However, not applying such processes could also compromise the quality of the fracture analysis. For instance, input data for our analysis were non-migrated thinking that migration could potentially smear out the scattering energy.

In practice, however, we found that unmigrated diffractions introduce ambiguity and make the *F-K* method unstable. As an example, figure C-3 shows the analysis of SHOT 40122 to determine fracture orientation. The backscattered energy and maximum amplitude functions peak at three azimuths: 140°, 220°, and 320°. Because the 220° response is the largest, the automatic *F-K* method picks this azimuth as the direction normal to fractures. However, closer inspection of the time-offset data (figure C-4) reveals that the negative wavenumber energy at this azimuthal gather is not associated to fracture scattering but to unmigrated diffractions. The orientation of fractures is repicked at this SHOT location to be orthogonal to the 140° (or 320°) azimuth.

Usually, and is the case of Lynx, seismic interpretation of main reflectors is carried out on migrated sections, therefore some discrepancies exist between the migrated picks and the time location of horizons, specially at places with prominent structural features. At these areas, the unmigrated seismic section contains dipping reflectors and diffractions.

For the *SI* method in particular, we wanted to understand the sensitivity of the results to uncertainties in the time position of the horizon analyzed. Besides migration, uncertainties could be introduced by automatic picking programs. For this purpose,

the horizon Falher was repicked on the stacked data (top figure C-5). In general, both interpretations agree for most of the survey and, when different, the misfits are less than 100 ms or 50 samples (lower figure C-5). The SI intensity map corresponding to Falher when the analysis is done centered at the horizon picked on the stack is shown in figure C-6. Comparing this result with that shown in figure 5-37, the scattering distribution does not change significantly except maybe at the western and central areas of the survey where the scattering signal is strong. These areas look better defined when using the migrated horizon. This means that the method is robust to horizon small shifts and increases our confidence about applying the method guided by the migrated horizons even though the data are not.

In short, errors in the size and correct location of fractured areas identified with the SI method are expected to occur if unmigrated data are the input for the analysis. However, the comparison we made for Falher indicates that these errors are relatively small if dips are moderate, as in Lynx. Fracture analysis with either the F-K or SI method on unmigrated data provides a map that not necessarily reflex the correct subsurface location of the fracture network. Re-mapping the results to the true positions is not a trivial task.

C.6 Reservoir Thickness

One of the challenges that the Lynx field data imposes on the performance of the fracture processing techniques is the thickness of the Cadotte reservoir. As explained in section 4.3, Cadotte thickness varies between 10 and 35 m, thus below seismic resolution for most of the survey area.

The question about how detectable fractures are in a thin bed was partly answered through the models shown in section 3.5. In the same section, SI analyses are shown to agree with the conclusion drawn from the spectral study, that is, the scattering signal is somewhat reduced when imparted by fractures in a thin bed, but not enough to not disrupt signals from later events and therefore be measurable. In the modeling experiments, scattering index in the direction parallel to fractures decreases in about

50% when the thickness is reduced by a factor of 20. In spite of this amplitude attenuation, scattering energy is still significant when compared to the energy of primaries and, more importantly, azimuthal differences in character are preserved.

Variations of Cadotte's thickness across the survey may have a stronger impact on the fracture processing techniques than the issue of it being a thin bed. This is especially the case for the *SI* method in which analysis windows are shorter. The *SI* method is a deconvolution process in which the character of the transfer function depends on the amount of scattering in an output window with respect to an input window. Therefore, variations in the reverberating character of the transfer function from one location to the next might be attributed to variations of thickness thus becoming indistinguishable from changes in character due to variations in the intensity of fracturing.

Considering Cadotte's thickness, the resolution power of the *SI* method to separate the responses of Cadotte and Falher is questionable. Separation of long and short resistivity curves, fracture observations in image logs, and velocity anisotropy logs, suggest that Falher has a greater fracture density than Cadotte (personal communication with Tad Smith- VeritasDGC). Cadotte and Falher *SI* windows of analysis overlap in about 120 out of 200 ms and indeed, fracture distribution obtained from the post-stack *SI* at these two levels are similar, although scattering indices are in general much lower for the Falher horizon. The pre-stack results for Cadotte and Falher suggest that the *SI* method is resolving some differences in fracture properties between these two formations despite their proximity. Figure 5-43 indicates that Falher's fracture orientations are often rotated with respect to the orientations found above at the Cadotte level. Whether the scattering signal observed corresponds exclusively to Cadotte or to a combination of fracture effects from Cadotte and Falher is not certain at this point.

Another consequence of Cadotte's thickness concerns the imprecision in the interpretation of the associated reflector. The results from both methods will not change drastically if the analysis window is slightly shifted (less than the window length).

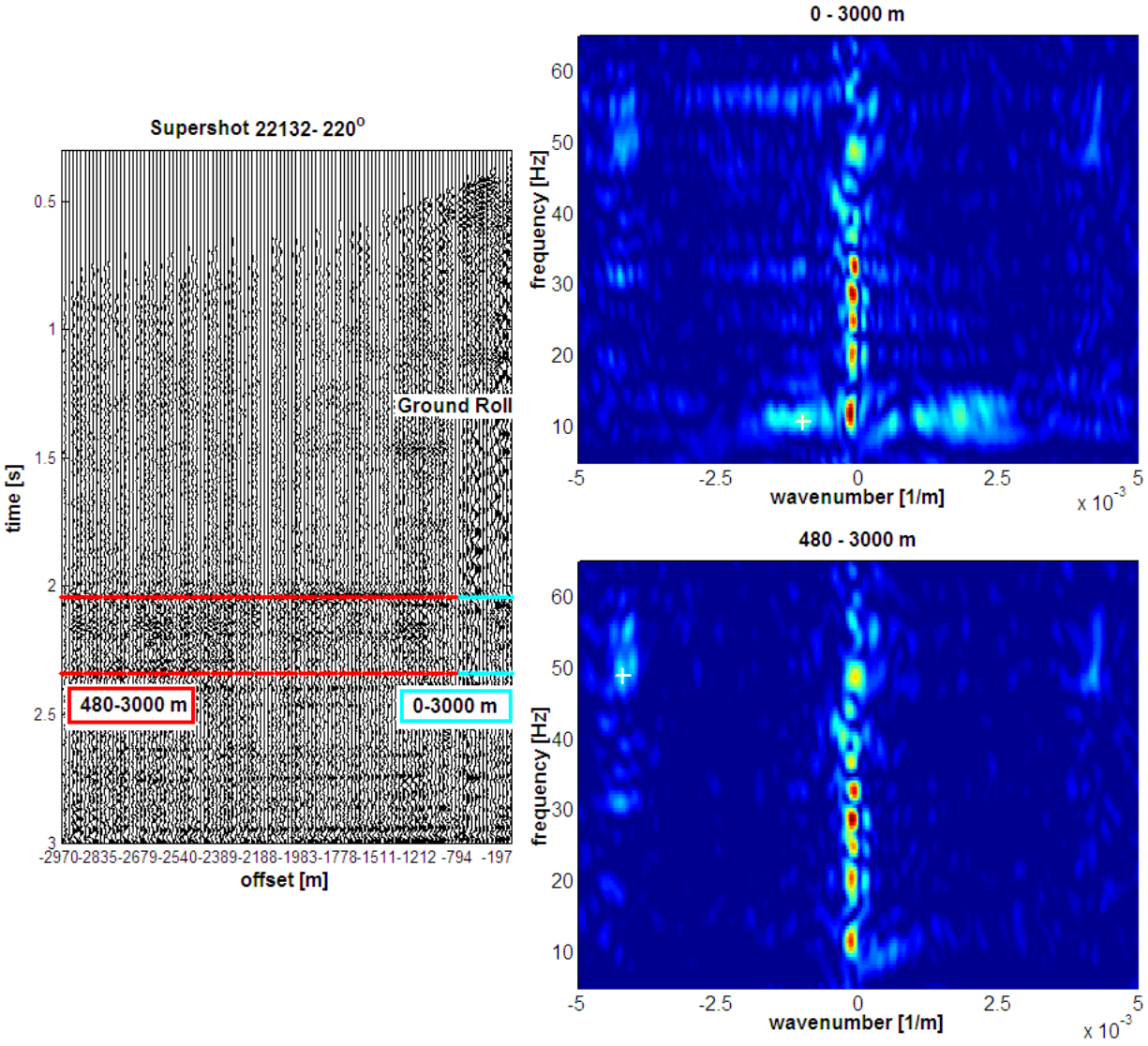

Figure C-1: Ground roll backscattered component can affect the performance of the *F-K* method by introducing undesired energy in the negative wavenumber interval. On the left, a supershot gather shows strong ground roll at near offsets. If these offsets are included in the transformation to the *f-k* domain, the *F-K* method will fail to detect the fractures' backscattered waves (white plus sign- top right). Limiting near offsets attenuates this noise spectral amplitude (bottom right).

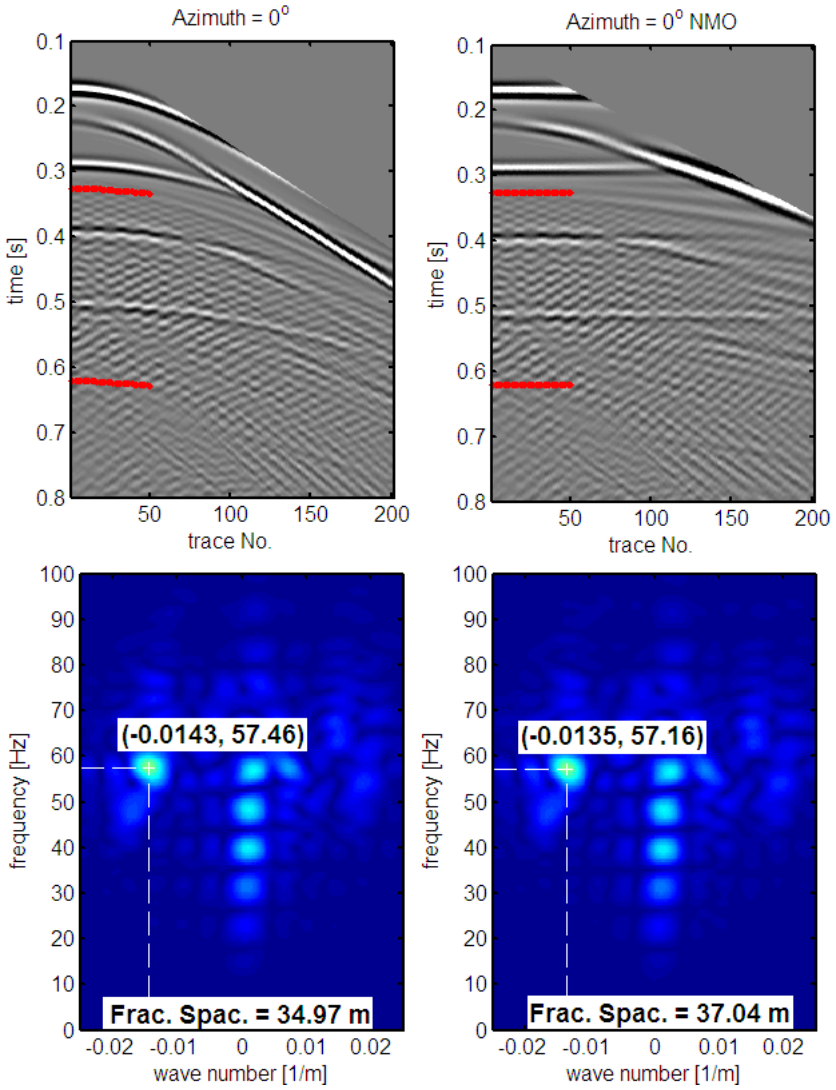

Figure C-2: Modeled shot record normal to fractures without (top left) and with NMO (top right). On the bottom, corresponding *f-k* spectra. Peak wavenumber-frequency in the negative wave number axis for each case is indicated, as well as the estimation of fracture spacing. Data come from the 5-layer model with fractures every 35 m in the 3rd. layer.

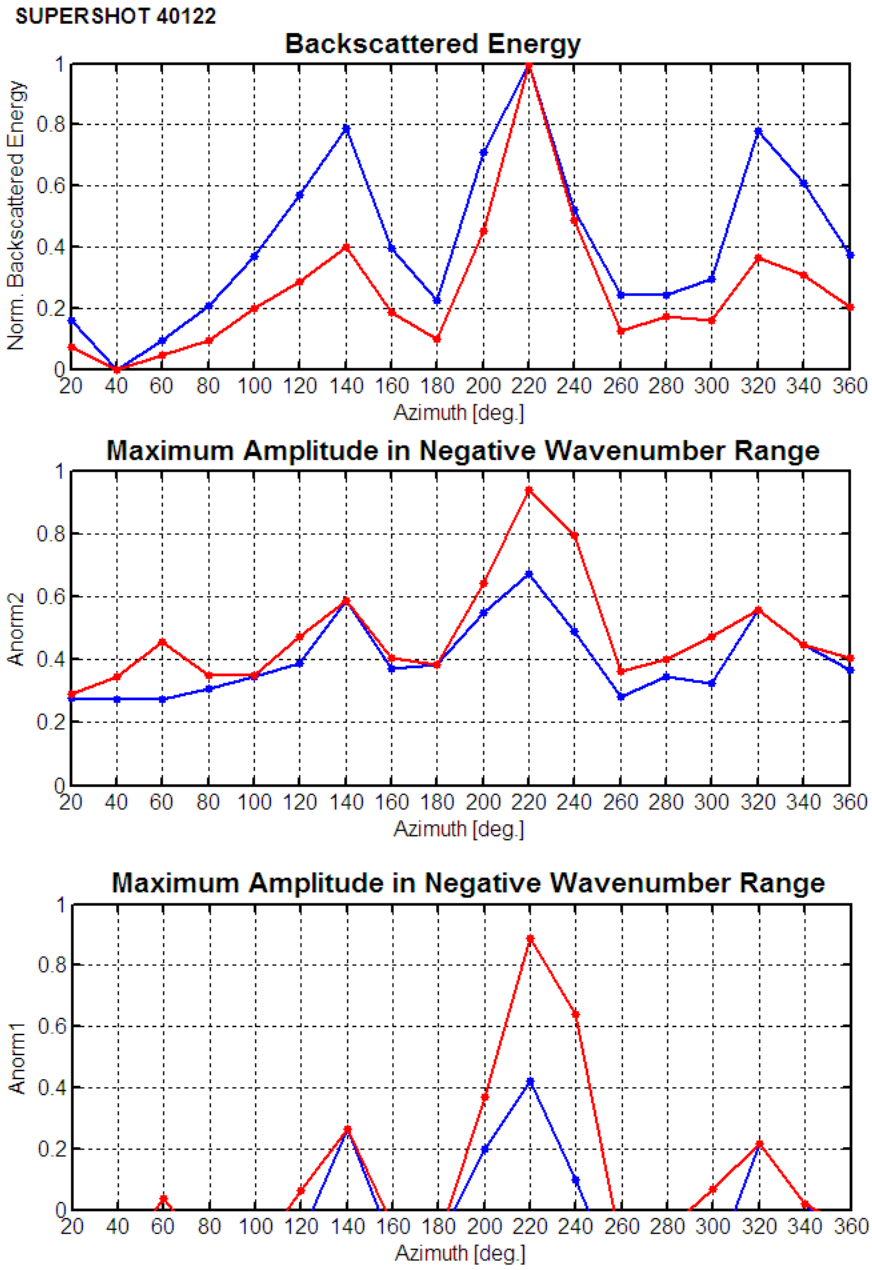

Figure C-3: Supershot 40122 backscattered energy (top) and maximum amplitude functions (middle plot $Anorm2$ and lower plot $Anorm1$). Function values in short wave number range are displayed in blue, and in red for the long wave number range. Both functions peak at 140, 220 and 320° azimuth.

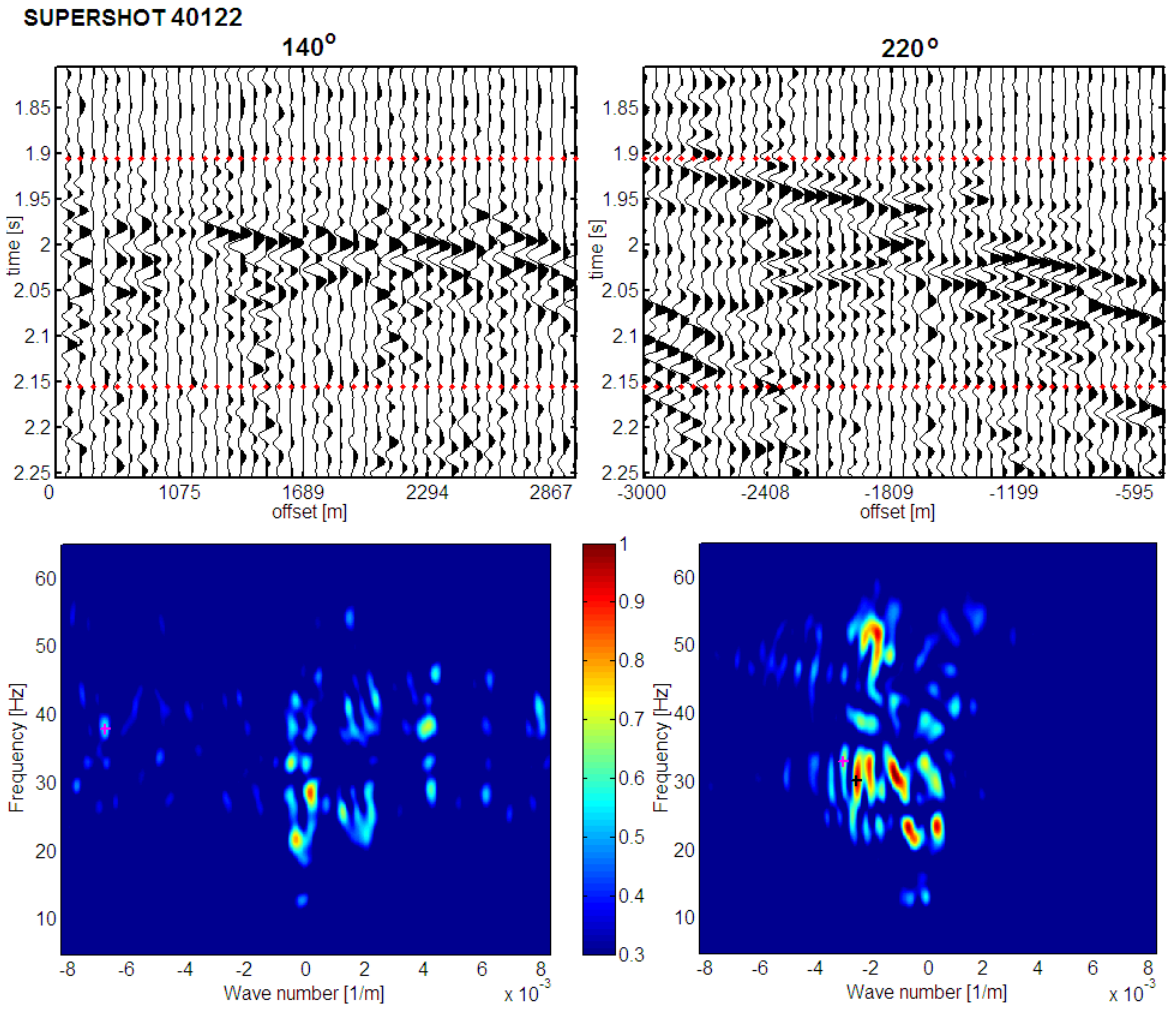

Figure C-4: 140 and 220° azimuthal gathers of supershot 40122. Although negative wavenumber energy maximizes at 220°, this is not the direction normal to fractures because energy is related to the presence of unmigrated diffractions in these data. Instead, 140° is the direction normal to fractures and therefore 40 or 220° is inferred as the fracture orientation at this location. Peak amplitude picked by the F-K method as the backscattered component off fractures is indicated with a magenta (+) sign for the short wave number range and a black (+) sign for the long wave number interval.

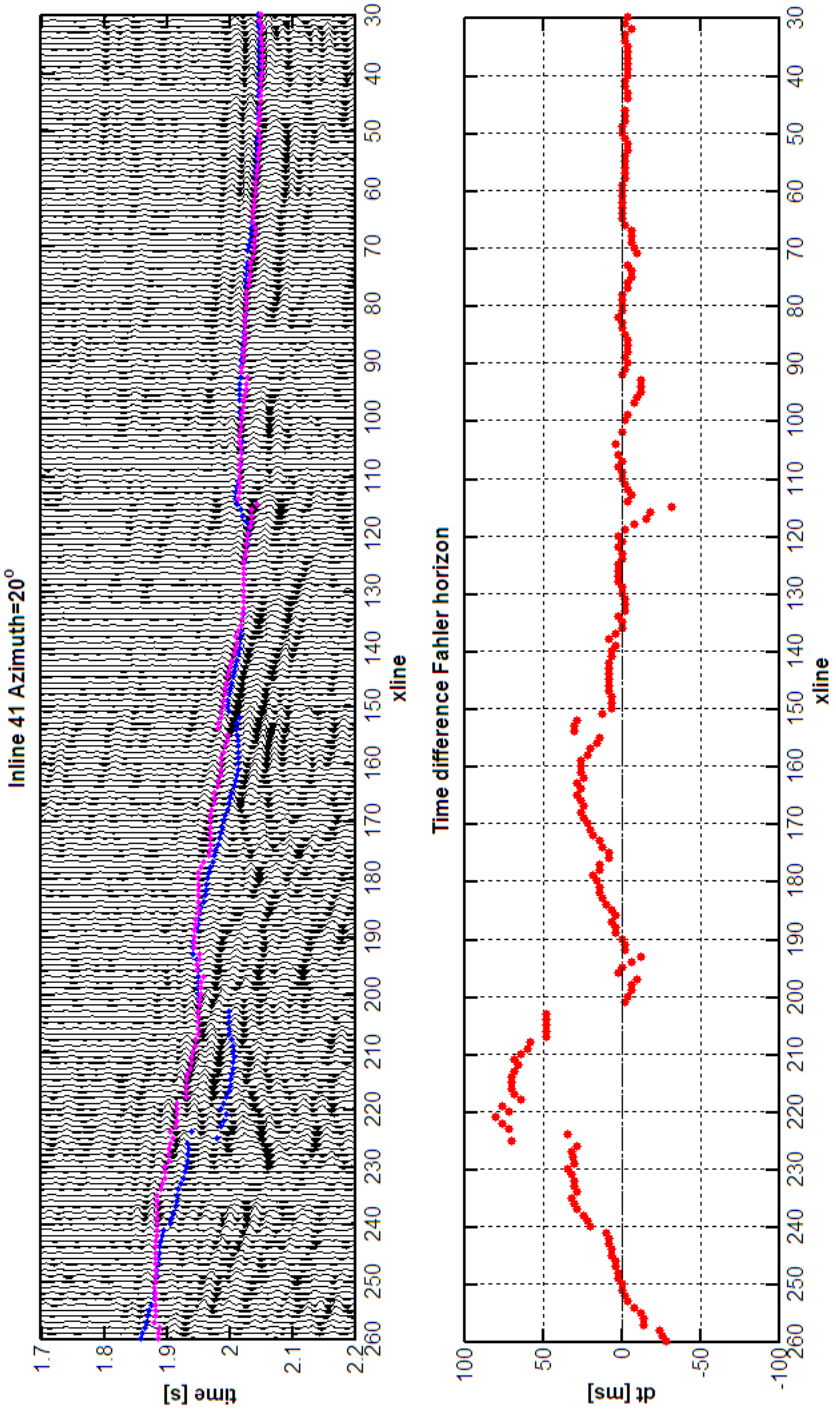

Figure C-5: At the top, inline 41 and interpretation of Falher following stacked data in magenta. The interpretation of this horizon on migrated data is shown in blue. At the bottom, differences in time of horizon picks on stacked and migrated data.

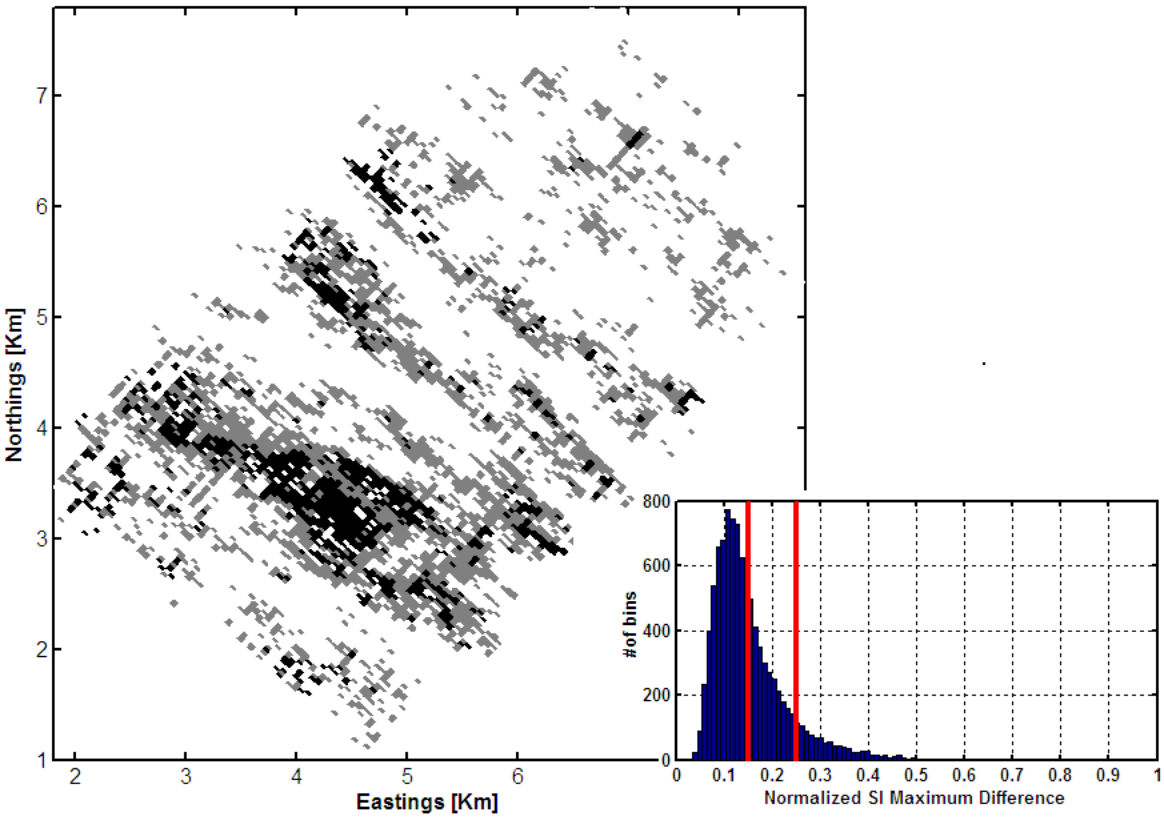

Figure C-6: *SI* post-stack map of fracture distribution and intensity at Falher following horizon picked on the stacked data. In the inset, histogram of normalized scattering indices. Red lines indicate thresholds used to distinguish levels of *SI* intensity in the map. The level at lowest *SI* determines the transition between white and gray areas and the level at largest *SI* marks the transition between gray and black areas.

Bibliography

Acock, A., ORourke, T., Shirmboh, D., Alexander, J., Andersen, G., Kaneko, T., Venkitaraman, A., de Cardenas, J. L., Nishi, M., Yoshioka, K., Roy, A., Wilson, A., and Twynam, A. (2004). Practical Approaches to Sand Management. *Oilfield Review*.

Addis, T., Boulter, D., Roca-Ramisa, L., and Plumb, D. (1993). The Quest for Borehole Stability in the Cusiana Field, Colombia. *Oilfield Review*.

Adushkin, V. V., Rodionov, V. N., Turuntaev, S., and Yudin, A. E. (2000). Seismicity in the oil field. *Oilfield Review*.

Aguilera, R. (1998). Geologic aspects of naturally fractured reservoirs. *The Leading Edge*, pages 1667–1670.

Alberta Energy and Utilities Board (2007). St98-2007: Alberta's energy reserves 2006 and supply/demand outlook 2007-2016. Technical report, Alberta Energy and Utilities Board.

Anderson, E. M. (1951). *The Dynamics of Faulting and Dyke Formation with Applications to Britain*. Ed. Oliver and Boyd, Edimburgh, 2nd edition.

Ata, E. and Michelena, R. (1995). Mapping distribution of fractures in a reservoir with p-s converted waves. *The Leading Edge*, 14(6):664–676.

Bai, T. and Pollard, D. P. (2000). Fracture spacing in layered rocks: a new explanation based on the stress transition. *Journal of Structural Geology*, 22:43–57.

Barkved, O. I. and Kristiansen, T. (2005). Seismic time-lapse effects and stess-changes: Examples from a compacting reservoir. *The Leading Edge*, 24(12):1244–1248.

Barton, C. A. and Zoback, M. D. (1988). Determination of In Situ Stress Orientation from Borehole Guided Waves. *Journal of Geophysical Research*, 93(B7):7834–7844.

Bell, J. S. (2006). *In situ* stress and coal bed methane potential in Western Canada. *Bulletin of Canadian Petroleum Geology*, 54(3):197–220.

Bell, J. S. and Babcock, E. A. (1986). The stress regime of the Western Canadian Basin and implications for hydrocarbon production. *Bulletin of Canadian Petroleum Geology*, 34(3):364–378.

Bell, J. S. and Bachu, S. (2003). *In situ* stress magnitude and orientation estimates for Cretaceous coal-bearing strata beneath the plains area of central and southern Alberta. *Bulletin of Canadian Petroleum Geology*, 51(1):1–28.

Bell, J. S., Price, P. R., and McLellan, P. J. (1994). Chapter 29: In-situ Stress in the Western Canada Sedimentary Basin. In *Geological Atlas of the Western Canada Sedimentary Basin*. Alberta Energy and Utilities Board and Alberta Geological Survey.

Bourbie, T., Coussy, O., and Zinszner, B. (1987). *Acoustics of Porous Media*. Editions Technip. Institute Français du Pètrole publications.

Bratton, T., Canh, D. V., Que, N. V., Duc, N. V., Gillespie, P., Hunt, D., Li, B., Marcinew, R., Ray, S., Montarin, B., Nelson, R., Schoderbek, D., and Sonneland, L. (2006). The nature of naturally fractured reservoirs. *Oilfield Review*.

Brie, A., Codazzi, D., Denoo, S., Mueller, M., and Plona, T. (1998). New Directions in Sonic Logging. *Oilfield Review*.

Bruno, M. S. and Winterstein, D. F. (1994). Some influences of stratigraphy and structure on reservoir stress orientation. *Geophysics*, 59(6):954–962.

Burns, D. R., Willis, M. E., and Toksöz, M. N. (2007). Fracture properties from seismic scattering. *The Leading Edge*, 26(9):1186–1196.

Canadian Discovery Digest (2004). Lynx Area Cadotte. Faults and folds give gas galore. Canadian Discovery Digest. pp.5-16.

Charlez, P. A. and Onaisi, A. (2001). Wellbore Stability: One of the Most Important Engineering Challenges when Drilling Smart Wells. In Lecourtier, J., editor, *Interactive Drilling for fast track Oilfield Development*, pages 77–102. TECHNIP, Rueil-Mailmaison, France.

Claerbout, J. (1985). *Fundamentals of geophysical data processing: with applications to petroleum prospecting*. Blackwell Scientific Publications.

Coates, G. R. and Denoo, S. (1981). Mechanical Properties Program using Borehole Analysis and Mohr's Circle. *SPWLA 22nd. Annual Logging Symposium*, pages DD 1– 16.

Coates, R. and Schoenberg, M. (1995). Finite-difference modeling of faults and fractures. *Geophysics*, 60(5):1514–1526.

Colmenares, L. and Zoback, M. D. (2003). Stress field and seismotectonics of northern South America. *Geology*, 31:721–724.

Crampin, S., Chesnokov, E. M., and Hipkin, R. G. (1984). Seismic anisotropy- the state of the art: II. *Geophysical Journal of the Royal Astronomical Society*, 76:1–16.

Dainty, A. M. and Harris, D. B. (1989). Phase velocity estimation of diffusely scattered waves. *Bulletin of the Seismological Society of America*, 79(4):1231–1250.

Dainty, A. M. and Toksöz, M. N. (1990). Array analysis of seismic scattering. *Bulletin of the Seismological Society of America*, 80(6):2242–2260.

Daley, T., Nihei, K., Myer, L., Majer, E., Queen, J., and Murphy, J. (2002). Numerical modeling of scattering from discrete fracture zones in a San Juan basin

gas reservoir. In *Expanded Abstracts*. Society of Exploration Geophysicists, 70th Annual International Meeting.

DeMets, C., Gordon, R. G., Argus, D. F., and Stein, S. (1990). Current plate motions. *Geophysical Journal International*, 101:425–478.

DeMets, C., Gordon, R. G., Argus, D. F., and Stein, S. (1994). Effect of recent revisions to the geomagnetic reversal time scale on estimates of current plate motions. *Geophysical Research Letters*, 21(20):2191–2194.

Ellefsen, K. J. (1990). *Elastic Wave Propagation Along a Borehole in an Anisotropic Medium*. PhD thesis, Massachusetts Institute of Technology.

Fjaer, E. (1999). Static and Dynamic Moduli of Weak Sandstones. *Rock Mechanics for Industry*, pages 675–681.

Fjaer, E. and Holt, R. M. (1994). Rock Acoustics and Rock Mechanics: Their Link in Petroleum Engineering. *The Leading Edge*, pages 255–258.

Frederick, J., Deitrick, G., Arguello, J., and de Rouffignac, E. (1988). Reservoir Compaction, Surface Subsidence and Casing Damage: a Geomechanics Approach to Mitigation and Reservoir Management. *SPE/ISRM EUROCK*.

Grandi, S., Yuh, S., Willis, M., and Toksöz, N. (2006). Fracture characterization from scattered energy: a case study. In *Expanded Abstracts*, pages 1732–1736. Society of Exploration Geophysicists, 74th Annual International Meeting.

Groenenboom, J. and Falk, J. (2000). Scattering by hydraulic fractures: Finite difference modeling and laboratory data. *Geophysics*, 65(2):612–622.

Gueguen, Y. and Palciauskas, V. (1994). *Introduction to the Physics of Rocks*. Princeton Univ. Press.

Haimson, B. C. and Cornet, F. H. (2003). ISRM suggested methods for rock stress estimation- Part 3: hydraulic fracturing (HF) and/or hydraulic testing of existing

fractures (HTPF). *International Journal of Rock Mechanics and Mining Science*, 40:1011–1020.

Hatchell, P. and Bourne, S. (2005). Rocks under strain: Strain-induced time-lapse time shifts are observed for depleting reservoirs. *The Leading Edge*, 24(12):1222–1225.

Hawkes, C. D., Bachu, S., Haug, K., and Thompson, A. W. (2005). Analysis of In-Situ Stress Regime in the Alberta Basin, Canada, for Performance Assessment of CO_2 Geological Sequestration Sites. In *Fourth Annual Conference of Carbon Capture and Sequestration*. DOE/NETL.

Hsu, C.-J. and Schoenberg, M. (1993). Elastic waves through a simulated fractured medium. *Geophysics*, 58(7):964–977.

Huang, X. (2003). *Effects of tool positions on borehole acoustic measurements: a stretched grid finite difference approach*. PhD thesis, Massachusetts Institute of Technology.

Huang, X., Zhu, Z., Toksöz, M. N., and Burns, D. R. (2000). Effects of formation stress on logging measurements. pages 10.1–10.21. Borehole Acoustics Logging and Reservoir Delineation Consortia, Earth Resources Laboratory, MIT.

Jaeger, J. C. and Cook, N. G. (1979). *Fundamentals of Rock Mechanics*. Chapman and Hall, London.

Krasovec, M. L., Burns, D. R., and Tokzöz, M. N. (2003). Finite difference modeling of attenuation and anisotropy. Borehole Acoustics and Logging and Reservoir Delineation Consortia, Earth Resources Laboratory, MIT.

Kreemer, C., Holt, W. E., and Haines, A. J. (2003). An integrated global model of present-day plate motions and plate boundary deformation. *Geophysical Journal International*, 154:8–34.

Last, N. C. (2001). Achieving and Maintaining Improved Drilling Performance in the Tectonically Stressed Andean Foothills of Colombia. In Lecourtier, J., editor, *Interactive Drilling for fast track Oilfield Development*, pages 59–75. TECHNIP, Rueil-Mailmaison, France.

Lee, S., Shaw, J., Ho, R., and Steeb, D. (1999). Deepwater reservoir prediction using seismic and geomechanical methods. *The Leading Edge*, 18(7):726–728.

Lewis, H. and Couples, G. D. (1993). Production evidence of geological heterogeneities in the Anschutz Ranch East Field, western USA. In North, C. P. and Posser, D. J., editors, *Characterization of Fluvial and Aeolian Reservoirs*, number 73, pages 321–338. Geological Society Publication.

Li, Y., Cheng, C. H., and Toksöz, M. N. (1998). Seismic monitoring of the growth of a hydraulic fracture zone at Fenton Hill, New Mexico. *Geophysics*, 63(1):120–131.

Liu, E., Hudson, J. A., and Pointer, T. (2000). Equivalent medium representation of fractured rock. *Journal of Geophysical Research*, 105(B2):2981–3000.

Ljunggren, C., Chang, Y., Janson, T., and Christiansson, R. (2003). An overview of rock stress measurements methods. *International Journal of Rick Mechanics and Mining Sciences*, 40:975–989.

Lo, T., Coyner, K. B., and Toksöz, M. N. (1986). Experimental determination of elastic anisotropy of Berea sandstone, Chicopee shale and Chelmsford granite. *Geophysics*, 51(1):164–171.

Lynn, H. (2004a). The winds of change: Anisotropic rocks- their preferred direction of fluid flow and their associated seismic signatures- Part 1. *The Leading Edge*, 23(11):1156–1162.

Lynn, H. (2004b). The winds of change: Anisotropic rocks- their preferred direction of fluid flow and their associated seismic signatures- Part 2. *The Leading Edge*, 23(12):1258–1268.

Malvern, L. E. (1969). *Introduction to the Mechanincs of a Continuous Medium*. Prentice-Hall.

McMechan, M. E. (1999). Geometry of the structural front in the Kakwa area, northern Foothills of Alberta. *Bulletin of Canadian Petroleum Geology*, 47(1):31–42.

Monger, J. and Price, R. (2002). The Canadian Cordillera: Geology and Tectonic Evolution. *CSEG Recorder*, pages 17–36.

Moos, D. and Zoback, M. D. (1990). Utilization of observations of well bore failure to constrain the orientation and magnitude of crustal stresses: application to continental, deep sea drilling project and ocean drilling program boreholes. *Journal of Geophysical Research*, 91(B6):9305–9325.

Naciri, M. and Mei, C. C. (1988). Bragg scattering of water waves by a doubly periodic seabed. *Journal of Fluid Mechanics*, 192:51–74.

Nakagawa, S., Nihei, K. T., Myer, L. R., and Majer, E. L. (2003). Three-dimensional elastic wave scattering by a layer containing vertical periodic fractures. *Journal of Acoustical Society of America*, 113(6):3012–3023.

Narr, W. and Suppe, J. (1991). Joint spacing in sedimentary rocks. *Journal of Structural Geology*, 13(9):1037–1048.

Nelson, R. A. (2001). *Geological Analysis of Naturally Fractured Reservoirs*. Gulf Professional Publishing, 2nd edition.

Newson, A. C. (2001). The future of natural gas exploration in the Foothills of the Western Canadian Rocky Mountains. *The Leading Edge*.

Nihei, K., Nakagawa, S., Myer, L., and Majer, E. (2002). Finite difference modeling of seismic wave interactions with discrete, finite length fractures. In *Expanded Abstracts*. Society of Exploration Geophysicists, 72nd Annual Meeting.

Nihei, K. T., Myer, L., Cook, N. G. W., and Yi, W. (1994). Effects of non-welded interfaces on guided SH-waves. *Geophysical Research Letters*, 21(9):745–748.

Nihei, K. T., Yi, W., Myer, L., and Cook, N. G. W. (1999). Fracture channel waves. *Journal of Geophysical Research*, 104(B3):4769–4781.

Norabuena, E., Leffler-Griffin, L., Mao, A., Dixon, T., Stein, S., Sacks, I. S., Ocola, L., and Ellis, M. (1998). Space Geodetic Observations of Nazca-South America Convergence Across the Central Andes. *Science*, 279.

Norabuena, E. O., Dixon, T. H., Stein, S., and Harrison, C. G. A. (1999). Decelerating Nazca-South America and Nazca-Pacific Plate Motions. *Geophysical Research Letters*, 26:3405–3408.

Ortega, O. L., Marrett, R. A., and Laubach, S. E. (2006). A scale independent approach to fracture intensity and average spacing measurements. *AAPG Bulletin*, 90(2):193–208.

Ozkaya, S. I., Kolkman, W., and Amthor, J. (2003). Mechanical layer-dependent fracture characteristics from fracture density vs tvd cross plots. Examples from horizontal wells in carbonate reservoirs, North Oman. AAPG, Annual Convention.

Parnaud, F., Gou, Y., Pascual, J. C., Truskowski, I., Gallango, O., Passalacqua, H., and Roure, F. (1995). Petroleum geology of the central part of eastern venezuela basin. In *Petroleum Basins of South America*, volume 62, pages 741–756. AAPG Memoir.

Partyka, G., Gridley, J., and Lopez, J. (1999). Interpretational applications of spectral decomposition in reservoir characterization. *The Leading Edge*, 18(3):353–360.

Pérez, M., Grechka, V., and Michelena, R. (1999). Fracture detection in a carbonate reservoir using a variety of seismic methods. *Geophysics*, 64(4):1266–1276.

Pérez, O., Bilham, R., Bendick, R., Velandia, J. R., Hernandez, N., Moncayo, C., Hoyer, M., and Kozuch, M. (2001). Velocity field across the southern Caribbean

plate boundary and estimates of Caribbean/South-American plate motion using GPS geodesy 1994-2000. *Geophysical Research Letters*, 28(15):2987–2990.

Plumb, R. A. and Hickman, S. H. (1985). Stress-Induced Borehole Elongation: A Comparison Between the Four-Arm Dipmeter and the Borehole Televiewer in the Auburn Geothermal Well. *Journal of Geophysical Research*, 90(B7):5513–5521.

Press, W., Teukolsky, S., Vetterling, W., and Flannery, B. (1999). *Numerical recipes in C. The Art of Scientific Computing*. Cambridge University Press.

Price, R. A. (1994). Chapter 2: Cordilleran Tectonics and the Evolution of the Western Canada Sedimentary Basin. In *Geological Atlas of the Western Canada Sedimentary Basin*. Alberta Energy and Utilities Board and Alberta Geological Survey.

Pyrak-Nolte, L. J. (1996). The seismic response of fractures and the interrelations among fracture properties. *International Journal of Rock Mechanics and Mining Science and Geomechanics Abstracts*, 33(8):785–802.

Pyrak-Nolte, L. J., Cook, N. G. W., and Myer, L. R. (1987). Seismic visibility of fractures. In *Rock Mechanics: Proceedings of the 28th U.S. Symposium*.

Pyrak-Nolte, L. J., Myer, L., and Cook, N. G. W. (1990). Anisotropy in seismic velocities and amplitudes from multiple parallel fractures. *Journal of Geophysical Research*, 95(B7):11345–11358.

Pyrak-Nolte, L. J. and Roy, S. (2000). Monitoring fracture evolution with compressional-mode interface waves. *Geophysical Research Letters*, 27(20):3397–3400.

Rao, R., Willis, M., Burns, D., Toksöz, N., and Vetri, L. (2005). Fracture spacing and orientation estimation from spectral analyses of azimuth stacks. In *Expanded Abstracts*, pages 1409–1412. Society of Exploration Geophysicists, 73rd Annual International Meeting.

Reddy, J. N. (1993). *An Introduction to the Finite Element Method*. McGraw Hill.

Reinecker, J., Heidbach, O., Tingay, M., Sperner, B., and Müller, B. (2005). The 2005 release of the World Stress Map. (available online at www.world-stress-map.org).

Robinson, E. and Treitel, S. (1980). *Geophysical signal analysis*.

Sayers, C. M. (2006). An introduction to velocity-based pore-pressure estimation. *The Leading Edge*, 25(12):1496–1500.

Sayers, C. M. (2007). Introduction to this special section: Fractures. *The Leading Edge*, 26(9):1102–1105.

Schoenberg, M. (1980). Elastic wave behavior across linear slip interfaces. *Journal of Acoustical Society of America*, 68(5):1516–1521.

Schoenberg, M. and Douma, J. (1988). Elastic wave propagation in media with parallel fractures and aligned cracks. *Geophysical Prospecting*, 36:571–589.

Schoenberg, M. and Sayers, C. M. (1995). Seismic anisotropy of fractured rock. *Geophysics*, 60(1):204–211.

Sella, G. F. (2002). Revel: A model for Recent plate velocities from space geodesy. *Journal of Geophysical Research*, 107.

Sen, M. K., Lane, F. D., and Foster, D. J. (2007). Anomalous reflection amplitudes from fractured reservoirs- Failure of AVOA? *The Leading Edge*, 26(9):1148–1152.

Sen, V. and Settari, A. (2005). Coupled geomechanical and flow modeling of compacting reservoirs. *The Leading Edge*, 24(12):1284–1287.

Sinha, B. K. and Kostek, S. (1996). Stress-induced azimuthal anisotropy in borehole flexural waves. *Geophysics*, 61(6):1899–1907.

Sinha, B. K., Norris, A. N., and Chang, S.-K. (1994). Borehole flexural modes in anisotropic formations. *Geophysics*, 59(7):1037–1052.

Sze, E. K.-M. (2005). *Induced seismicity analysis for reservoir characterization at a petroleum field in Oman*. PhD thesis, Massachusetts Institute of Technology.

van der Pluijm, B. A. and Marshak, S. (2004). *Earth Structure: An introduction to Structural Geology and Tectonics*. Mc Graw Hill.

Vlastos, S., Liu, E., Main, I., and Li, X. (2003). Numerical simulation of wave propagation in media with discrete distribution of fractures: effects of fracture sizes and spatial distributions. *Geophys. J. Int.*, 152:649–668.

Weber, J. C., Dixon, T. H., DeMets, C., Ambeh, W. B., Jansma, P., Mattioli, G., Saleh, J., Sella, G., Bilham, R., and Pérez, O. (2001). GPS estimate of relative motion between the Caribbean and South American plates, and geologic implications for Trinidad and Venezuela. *Geology*, 29:75–78.

Wennekers, J. H. N. (2007a). Wcsb Structural Domains-1: W. Canada structured belt given high gas potential. *Oil and Gas Journal*, 105(21).

Wennekers, J. H. N. (2007b). Wcsb Structural Domains-2: Massive rock ploughs formed structures in western Canada. *Oil and Gas Journal*, 105(22).

Widess, M. B. (1973). How thin is a thin bed? *Geophysics*, 38(6):1176–1180.

Willis, M., Burns, D., Rao, R., Minsley, B., Toksöz, N., and Vetri, L. (2006). Spatial orientation and distribution of reservoir fractures from scattered seismic energy. *Geophysics*, 71(5):O43–O51.

Willis, M., Burns, D. R., Rao, R., and Minsley, B. (2003). Characterization of scattered waves from fractures by estimating the transfer function between reflected events above and below each interval. Borehole Acoustics and Logging and Reservoir Delineation Consortia, Earth Resources Laboratory, MIT.

Willis, M., Rao, R., Burns, D., and Byun, J. (2004a). Spatial orientation and distribution of reservoir fractures from scattered seismic energy. In *Expanded Abstracts*, pages 1535–1538. SEG, 72nd Annual International Meeting.

Willis, M., Zhang, Y., and Burns, D. R. (2004b). Comparison of scattering energy using point scatterers versus full 3d finite difference modelling. Borehole Acoustics and Logging and Reservoir Delineation Consortia, Earth Resources Laboratory, MIT.

Willis, M. E., Burns, D. R., Lu, R., Toköz, M. N., and House, N. (2007). Fracture quality from integrating time-lapse VSP and microseismic data. *The Leading Edge*, 26(9):1198–1199.

Winkler, K. W. (1997). Acoustic evidence of mechanical damage surrounding stressed boreholes. *Geophysics*, 62(1):16–22.

Winkler, K. W., Sinha, B. K., and Plona, T. J. (1998). Effects of borehole stress concentrations on dipole anisotropy measurements. *Geophysics*, 63(1):11–17.

Worthington, M. (2007). The compliance of macrofractures. *The Leading Edge*, 26(9):1118–1122.

Xian, C., Nolte, D. D., and Pyrak-Nolte, L. J. (2001). Compressional waves guided between parallel fractures. *International Journal of Rock Mechanics and Mining Science*, 38:765–776.

Yale, D. P. (2003). Fault and stress magnitude controls on variations in the orientation of *in situ* stress. In Ameen, M., editor, *Fracture and In-Situ Stress Characterization of Hydrocarbon Reservoirs*, volume 209, pages 55–64. Geological Society, London, Special Publications.

Yi, W., Nakagawa, S., Nihei, K., Rector, J., Myer, L., and Cook, N. (1997). Numerical investigation of fracture-induced seismic anisotropy. In *Expanded Abstracts*. Society of Exploration Geophysicists, 67th Annual International Meeting.

Yi, W., Nakagawa, S., Nihei, K., Rector, J., Myer, L., and Cook, N. (1998). Numerical investigation of fracture channel waves. In *Expanded Abstracts*. Society of Exploration Geophysicists, 68th Annual International Meeting.

Yilmaz, O. (2001). *Seismic Data Analysis. Processing, Inversion, and Interpretation of Seismic Data*, volume 1. Investigations in Geophysics. No. 10. Society of Exploration Geophysicists.

Zoback, M. D. (2007). *Reservoir Geomechanics*. Cambridge University Press.

Zoback, M. D., Mastin, L., and Barton, C. (1986). In-Situ Stress Measurements in Deep Boreholes using Hydraulic Fracturing, Wellbore Breakouts, and Stoneley Wave Polarization. In *Proceedings of the International Symposium on Rock Stress and Rock Stress Measurements*, pages 289–299, Stockholm.

Zoback, M. D., Moos, D., and Mastin, L. (1985). Well Bore Breakouts and In Situ Stress. *Journal of Geophysical Research*, 90(B7):5523–5530.

Zoback, M. D. and Zoback, M. L. (1989). Stress in the Earth's Lithosphere. In Fairbridge, R., editor, *Encyclopedia of Earth Sciences Series*, pages 1221–1232. Van Nostrand Reinhold Co., New York.